UNRAVELLING EFFICIENT AND SUSTAINABLE NEXT-GENERATION SOLAR CELLS *via* DOPING AND INTERFACE ENGINEERING

Ph.D. Thesis

By

ABHISHEK SRIVASTAVA



DEPARTMENT OF METALLURGICAL ENGINEERING AND MATERIALS SCIENCE

INDIAN INSTITUTE OF TECHNOLOGY INDORE

MARCH 2026

UNRAVELLING EFFICIENT AND SUSTAINABLE NEXT-GENERATION SOLAR CELLS *via* DOPING AND INTERFACE ENGINEERING

A THESIS

Submitted in partial fulfillment of the
requirements for the award of the degree
of
DOCTOR OF PHILOSOPHY

by

ABHISHEK SRIVASTAVA



DEPARTMENT OF METALLURGICAL ENGINEERING AND MATERIALS SCIENCE
INDIAN INSTITUTE OF TECHNOLOGY INDORE

MARCH 2026

INDIAN INSTITUTE OF TECHNOLOGY INDORE

CANDIDATE'S DECLARATION

I hereby certify that the work which is being presented in the thesis entitled **"UNRAVELLING EFFICIENT AND SUSTAINABLE NEXT-GENERATION SOLAR CELLS *via* DOPING AND INTERFACE ENGINEERING"** in the partial fulfillment of the requirements for the award of the degree of **DOCTOR OF PHILOSOPHY** and submitted in the **DEPARTMENT OF METALLURGICAL ENGINEERING AND MATERIALS SCIENCE, Indian Institute of Technology Indore**, is an authentic record of my own work carried out during the time period from August 2021 to March 2026 under the supervision of Prof. Parasharam M. Shirage, Department of Metallurgical Engineering and Materials Science and Prof. Kiran Bala, Mehta Family School of Biosciences and Biomedical Engineering.

The matter presented in this thesis has not been submitted by me for the award of any other degree of this or any other institute.

03 June 2026

Signature of the student with date

ABHISHEK SRIVASTAVA

This is to certify that the above statement made by the candidate is correct to the best of my/our knowledge.

Dr. Parasharam M. Shirage
Professor
Department of Metallurgy Engineering and Materials Science (MEMS)
Indian Institute of Technology Indore
Khandwa Road, Simrol,
INDORE-453552 INDIA

Signature of Thesis Supervisor with date

(Prof. PARASHARAM M. SHIRAGE)

Signature of Thesis Co-Supervisor with date

(Prof. KIRAN BALA)

ABHISHEK SRIVASTAVA has successfully given his Ph.D. Oral Examination held on 02 June, 2026.

Dr. Parasharam M. Shirage
Professor
Department of Metallurgy Engineering and Materials Science (MEMS)
Indian Institute of Technology Indore
Khandwa Road, Simrol,
INDORE-453552 INDIA

Signature of Thesis Supervisor with date

(Prof. PARASHARAM M. SHIRAGE)

Signature of Thesis Co-Supervisor with date

(Prof. KIRAN BALA)

ACKNOWLEDGEMENTS

First and foremost, I would like to express my profound and heartfelt gratitude to **Prof. Parasharam M. Shirage**, Professor in the Department of Metallurgical Engineering and Materials Science at the Indian Institute of Technology Indore. His exceptional mentorship, visionary guidance, and unwavering support have been the cornerstone of the successful completion of this research work. I am deeply indebted to him for his continuous encouragement, intellectual insight, and generous investment of his valuable time in critically reviewing my work. His thoughtful suggestions and constructive feedback greatly contributed to refining the manuscript in its final form. Beyond academic guidance, his passion for scientific inquiry, dedication to excellence, and inspiring leadership have been a constant source of motivation throughout my Ph.D. journey, shaping both my research perspective and professional growth.

I extend my sincere and heartfelt appreciation to my co-supervisor, **Prof. Kiran Bala**, for her valuable guidance, constant encouragement, and insightful discussions throughout the course of my research. Her thoughtful suggestions and academic support have been instrumental in strengthening various aspects of this work. I would also like to express my gratitude to the members of my Ph.D. Student Progress Committee (PSPC), **Prof. Sunil Kumar** and **Prof. Preeti A. Bhobe**, for their continuous evaluation of my research progress and their constructive feedback. Their critical observations and valuable suggestions significantly contributed to refining the technical depth and overall quality of this research.

I am also sincerely grateful to **Prof. Pradeep Mathur**, the founding Director of Indian Institute of Technology Indore, and **Prof. Suhash S. Joshi**, the current Director, for fostering an outstanding academic and research environment at the institute. Their leadership and vision have been instrumental in providing state-of-the-art facilities and an enabling atmosphere that greatly supported the successful execution of this research work.

I gratefully acknowledge the financial support provided by the **Department of Science and Technology, Government of India**, through the **INSPIRE Fellowship**. The fellowship supported my Ph.D. research and facilitated my participation in national and international

conferences, which greatly contributed to the progress and dissemination of my work. I also sincerely acknowledge the **Department of Metallurgical Engineering and Materials Science**, **IIT Indore**, and the **Sophisticated Instruments Center (SIC)**, **IIT Indore**, for providing access to state-of-the-art experimental and characterization facilities, which were essential for successfully carrying out this research.

I would like to express my sincere gratitude to **Dr. Sawanta S. Mali**, **Dr. Jyoti V. Patil**, and **Prof. Chang Kook Hong** from the Chonnam National University, Gwangju, South Korea, and to **Dr. Hyunju Lee**, **Prof. Yoshio Ohshita**, and **Prof. Atsushi Ogura** from the Meiji University and Toyota Technological Institute, Nagoya, Japan, for their support in conducting the XPS and HRTEM characterisation essential to this research. I would also like to extend my sincere thanks to **Prof. Pooja Devi** (CSIO, Chandigarh), **Dr. Sandesh Chougule**, and **Prof. Christos Markides** (Imperial College London) for their valuable support and encouragement throughout my research journey.

I would like to express my appreciation to all the technical staff at IIT Indore for their assistance with various technical and non-technical matters. Their contributions were crucial to overcoming several challenges encountered during this research.

My heartfelt thanks extend to my colleagues from the Advanced Functional Materials Research Group, including Dr. Manish Kumar Tiwari, Dr. Jena Akash Kumar Satrughna, Archana, Shraddhha, Anushka, Shubham, Pratik, and Pravin. Their companionship, insights, and shared experiences have been invaluable, providing both technical assistance and much-needed moral support.

I would also like to sincerely thank the students I had the opportunity to mentor, especially Bhaskar, Surya, Azhar, Daksh, Neyasha, Manas, Gauttam, Niketan, and Ujjwal. Beginning my mentoring journey with a few of them and gradually expanding the group has been a deeply rewarding experience. Their curiosity, enthusiasm, and collaborative spirit not only enriched our research environment but also played a meaningful role in shaping and strengthening my own research journey.

Finally, I would like to express my heartfelt gratitude to my dearest friends: Anugrah, Mrityunjay, Manopriya, Anandita, Shreya, Nitya, Reetika, Bhim, Manish, Pratik, Avik, and the

countless others who stood by me throughout this Ph.D. journey. Their constant support, belief in my abilities, and the warmth with which they cared for and encouraged me made this long journey far more meaningful. Their friendship, kindness, and unwavering presence have been a source of strength, comfort, and motivation during both the challenging and joyful moments of this journey.

Above all, I offer my deepest and most heartfelt gratitude to my parents, **Shri Anil Srivastava** and **Smt. Amita Srivastava**, who has always been my guiding force and greatest source of inspiration in life. Their unconditional love, sacrifices, and unwavering faith in me have been the foundation of every step I have taken in life. I am equally thankful to my younger brother, **Anjesh**, and my sister, **Akancha**, for their constant encouragement and support. A special mention goes to my beloved niece and nephew, **Keshav** and **Madhavi**, whose innocence and affection have brought countless moments of joy and positivity during this journey. Their blessings, love, and belief in me have made this achievement possible.

Date: 02 June, 2026 Abhishek Srivastava

Dedicated

To

My Parents

Shri Anil Kumar Srivastava

&

Smt. Amita Srivastava

LIST OF PUBLICATIONS

(From the Thesis Work)

(A) JOURNAL ARTICLES

PAPER-1

Abhishek Srivastava, Jena Akash Kumar Satrughna, Manish Kumar Tiwari, Archana Kanwade, Subhash Chand Yadav, Kiran Bala, and Parasharam M. Shirage. "Lead metal halide perovskite solar cells: Fabrication, advancement strategies, alternatives, and future perspectives." ***Materials Today Communications*** **35 (2023): 105686. [IF = 4.5]**

PAPER-2

Abhishek Srivastava, Jena Akash Kumar Satrughna, Manish Kumar Tiwari, Archana Kanwade, Subhash Chand Yadav, Kiran Bala, and Parasharam M. Shirage. "Effect of $Ti_{1-x}Fe_xO_2$ photoanodes on the performance of dye-sensitized solar cells utilizing natural betalain pigments extracted from Beta vulgaris (BV)." ***Energy Advances*** **2, 1 (2023): 148-160. [IF = 4.3]**

PAPER-3

Abhishek Srivastava, Yuta Ito, Hyunju Lee, Yoshio Ohshita, Atsushi Ogura, Mahesh Dhonde, and Parasharam M. Shirage. "Multilayered 2D $Ti_3C_2T_X$-MXene: Best Interfacial Passivating Agent for Dye-Sensitized Solar Cells with V_{OC} Approaching 1 V." ***ACS Applied Electronic Materials*** **7, 4 (2025): 1531-1549. [IF = 4.7]**

PAPER-4

Abhishek Srivastava, Manas Kasliwal, and Parasharam M. Shirage. "From HTL to HTL-free: Experimental and numerically modelled performance dynamics of $Cs_2AgBiBr_6$ double perovskite solar cells." ***Solar Energy*** **298 (2025): 113733. [IF = 6.6]**

PAPER-5

Abhishek Srivastava and Parasharam M. Shirage. "$Ti_3C_2T_X$-MXene Assisted Dual-Interfacial Passivation for HTL-Free $Cs_2AgBiBr_6$ Double Perovskite Solar Cells." ***ACS Applied Energy Materials*** **9, 4 (2026): 2422–2433. [IF = 5.6]**

(B) BOOK

Abhishek Srivastava and Parasharam M. Shirage. "*Perovskite Solar Cells: Fundamental Approaches and Materials Processing for Sustainable Future.*" pp. 01-203. Singapore: Springer Nature Singapore, 2024. Online ISBN: 978-981-97-7624-5

CHAPTER-1

Abhishek Srivastava and Parasharam M. Shirage. (2024). Perovskite Solar Cells: Futuristic Reliable Renewable Energy Technology. In: Perovskite Solar Cells. Springer Tracts in Electrical and Electronics Engineering. Springer, Singapore. https://doi.org/10.1007/978-981-97-7624-5_1

CHAPTER-2

Abhishek Srivastava and Parasharam M. Shirage. (2024). Overcoming Intrinsic and Extrinsic Challenges in Perovskite Solar Cells: A Pathway Toward Advancement. In: Perovskite Solar Cells. Springer Tracts in Electrical and Electronics Engineering. Springer, Singapore. https://doi.org/10.1007/978-981-97-7624-5_2

CHAPTER-3

Abhishek Srivastava and Parasharam M. Shirage. (2024). Operational Stability Management Approaches for Perovskite Solar Cells. In: Perovskite Solar Cells. Springer Tracts in Electrical and Electronics Engineering. Springer, Singapore. https://doi.org/10.1007/978-981-97-7624-5_3

CHAPTER-4

Abhishek Srivastava and Parasharam M. Shirage. (2024). Possible Perovskite Substitutes, Advances, and Future Prospects. In: Perovskite Solar Cells. Springer Tracts in Electrical and Electronics Engineering. Springer, Singapore. https://doi.org/10.1007/978-981-97-7624-5_4

CHAPTER-5

Abhishek Srivastava and Parasharam M. Shirage. (2024). Pioneering the Path: Unveiling Exciting Applications for Integrated Perovskite Solar Cells. In: Perovskite Solar Cells. Springer Tracts in Electrical and Electronics Engineering. Springer, Singapore. https://doi.org/10.1007/978-981-97-7624-5_5

LIST OF PUBLICATIONS

(Other than the Thesis)

(A) AUTHOR/EQUAL AUTHOR

1. **Abhishek Srivastava**, Bhaskar Singh Chauhan, Subhash Chand Yadav, Manish Kumar Tiwari, Jena Akash Kumar Satrughna, Archana Kanwade, Kiran Bala, and Parasharam M. Shirage. "Performance of dye-sensitized solar cells by utilizing Codiaeum Variegatum Leaf and Delonix Regia Flower as natural sensitizers." ***Chemical Physics Letters*** **807 (2022): 140087. [IF = 3.1]**
2. **Abhishek Srivastava**[#], Sweta Sharma[#], Yuta Ito, Hyunju Lee, Yoshio Ohshita, Atsushi Ogura, Pooja Devi, Parasharam M. Shirage. "Oxygen Vacancy Enriched Bi-functional $Ti_{1-x}Fe_xO_{2-\delta}$ Photoanodes for Synergistic Photoelectrochemical Hydrogen Evolution and Wastewater Remediation." ***Journal of Power Sources*** **677 (2026) 240003**. **[IF = 7.9]**
3. Sandesh S. Chougule[#], **Abhishek Srivastava**[#], Gaurav G. Bolegave, Bhagyashree A. Gaikwad, Parasharam M. Shirage, and Christos N. Markides. "Next-generation solar technologies: Unlocking the potential of Ag-ZnO hybrid nanofluids for enhanced spectral-splitting photovoltaic-thermal systems." *Renewable Energy* 236 (2024): 121405. **[IF = 9.1]**
4. Rahul Chauhan[#], **Abhishek Srivastava**[#], Parasharam M. Shirage, and Kiran Bala. "Innovating dye-sensitized solar cells through novel microalgal and cyanobacterial species extricated dyes: A sustainable tack for material scarce earth." *Solar Energy* 270 (2024): 112369. **[IF =6.6]**
5. Akula Surya Teja[#], **Abhishek Srivastava**[#], Jena Akash Kumar Satrughna, Manish Kumar Tiwari, Archana Kanwade, Hyunju Lee, Atsushi Ogura, and Parasharam M. Shirage. "Synergistic co-sensitization of environment-friendly chlorophyll and anthocyanin-based natural dye-sensitized solar cells: An effective approach towards enhanced efficiency and stability." *Solar Energy* 261 (2023): 112-124. **[IF = 6.6]**
6. Akula Surya Teja[#], **Abhishek Srivastava**[#], Jena Akash Kumar Satrughna, Manish Kumar Tiwari, Archana Kanwade, Subhash Chand Yadav, and

Parasharam M. Shirage. "Optimal processing methodology for futuristic natural dye-sensitized solar cells and novel applications." *Dyes and Pigments* 210 (2023): 110997. **[IF = 4.2]**

(B) CO-AUTHOR

7. Shubham Upadhyay, **Abhishek Srivastava**, Anushka Singh, Archana R. Kanwade, Pratik Pawar, and Parasharam M. Shirage. "Recent Developments and Future Roadmap of Next Generation Quantum Dot Perovskite Solar Cells: A Review." *Solar Energy Materials and Solar Cells* (Under Review, **IF=6.3**)
8. Pratik Pawar, Archana R. Kanwade, Jena Akash K. Satrughna, **Abhishek Srivastava**, and Parasharam M. Shirage. "Advancements in Anode Materials for Sodium-ion Batteries: Current Trends and Future Prospects." *Journal of Power Sources* (Revision Submitted, **IF=7.9**)
9. Minaz M. Faras, Archana R. Kanwade, Shraddha M. Rajore, Jena Akash K. Satrughna, Manish K. Tiwari, **Abhishek Srivastava**, Anushka Singh, Pratik Pawar, Jyoti V. Patil, Sawanta S. Mali, Chang K. Hong, Anita R. Mali, and Parasharam M. Shirage. "$ZnCo_2O_4$ Architecture for Fast Na^+ Diffusion and Stable Sodium-Ion Storage." *Chemnanomat* 12, 4 (2026), e202500745. [**IF=2.6**]
10. Ujjwal Mahajan, **Abhishek Srivastava**, Mahesh Dhonde, Kirti Sahu, Parasharam M. Shirage. "Interface engineered $Ba_{1-x}Zn_xSnO_3/TiO_2$ nanorod heterostructured photoanodes for efficient dye-sensitized solar cells." *Ceramic International* 52, 6 (2026), 7132-7147. **[IF = 5.6]**
11. Ujjwal Mahajan, **Abhishek Srivastava**, Ashok Kumar, Mahesh Dhonde, Kirti Sahu, and Parasharam M. Shirage. "Cr-Doped Barium Stannate Perovskite as an Advanced Photocatalyst for Degrading Carcinogenic Rhodamine B." *Ceramics International* 52, 1 (2026), 1083-1095. **[IF = 5.6]**
12. Anushka Singh, **Abhishek Srivastava**, Jena Akash Kumar Satrughna, Shraddha M. Rajore, Archana R. Kanwade, and Parasharam M. Shirage. "Spectral accessibility tuning through perovskite quantum dots for up-/down-converting photovoltaic applications: a review." *Nanoscale* 17 (2025), 27111-27150. **[IF = 5.1]**

13. Niketan D. Dhage, **Abhishek Srivastava**, Anita R. Mali, and Parasharam M. Shirage. "$TiCl_4/MgCl_2$ passivated TiO_2 photoanodes sensitized with Dendrobium Sonia Orchid, Woodfordia fruiticosa, and Couroupita guianensis bio-photosensitizers for DSSC application." *New Journal of Chemistry* 49, no. 40 (2025): 17546-17560. **[IF = 2.5]**
14. Ujjwal Mahajan, **Abhishek Srivastava**, Mahesh Dhonde, Kirti Sahu, Pintu Ghosh, and Parasharam M. Shirage. "Zinc-modified barium stannate micro-rods: Investigating structural, morphological, and optical features." *Chemical Physics Impact* 8 (2024): 100622. **[IF = 4.3]**
15. Azaharuddin Saleem Shaikh, Subhash Chand Yadav, **Abhishek Srivastava**, Archana R. Kanwade, Manish Kumar Tiwari, Shraddha Manohar Rajore, Jena Akash Kumar Satrughna, Mahesh Dhonde, and Parasharam M. Shirage. "Dynamic synergy of tin in the electron-transfer layer and absorber layer for advancing perovskite solar cells: a comprehensive review." *Energy Advances* 3, no. 7 (2024): 1505-1552. **[IF = 4.3]**
16. Jena Akash Kumar Satrughna, Archana Kanwade, **Abhishek Srivastava**, Manish Kumar Tiwari, Subhash Chand Yadav, Surya Teja Akula, and Parasharam M. Shirage. "Experimental and computational advancement of cathode materials for futuristic sodium ion batteries." *Materials Today* 91 (2025): 375-408. **[IF = 22.0]**
17. Manish Kumar Tiwari, Archana Kanwade, Subhash Chand Yadav, **Abhishek Srivastava**, Jena Akash Kumar Satrughna, and Parasharam M. Shirage. "NASICON-type $Na_3Fe_2(PO_4)_3$ material for an excellent room temperature CO sensor." *Journal of Materials Chemistry C* 11, no. 16 (2023): 5469-5480. **[IF = 5.2]**
18. Subhash C. Yadav, Vishesh Manjunath, **Abhishek Srivastava**, Rupesh S. Devan, and Parasharam M. Shirage. "Stable lead-free $Cs_4CuSb_2Cl_{12}$ layered double perovskite solar cells yielding theoretical efficiency close to 30%." *Optical Materials* 132 (2022): 112676. **[IF = 4.2]**
19. Subhash Chand Yadav, **Abhishek Srivastava**, Vishesh Manjunath, Archana Kanwade, Rupesh S. Devan, and Parasharam M. Shirage. "Properties,

performance and multidimensional applications of stable lead-free $Cs_2AgBiBr_6$ double perovskite." *Materials Today Physics* 26 (2022): 100731. **[IF = 9.7]**

20. Manish Kumar Tiwari, Subhash Chand Yadav, **Abhishek Srivastava**, Archana Kanwade, Jena Akash Kumar Satrughna, Sawanta S. Mali, Jyoti V. Patil, Chang Kook Hong, and Parasharam M. Shirage. "Enhancement of CO gas sensing performance by Mn-doped porous $ZnSnO_3$ microspheres." *RSC advances* 12, no. 50 (2022): 32249-32261. **[IF = 4.6]**
21. Archana Kanwade, Sheetal Gupta, Akash Kankane, **Abhishek Srivastava**, Subhash Chand Yadav, and Parasharam M. Shirage. "Phosphate-based cathode materials to boost the electrochemical performance of sodium-ion batteries." *Sustainable Energy & Fuels* 6, no. 13 (2022): 3114-3147. **[IF = 4.1]**
22. Archana Kanwade, Sheetal Gupta, Akash Kankane, Manish Kumar Tiwari, **Abhishek Srivastava**, Jena Akash Kumar Satrughna, Subhash Chand Yadav, and Parasharam M. Shirage. "Transition metal oxides as a cathode for indispensable Na-ion batteries." *RSC advances* 12, no. 36 (2022): 23284-23310. **[IF = 4.6]**

LIST OF CONFERENCE/WORKSHOP/COURSES ATTENDED

1. Oral presentation at "Research Industrial Conclave-2026 (RIC-26)" organized by Academic Council-IIT Indore, Indian Institute of Technology Indore, India, 17 January 2026.
2. Oral presentation at the International Conference on "Modern Perspectives in Chemical Materials and Technologies (MPCMT-2026)," held at D.P. Bhosale College, Koregaon, Maharashtra, India, 13 January 2026.
3. Participated in the 10th International & 31st "All India Manufacturing Technology, Design & Research (AIMTDR 2025)" Conference organized by IIT Indore, 11-13 December 2025.
4. Participated in "Poster and Project Model Presentation at Technovation Event" at SAGE University-Indore, 6-7 January 2025.
5. Oral Presentation at "4th International Conference on Advanced Materials Synthesis, Characterisation, and Applications-2024" held at Queensland University of Technology, Brisbane, Australia, during 25-27 September 2024.
6. Resource Person in "International Workshop on Energy Conversion and Sustainable Future" sponsored by the Science and Education Research Board (SERB) under Accelerate Vigyan Scheme "KARYASHALA," 23-24 January 2024.
7. Participated in the "International Conference on Advances in Photovoltaic Materials and Devices" organized by S&T Digital, 2-4 June 2023.
8. Poster presentation in "International Conference on Advanced Materials: Properties and Applications", Goa University-India, 2023.
9. Resource Person in "Recent Development in Energy Materials for Sustainable Future" sponsored by AICTE Training and Learning Academy (ATAL) at IIT Indore, India, from 21 November to 01 December 2022.
10. Attended a short-term course titled "Materials Engineering from Synthesis to

Applications", a quality improvement program sponsored by AICTE, Department of MEMS, IIT Indore, 2022.

TABLE OF CONTENTS

ACKNOWLEDGEMENTS	vii
LIST OF PUBLICATIONS	xi
LIST OF CONFERENCES/WORKSHOPS/COURSES ATTENDED	xviii
TABLE OF CONTENTS	xix
LIST OF FIGURES	xxv
LIST OF TABLES	xxxv
ACRONYMS/ABBREVIATIONS	xxxix
Chapter 1: Introduction	1
1.1 Dye-Sensitized Solar Cells	2
1.1.1 Brief History of DSSC	4
1.1.2 Selection Rule and Criteria for Dye Extraction	6
1.1.3 Working Principle of DSSCs	8
1.2 Perovskite Solar Cells	9
1.2.1 Brief History of PSCs	11
1.2.2 Key Structural Parameters for Perovskites	13
1.2.3 Working Principle of PSCs	14
1.3 Shockley-Queisser Limit	16
1.4 Natural DSSCs and Pb-Free DPSCs	18
1.5 Factors Affecting Solar Cells' Performance	19
1.5.1 Light Absorption and Band Gap Engineering	20
1.5.2 Interfacial Charge Transport and Recombination	20
1.5.3 Charge Transport and Carrier Diffusion	20
1.5.4 Materials Stability and Environmental Effects	21
1.5.5 Electrode and Device Architecture	21
1.6 Research Gap, Challenges, and Motivation	22
1.7 Materials of Choice	23
1.7.1 Photoanode or ETL	23

1.7.2 Dye-Sensitizers 25
1.7.3 Electrolyte 25
1.7.4 Pb-Free Double Perovskite Photo Harvester 26
1.7.5 2D-$Ti_3C_2T_X$ MXene 27
1.7.6 Back Carbon Electrodes 29
1.8 Scope and Goals of the Thesis 29
1.8.1 Thesis Objectives 30
1.8.2 Thesis Outlines 31
References 34
Chapter 2: Experimental and Characterization Techniques 43
2.1 Introduction 44
2.2 Synthesis Methods for DSSC Materials 45
2.2.1 Synthesis of TiO_2 Nanorod Photoanodes 45
2.2.2 Preparation of Dye-Sensitizers 47
2.2.3 Tri-iodide (I^-/I_3^-) Electrode Preparation 47
2.3 Synthesis Methods for DPSC Materials 47
2.3.1 Thin Film Synthesis of TiO_2-ETLs 48
2.3.2 Synthesis of CABB Powder 49
2.4 Synthesis of Ti_3AlC_2-MAX Phase and $Ti_3C_2T_X$-MXene 50
2.5 Materials Characterization Techniques 52
2.5.1 X-Ray Diffraction 52
2.5.2 Field Emission Scanning Electron Microscopy/Energy Dispersive X-ray Spectroscopy 53
2.5.3 Transmission Electron Microscopy 55
2.5.4 X-Ray Photoelectron Spectroscopy 56
2.5.5 UV-visible Absorption Spectroscopy 57
2.5.6 Atomic Force Microscopy 58
2.5.7 Electrochemical Impedance Spectroscopy 60
2.5.8 Raman Spectroscopy 61
2.5.9 Photovoltaic Studies 62

References 64
Chapter 3: $Ti_3C_2T_X$ Optimized Interfacial Passivation for Dye-Sensitized Solar Cells 71
3.1 Introduction 72
3.2 Experimental Section 74
3.2.1 Materials 74
3.2.2 Passivation Protocol 75
3.2.3 DSSC Fabrication and Working Mechanism 76
3.3 Results and Discussion 77
3.3.1 Morphological and Structural Analysis of $Ti_3C_2T_X$-MXene 77
3.3.2 Morphological Analysis of Bare and Passivated TiO_2 Photoanodes 82
3.3.3 Structural Analysis 87
3.3.4 UV-visible Absorption and FTIR Studies 89
3.3.5 XPS Analysis 93
3.3.6 J-V Analysis 95
3.3.7 AFM Analysis 101
3.3.8 EIS Analysis 103
3.4 Conclusions 106
References 107
Chapter 4: $Ti_{1-x}Fe_xO_{2-\delta}$ Photoanodes for Natural Dye-Sensitized Solar Cells 117
4.1 Introduction 118
4.2 Experimental Section 123
4.2.1 Materials 123
4.2.2 DSSC Fabrication 123
4.2.3 Working Mechanism 123
4.3 Results and Discussion 126
4.3.1 Structural Analysis 126
4.3.2 Morphological Analysis 128

4.3.3 XPS Analysis 131
4.3.4 UV-visible Absorption Analysis 134
4.3.5 FTIR Analysis 135
4.3.6 J-V Analysis 136
4.4 Conclusions 142
References 143
Chapter 5: HTL and HTL-free $Cs_2AgBiBr_6$ Double Perovskite Solar Cells 155
5.1 Introduction 156
5.2 Experimental Section 159
5.2.1 Materials 159
5.2.2 HTL-free DPSC Fabrication 160
5.3 SCAPS-1D Simulation Details 161
5.4 Results and Discussion 164
5.4.1 Experimental Results 164
5.4.2 Simulation Results 174
5.5 Conclusions 193
References 194
Chapter 6: $Ti_3C_2T_X$ Assisted Dual Interfacial Passivation for $Cs_2AgBiBr_6$ Double Perovskite Solar Cells 205
6.1 Introduction 206
6.2 Experimental Section 208
6.2.1 Materials 208
6.2.2 Synthesis of CABB and DPSC Fabrication 208
6.3 Results and Discussion 210
6.3.1 Morphological Analysis 210
6.3.2 Structural and Optical Studies 215
6.3.3 J-V Analysis 220
6.3.4 Surface Roughness and Topological Analysis 224
6.3.5 Charge Transport Properties 226

6.4 Conclusions 230
References 231

Chapter 7: Conclusions and Scope for Future Work 239

7.1 Introduction 240
7.2 Dissertation Summary 241
7.3 Current Progress and Future Scope 244

ANNEXURE A: Copyright Permissions for Reproduced Figures 251

LIST OF FIGURES

Figure No.	Figure Caption	Page No.
Chapter 1		
Figure 1.1	Classification of all three generations of Photovoltaic Technologies, Reproduced with permission from Ref. [1]	2
Figure 1.2	Schematics of Dye-Sensitized Solar Cells, their components, and workflow, Reproduced with permission from Ref. [3]	3
Figure 1.3	Schematic selection criterion framework for sustainable and eco-friendly DSSC technology, Reproduced with permission from Ref. [13]	7
Figure 1.4	(a) $CaTiO_3$ Perovskite, and (b) crystal structure of $MAPbI_3$, where the MA^+ cation is surrounded by four PbX_6 octahedra, Reproduced with permission from Ref. [17]	10
Figure 1.5	(a) octahedral factor (μ) for various perovskite materials, reproduced with permission from Ref. [39] and (b) Map of (t,μ) for estimating the relative stability of the different perovskite materials, reproduced with permission from Ref. [40]	14
Figure 1.6	Typical schematics of commonly explored PSC architectures, Reproduced with permission from Ref. [1]	15
Figure 1.7	(a) The Shockley-Queisser limit represents the theoretical maximum efficiency of a solar cell without solar concentration, with the inset region highlighting the bandgap range where peak efficiency occurs. (b) Quantitative breakdown of efficiency losses limiting single-junction solar cell performance according to the Shockley-Queisser theory, Reproduced with permission from Ref. [41]	17
Figure 1.8	Crystal structure of $Cs_2AgBiBr_6$. Orange, grey, turquoise, and brown spheres represent Bi, Ag, Cs, and Br atoms, respectively, Reproduced with permission from Ref. [50]	27
Figure 1.9	Typical crystal structure of (a) 211, (b) 312, and (c) 413-type MAX-phases exhibiting a hexagonal lattice arrangement. The general formula for MAX-phases is $M_{n+1}AX_n$, where M represents transition metal elements (usually Ti, Zr, or Tl, etc.), A represents an element from the A group (typically Si or Al), and X represents carbon (C) or nitrogen (N), Reproduced with permission from Ref. [46]	28

Chapter 2

Figure 2.1	Typical schematics of hydrothermal synthesis of 1-D TNRs. (a) a c-TiO_2-coating process on cleaned FTO substrates, and (b) the final step of hydrothermal synthesis of 1-D TNRs on c-TiO_2-coated FTO substrates	46
Figure 2.2	Typical spin coating synthesis method of (a) c-TiO_2 layer (blocking layer), and (b) n-type TiO_2 electron transfer layer	48
Figure 2.3	Schematic synthesis procedure of CABB powder using the solution precipitation method under open environment conditions	49
Figure 2.4	Schematic of various steps involved in synthesizing MAX-phase Ti_3AlC_2 and obtaining $Ti_3C_2T_X$ MXene via selective HCl-HF etching	50
Figure 2.5	Schematic illustration of (a) Bragg's law formulation from crystal planes, (b) Empyrean, Malvern Panalytical X-ray diffractometer, and (c) closer view of XRD stage along with X-ray source and detector	52
Figure 2.6	(a) Schematic working mechanism and accessories, (b) typical strike and scattering of the high-energy electron beam from the sample's surface, and (c) real-time captured JSM-7610F Plus JEOL FESEM	54
Figure 2.7	Typical schematic working mechanism of Transmission Electron Microscopy and various instrumental components	55
Figure 2.8	Schematic working mechanism illustration of X-ray Photoelectron Spectroscopy	57
Figure 2.9	Schematic illustration of the UV-visible spectroscopy working principle and instrumental setup	58
Figure 2.10	Schematic working mechanism of the Atomic Force Microscopy and components	59
Figure 2.11	Schematic illustration of a three-electrode electrochemical setup for Electrochemical Impedance Spectroscopy analysis	60
Figure 2.12	(a) Schematic working mechanism of RAMAN Spectroscopy and (b) real-time image of HJY micro-RAMAN spectrophotometer	62
Figure 2.13	PET class AAA solar simulator equipped with Xenon arc (AM 1.5G optical filter) for testing solar cells	63

Chapter 3

Figure 3.1	Schematics of photoanode passivation strategy used to prepare TC-TNR, MX-TNR, TL-TNR, and CB-TNRs.	75
Figure 3.2	(a) Typical schematic of the fabricated DSSC device, and (b) a standard plausible working mechanism of the fabricated DSSC	77
Figure 3.3	(a-b) The morphology of multi-layered $Ti_3C_2T_X$-MXene was obtained at different magnifications from FESEM analysis, (c-e) Elemental mapping confirmed the uniform distribution of Ti and C across the layers, and (f) XRD patterns of MAX-phase Ti_3AlC_2 (black) and multi-layered 2D $Ti_3C_2T_X$-MXene (red)	79
Figure 3.4	Rietveld refined XRD pattern of MAX phase Ti_3AlC_2, and corresponding Bragg's positions	80
Figure 3.5	(a) XPS Survey-scan spectra of $Ti_3C_2T_X$-MXene in the binding energy range of 900 to 150 eV. Core-level XPS spectra of the multi-layered $Ti_3C_2T_X$-MXene deconvoluted by Gaussian-Lorenzen mix functions with Shirley's background (b) C(1s), (c) Ti(2p), and (d) F(1s)	81
Figure 3.6	Morphological analysis of the hydrothermally grown B-TNRs (8hr @150°C). (a) The top-view FESEM image of the B-TNRs shows vertical growth of the FTO substrate at 30000X magnification, and (b-d) elemental mapping of the respective TNR photoanode confirms the uniform distribution of the Ti and O	83
Figure 3.7	Top view of FESEM images of all the passivated TNRs and their elemental composition. (a) B-TNRs, (b) EDX spectra of B-TNRs confirming the stoichiometric presence of Ti and O-atoms across the surface, (c) TC-TNRs, (d) MX-TNRs, (e) TL-TNRs, and (f) CB-TNRs	84
Figure 3.8	High-resolution TEM Analysis. (a) TEM image of a single B-TNR in a resolution scale of 50 nm, (b) HRTEM image of a selected portion of the B-TNR (highlighted in red color box), and estimated lattice spacing of [001] and [110] crystallographic planes, and (c) Respective SAED pattern confirming the crystalline nature and orientation of the TNRs	86
Figure 3.9	(a) XRD pattern of FTO, hydrothermally synthesized B-TNRs, and other passivated (TC-, MX-, TL-, and CB-) TNRs. The continuous XRD scan was performed from	87

	20° to 60° with a step size of 0.026°, using a Cu Kα (1.5406 Å) source	
Figure 3.10	UV-vis absorption studies of (a) bare-TNRs and other passivated TNRs, and (b) 0.5mM-N719 dyes tested three times in 30 days and showed their UV-visible absorption spectra on the 1st, 15th, and 30th day, which were preserved under dark conditions at 25 °C with RH 40%. (c) photocurrent response from all the passivated photoanodes on the testing on day 1st, 15th, and 30th, showing maximum J_{SC} of 11.60 mA cm^{-2}, (d) FTIR Spectra of hydrothermally synthesized B-TNRs and passivated TNRs, where the passivating agents are TC, MX, TL, and CB	90
Figure 3.11	(a) XPS survey spectra of Hydrothermally synthesized B-TNR photoanode, (b) core-level C1s spectra used for carbon correction, and (c-d) Typical core-level XPS spectra of Ti(2p) and O(1s) deconvoluted with Shirley background and Voigt function fitting. The distinct characteristic peaks are $Ti(2p)_{3/2}$, $Ti(2p)_{1/2}$, O(1s): lattice oxygen and O_{SC} (surface contamination) observed at 457.6, 463.4, 528.7, and 530.3 eV, respectively	94
Figure 3.12	J-V analysis of the fabricated FTO/c-TiO_2/TNRs/N719/(I^-/I_3^-)/Carbon-structured DSSC at standard solar irradiance of 100mW/cm^2 (AM1.5G), temperature 37 ± 6°C and RH of 47 ± 5%. (a, c, and e) J-V curves were obtained from the DSSC on the 1st day, 15th day, and 30th day, respectively. (b, d, and f) Relative PV parameter variations with respect to the different passivating agents	97
Figure 3.13	(a) IPCE obtained from MX-TNRs-based DSSC on the measurement days 1st, 15th, and 30th, and (b) Calculated charge collection efficiency variation for different passivated photoanode-based DSSC	100
Figure 3.14	Atomic force microscopy (AFM) analysis of (a) c-TiO_2, (b) B-TNR, (c) TC-TNR, (d) MX-TNR, (e) TL-TNR, and (f) CB-TNR photoanodes	101
Figure 3.15	(a) EIS analysis of the bare TNR and all other passivated TNRs performed in 1M KOH aqueous electrolyte in the frequency range of 0.1 Hz to 100 kHz. A High-resolution Nyquist plot and equivalent electrical circuit are shown	103

in the inset for passivated TNR photoanodes, (b) Variation of $\mathbf{R}_S$, $\mathbf{R}_{CT}$, and W with respect to different passivated TNRs, depicting TC and MX as the best-performing passivation agents

Chapter 4

Figure 4.1 (a) The process of charge transport involving elevated electrons and VBs of the TiO_2 nanorods with Fe^{3+} ions of $Ti_{1-x}Fe_xO_2$ (x=0-0.1), and (b) Schematics of the local topologies of Fe-dopants in the different Fe^{4+}, Fe^{2+}, and Fe^{3+} doped TiO_2 models, respectively. B^{1-6} are the bond lengths of Fe-O bonds, and the bond angle between Fe-O-Ti and Fe-O-Fe is denoted by δ 120

Figure 4.2 Typical schematics and working mechanism of the Dye Sensitized Solar Cells 125

Figure 4.3 XRD patterns of the (a) FTO, (b) bare TiO_2, (c) $Ti_{0.975}Fe_{0.025}O_2$, (d) $Ti_{0.95}Fe_{0.05}O_2$, (e) $Ti_{0.925}Fe_{0.075}O_2$, (f) $Ti_{0.9}Fe_{0.1}O_2$ TiO_2 NRs, respectively. The asterisk (*) represents FTO diffraction peaks 127

Figure 4.4 (a-e) FESEM top view image of $Ti_{1-x}Fe_xO_2$(x=0-0.1) NRs grown. (a) Undoped (x=0) TiO_2 NRs, (b) x=0.025, (c) x=0.05, (d) x=0.075, (e) x=0.1, and (f) Cross-sectional image of undoped TiO_2 NR arrays 129

Figure 4.5 EDX spectra of (a) TiO_2 and (b) $Ti_{0.95}Fe_{0.05}O_2$ confirm the stoichiometric presence of Ti and O atoms. As no traces of Fe were found in EDX, elemental mapping (c-e) was done to confirm the presence of Fe and the uniform distribution of Ti and O 130

Figure 4.6 (a) TEM images of a single TiO_2 NR, and (b) Corresponding HRTEM image of a single TiO_2 NR. The inset image of (b) displays the lattice spacing between (101) planes of the rutile phase TiO_2 131

Figure 4.7 The XPS spectra of bare TiO_2 and $Ti_{0.95}Fe_{0.05}O_2$ photoanodes. (a) Comparison of XPS survey scan spectra, (b) TiO_2: Ti(2p) core-level XPS spectra, (c) TiO_2: O(1s) core-level XPS spectra, (d) $Ti_{0.95}Fe_{0.05}O_2$: Fe(2p) XPS spectra, (e) $Ti_{0.95}Fe_{0.05}O_2$: Ti(2p) core-level XPS spectra, and (f) $Ti_{0.95}Fe_{0.05}O_2$: O(1s) core-level XPS spectra 132

Figure 4.8 Absorption spectra of (a) $Ti_{1-x}Fe_xO_2$ (x=0-0.1) NRs, (b) Tauc's plot of the $Ti_{1-x}Fe_xO_2$ (x=0-0.1) NRs, and (c) UV-Visible spectra of extracted BV dye 134

Figure 4.9	(a) FT-IR spectrum of the dye extracted from the BV, (b) Raman spectra for tetragonal rutile phase $Ti_{1-x}Fe_xO_2$ (x=0-0.1) NRs grown hydrothermally on FTO substrate	136
Figure 4.10	(a) J-V characteristics of the $Ti_{1-x}Fe_xO_2$ (x=0-0.1) NRs-based DSSC utilizing BV dyes as sensitizers, (b) Stability analysis on the fabricated DSSCs consists of $Ti_{1-x}Fe_xO_2$ (x=0-0.1) photoanodes and BV dyes, (c) IPCE spectra of $Ti_{1-x}Fe_xO_2$ (x=0-0.1) NR photoanodes-based DSSCs, and (d) EIS Nyquist plots of undoped and doped TiO_2 photoanodes at a bias of $V=V_{OC}$	137
Chapter 5		
Figure 5.1	(a) Schematic of CABB-ink preparation and coating on TiO_2-ETL-coated FTO substrates. (b) HTL-free DPSC (FTO/c-TiO_2/TiO_2 ETL/CABB/Carbon) fabricated in the open environment	160
Figure 5.2	(a) Rietveld refined XRD pattern of as-synthesized CABB powder, (b) layer-by-layer XRD pattern of FTO, TiO_2 ETL, and TiO_2 + CABB layer comprising CABB-based HTL-free DPSC	166
Figure 5.3	Detailed XPS patterns of (a) survey scan of CABB in the range 0 to 1000 eVs and characteristic core level XPS spectra of (b) C (1s), (c) Cs (3d), (d) Ag (3d), (e) Bi (4f), and (f) Br (3d)	167
Figure 5.4	(a-b) FESEM images of as-synthesized CABB powder showing octahedral crystals having edges larger than 3 μm	168
Figure 5.5	Top-view FESEM images of (a) FTO, (b) c-TiO_2, (c) TiO_2 ETL, and (d) CABB layer. Inset images attached (b) and (d) are the real-time images of opaque TiO_2 ETL and CABB absorber layers along with the grain size distribution	169
Figure 5.6	EDX and elemental mapping of (a-c) TiO_2 ETL and (d-h) as-synthesized CABB powder	170
Figure 5.7	Photophysical properties of TiO_2 ETL and CABB absorber layer. (a-b) UV-vis absorption and Tauc's plot of TiO_2 ETL, and (c-d) UV-vis absorption and Tauc's plot of CABB photo absorber layer	171
Figure 5.8	(a) J-V analysis of the DPSCs (**DT0** and **DT200**) structured as FTO/TiO_2/CABB/Carbon, (b) Open-air	172

	stability of all the 16 fabricated DPSCs with optimized solution-processed CABB absorber ink	
Figure 5.9	(a) Nyquist and (b) Bode plot of FTO/TiO_2/CABB electrodes in 0.1 M $TBAPF_6$ electrolyte in DCM solution for diffusion-recombination model. The inset image shows the equivalent electrical circuit model used to fit the Nyquist plot	173
Figure 5.10	Comparative PV performances were obtained from DPSCs by varying the thickness of (a) ETL layers (25-250 nm), (b) CABB photo absorber layer (100-1000 nm), and (c) Spiro-OMeTAD HTL layer (10-100 nm). The portion highlighted in cyan is the optimal thickness range for each layer	177
Figure 5.11	Variation in characteristic PV parameters with respect to the changes in (a) N_a of the CABB layer, (b) N_t of the CABB layer, and (c) N_a of the Spiro-OMeTAD HTL layer	179
Figure 5.12	Comparative PV-performance analysis by varying (a) N_d of all ETL layers, (b) N_{if} between ETL/CABB layers, and (c) N_{if} between CABB/HTL layers	181
Figure 5.13	Variation of characteristic PV parameters by changing the (a) R_S, (b) R_{Sh}, and (c) T_{opt} of the DPSCs consisting of four distinct ETLs	182
Figure 5.14	EQE variation for distinct ETL-based DPSCs by changing (a-d) t_{CABB}, and (e-h) $N_{t\ (CABB)}$	183
Figure 5.15	Comparative performance analysis of HTL-free CABB-based DPSCs with varying (a) t_{ETL}, (b) t_{CABB}, and (c) N_t of the CABB layer	186
Figure 5.16	Variational analysis of PV parameters in HTL-free DPSCs by varying (a) N_d of ETL, (b) N_a of CABB, and (c) N_{if} at the ETL/CABB interface	187
Figure 5.17	Comparative PV parameter analysis for HTL-free DPSCs by varying (a) R_S, (b) R_{Sh}, and (c) T_{opt} of the device	188
Figure 5.18	EQE variation for distinct ETL-based HTL free DPSCs by changing (a-d) t_{CABB}, and (e-h) $N_{t\ (CABB)}$	189
Figure 5.19	Final J-V variation of (a) FTO/ETLs/CABB/Spiro-OMeTAD/Au, and (b) HTL-free FTO/ETLs/CABB/Au-based DPSCs. (c-d) corresponding EQE for FTO/ETLs/CABB/Spiro-OMeTAD/Au and HTL-free FTO/ETLs/CABB/Au-DPSCs	191

Chapter 6

Figure 6.1	A typical $Ti_3C_2T_X$-MXene passivation process is followed to prepare FT-, FMT-, and FTM-type ETLs, resulting in the formation of **DPSC1**, **DPSC2**, and **DPSC3**, respectively	209
Figure 6.2	(a-b) FESEM images of octahedral CABB crystals, (c) corresponding EDX spectra, and (d) elemental mapping (Cs: red, Ag: green, Bi: cyan, and Br: pink)	211
Figure 6.3	(a) High-resolution TEM image, (b) lattice spacing between (444), (044), (222) planes, and Fourier transform image, (c) SAED-pattern of octahedral CABB crystals	212
Figure 6.4	(a) Thermogravimetric Analysis (TGA) of CABB crystals, and (b) Brunauer-Emmett-Teller (BET) adsorption/desorption isotherms and pore-size distribution in CABB powder	213
Figure 6.5	Top-view FESEM micrographs of (a) bare FTO, (b) **FT**, (c) **FMT** (FTO/Mx/TiO_2), and (d) **FTM** (FTO/TiO_2/Mx)	214
Figure 6.6	(a) Reitvil refined the XRD diffraction pattern of CABB powder, (b) Comparative XRD patterns of bare FTO, FT, FMT, and FTM, (c) UV-vis absorption spectra and Tauc's plot of FT, FMT, and FTM ETLs, and (d) UV-vis absorption spectra of CABB-loaded ETLs	216
Figure 6.7	(a) Diffused reflectance spectra, (b) corresponding Tauc's plot, and (c) RAMAN spectra of CABB powder	218
Figure 6.8	(a) FTIR, and (b) Raman spectra of bare $Ti_3C_2T_X$ MXene powder	220
Figure 6.9	Statistical analysis of various PV-parameters, such as (a) J_{SC}, (b) V_{OC}, (c) FF, and (d) PCE for DPSCs fabricated using **FT**, **FMT**, and **FTM**-ETLs	221
Figure 6.10	(a) J-V curves of all three best-performing DPSCs employing **FT**, **FMT**, and **FTM** electrodes. Typical electronically favourable band alignment for (b) FTO/TiO_2/CABB/Carbon, (c) FTO/Mx/TiO_2/CABB/Carbon, and (d) FTO/TiO_2/Mx/CABB/Carbon structured DPSCs.	223
Figure 6.11	Surface roughness and topological features of (a) FT, (b) FMT, (c) FTM, and (d) FMT/CABB layers	225
Figure 6.12	(a) Nyquist plot, (b-d) corresponding Bode plot of **FTC**, **FMTC**, and **FTMC** electrodes in 0.1M $TBAPF_6$ electrolyte in DCM	227

LIST OF TABLES

Table No.	Table Title	Page No.
Chapter 1		
Table 1.1	Summary of various selection rules and extraction criteria	8
Chapter 3		
Table 3.1	Binding energies obtained from XPS fitting of core-level C (1s), Ti (2p), and F (1s) spectra for 2D $Ti_3C_2T_X$-MXene	81
Table 3.2	Various Raman Vibration modes of rutile phase tetragonal TNRs and respective frequencies at Γ, X, M, and Z of the Brillouin zone at RT	89
Table 3.3	Summary of all the photovoltaic parameters such as V_{OC}, J_{SC}, FF, and PCE obtained from the FTO/c-TiO_2/TNRs/N719/(I^-/I_3^-)/Carbon-structured DSCCs on the 1st, 15th, and 30th day	98
Table 3.4	Comparison of different photoanode passivating agents used to date and possible performance enhancement mechanisms in DSSCs	100
Table 3.5	Different surface roughness parameters were analyzed using AFM analysis of the passivated TNR photoanodes	102
Table 3.6	All the corresponding EIS circuit parameters for different passivated-TNR photoanodes were studied in 1M KOH electrolyte	105
Chapter 4		
Table 4.1	Variation in the Lattice constant values with different concentrations of Fe-doping in TiO_2 NRs	127
Table 4.2	Corresponding circuit parameters of $Ti_{1-x}Fe_xO_2$ (*x=0-0.1*) photoanodes in 1M KOH electrolyte	139
Table 4.3	Photovoltaic studies of $Ti_{1-x}Fe_xO_2$ (*x=0-0.1*) photoanode-based DSSC utilizing BV dyes as light harvester	139
Table 4.4	Comparative study of the BV dyes-based DSSC performance from the available literature	141
Chapter 5		
Table 5.1	Typical optoelectrical properties of FTO, CABB, and Spiro-OMeTAD-HTL layer for SCAPS-1D simulation	163
Table 5.2	Typical optoelectrical properties of distinct ETL layers (TiO_2, SnO_2, WO_3, and ZnO) for SCAPS-1D simulation	164
Table 5.3	Defect parameters for different layers and interfaces of ETL/CABB and CABB/HTL[32,50,51]	164
Table 5.4	Crystal type, space group, and lattice parameters obtained from refined p-XRD of CABB	165
Table 5.5	Estimated values of β, D, δ, and ε for (220), (400), and (440) highly intense diffraction peaks	166

Table 5.6	Summary of stoichiometric compositional data, including binding energy, FWHM, area, and at%, obtained from different core-level XPS spectra of CABB	168
Table 5.7	Summary of fitted EIS circuit parameters and deduced electrical parameters such as τ_e, L_n, D_{eff}, η_{cce}, L_{eff}, and τ_d	174
Table 5.8	Summary of the various optimized parameters such as thickness, $N_{d(ETL)}$, $N_{a\ (CABB\ and\ HTL)}$, $N_{t\ (CABB)}$, $N_{if\ (ETL/CABB\ and\ CABB/HTL)}$, R_S, R_{Sh}, and T_{opt} for best performing HTL and HTL-free DPSCs	184
Table 5.9	Summary of the PV parameters obtained from best-performing CABB-based DPSCs, including experimental (FTO/TiO_2/CABB/Carbon) and simulation (FTO/ETLs/CABB/Spiro-OMeTAD/Au & FTO/ETLs/CABB/Au) results	191
Chapter 6		
Table 6.1	Crystal type, space group, and lattice parameters obtained from refined p-XRD of CABB	216
Table 6.2	Summary of all the J-V parameters of distinct DPSCs fabricated using FT, FMT, and FTM-ETLs	222
Table 6.3	Collective summary of all roughness and topological parameters of **FT**, **FMT**, **FTM**, and **FMT**/CABB layers	225
Table 6.4	EIS fitted parameters (R_S, R_{Ct}, R_{Rec}, C_1, C_2, and f_{max}) obtained for CABB loaded **FT**, **FMT**, and **FTM**-ETLs in 0.1M $TBAPF_6$ electrolyte in DCM solution	228
Table 6.5	Summary of various calculated electrical parameters, such as electron lifetime (τ_e), diffusion length (L_n), diffusion Coefficient (D_e), charge collection efficiency (η_{cc}), effective diffusion lifetime of electron (τ_D), and conductivity (σ) for all three CABB-loaded FT, FMT, and FTM-ETLs	229

ACRONYMS/ABBREVIATIONS

	1D	One-dimensional
	2D	Two-dimensional
A	α	Absorption coefficient
	AAA	Class A: Spectral Match, Class A: Spatial Uniformity, and Class A: Temporal Stability
	AFM	Atomic force microscopy
	AM	Air-Mass
B	BIPV	Building-integrated photovoltaic
	BE	Binding Energy
	BET	Brunauer–Emmett–Teller
	BV	Beta vulgaris
	BSEs	Backscattered Electrons
C	CABB	$Cs_2AgBiBr_6$
	CABC	$Cs_2AgBiCl_6$
	CB	Conduction band
	CBO	Conduction band offset
	CCE	Charge collection efficiency
	CBM	Conduction band minimum
	CE	Counter electrode
	τ_e	Charge-carrier lifetime
D	DCM	Dichloromethane
	DSSC	Dye-sensitized solar cell
	DMSO	Dimethyl sulphide
	DPSC	Double perovskite solar cell
	D_e	Diffusion Coefficient
	DRS	Diffuse reflectance spectroscopy
E	EPFL	École Polytechnique Fédérale de Lausanne
	EDS	Energy Dispersive X-ray Spectroscopy
	EIS	Electrochemical impedance spectroscopy
	ELIS	Electronics and Information Systems
	EPBT	Energy payback time
	ETL	Electron transport layer
	E_A	Activation Energy
	E_{bi}	Built-in electric field
	E_g	Band gap
F	FCC	Face-centered cubic
	FEG	Field Emission Gun
	FESEM	Field Emission Scanning Electron Microscopy
	FF	Fill factor
	FTO	Fluorine-doped tin oxide
	FWHM	Fill-width half maxima

H	HFP	Hexafluoropropylene
	HJY	Horiba Jobin Yvon
	HRTEM	High Resolution Transmission Electron Microscopy
	HTL	Hole transport layer
	HOMO	Highest occupied molecular orbital
	HTTF	High-temperature tube furnace
I	ICDD	International Centre for Diffraction Data
	IPCE	Incident-photon conversion efficiency
	I_{SC}	Short-circuit current
J	JCPDS	Joint Committee on Powder Diffraction Standards
K	KRICT	Korea University of Science and Technology
L	LUMO	Lowest unoccupied molecular orbital
	LCOE	Levelized cost of electricity
	LHE	Light harvesting efficiency
	LLCT	Ligand-to-ligand charge transfer
	L_D	Electron diffusion length
M	MPN	3-methoxypropionitrile
	MLCT	Metal-to-ligand charge transfer
	μ	Mobility
N	NRs	Nanorods
	N_{if}	Interfacial defect density
	N_t	Trap density
	N_a/N_d	Acceptor/donor doping concentration
O	O_V	Oxygen Vacancies
P	PCE	Power conversion efficiency
	PV	Photovoltaic
	PVDF	Poly (vinylidene fluoride)
	PTAA	Poly (triaryl amine)
	PVP	Poly (vinylpyrrolidone)
Q	QE	Quantum efficiency
R	R_a	Average roughness
	R_{Ct}	Charge-transfer resistance
	R_q	Rms-roughness
	R_{Rec}	Recombination resistance
	R_S	Series resistance
	R_{Sh}	Shunt Resistance
	RT	Room temperature
	R_z	Peak to valley height
S	SAED	Selected Area Electron Diffraction
	SEM	Scanning electron microscopy
	SEs	Secondary Electrons
	SPR	Surface plasmon resonance
	SQ	Shockley-Queisser
	SRH	Shockley-Read-Hall

	SSS	Solid state synthesis
T	TCO	Transparent conducting oxide
	TEM	Transmission Electron Microscopy
	TGA	Thermogravimetric Analysis
	t_{layers}	Thickness of layers
U	UCLA	University of California, Los Angeles
	UNIST	Ulsan National Institute of Science and Technology
	UNSW	University of New South Wales
	UV-vis	Ultraviolet-visible
V	V_{OC}	Open-circuit voltage
	VBM	Valence band maximum
	V_{OC}	Volatile Organic Compounds
	V_{Br}	Bromine vacancies
	VBO	Valence band offset
W	WHO	World Health Organization
X	XPS	X-Ray Photoelectron Spectroscopy
	XRD	X-Ray Diffraction

Chapter 1

Introduction

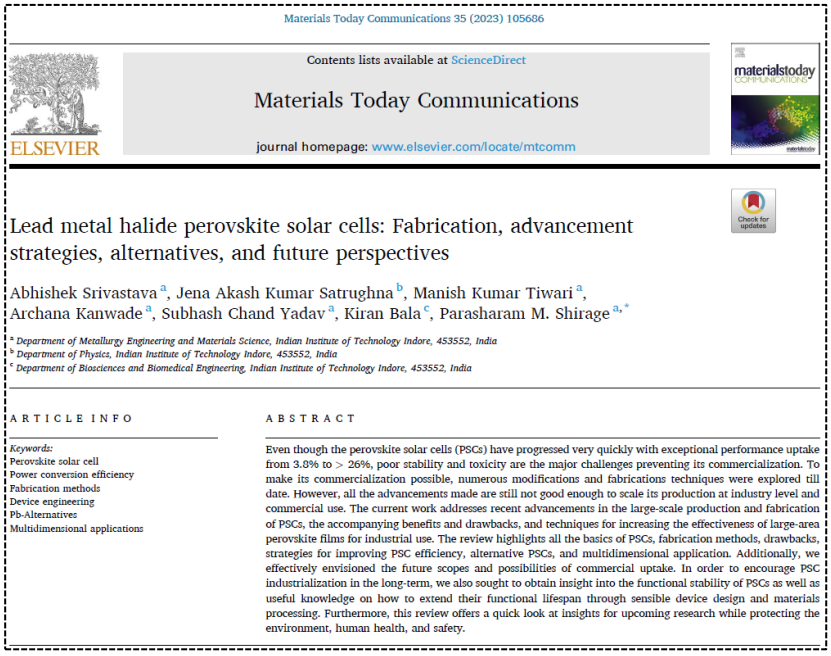

Materials Today Communications 35 (2023) 105686

Contents lists available at ScienceDirect

Materials Today Communications

journal homepage: www.elsevier.com/locate/mtcomm

Lead metal halide perovskite solar cells: Fabrication, advancement strategies, alternatives, and future perspectives

Abhishek Srivastava [a], Jena Akash Kumar Satrughna [b], Manish Kumar Tiwari [a], Archana Kanwade [a], Subhash Chand Yadav [a], Kiran Bala [c], Parasharam M. Shirage [a,*]

[a] Department of Metallurgy Engineering and Materials Science, Indian Institute of Technology Indore, 453552, India
[b] Department of Physics, Indian Institute of Technology Indore, 453552, India
[c] Department of Biosciences and Biomedical Engineering, Indian Institute of Technology Indore, 453552, India

ARTICLE INFO

Keywords:
Perovskite solar cell
Power conversion efficiency
Fabrication methods
Device engineering
Pb-Alternatives
Multidimensional applications

ABSTRACT

Even though the perovskite solar cells (PSCs) have progressed very quickly with exceptional performance uptake from 3.8% to > 26%, poor stability and toxicity are the major challenges preventing its commercialization. To make its commercialization possible, numerous modifications and fabrications techniques were explored till date. However, all the advancements made are still not good enough to scale its production at industry level and commercial use. The current work addresses recent advancements in the large-scale production and fabrication of PSCs, the accompanying benefits and drawbacks, and techniques for increasing the effectiveness of large-area perovskite films for industrial use. The review highlights all the basics of PSCs, fabrication methods, drawbacks, strategies for improving PSC efficiency, alternative PSCs, and multidimensional application. Additionally, we effectively envisioned the future scopes and possibilities of commercial uptake. In order to encourage PSC industrialization in the long-term, we also sought to obtain insight into the functional stability of PSCs as well as useful knowledge on how to extend their functional lifespan through sensible device design and materials processing. Furthermore, this review offers a quick look at insights for upcoming research while protecting the environment, human health, and safety.

This chapter introduces third-generation photovoltaic technologies, focusing on dye-sensitized solar cells (DSSCs) and lead-free double perovskite solar cells (DPSCs). The fundamental working principles, device architectures, and performance-limiting factors of DSSCs are discussed, with an emphasis on the role of photoanode design, doping, and interfacial recombination. The chapter further outlines the evolution of metal halide perovskite solar cells, highlighting key challenges related to lead toxicity, stability, and interface losses. Particular attention is given to $Cs_2AgBiBr_6$-based HTL-free double perovskite solar cells as environmentally benign and stable alternatives. The significance of doping and interfacial passivation strategies in improving charge transport, suppressing defects, and enhancing device performance and stability across both photovoltaic platforms is highlighted, followed by an overview of the scope and objectives of this thesis.

1.1 Dye-Sensitized Solar Cells

The rapid depletion of fossil fuels, driven by excessive consumption and escalating environmental pollution, has necessitated a transition to sustainable, renewable energy sources. Among these, solar energy is particularly attractive owing to its abundance, non-perishable nature, and minimal environmental impact. Solar cells directly convert solar radiation into electrical energy, and extensive research has focused on identifying and optimizing suitable materials and device architectures for efficient solar energy harvesting. Solar cells are generally classified into three generations based on the materials employed and the fabrication techniques adopted, as illustrated in **Figure 1.1**.[1]

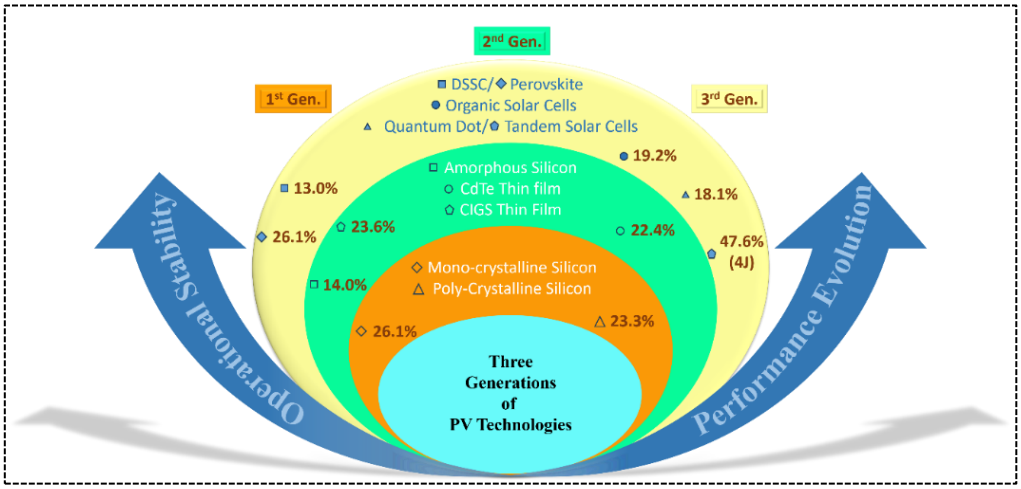

Figure 1.1 Classification of all three generations of Photovoltaic Technologies, Reproduced with permission from Ref. [1].

Within this context, third-generation DSSCs have attracted significant attention due to their low-cost fabrication, simple processing, and moderate power conversion efficiencies (~14% with synthetic dyes and ~6% with natural dyes). Despite these advantages, challenges related to long-term stability under ambient conditions and suboptimal device performance hinder their large-scale commercialization.[2] Consequently, intensive research efforts have focused on advanced engineering strategies, including grain boundary, transport layer, interfacial, precursor, and surface passivation engineering, to mitigate recombination losses and enhance the efficiency and durability of DSSCs.

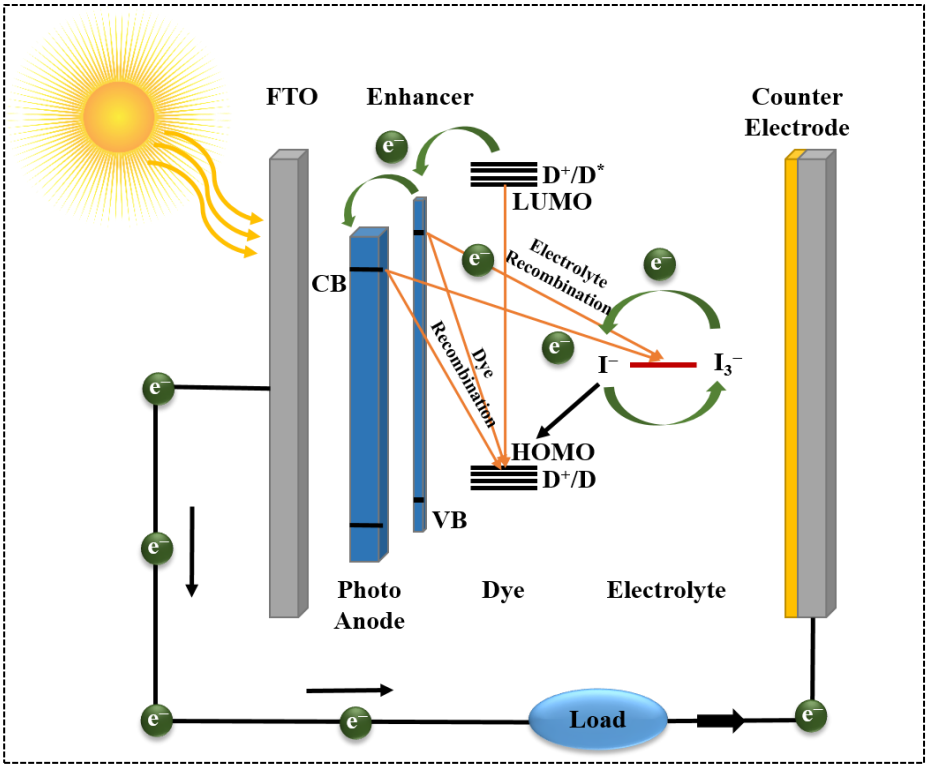

Figure 1.2 Schematics of Dye-Sensitized Solar Cells, their components, and workflow, Reproduced with permission from Ref. [3].

DSSCs are photoelectrochemically operated thin-film solar cells comprising five key components: (i) a transparent conducting oxide (TCO) substrate, which requires high electrical conductivity and optical transparency (≥ 80%) to minimize energy losses; (ii) a photoanode, typically based on wide-bandgap metal oxides such as TiO_2, SnO_2, ZnO, or Nb_2O_5, with TiO_2 being most widely employed due to its suitable bandgap (~3.2 eV), chemical stability, and favourable band alignment; (iii) a sensitizer dye responsible for light absorption and electron injection, where both synthetic dyes and naturally derived organic dyes have been extensively investigated; (iv) an electrolyte, commonly the I^-/I_3^- redox couple, which facilitates dye regeneration but may induce corrosion of TCOs, thereby motivating the development of solid or quasi-solid electrolytes; and (v) a counter electrode, which catalyses the reduction of the redox species and completes the electrical circuit. A schematic representation of a typical DSSC architecture incorporating these components is shown in **Figure 1.2**.[3]

1.1.1 Brief History of DSSC

The DSSCs, also known as Grätzel cells, are a class of low-cost thin-film photovoltaic (PV) technologies that operate on a photoelectrochemical principle, involving a photo-sensitized semiconductor anode in contact with an electrolyte. The modern concept of DSSCs was co-invented by Brian O'Regan and Michael Grätzel in 1988, with subsequent development at the École Polytechnique Fédérale de Lausanne (EPFL), culminating in the landmark demonstration of the first high-efficiency DSSC in 1991 at the University of California, Berkeley.[4]

This pioneering device, fabricated using a mesoporous TiO_2 photoanode sensitized with ruthenium-based dye complexes, achieved a power conversion efficiency of 7.12%, establishing DSSCs as a viable alternative to conventional photovoltaics. In recognition of this transformative contribution to solar energy research, Michael Grätzel was awarded the Millennium Technology Prize in 2010. Since their inception, DSSCs have attracted sustained global research interest due to their low-cost fabrication, environmental benignity, potential for lightweight, flexible design, and simple processing, positioning them as a promising third-generation photovoltaic technology aimed at addressing energy sustainability and environmental challenges.

In the late 1960s, it was discovered that illuminated organic dyes could generate electrical current at oxide electrodes in electrochemical cells, marking an early milestone in photoelectrochemical energy conversion.[5] To better understand and emulate the fundamental charge-transfer processes occurring in natural photosynthesis, this phenomenon was extensively investigated at the University of California, Berkeley, using chlorophyll extracted from spinach as a bio-mimetic or bionic model system.[6] Building on these foundational studies, the principle of DSSC operation was formally demonstrated and discussed in 1972, establishing the conceptual basis for DSSCs.[7]

Early DSSCs employed dyes from circa 1995 that were primarily sensitive to the UV-blue region of the solar spectrum, limiting photocurrent generation. This constraint was addressed with the development of broad-spectrum ruthenium-based sensitizers, particularly triscarboxy-ruthenium terpyridine [$Ru(4,4',4''\text{-}(COOH)_3\text{-terpy})(NCS)_3$], commonly referred to as "black dye" (circa 1999), which enabled efficient light harvesting

across the visible and near-infrared regions. To satisfy long-term operational stability requirements (≥ 20 years), subsequent research focused on chemically and thermally stable sensitizers, including 1-ethyl-3-methylimidazolium tetrocyanoborate [$EMIB(CN)_4$] and copper diselenium [$Cu(In,Ga)Se_2$], leading to improved spectral response, stability, and power conversion efficiency.[8]

From the early 2000s, significant progress in DSSCs was driven by efforts to overcome long-term stability limitations. In 2003, researchers at the EPFL, Switzerland, demonstrated a major breakthrough by employing an amphiphilic ruthenium dye (Z-907) in combination with a quasi-solid-state gel electrolyte based on 3-methoxypropionitrile (MPN) immobilized using poly(vinylidene fluoride-co-hexafluoropropylene) (PVDF-HFP). These devices exhibited exceptional thermal and photochemical stability, retaining ~ 94% of their initial efficiency after 1,000 hours at 80 °C and showing minimal degradation under prolonged light soaking, thereby meeting durability criteria comparable to those of conventional silicon (Si) solar cells.[9] Subsequent studies (2006-2008) further validated the robustness of DSSCs through solid-hybrid architectures, chemically stable electrolytes such as 1-ethyl-3-methylimidazolium tetracyanoborate, and solvent-free molten-salt redox systems, while alternative semiconductor morphologies (nanowires and nanowire-nanoparticle hybrids) were introduced to enhance electron transport and red-light harvesting.

Between 2009 and 2013, DSSC research expanded to focus on advanced device architectures and solid-state configurations. Innovations such as fibre-shaped DSSCs based on ZnO nanowires, porphyrin-based low-cost organic dyes, and platinum-free counter electrodes (e.g., cobalt sulfide) significantly reduced material costs while improving efficiency and stability. A major paradigm shift occurred with the emergence of solid-state DSSCs, where liquid electrolytes were replaced by solid hole-transport materials. This transition culminated in efficiencies rising from ~ 4% to 15%, notably through the use of hybrid perovskite sensitizers such as $CH_3NH_3PbI_3$, marking a crucial link between DSSCs and modern perovskite solar cell (PSC) technologies. Parallel efforts also demonstrated large-area module fabrication, building-integrated photovoltaics

(BIPV), and steel-based DSSC modules, highlighting their scalability and architectural compatibility.[10,11]

More recent developments (2018-2022) have focused on light-management strategies, cost-effective materials, and high-performance sensitization schemes. Enhancements using plasmonic gold nanorods, one-dimensional TiO_2 nanostructures, stainless steel counter electrodes, and copper-complex redox electrolytes have increased DSSC efficiencies to over 13% under standard illumination.[12–14]

In recent years, concerns over the high cost, toxicity, and complex synthesis of conventional synthetic sensitisers, particularly ruthenium-based dyes, have driven interest in naturally derived dyes as sustainable alternatives for DSSCs. Natural dyes extracted from plant sources, such as anthocyanins, betalains, chlorophylls, and carotenoids, are environmentally benign, low-cost, and readily available. However, their application in DSSCs is constrained by narrow absorption bandwidths, low molar extinction coefficients, suboptimal energy level alignment with TiO_2, weak surface anchoring, rapid photodegradation, and poor long-term stability. Additionally, compositional variability and inefficient charge injection lead to lower power conversion efficiencies than those of synthetic dyes, necessitating advanced interface engineering and sensitization strategies to realize their practical potential.

1.1.2 Selection Rule and Criteria for Dye Extraction

Although synthetic dyes have steadily improved the efficiency of DSSCs, concerns about environmental impact, cost, and toxicity necessitate exploring sustainable alternatives. Natural dyes derived from plants offer an eco-friendly and economically viable solution, as they inherently function as light-harvesting pigments during photosynthesis. The primary selection criterion for natural dye extraction is strong photon absorption within the visible spectrum, ensuring effective solar energy harvesting. Additionally, the chosen plant sources must be abundant, easily accessible, non-toxic, and renewable to maintain cost-effectiveness and environmental compatibility. The widespread availability of naturally occurring pigments and their intrinsic light-absorbing capability make them suitable candidates for sustainable DSSC fabrication, aligning photovoltaic development with green energy principles.

Since dyes can be extracted from various plant parts irrespective of species, the selection process must prioritize availability, renewability, and environmental compatibility alongside photovoltaic suitability. A systematic selection strategy forms the foundation of DSSC fabrication, beginning with identifying plant sources rich in light-absorbing pigments and followed by optimizing extraction conditions (solvent type, pH, temperature, and time) to maximize dye stability and adsorption efficiency, as shown in **Figure 1.3**.

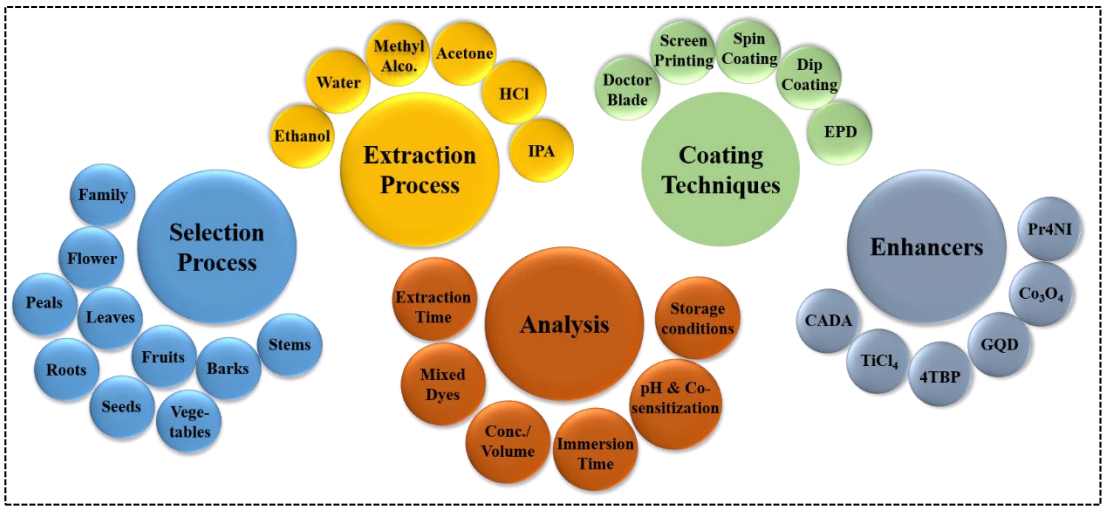

Figure 1.3 Schematic selection criterion framework for sustainable and eco-friendly DSSC technology, Reproduced with permission from Ref. [13].

The extraction methodology significantly influences device performance, as it governs dye purity, bonding capability with TiO_2, and resistance to degradation. Therefore, ideal criteria include strong solar-spectrum absorption, chemical compatibility with photoanodes, minimal toxicity, cost-effectiveness, and long-term operational stability. Additionally, understanding fabrication dependencies and potential performance limitations enables the development of improved strategies to enhance efficiency, reduce costs, facilitate commercialization, and ensure environmentally responsible solar energy generation.

Plant selection plays a decisive role in the performance and stability of natural DSSCs. The chosen plant must contain pigments capable of absorbing a significant portion of the solar spectrum and forming strong chemical bonds with TiO_2 photoanodes

for efficient electron injection. Key natural pigments, such as carotenoids, betalains, anthocyanins, and chlorophyll, exhibit distinct absorption ranges, making some more suitable than others for photovoltaic applications.[15] In addition to optical properties, factors such as plant type, family, abundance, and extraction feasibility must be considered to ensure sustainability and reproducibility. It is also important to distinguish between pigments and dyes: pigments are naturally occurring colorants within plants, while dyes are solvent-extracted, more soluble, and application-ready forms used in DSSC fabrication. Thus, careful plant selection and proper extraction are essential to achieving optimal light absorption, interfacial bonding, and long-term device stability as summarized in **Table 1.1**.

Table 1.1 Summary of various selection rules and extraction criteria.

Parameters	**Optimized Conditions**
Solvent	Ethanol (alcohol), Water
Processing temperature	70-80 °C
Dye extraction method	Cold extraction and Soxhlet extraction
Dye concentration	Need to be optimized for the individual case
pH	2-4
Extraction time	16-24 h
Storage temperature	-20 to 4 °C

1.1.3 Working Principle of DSSCs

The working mechanism of a DSSC is governed by four fundamental processes: photoabsorption, electron injection, charge carrier transport, and current collection, as schematically illustrated in **Figure 1.2**. Upon illumination, photons are absorbed by the dye molecules, which act as photosensitizers, exciting electrons from the ground state (S^+/S) to the excited state (S^+/S^*). The photoexcited electrons, possessing lifetimes in the nanosecond range, are subsequently injected into the conduction band (CB) of TiO_2 photoanodes, which lies energetically below the excited state of the dye ($CB_{photoanode} < S^+/S^*$). In addition, photoanodes contribute marginally to photon absorption in the ultraviolet region, as reported in the literature. This process results in the oxidation of the dye molecule, initiating charge separation, which can be represented by the following chemical reaction:

$$S^+/S + h\upsilon \rightarrow S^+/S^* \quad 1.1$$

$$S^+/S^* \rightarrow S^+/S + e^- \text{ (photoanode)} \quad 1.2$$

Following the injection, the photogenerated electrons are transported through the photoanodes and diffuse towards the transparent conducting oxide (FTO) electrode. These electrons subsequently flow through the external circuit to the counter electrode (CE), where they participate in the reduction of triiodide (I_3^-) to iodide (I^-). The regenerated iodide ions then donate electrons to the oxidized dye molecules, restoring the dye to its ground state. Concurrently, iodide ions are oxidized back to triiodide (I_3^-), thereby completing the redox cycle, as described by **equation 1.3**.

$$S^+/S^* + e^- \rightarrow S^+/S \quad 1.3$$

$$I_3^- + 2e^- \rightarrow 3I^- \quad 1.4$$

Subsequently, the oxidized I_3^- species diffuse towards the CE, where they are reduced to I^-, as represented by **equation 1.4**. Upon solar illumination, dye sensitization occurs through the formation of the highest occupied molecular orbital (HOMO) and lowest unoccupied molecular orbital (LUMO) levels within the sensitizer molecules. When incident photons have

sufficient energy, electrons are excited from the HOMO to the LUMO and injected into the $CB_{photoanodes}$, accompanied by oxidation of the dye. The external circuit facilitates the transport of these injected e^- to the CE, where they reduce the I_3^-/I^- redox couple in the electrolyte, enabling continuous regeneration of the dye molecules and sustained photocurrent generation.[16]

1.2 Perovskite Solar Cells

Materials exhibiting a crystal structure analogous to the first discovered calcium titanate ($CaTiO_3$) are classified as perovskites. Perovskites adopt a general ABX_3 crystal structure, where A and B represent monovalent and divalent cations, respectively, and X represents an oxygen or halide anion. In the perovskite structure, each B-site cation is octahedrally coordinated by six X^- anions to form $[BX_6]^{4-}$ octahedra, which are

interconnected through corner sharing to generate a ReO_3-type framework, while the A-site cation occupies the cuboctahedral voids within the lattice, as illustrated in **Figure 1.4**. A key advantage of the perovskite structure lies in its ability to accommodate cations with different valence states; for oxide perovskites ($X = O^{2-}$), A- and B-site cations are typically divalent and trivalent, whereas for halide perovskites ($X = Cl^-$, Br^-, or I^-), the corresponding cations are monovalent and divalent. This compositional flexibility enables efficient tuning of material properties, particularly the bandgap.

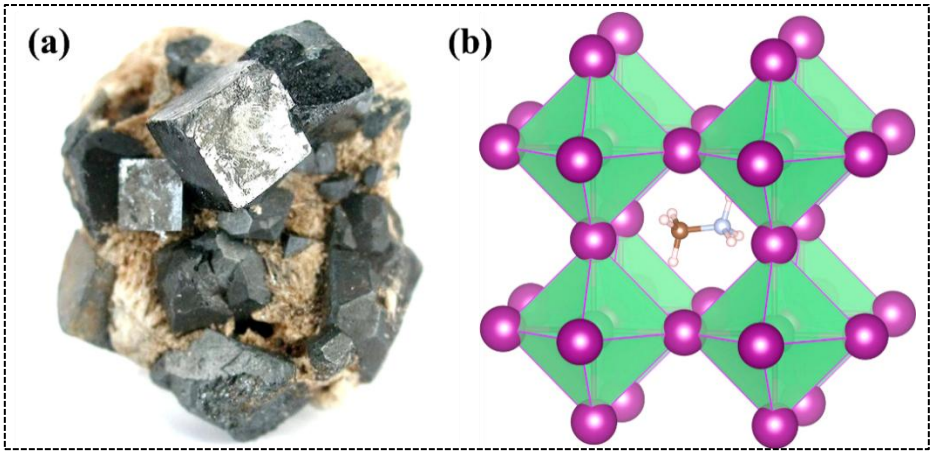

Figure 1.4 (a) $CaTiO_3$ Perovskite, and (b) crystal structure of $MAPbI_3$, where the MA^+ cation is surrounded by four PbX_6 octahedra, Reproduced with permission from Ref. [17]

Currently, PSCs are a rapidly emerging class of photovoltaic devices that utilize perovskite (ABX_3)-structured halide compounds, most commonly hybrid organic-inorganic or all-inorganic lead/tin halides (such as $CH_3NH_3PbX_3$ or $MAPbX_3$, $CH(NH_2)_2PbX_3$ or $FAPbX_3$) as the light-harvesting active layer. These materials are attractive due to their low-cost raw constituents, simple solution-based fabrication routes, and exceptional optoelectronic properties, including high absorption coefficients, low exciton binding energies, long carrier diffusion lengths, and high charge-carrier mobilities. The ability of perovskites to absorb the full visible spectrum using ultrathin films (~500 nm) enables the fabrication of lightweight, flexible, and high-performance solar modules.

Due to their defect tolerance and suppressed non-radiative recombination, PSCs have demonstrated an unprecedented increase in power conversion efficiency, rising from

3.8% in 2009 to ~27% in single-junction architectures and exceeding 34% in perovskite-silicon tandem devices.[18–20] These rapid efficiency gains, combined with a low energy payback time (EPBT) and a reduced levelized cost of electricity (LCOE), position PSCs as strong contenders for next-generation photovoltaic technologies. However, critical challenges related to lead toxicity, long-term operational instability, moisture sensitivity, and the complexity and hygroscopic nature of conventional hole transport layers (HTLs) limit large-scale deployment.[21]

To address these concerns, lead-free double perovskite solar cells, particularly those based on environmentally benign compounds such as $Cs_2AgBiBr_6$, have emerged as promising alternatives due to their superior thermal and chemical stability. In parallel, HTL-free device architectures are gaining increasing attention as they simplify fabrication, reduce material costs, suppress interfacial degradation, and enhance device durability. Together, the development of lead-free absorbers and HTL-free architectures represents a crucial strategy for advancing stable, sustainable, and commercially viable perovskite photovoltaic technologies.

1.2.1 Brief History of PSCs

Although perovskite materials have been known for several decades, their first application in PV devices was reported by Tsutomu Miyasaka *et al.*[18] in 2009, using a DSSC architecture in which a thin $MAPbI_3$ perovskite layer deposited on mesoporous TiO_2 served as the light absorber and electron collector, yielding a power conversion efficiency (PCE) of 3.8%. However, the use of a liquid, corrosive lithium halide and halogen (redox couple) electrolyte resulted in severe instability, limiting device operation to only a few minutes. Building on this concept, Park *et al.*[22] demonstrated improved device performance in 2011, achieving a PCE of 6.5% while retaining the DSSC-inspired configuration.

A major breakthrough occurred in 2012, when Mike Lee and Henry Snaith at the University of Oxford demonstrated that perovskite absorbers could operate efficiently with a solid-state HTL, such as spiro-OMeTAD, eliminating the need for a liquid electrolyte and significantly enhancing device stability. They further revealed that mesoporous TiO_2 was not essential for electron transport, as higher efficiencies exceeding

10% were achieved by replacing it with an inert scaffold.[23] Subsequent substitution of TiO_2 with Al_2O_3 resulted in increased open-circuit voltage (V_{OC}) and a 3-5% relative efficiency enhancement, providing the critical insight that a mesoporous scaffold was unnecessary for charge extraction. This finding was soon followed by the demonstration that perovskite materials themselves exhibit ambipolar charge transport, enabling both electron and hole conduction, and ultimately culminating in the realization of planar thin-film PSCs without a mesoporous scaffold, achieving efficiencies exceeding 10%.[24–26]

From 2013 onwards, rapid advancements were achieved in both sensitized and planar PSC architectures through innovations in deposition techniques and device design. In 2013, Burschka *et al.*[11] reported a two-step solution-processing method for sensitized architectures, achieving PCEs exceeding 15%. In parallel, Malinkiewicz *et al.*[27] and Liu *et al.*[28] demonstrated planar PSCs fabricated via thermal co-evaporation, reaching efficiencies above 12% and 15% in p-i-n and n-i-p configurations, respectively. During the same period, Docampo *et al.*[29] introduced an inverted planar architecture analogous to organic solar cells, in which the HTL is positioned beneath, and the electron-collecting layer is above the perovskite absorber.

Further progress in 2014 led to a reported reverse-scan efficiency of 19.3% using a planar thin-film architecture by Yang Yang at the University of California, Los Angeles (UCLA), followed by a certified non-stabilized efficiency of 20.1% achieved by researchers at Korea University of Science and Technology (KRICT).[30,31] Since 2015, single-junction PSCs have consistently set new efficiency records each year, predominantly driven by research groups at KRICT and UNIST, culminating in a record 25.7% reported by UNIST in 2021.[19] Most recently, in 2025, researchers from Soochow University, in collaboration with UNSW, reported a record power conversion efficiency of 26.95% for single-junction PSCs, representing the highest efficiency achieved to date for this device architecture.

Concurrently, significant efforts have been directed towards cost reduction and scalability, exemplified by the Apolo project consortium at CEA laboratories, which aims to achieve module costs below €0.40/Watt peak. Moreover, since 2016, perovskite-silicon tandem solar cells have consistently outperformed single-junction perovskite devices,

with record efficiencies repeatedly set by Oxford Photovoltaics and Helmholtz-Zentrum Berlin, the latter achieving a landmark 34.85% efficiency by Longi (Chinese Solar Module Manufacturer) in 2025.[31,32]

1.2.2 Key Structural Parameters for Perovskites

The structural geometry and long-term stability of perovskite materials are strongly governed by the ionic radii and charge states of the constituent ions. The formation of stable metal halide perovskites is constrained by three fundamental criteria:

(i) **charge neutrality** among the A-, B-, and X-sites[33]

$$N(A) + N(B) = 3N(X) \quad (1.5)$$

(ii) the **octahedral factor (μ)**, which predicts the structural stability of the BX_6 octahedra[34]

$$\mu = \frac{r_B}{r_X} \quad (1.6)$$

(iii) the **Goldschmidt tolerance factor (t)**, the most widely adopted descriptor for assessing perovskite structural stability[35]

$$t = \frac{r_A + r_X}{\sqrt{2}(r_B + r_X)} \quad (1.7)$$

where N and r_A, r_B, and r_X represent the valence states and ionic radii of the A-, B-, and X-site ions, respectively.

The size constraints imposed by the BX_6 octahedral framework limit the incorporation of the B-site cation, and metal halide perovskites are reported to be structurally stable when the μ lies within the range $0.442 \leq \mu \leq 0.895$.[36] The degree of geometric compatibility of the A-site cation within the perovskite lattice is quantitatively described by the t, with stable perovskite formation occurring only when $0.8 \leq t \leq 1$. A value of $t \approx 1$ corresponds to an ideal cubic ABX_3 perovskite structure.[34] When t falls within the range 0.9-1.0, predominantly cubic phases are favoured, whereas values between 0.8 and 0.89 typically result in distorted perovskite structures, such as orthorhombic, tetragonal, or rhombohedral phases, due to the progressive reduction in r_A.

Conversely, when t > 1, indicating an oversized r_A, the perovskite framework becomes unstable and preferentially transforms into hexagonal structures composed of face-sharing octahedral stacks.[37,38]

The ideas of isovalent and aliovalent substitution in metal halide perovskites can also be explained using these replacement principles. To forecast new lead-free perovskite complexes for solar applications based on the ionic radii of the participating ions, the Goldschmidt substitution rules have recently attracted considerable attention. **Figure 1.5 (a)** shows the estimated t and μ values for different perovskite materials. In contrast, **Figure 1.5 (b)** depicts the investigated (t, μ) values for relative stability between any two perovskites according to the new factor $(\mu + t)^{\eta}$ (where η: atomic packing fraction) demonstrated by Chen *et al.*[39] and Sun *et al.*[40]

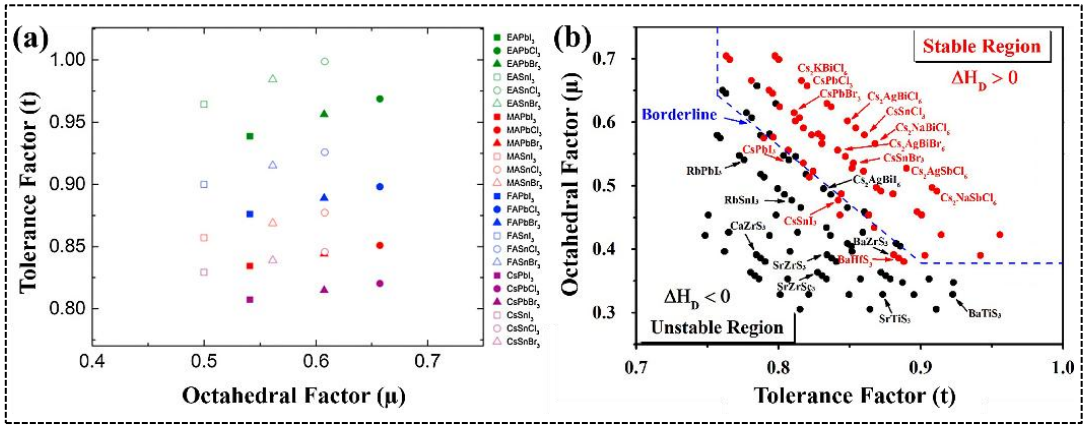

Figure 1.5 (a) octahedral factor (μ) for various perovskite materials, reproduced with permission from Ref. [39] and (b) Map of (t,μ) for estimating the relative stability of the different perovskite materials, reproduced with permission from Ref. [40].

1.2.3 Working Principle of PSCs

PSCs operate by converting incident solar radiation into electrical energy through photon absorption, charge generation, charge separation, charge transport, and current collection. Depending on the stacking order of the functional layers, PSCs are generally categorized into **n-i-p (planar)**, **p-i-n (inverted)**, and **mesoporous** device architectures, as shown in **Figure 1.6**. While the charge-generation mechanism remains the same in all

three configurations, the direction of charge extraction and the nature of the transport layers differ.[1]

i. n-i-p (planar) Architecture

In the n-i-p structure (**Figure 1.6(a)**), the device typically consists of a TCO/ETL/perovskite/HTL/Au stack. Upon illumination, photons are absorbed by the perovskite layer, generating free charge carriers (electrons: e^- and holes: h^+) due to the low exciton binding energy of the perovskite. The photoexcited e^- are transferred from the $CB_{perovskite}$ to the ETL (commonly TiO_2 or SnO_2), while h^+ remain in the $VB_{perovskite}$ and are extracted by the HTL (such as spiro-OMeTAD or PTAA). The ETL selectively transports e^- to the TCO electrode, whereas the HTL transports h^+ to the Au-metal back contact. The built-in electric field across the junction, combined with favourable energy-level alignment, suppresses charge recombination and drives efficient charge separation and collection, thereby generating photocurrent.

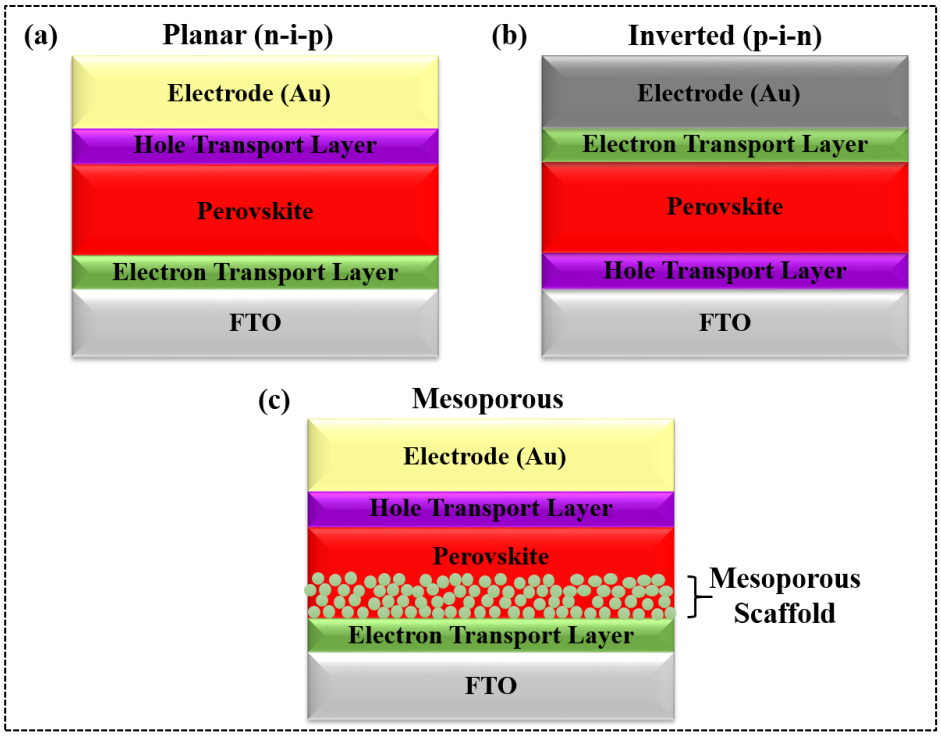

Figure 1.6 Typical schematics of commonly explored PSC architectures, Reproduced with permission from Ref. [1].

ii. p-i-n (inverted) Architecture

In the p-i-n configuration (**Figure 1.6(b)**), the layer sequence is reversed, consisting of a TCO/HTL/perovskite/ETL/Au stack. Upon solar illumination, the perovskite absorber generates e^--h^+ pairs in the same manner as in n-i-p devices. However, in this architecture, photogenerated h^+ are first extracted by the HTL (typically PEDOT: PSS, NiO_x, or PTAA) and transported to the TCO electrode, while e^- are selectively transferred to the ETL (such as PCBM, C60, or ZnO) and collected at the Au electrode. The inverted structure often exhibits reduced hysteresis, improved interfacial stability, and compatibility with low-temperature fabrication processes, making it particularly suitable for flexible substrates and tandem applications.

iii. Mesoporous PSC Architecture

In mesoporous PSCs (**Figure 1.6(c)**), the structure generally consists of FTO/ETL/mesoporous scaffold/perovskite/HTL/Au. The mesoporous layer (commonly TiO_2 or Al_2O_3) provides a high-surface-area scaffold that is infiltrated by the perovskite absorber. Upon illumination, photogenerated e^- are rapidly injected into the mesoporous ETL network, while h^+ are transported through the perovskite phase to the HTL. When TiO_2 is used, it actively participates in electron extraction; in contrast, Al_2O_3 is electrically inert, confirming that the perovskite itself acts as a bipolar charge transporter. The mesoporous architecture enhances charge separation and interfacial contact, leading to high efficiencies, albeit often requiring higher processing temperatures.

1.3 Shockley-Queisser Limit

The radiative efficiency limit, commonly known as the Shockley-Queisser (SQ) limit, defines the maximum theoretical PCE of a single p-n junction solar cell under the assumption that radiative recombination is the sole loss mechanism. First derived by William Shockley and Hans-Joachim Queisser in 1961, the SQ limit predicts a maximum efficiency of ~30% for a bandgap of 1.1 eV using a 6000 K black-body approximation of the solar spectrum.[41] Subsequent refinements employing the AM 1.5 solar spectrum and incorporating a rear-surface reflector increased the theoretical limit to 33.16% for an optimal bandgap of 1.34 eV, corresponding to a maximum extractable power of ~337 W m^{-2} from incident sunlight (~1000 W m^{-2}).[42] Silicon, with a bandgap of 1.1 eV, has a

theoretical limit of ~32%, while state-of-the-art commercial monocrystalline silicon solar cells currently achieve efficiencies of around 24%, primarily limited by optical and resistive losses, as shown in **Figure 1.7(a)**.

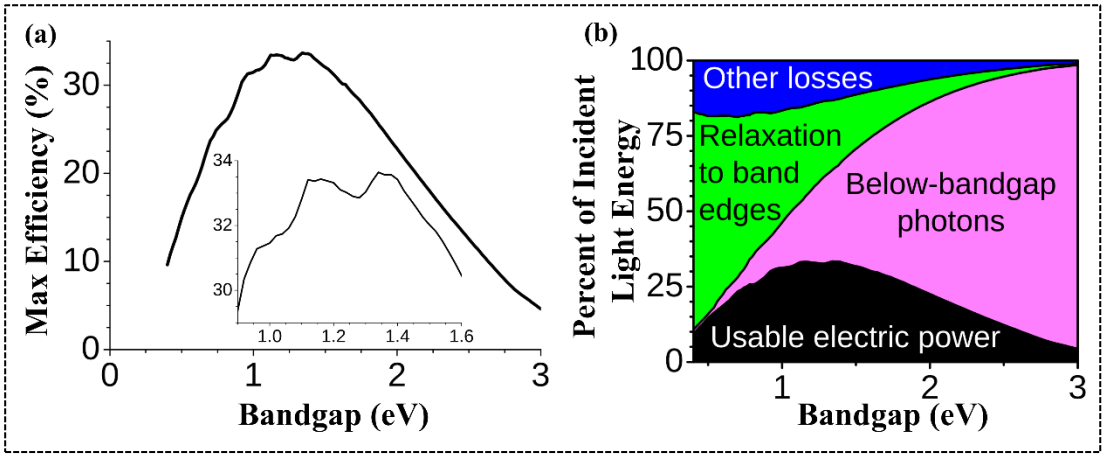

Figure 1.7 (a) The Shockley-Queisser limit represents the theoretical maximum efficiency of a solar cell without solar concentration, with the inset region highlighting the bandgap range where peak efficiency occurs. (b) Quantitative breakdown of efficiency losses limiting single-junction solar cell performance according to the Shockley-Queisser theory, Reproduced with permission from Ref. [41].

The Shockley-Queisser analysis assumes that each absorbed photon generates one electron-hole pair, excess photon energy is lost through thermal relaxation, and the solar cell operates under non-concentrated sunlight. Based on these assumptions, efficiency losses arise from three main processes: transmission of sub-bandgap photons (pink), thermalization of hot carriers to the band edges (green), and recombination-voltage trade-offs (blue). The black region represents the portion of incident solar energy that can be converted into useful electrical power, corresponding to the Shockley-Queisser efficiency limit (**Figure 1.7(b)**).

Based on the AM1.5G global solar spectrum, the maximum PCE of a single-junction solar cell exhibits a parabolic dependence on the absorber bandgap, reflecting the balance between photon absorption and voltage losses. This theoretical limit can be expressed as:

$$\eta = t_s \times u(x_g) \times v(f, x_g, x_c) \times m\left(\frac{v\, x_g}{x_c}\right) \quad 1.8$$

where $x_g = \frac{V_g}{V_s}$, $x_c = \frac{V_c}{V_s}$. Here, u represents the ultimate photon-absorption efficiency, v denotes the ratio of the open-circuit voltage (V_{OC}) to the bandgap voltage (V_g), and m is the impedance-matching factor that accounts for maximum power extraction. V_C is the thermal voltage, and V_S is the voltage equivalent of the Sun's temperature. Together, these factors define the fundamental efficiency ceiling for single-junction photovoltaic devices under standard solar illumination.

The SQ limit applies strictly to single-junction devices, while multi-junction solar cells can surpass this constraint, with theoretical efficiencies reaching 68.7% under unconcentrated sunlight and up to 86.8% under concentrated illumination.[43,44]

1.4 Natural DSSCs and Pb-Free DPSCs

Although remarkable progress has been achieved in photovoltaic device efficiencies, the reliance on toxic, scarce, and environmentally hazardous materials continues to limit long-term sustainability. Consequently, the exploration of eco-friendly, earth-abundant photovoltaic materials with stable and efficient performance has become a critical research priority.

In recent years, natural-dye-sensitized DSSCs have emerged as a sustainable alternative to conventional ruthenium-based systems, driven by concerns about the cost, toxicity, and environmental persistence of synthetic dyes. Natural pigments, such as betalains, anthocyanins, chlorophylls, and carotenoids, offer advantages including abundance in the earth, biodegradability, low toxicity, and simple extraction protocols.[16,45] However, their practical implementation is hindered by narrow absorption bandwidths, lower molar extinction coefficients, weak binding to TiO_2 surfaces, and poor photochemical stability. To address these challenges, synergistic dye-sensitization strategies involving the co-sensitization of complementary natural dyes have been explored to broaden spectral coverage and enhance photon harvesting. Such approaches improve light absorption across the visible region while mitigating competitive adsorption and recombination losses at the dye/ETL interface.

Beyond dye engineering, ETL modification plays a crucial role in improving charge extraction and mitigating interfacial recombination in natural-dye-based DSSCs. Aliovalent and isovalent doping of ETLs (e.g., Fe-, Cu-, or metal-ion-doped TiO_2) has been employed to induce bandgap tuning, defect passivation, and enhanced visible-light absorption, while simultaneously improving carrier mobility and conductivity.[16] Additionally, surface passivation treatments, including chemical modifiers (such as $TiCl_4$, toluene, and chlorobenzene) and emerging 2D materials ($Ti_3C_2T_X$ MXene), reduce surface trap states and optimize the ETL work function. These modifications facilitate favourable energy level alignment between the $LUMO_{dye}$ and the CB_{ETL}, resulting in improved electron injection efficiency, suppressed back-electron transfer, and enhanced V_{OC}.[46]

Parallel to advancements in DSSCs, lead-free DPSCs have gained significant attention as environmentally benign alternatives to Pb-based perovskites. Among them, double perovskites with the general formula $A_2B'B'''X_6$, particularly $Cs_2AgBiBr_6$ (CABB), have demonstrated excellent thermal, moisture, and photochemical stability, owing to their robust inorganic framework.[47] Despite possessing an indirect and relatively wide bandgap, performance limitations in CABB-based DPSCs can be effectively mitigated through interfacial and band-structure engineering. In this context, surface passivation and dual interfacial passivation strategies targeting both the FTO/ETL and ETL/perovskite interfaces have proven effective in reducing non-radiative recombination, tuning band offsets, and enhancing charge selectivity. Such dual interfacial passivation establishes optimized energy band alignment, improves carrier extraction kinetics, and significantly enhances device stability and photovoltaic performance, positioning lead-free double perovskites as promising candidates for next-generation sustainable photovoltaics.

1.5 Factors Affecting Solar Cells' Performance

The performance of photovoltaic devices such as DSSCs and DPSCs is governed by several physical, chemical, and interfacial parameters that influence light harvesting, charge generation, charge transport, and recombination dynamics. Understanding these factors is essential for optimizing device efficiency, stability, and scalability in next-generation photovoltaic systems.

1.5.1 Light Absorption and Band Gap Engineering

The ability of a photovoltaic material to efficiently absorb sunlight is primarily determined by its optical band gap and absorption coefficient.

- Materials with an appropriate band gap (1.1-1.8 eV) can effectively harvest a large portion of the solar spectrum.
- In DSSCs, the dye sensitizer determines the spectral absorption range, while in perovskite solar cells, the absorber layer directly governs photon harvesting.
- Insufficient light absorption leads to lower photogenerated carrier density and reduced short-circuit current density (J_{SC}).

Strategies such as band gap tuning through doping, compositional engineering, and absorber optimization are therefore critical for enhancing solar cell performance.[16,48]

1.5.2 Interfacial Charge Transport and Recombination

Interfaces between different layers in photovoltaic devices play a decisive role in determining charge extraction efficiency.

- Poor band alignment between the electron transport layer (ETL), absorber layer, and electrodes can hinder carrier transport.
- Interfacial defects often act as recombination centres, reducing the open-circuit voltage (V_{OC}) and overall device efficiency.
- In DSSCs, recombination frequently occurs at the TiO_2/dye/electrolyte interface, while in perovskite devices, recombination is prominent at ETL/absorber and absorber/electrode interfaces.

Interfacial engineering approaches such as surface passivation, defect suppression, and band alignment tuning are therefore essential for minimizing recombination losses.[49]

1.5.3 Charge Transport and Carrier Diffusion

Efficient carrier transport within the device layers is crucial for achieving high photocurrent and fill factor.

- Low carrier mobility and short diffusion lengths can lead to carrier trapping and recombination before charge extraction.
- The morphology and crystallinity of the transport layers significantly affect electron mobility and charge diffusion pathways.
- In DSSCs, one-dimensional TiO_2 nanostructures can enhance directional electron transport, while in perovskite devices, optimized ETLs improve electron extraction.

Improving charge mobility through material engineering, defect control, and optimized layer thickness is therefore critical for enhancing device performance.[47,49]

1.5.4 Material Stability and Environmental Effects

Long-term operational stability remains a major challenge for emerging photovoltaic technologies.

- Conventional perovskite materials often suffer from moisture sensitivity, thermal degradation, and ion migration, which lead to rapid performance degradation.
- DSSCs can also experience stability issues due to electrolyte leakage, dye degradation, and interfacial instability.
- Environmental factors such as humidity, temperature fluctuations, and continuous illumination further influence device durability.

Developing stable absorber materials, robust interfaces, and protective electrode structures is therefore essential for improving device lifetime.

1.5.5 Electrode and Device Architecture

The selection of electrode materials and device configuration significantly influences the overall photovoltaic performance.

- Noble metals such as Au and Ag offer excellent conductivity but increase device cost and may introduce chemical instability.

- Alternative electrodes such as carbon-based materials provide a cost-effective and chemically stable option with favourable work function alignment.
- Device architecture, including HTL-free configurations, can simplify fabrication while maintaining efficient charge extraction if interfacial recombination is properly controlled.

Optimizing electrode materials and device architecture is therefore essential for developing scalable and economically viable photovoltaic technologies.[47,49]

1.6 Research Gaps, Challenges, and Motivation

Despite considerable progress in third-generation photovoltaic technologies, several critical scientific and technological gaps persist, limiting the efficiency, stability, and large-scale applicability of DSSCs and lead-free DPSCs. The key research gaps addressed in this thesis are outlined below:

- **Interfacial Recombination Losses in DSSCs**
  Severe charge recombination at the photoanode/electrolyte interface limits V_{OC} and overall efficiency, necessitating advanced passivation and interface engineering strategies.
- **Sustainability-Performance Trade-off in Dye Systems**
  Synthetic dyes offer higher efficiency but raise environmental concerns, while natural dyes suffer from poor absorption and charge-transfer properties, highlighting the need to enhance the performance of eco-friendly sensitizers.
- **Limited Insight into Doping-Induced Charge Dynamics**
  The role of dopants (e.g., Fe) in tuning charge transport, defect states, and recombination behaviour in TiO_2-based photoanodes remains poorly understood, particularly in natural DSSCs.
- **Low Efficiency of Lead-Free Double Perovskites**
  CABB-based DPSCs exhibit excellent stability but suffer from low carrier mobility, high defect density, and weak absorption, resulting in poor photovoltaic performance.
- **Charge Extraction Limitations in HTL-Free Architectures**

HTL-free devices simplify fabrication and cost but introduce higher recombination and inefficient charge extraction, requiring optimized interface and electrode engineering.

- **Underexplored MXene-Based Interfacial Engineering**
  The potential of $Ti_3C_2T_X$ MXene for defect passivation, band alignment tuning, and dual-interface engineering in DSSCs and DPSCs remains insufficiently explored.

Motivation of the Present Work

Motivated by these challenges, this thesis focuses on advanced material design and interfacial engineering strategies to enhance the performance and sustainability of photovoltaic devices. By integrating MXene-based passivation, controlled doping of photoanodes, and optimized HTL-free device architectures, the work aims to address recombination losses, improve charge-carrier dynamics, and develop efficient, stable, and environmentally benign DSSCs and lead-free DPSCs, thereby advancing next-generation green energy technologies.

1.7 Materials of Choice

The selection of materials in this research was driven by the critical requirements of third-generation PV devices, including efficient light harvesting, favourable energy-band alignment, low recombination losses, chemical stability, environmental benignity, and cost-effective fabrication. Accordingly, this work is structured around five key material components: (i) photoanodes/electron transport layers (ETLs), (ii) dye photosensitizers, (iii) electrolytes, (iv) Pb-free perovskite light absorbers, and (v) counter/back contact electrodes, each chosen for its functional relevance and synergistic role in DSSCs and PSCs performance.

1.7.1 Photoanode or ETL

One-dimensional and thin-film TiO_2 architectures were employed as photoanodes and ETLs due to their excellent electron mobility, suitable conduction-band positions, chemical stability, and compatibility with both DSSCs and perovskite solar cells. The

morphology-enabled large surface area of 1D TiO_2 nanorods facilitates high monolayer dye loading in DSSCs and efficient charge extraction in perovskite devices, while also providing efficient UV-light blocking.

From an electronic perspective, TiO_2 possesses a wide bandgap of approximately 3.0-3.2 eV, depending on its crystalline phase (anatase or rutile), which ensures high optical transparency in the visible region. This maximizes photon transmission to the active light-harvesting layer, whether it is dye molecules in DSSCs or $Cs_2AgBiBr_6$ perovskite absorbers in PSCs. Additionally, the conduction band minimum (CBM) of TiO_2 (~-4.0 to -4.2 eV with respect to vacuum) is well aligned with the excited-state energy levels of most sensitizing dyes and the conduction band of $Cs_2AgBiBr_6$ perovskite absorbers. Such favourable band alignment enables efficient downhill electron injection from the dye excited state (LUMO) or perovskite CB into TiO_2, thereby minimizing energetic losses.

In DSSCs, 1D TNR offers a high specific surface area, enabling efficient dye adsorption and enhanced light harvesting. Following photoexcitation, electrons are injected from the dye's excited state into the TiO_2 conduction band on an ultrafast timescale (femtosecond to picosecond), effectively outcompeting charge recombination. The interconnected TiO_2 network facilitates electron diffusion toward the FTO electrode, while appropriate surface passivation suppresses back-electron transfer to the oxidized dye or the electrolyte. Furthermore, TiO_2 exhibits excellent chemical compatibility and long-term stability with the conventional I^-/I_3^- redox electrolyte.

In PSCs, TiO_2 serves as an electron-selective transport layer, efficiently extracting photogenerated electrons while blocking holes due to its deep valence band (~ -7.2 eV), thereby minimizing interfacial recombination losses. TiO_2-based ETLs are particularly effective in n-i-p architectures, where compact and mesoporous layers promote uniform perovskite crystallization and efficient charge extraction. Importantly, TiO_2 forms stable interfaces with lead-free absorbers such as $Cs_2AgBiBr_6$, providing favourable band alignment for selective electron transport despite their wider band gaps.[16,47,49]

1.7.2 Dye Sensitizers

The choice of dye sensitisers in this work was guided by the need to balance optical absorption, charge-injection efficiency, environmental sustainability, and cost-effectiveness in DSSCs. Both natural and synthetic dyes were employed to systematically evaluate their individual and synergistic contributions to device performance.

Betalain pigments, extracted from beetroot (*Beta vulgaris*), were selected due to their strong absorption in the visible region (typically 450-550 nm), high molar extinction coefficient, and favourable anchoring capability on TiO_2 surfaces through carboxyl and hydroxyl functional groups. In addition to their excellent light-harvesting ability, betalains are non-toxic, biodegradable, and abundantly available, making them attractive candidates for environmentally benign DSSCs.[16]

To further enhance light harvesting, synergistic dye sensitization was explored using extracts from the leaves of *Codiaeum variegatum* and the flowers of *Delonix regia*. These natural dyes contain complementary pigments, primarily **chlorophylls** and **anthocyanins**, that extend the absorption spectrum into different regions of the visible spectrum. Co-sensitization improves spectral coverage, reduces competitive adsorption, and promotes more efficient photon utilisation, thereby enhancing photocurrent generation.

The widely used **N719 ruthenium**-based synthetic dye was employed as a benchmark sensitizer owing to its broad spectral response, high photochemical stability, and well-established energy level alignment with TiO_2 and the I^-/I_3^- redox electrolyte. Its inclusion enables direct comparison between conventional high-performance DSSCs and natural dye-based devices, thereby highlighting the strengths and limitations of sustainable sensitization strategies.[16]

1.7.3 Electrolyte

The iodide/triiodide (I^-/I_3^-) liquid redox electrolyte was selected in this work for both natural-dye-sensitized and synthetic-dye-based DSSCs due to its well-established electrochemical stability, fast redox kinetics, and excellent compatibility with TiO_2 photoanodes. The I^-/I_3^- redox couple provides efficient regeneration of the oxidized dye molecules following electron injection, thereby sustaining continuous photocurrent generation. Its redox potential (~0.35-0.4 V vs NHE) is favourably aligned with the

highest occupied molecular orbitals (HOMO) of both natural pigments (betalains, anthocyanins, chlorophyll derivatives) and the N719 dye, ensuring rapid dye regeneration while minimising energy losses.

Furthermore, the I^-/I_3^- electrolyte exhibits high ionic conductivity and diffusion coefficients, which facilitate effective charge transport between the photoanode and counter electrode. Its proven chemical compatibility with natural dyes and ruthenium-based sensitisers, along with long-term operational reliability, makes it a preferred choice for fundamental performance evaluation and comparative studies. Despite known limitations, such as corrosivity and volatility, the I^-/I_3^- redox system remains the most reliable benchmark electrolyte for DSSCs, enabling a clear assessment of photoanode engineering, dye-sensitization strategies, and interfacial passivation effects.[16,48]

1.7.4 Pb-Free Double Perovskite Photo Harvester

Although conventional lead-based perovskites such as $MAPbI_3$ and $FAPbI_3$ have achieved remarkable power conversion efficiencies exceeding 25%, their practical deployment faces critical challenges related to toxicity, environmental instability, and regulatory constraints. The presence of soluble Pb^{2+} ions poses significant environmental and health risks, particularly under moisture-induced degradation, where lead leakage becomes a serious concern. Furthermore, organic-inorganic hybrid perovskites suffer from thermal instability, ion migration, and sensitivity to humidity and UV exposure, limiting their long-term operational durability.

In contrast, the CABB double perovskite offers a structurally stable and environmentally benign alternative. By replacing toxic Pb^{2+} with non-toxic Ag^+ and Bi^{3+} ions, CABB eliminates lead-related hazards while maintaining a perovskite-derived crystal framework. CABB crystallizes in a cubic elpasolite structure (**Figure 1.8**), exhibits a bandgap of ~1.9-2.2 eV, and offers superior thermal and moisture stability compared to hybrid lead perovskites.[50] Its all-inorganic composition provides superior thermal and moisture stability compared to $MAPbI_3$ or $FAPbI_3$, reducing degradation under ambient conditions and enhancing long-term stability. Additionally, CABB exhibits lower ion migration tendencies and enhanced defect tolerance, contributing to improved long-term stability even under open-air fabrication conditions.

Although CABB's current photovoltaic performance remains lower due to its indirect bandgap and comparatively low absorption coefficient, its intrinsic chemical robustness, reduced toxicity, and ambient stability make it highly attractive for sustainable, scalable photovoltaic applications. From a long-term technological and environmental perspective, prioritising stability, safety, and regulatory compliance over peak efficiency aligns better with global sustainability goals. Therefore, selecting CABB represents a strategic shift toward developing durable, eco-friendly, and commercially viable lead-free photovoltaic systems.[47,49]

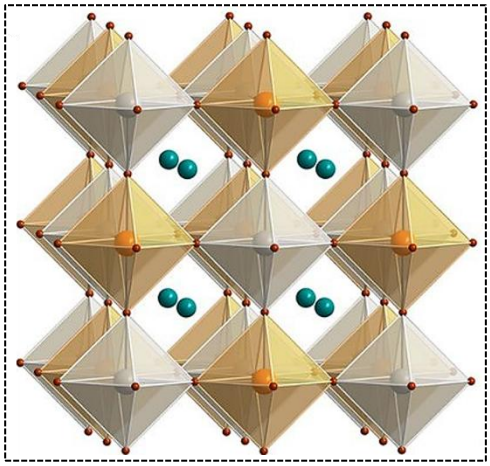

Figure 1.8 Crystal structure of $Cs_2AgBiBr_6$. Orange, grey, turquoise, and brown spheres represent Bi, Ag, Cs, and Br atoms, respectively, Reproduced with permission from Ref. [50].

1.7.5 2D-$Ti_3C_2T_X$ MXene

$Ti_3C_2T_X$ MXene was employed as an interfacial passivating agent owing to its unique combination of metallic conductivity, two-dimensional layered structure, and surface-terminated functional groups (–O, –OH, –F). These surface terminations effectively passivate surface defects and trap states at the photoanode/dye/electrolyte interface in DSSCs, FTO/TiO_2, and TiO_2/CABB, thereby suppressing charge recombination and enhancing interfacial charge transfer. Additionally, the high electrical conductivity of $Ti_3C_2T_X$ facilitates rapid electron extraction and transport, while its atomically thin morphology enables intimate interfacial contact without obstructing light absorption.

In recent years, there has been a notable increase in the study of MAX phases, a new class of ternary ceramics. MAX phases are characterized by a stacked structure comprising nitride ceramics or ternary carbides, with a hexagonal lattice. The known structure of MAX phases is $M_{n+1}AX_n$, where n ranges from 1 to 4, with M representing transition metal elements (usually Ti, Zr, or Tl, etc.), A representing an element from the A group (typically Si or Al), and X representing carbon (C) or nitrogen (N). The early generations of MAX phases, including 211, 312, and 413, are categorized by n. These phases feature alternating layers of $M_{n+1}X_n$ and A along the c-axis, forming a crystal structure shown in **Figure 1.9(a-c)**.

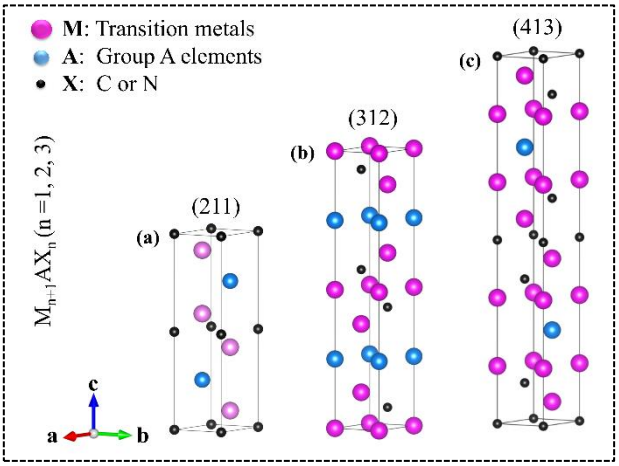

Figure 1.9 Typical crystal structure of (a) 211, (b) 312, and (c) 413-type MAX-phases exhibiting a hexagonal lattice arrangement. The general formula for MAX-phases is $M_{n+1}AX_n$, where M represents transition metal elements (usually Ti, Zr, or Tl, etc.), A represents an element from the A group (typically Si or Al), and X represents carbon (C) or nitrogen (N), Reproduced with permission from Ref. [46]

The incorporation of $Ti_3C_2T_X$ MXene is expected to reduce interfacial recombination, extend carrier lifetimes, improve energy band alignment, and enhance open-circuit voltage and photocurrent density, ultimately leading to superior power conversion efficiency and device stability. These attributes make $Ti_3C_2T_X$ MXene a highly effective passivation material for advanced interface engineering in third-generation photovoltaic devices.[46]

1.7.6 Back Carbon Electrodes

Carbon electrodes were selected as back contacts in this work as a cost-effective and chemically stable alternative to conventional noble metals such as Au and Ag. Although Au and Ag possess high electrical conductivity, their high cost, vacuum-based deposition requirements, and susceptibility to diffusion or chemical reactions (particularly Ag migration under bias and halide-rich environments) limit their long-term stability in perovskite and DSSC architectures.

From an electronic perspective, carbon materials typically exhibit a work function in the range of ~4.8-5.0 eV, which aligns well with the valence band of $Cs_2AgBiBr_6$ and the redox potential of common electrolytes in DSSCs. This favorable energy-level alignment facilitates efficient hole extraction while suppressing interfacial recombination. In contrast, although Au has a comparable work function (~5.1 eV), its diffusion into halide-based absorbers can induce instability, while Ag (work function ~4.3-4.7 eV) may form undesirable interfacial reactions and suffer from oxidation or ion migration.

Scientifically, carbon electrodes offer several advantages: chemical inertness against halide corrosion, hydrophobic nature that enhances moisture resistance, minimal metal-ion diffusion, and compatibility with low-temperature, solution-processable fabrication. Additionally, carbon-based electrodes enable vacuum-free, scalable deposition techniques such as doctor blading or screen printing, significantly reducing fabrication costs and energy consumption. Therefore, the use of carbon electrodes not only ensures appropriate work function alignment and stable charge collection but also supports the development of low-cost, durable, and environmentally sustainable photovoltaic devices.[51]

1.8 Scope and Goals of the Thesis

The overall goal of this thesis is to develop sustainable, stable, and high-performance third-generation photovoltaic technologies through systematic material innovation, defect engineering, and interfacial optimization. Emphasis is placed on designing environmentally benign solar cells by transitioning from conventional dye-sensitized systems to natural-dye-based devices and, ultimately, to lead-free

CABB double perovskite solar cells. The research aims to address critical challenges mentioned in **Section 1.6**, including charge recombination, interfacial trap states, instability, and efficiency limitations, while ensuring cost-effectiveness and scalability.

The scope of the thesis encompasses the synthesis of functional materials (ETLs, absorbers, passivating agents, and electrodes), advanced physicochemical characterization, electrochemical and photovoltaic performance evaluation, and simulation-assisted device optimization. Special focus is given to band alignment engineering, MXene-based passivation strategies, and HTL-free device architectures to simplify fabrication and enhance long-term stability. Collectively, the work seeks to bridge the gap between environmental sustainability, device durability, and improved power conversion efficiency, contributing toward the realization of next-generation green photovoltaic systems.

1.8.1 Thesis Objectives

The thesis reports an investigation into the following objectives to answer the questions arising from the literature survey/research gaps. The primary objective of this research is to develop and investigate eco-friendly, affordable solar cells with improved charge-carrier dynamics and performance. The specific objectives are outlined as follows:

1. To investigate the best passivating agent for DSSCs, aiming to suppress charge recombination, reduce surface defects, and enhance charge transport**.**
2. To systematically investigate the effect of Fe-doping in TiO_2 nanorod photoanodes on charge transport and light absorption in betalain-based natural DSSCs from Beta Vulgaris.
3. To investigate the performance dynamics of HTL and HTL-free CABB DPSCs by correlating experimental performance with charge transport mechanism and optimize device architecture through SCAPS-1D for enhanced efficiency using suitable ETLs**.**
4. To incorporate the best passivating agent (MXene) in HTL-free CABB DPSCs, aiming to suppress interfacial recombination, enhance charge extraction, and improve operational performance through optimized dual interface engineering**.**

To develop efficient, stable, and open-air processable sustainable photovoltaic devices by integrating MXene-based interfacial passivation, doping strategies, and optimized device architectures in DSSCs and lead-free double perovskite solar cells.

1.8.2 Thesis Outlines

The work has been divided into seven chapters, encompassing the introduction (Chapter 1) and the conclusions and future scope (Chapter 7). The chapter-wise organization is summarized as follows:

Chapter 1: Introduction. This chapter lays the scientific foundation for the thesis by introducing third-generation photovoltaic technologies, with particular focus on DSSCs and lead-free DPSCs. It outlines their operating principles, device architectures, and key performance-limiting mechanisms, including interfacial recombination, defect states, and charge-transport constraints. The transition from conventional lead-based perovskites to environmentally benign CABB systems is rationalized in light of toxicity and stability concerns. Emphasis is placed on doping and interfacial passivation as central strategies for improving carrier dynamics and device durability. This framework establishes the research direction and objectives pursued in the subsequent chapters.

Chapter 2: Materials Synthesis and Experimental Techniques. This chapter describes the synthesis methods used for the selected materials and the experimental techniques employed for material characterization and PV measurements. Overall, this chapter establishes the experimental and analytical framework for the study.

Chapter 3: $Ti_3C_2T_X$ Optimized Interfacial Passivation for Dye-Sensitized Solar Cells. This chapter demonstrates that 2D-$Ti_3C_2T_X$ MXene-based interfacial passivation significantly enhances DSSC performance by improving surface uniformity, suppressing recombination, and facilitating charge transport. The optimized FTO/c-TiO_2/MX-TNRs/N719/(I^-/I_3^-)/Carbon device achieved a PCE of 4.83% (vs. 3.42% for bare DSSC), with ~57% reduced surface roughness, ~82% lower charge-transfer resistance, and a high V_{OC} > 1 V, confirming the effectiveness of MXene-induced interface engineering.

Chapter 4: $Ti_{1-X}Fe_XO_{2-\delta}$ Photoanodes for Natural Dye-Sensitized Solar Cells. This chapter replaces synthetic N719 with eco-friendly beetroot (Beta vulgaris) dye and employs Fe-doped TiO_2 nanorod photoanodes to enhance performance. At 5 at% Fe doping, the DSSC showed improved charge injection and collection, increasing J_{SC} from 80 to 129.8 μA cm^{-2} and nearly doubling the PCE from 0.26% to 0.52%, highlighting the potential of $Ti_{1-x}Fe_xO_2$ for sustainable photovoltaic applications.

Chapter 5: HTL and HTL-free $Cs_2AgBiBr_6$ Double Perovskite Solar Cells. Due to the limited performance of natural-dye-based DSSCs, the research focus was strategically shifted to lead-free perovskite materials to develop higher-efficiency photovoltaic systems without compromising environmental safety. In this context, HTL-free FTO/TiO_2/CABB/Carbon-DPSCs were developed, demonstrating excellent operational stability with >95% PCE retention over 200 hours. Charge-transport analysis revealed high recombination resistance, prolonged carrier lifetimes, and efficient charge collection, confirming strong interfacial stability. Although the experimental efficiency remained modest (1.63%), numerical optimization using SCAPS-1D identified ZnO and TiO_2 as the most suitable ETL, predicting significantly enhanced efficiencies of 27.30% and 25.48% (HTL) and 23.09% and 22.72% (HTL-free). These findings establish a pathway to bridge the performance gap while advancing CABB as a sustainable, lead-free photovoltaic absorber.

Chapter 6: $Ti_3C_2T_X$ Assisted Dual Interfacial Passivation for $Cs_2AgBiBr_6$ Double Perovskite Solar Cells. Building on our previous findings that 2D $Ti_3C_2T_X$ MXene acts as an effective interfacial passivating agent, significantly suppressing recombination and enhancing charge transport, we extended its application to lead-free CABB-based double perovskite solar cells. In this study, bifacial MXene engineering was implemented in HTL-free FTO/TiO_2/CABB/Carbon architectures by introducing MXene at the FTO/TiO_2 (**FMT**) and TiO_2/CABB (**FTM**) interfaces. Among these configurations, the **FMT** structure demonstrated the most uniform ETL morphology with reduced surface roughness and improved interfacial contact. EIS analysis revealed lower series and charge-transfer resistances, higher recombination resistance, extended carrier lifetime, and significantly enhanced diffusion length. As a result, the FMT-based device achieved

a superior PCE of 6.92% (V_{OC} = 0.98 V, J_{SC} = 16.19 mA cm^{-2}), outperforming both bare and FTM configurations. The improvement is attributed to efficient electron extraction and strong suppression of interfacial recombination enabled by favorable MXene-TiO_2 band alignment and reduced defect density.

Chapter 7: Conclusions and Scope for Future Work. The core theme of this thesis is the development of economical, environmentally benign, and stable photovoltaic technologies through rational material selection and interface engineering. The research journey began with synthetic N719 dye-based DSSCs with passivated TiO_2 photoanodes, followed by a transition to naturally derived beetroot dye with Fe-doped TiO_2 photoanodes to promote sustainability and reduce cost. Although natural dyes offer ecological advantages due to their strong absorption in the visible region, their limited efficiency and stability have prompted the exploration of alternative photo absorbers. This led to the implementation of lead-free CABB double perovskite in an HTL-free architecture, achieving a PCE of 1.63% under open-air fabrication with >95% PCE retention after 200 h, highlighting its excellent environmental stability.

To understand the efficiency limitations, systematic numerical simulations using SCAPS-1D were conducted for HTL-based and HTL-free device architectures with TiO_2, SnO_2, WO_3, and ZnO as ETLs. The optimized HTL-based configuration yielded PCEs exceeding 27%, while HTL-free devices showed only ~4% lower efficiency, providing critical insights into defect tolerance, optimal thickness, doping density, interfacial recombination limits, and resistive parameters. Guided by these findings, dual interfacial passivation using 2D $Ti_3C_2T_X$ MXene at the FTO/TiO_2 and TiO_2/CABB interfaces was implemented to optimize the band alignment and suppress recombination. This strategy enhanced the experimental device's performance from 3.74% to a champion PCE of 6.92%, among the highest reported for CABB-based double perovskite solar cells.

Hence, special attention has been given to the role of doping, nano-structuring, interfacial passivation, and device engineering in optimizing charge transport, defect tolerance, and band alignment, making these materials highly promising for next-generation sustainable photovoltaic and optoelectronic applications.

References

[1] A. Srivastava, J.A.K. Satrughna, M.K. Tiwari, A. Kanwade, S.C. Yadav, K. Bala, P.M. Shirage, Lead metal halide perovskite solar cells: Fabrication, advancement strategies, alternatives, and future perspectives, Mater. Today Commun. 35 (2023) 105686. https://doi.org/10.1016/j.mtcomm.2023.105686.

[2] S. Qamar, S. Erten Ela, Dye-sensitized solar cells (DSSC): Principles, materials and working mechanism, Curr. Opin. Colloid Interface Sci. 74 (2024) 101871. https://doi.org/10.1016/j.cocis.2024.101871.

[3] A. Srivastava, B. Singh Chauhan, S. Chand Yadav, M. Kumar Tiwari, J. Akash Kumar Satrughna, A. Kanwade, K. Bala, P.M. Shirage, Performance of dye-sensitized solar cells by utilizing Codiaeum Variegatum Leaf and Delonix Regia Flower as natural sensitizers, Chem. Phys. Lett. 807 (2022) 140087. https://doi.org/10.1016/j.cplett.2022.140087.

[4] B. O'Regan, M. Grätzel, A low-cost, high-efficiency solar cell based on dye-sensitized colloidal TiO_2 films, Nature. 353 (1991) 737–740. https://doi.org/10.1038/353737a0.

[5] H. Gerischer, M.E. Michel-Beyerle, F. Rebentrost, H. Tributsch, Sensitization of charge injection into semiconductors with large band gap, Electrochim. Acta. 13 (1968) 1509–1515. https://doi.org/10.1016/0013-4686(68)80076-3.

[6] H. TRIBUTSCH, M. CALVIN, Electrochemistry of Excited Molecules: Photo-Electrochemical Reactions of Chlorophylls*, Photochem. Photobiol. 14 (1971) 95–112. https://doi.org/10.1111/j.1751-1097.1971.tb06156.x.

[7] H. TRIBUTSCH, Reaction of Excited Chlorophyll Molecules At Electrodes and In Photosynthesis*, Photochem. Photobiol. 16 (2008) 261–269. https://doi.org/10.1111/j.1751-1097.1972.tb06297.x.

[8] K. Sharma, V. Sharma, S.S. Sharma, Dye-Sensitized Solar Cells: Fundamentals and Current Status, Nanoscale Res. Lett. 13 (2018) 381. https://doi.org/10.1186/s11671-018-2760-6.

[9] D. Kuang, P. Wang, S. Ito, S.M. Zakeeruddin, M. Grätzel, Stable Mesoscopic Dye-Sensitized Solar Cells Based on Tetracyanoborate Ionic Liquid Electrolyte, J. Am. Chem. Soc. 128 (2006) 7732–7733. https://doi.org/10.1021/ja061714y.

[10] B. Weintraub, Y. Wei, Z.L. Wang, Optical Fiber/Nanowire Hybrid Structures for Efficient Three-Dimensional Dye-Sensitized Solar Cells, Angew. Chemie Int. Ed. 48 (2009) 8981–8985. https://doi.org/10.1002/anie.200904492.

[11] J. Burschka, N. Pellet, S.-J. Moon, R. Humphry-Baker, P. Gao, M.K. Nazeeruddin, M. Grätzel, Sequential deposition as a route to high-performance perovskite-sensitized solar cells, Nature. 499 (2013) 316–319. https://doi.org/10.1038/nature12340.

[12] P.S. Chandrasekhar, P.K. Parashar, S.K. Swami, V. Dutta, V.K. Komarala, Enhancement of Y123 dye-sensitized solar cell performance using plasmonic gold nanorods, Phys. Chem. Chem. Phys. 20 (2018) 9651–9658. https://doi.org/10.1039/C7CP08445E.

[13] A.S. Teja, A. Srivastava, J.A.K. Satrughna, M.K. Tiwari, A. Kanwade, S.C. Yadav, and P.M. Shirage, Optimal processing methodology for futuristic natural dye-sensitized solar cells and novel applications. Dyes and Pigments, 210 (2023), p.110997. https://doi.org/10.1016/j.dyepig.2022.110997.

[14] Y. Cao, Y. Liu, S.M. Zakeeruddin, A. Hagfeldt, M. Grätzel, Direct Contact of Selective Charge Extraction Layers Enables High-Efficiency Molecular Photovoltaics, Joule. 2 (2018) 1108–1117. https://doi.org/10.1016/j.joule.2018.03.017.

[15] M.J. García-Salinas, M.J. Ariza, Optimizing a Simple Natural Dye Production Method for Dye-Sensitized Solar Cells: Examples for Betalain (Bougainvillea and Beetroot Extracts) and Anthocyanin Dyes, Appl. Sci. 9 (2019) 2515. https://doi.org/10.3390/app9122515.

[16] A. Srivastava, J.A.K. Satrughna, M.K. Tiwari, A. Kanwade, S.C. Yadav, K. Bala, P.M. Shirage, Effect of $Ti_{1-x}Fe_xO_2$ photoanodes on the performance of dye-

sensitized solar cells utilizing natural betalain pigments extracted from Beta vulgaris (BV), Energy Adv. 2 (2023) 148–160. https://doi.org/10.1039/d2ya00197g.

[17] C. Eames, J.M. Frost, P.R.F. Barnes, B.C. O'Regan, A. Walsh, M.S. Islam, Ionic transport in hybrid lead iodide perovskite solar cells, Nat. Commun. 6 (2015) 7497. https://doi.org/10.1038/ncomms8497.

[18] A. Kojima, K. Teshima, Y. Shirai, T. Miyasaka, Organometal Halide Perovskites as Visible-Light Sensitizers for Photovoltaic Cells, J. Am. Chem. Soc. 131 (2009) 6050–6051. https://doi.org/10.1021/ja809598r.

[19] H. Min, D.Y. Lee, J. Kim, G. Kim, K.S. Lee, J. Kim, M.J. Paik, Y.K. Kim, K.S. Kim, M.G. Kim, T.J. Shin, S. Il Seok, Perovskite solar cells with atomically coherent interlayers on SnO_2 electrodes, Nature. 598 (2021) 444–450. https://doi.org/10.1038/s41586-021-03964-8.

[20] Longi, Longi achieves 34.85% efficiency for two-terminal tandem perovskite solar cell, PV Mag. (2025). https://www.pv-magazine.com/2025/04/18/longi-achieves-34-85-efficiency-for-two-terminal-tandem-perovskite-solar-cell/.

[21] V. Larini, M. Degani, S. Cavalli, G. Grancini, Sustainable decommissioning of perovskite solar cells: from waste to resources, Chem. Soc. Rev. 54 (2025) 7252–7270. https://doi.org/10.1039/D5CS00359H.

[22] J.-H. Im, C.-R. Lee, J.-W. Lee, S.-W. Park, N.-G. Park, 6.5% efficient perovskite quantum-dot-sensitized solar cell, Nanoscale. 3 (2011) 4088. https://doi.org/10.1039/c1nr10867k.

[23] H.-S. Kim, C.-R. Lee, J.-H. Im, K.-B. Lee, T. Moehl, A. Marchioro, S.-J. Moon, R. Humphry-Baker, J.-H. Yum, J.E. Moser, M. Grätzel, N.-G. Park, Lead Iodide Perovskite Sensitized All-Solid-State Submicron Thin Film Mesoscopic Solar Cell with Efficiency Exceeding 9%, Sci. Rep. 2 (2012) 591. https://doi.org/10.1038/srep00591.

[24] J.M. Ball, M.M. Lee, A. Hey, H.J. Snaith, Low-temperature processed meso-superstructured to thin-film perovskite solar cells, Energy Environ. Sci. 6 (2013) 1739. https://doi.org/10.1039/c3ee40810h.

[25] M. Saliba, K.W. Tan, H. Sai, D.T. Moore, T. Scott, W. Zhang, L.A. Estroff, U. Wiesner, H.J. Snaith, Influence of Thermal Processing Protocol upon the Crystallization and Photovoltaic Performance of Organic–Inorganic Lead Trihalide Perovskites, J. Phys. Chem. C. 118 (2014) 17171–17177. https://doi.org/10.1021/jp500717w.

[26] K.W. Tan, D.T. Moore, M. Saliba, H. Sai, L.A. Estroff, T. Hanrath, H.J. Snaith, U. Wiesner, Thermally Induced Structural Evolution and Performance of Mesoporous Block Copolymer-Directed Alumina Perovskite Solar Cells, ACS Nano. 8 (2014) 4730–4739. https://doi.org/10.1021/nn500526t.

[27] O. Malinkiewicz, A. Yella, Y.H. Lee, G.M. Espallargas, M. Graetzel, M.K. Nazeeruddin, H.J. Bolink, Perovskite solar cells employing organic charge-transport layers, Nat. Photonics. 8 (2014) 128–132. https://doi.org/10.1038/nphoton.2013.341.

[28] M. Liu, M.B. Johnston, H.J. Snaith, Efficient planar heterojunction perovskite solar cells by vapour deposition, Nature. 501 (2013) 395–398. https://doi.org/10.1038/nature12509.

[29] P. Docampo, J.M. Ball, M. Darwich, G.E. Eperon, H.J. Snaith, Efficient organometal trihalide perovskite planar-heterojunction solar cells on flexible polymer substrates, Nat. Commun. 4 (2013) 2761. https://doi.org/10.1038/ncomms3761.

[30] H. Zhou, Q. Chen, G. Li, S. Luo, T. Song, H.-S. Duan, Z. Hong, J. You, Y. Liu, Y. Yang, Interface engineering of highly efficient perovskite solar cells, Science (80-.). 345 (2014) 542–546. https://doi.org/10.1126/science.1254050.

[31] NREL, The national renewable energy laboratory, best research-cell efficiency chart, 2025. www.nrel.gov/pv/cell-efficiency.html.

[32] J. Liu, Y. He, L. Ding, H. Zhang, Q. Li, L. Jia, J. Yu, T.W. Lau, M. Li, Y. Qin, X. Gu, F. Zhang, Q. Li, Y. Yang, S. Zhao, X. Wu, J. Liu, T. Liu, Y. Gao, Y. Wang, X. Dong, H. Chen, P. Li, T. Zhou, M. Yang, X. Ru, F. Peng, S. Yin, M. Qu, D. Zhao, Z. Zhao, M. Li, P. Guo, H. Yan, C. Xiao, P. Xiao, J. Yin, X. Zhang, Z. Li, B. He, X. Xu, Perovskite/silicon tandem solar cells with bilayer interface passivation, Nature. 635 (2024) 596–603. https://doi.org/10.1038/s41586-024-07997-7.

[33] J. Qian, B. Xu, W. Tian, A comprehensive theoretical study of halide perovskites ABX_3, Org. Electron. 37 (2016) 61–73. https://doi.org/10.1016/j.orgel.2016.05.046.

[34] W. Travis, E.N.K. Glover, H. Bronstein, D.O. Scanlon, R.G. Palgrave, On the application of the tolerance factor to inorganic and hybrid halide perovskites: a revised system, Chem. Sci. 7 (2016) 4548–4556. https://doi.org/10.1039/C5SC04845A.

[35] T.J. Huang, Z.X. Thiang, X. Yin, C. Tang, G. Qi, H. Gong, $(CH_3NH_3)_2PdCl_4$: A Compound with Two-Dimensional Organic–Inorganic Layered Perovskite Structure, Chem. – A Eur. J. 22 (2016) 2146–2152. https://doi.org/10.1002/chem.201503680.

[36] C. Li, X. Lu, W. Ding, L. Feng, Y. Gao, Z. Guo, Formability of ABX_3 (X = F, Cl, Br, I) halide perovskites, Acta Crystallogr. Sect. B Struct. Sci. 64 (2008) 702–707. https://doi.org/10.1107/S0108768108032734.

[37] J.I. Uribe, D. Ramirez, J.M. Osorio-Guillén, J. Osorio, F. Jaramillo, $CH_3NH_3CaI_3$ Perovskite: Synthesis, Characterization, and First-Principles Studies, J. Phys. Chem. C. 120 (2016) 16393–16398. https://doi.org/10.1021/acs.jpcc.6b04207.

[38] G. Kieslich, S. Sun, A.K. Cheetham, Solid-state principles applied to organic–inorganic perovskites: new tricks for an old dog, Chem. Sci. 5 (2014) 4712–4715. https://doi.org/10.1039/C4SC02211D.

[39] Q. Chen, N. De Marco, Y. (Michael) Yang, T.-B. Song, C.-C. Chen, H. Zhao, Z.

Hong, H. Zhou, Y. Yang, Under the spotlight: The organic–inorganic hybrid halide perovskite for optoelectronic applications, Nano Today. 10 (2015) 355–396. https://doi.org/10.1016/j.nantod.2015.04.009.

[40] Q. Sun, W.-J. Yin, Thermodynamic Stability Trend of Cubic Perovskites, J. Am. Chem. Soc. 139 (2017) 14905–14908. https://doi.org/10.1021/jacs.7b09379.

[41] W. Shockley, H.J. Queisser, Detailed Balance Limit of Efficiency of p-n Junction Solar Cells, J. Appl. Phys. 32 (1961) 510–519. https://doi.org/10.1063/1.1736034.

[42] S. Rühle, Tabulated values of the Shockley–Queisser limit for single junction solar cells, Sol. Energy. 130 (2016) 139–147. https://doi.org/10.1016/j.solener.2016.02.015.

[43] A. De Vos, H. Pauwels, On the thermodynamic limit of photovoltaic energy conversion, Appl. Phys. 25 (1981) 119–125. https://doi.org/10.1007/BF00901283.

[44] A. De Vos, Detailed balance limit of the efficiency of tandem solar cells, J. Phys. D. Appl. Phys. 13 (1980) 839–846. https://doi.org/10.1088/0022-3727/13/5/018.

[45] R. Chauhan, A. Srivastava, P.M. Shirage, K. Bala, Innovating dye-sensitized solar cells through novel microalgal and cyanobacterial species extricated dyes: A sustainable tack for material scarce earth, Sol. Energy. 270 (2024) 112369. https://doi.org/10.1016/j.solener.2024.112369.

[46] A. Srivastava, Y. Ito, H. Lee, Y. Ohshita, A. Ogura, M. Dhonde, P.M. Shirage, Multilayered 2D $Ti_3C_2T_X$-MXene: Best Interfacial Passivating Agent for Dye-Sensitized Solar Cells with V_{OC} Approaching 1 V, ACS Appl. Electron. Mater. 7 (2025) 1531–1549. https://doi.org/10.1021/acsaelm.4c02107.

[47] A. Srivastava, M. Kasliwal, P.M. Shirage, From HTL to HTL-free: Experimental and numerically modelled performance dynamics of $Cs_2AgBiBr_6$ double perovskite solar cells, Sol. Energy. 298 (2025) 113733. https://doi.org/10.1016/j.solener.2025.113733.

[48] A.S. Teja, A. Srivastava, J. Akash Kumar Satrughna, M. Kumar Tiwari, A.

Kanwade, H. Lee, A. Ogura, P.M. Shirage, Synergistic co-sensitization of environment-friendly chlorophyll and anthocyanin-based natural dye-sensitized solar cells: An effective approach towards enhanced efficiency and stability, Sol. Energy. 261 (2023) 112–124. https://doi.org/10.1016/j.solener.2023.06.004.

[49] A. Srivastava, P.M. Shirage, $Ti_3C_2T_X$-MXene-Assisted Dual-Interfacial Passivation for HTL-Free $Cs_2AgBiBr_6$ Double Perovskite Solar Cells, ACS Appl. Energy Mater. 9 (2026) 2422–2433. https://doi.org/10.1021/acsaem.5c04086.

[50] A.H. Slavney, T. Hu, A.M. Lindenberg, H.I. Karunadasa, A Bismuth-Halide Double Perovskite with Long Carrier Recombination Lifetime for Photovoltaic Applications, J. Am. Chem. Soc. 138 (2016) 2138–2141. https://doi.org/10.1021/jacs.5b13294.

[51] J. He, Y. Bai, Z. Luo, R. Ran, W. Zhou, W. Wang, Z. Shao, Advanced carbon-based rear electrodes for low-cost and efficient perovskite solar cells, Energy Environ. Sci. 18 (2025) 2136–2164. https://doi.org/10.1039/D4EE05462H.

Chapter 2

Experimental and Characterization Techniques

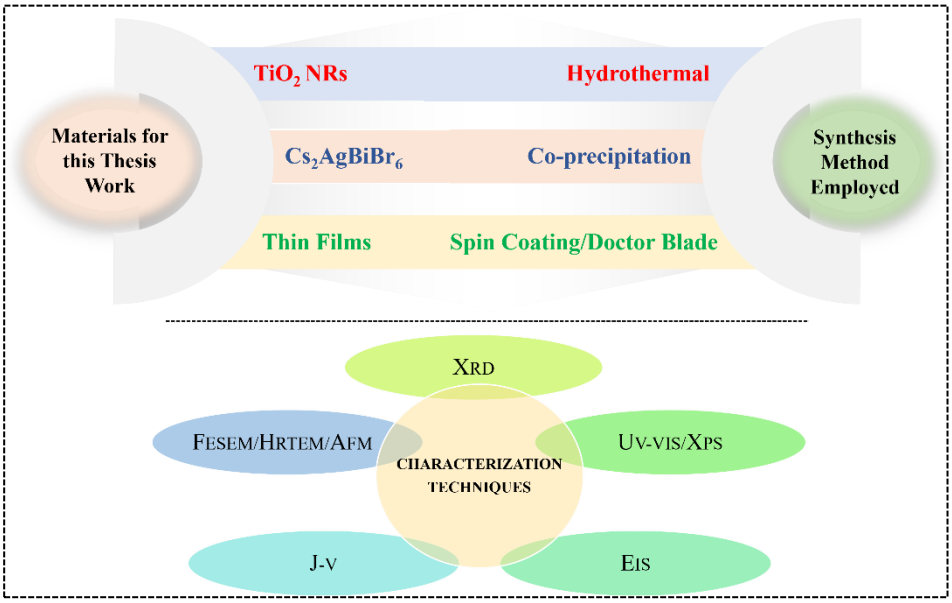

This chapter outlines the synthesis of materials using hydrothermal, co-precipitation, and solid-state methods, followed by device fabrication via spin- and doctor-blade coating. Comprehensive characterization (XRD, FESEM-EDS, TEM, XPS, Raman, UV-Vis, AFM, and EIS) was performed to analyze structural, optical, and interfacial properties, while photovoltaic performance was evaluated using a AAA-class solar simulator. This chapter provides a comprehensive understanding of the experimental workflow and analytical techniques used in the study.

2.1 Introduction

Solar energy conversion technologies, particularly dye-sensitized solar cells (DSSCs) and lead-free perovskite solar cells (PSCs), have emerged as promising candidates for sustainable and cost-effective photovoltaic applications. The performance of these devices is critically governed by the properties of the constituent materials and interfaces, which are strongly influenced by the synthesis routes, deposition techniques, and post-treatment processes employed during fabrication. Precise control over material composition, morphology, crystallinity, and surface chemistry is therefore essential for achieving efficient charge generation, transport, and collection.

This chapter presents a comprehensive overview of the material synthesis and device fabrication methodologies adopted for DSSCs and lead-free double perovskite solar cells. Emphasis is placed on wet chemical and solution-based techniques, including hydrothermal, solvothermal, and chemical deposition methods, which offer excellent control over nanostructure morphology, particle size, and surface properties. These approaches enable the fabrication of nanostructured photoanodes and electron transport layers with high surface area, enhanced light harvesting, and optimised charge transport characteristics. Furthermore, these methods facilitate elemental doping, surface passivation, and interfacial engineering, which are crucial for suppressing recombination losses and improving device efficiency and stability.

The chapter also details the characterization techniques employed to systematically evaluate the structural, morphological, compositional, and electronic properties of the synthesized materials. Techniques such as X-ray diffraction (XRD), field-emission scanning electron microscopy (FESEM), transmission electron microscopy (TEM/HRTEM), thermogravimetric analysis (TGA), X-ray photoelectron spectroscopy (XPS), atomic force microscopy (AFM), Raman Spectroscopy, and Brunauer-Emmett-Teller (BET) surface area analysis provide critical insights into phase purity, crystallinity, nanoscale architecture, chemical states, and surface characteristics. These analyses are essential for correlating material properties with photovoltaic performance.

In addition, this chapter describes the fabrication and measurement protocols for photovoltaic devices, including current density-voltage (J-V) characterization, electrochemical impedance spectroscopy (EIS), and stability testing. These techniques are employed to assess key performance parameters, including power conversion efficiency (PCE), charge transport resistance (R_{Ct}), recombination dynamics, and operational durability. The experimental methodologies outlined in this chapter form the foundation for understanding structure-property-performance relationships and for optimizing DSSC and lead-free PSC devices for sustainable photovoltaic applications.

2.2 Synthesis Methods for DSSC Materials

In this section, a systematic approach to preparing nanostructured photoanodes, dye sensitizers, and liquid electrolytes is discussed to ensure reproducibility, optimal charge transport, and efficient light harvesting.

2.2.1 Synthesis of TiO_2 Nanorod Photoanodes

Nanostructured TiO_2 nanorods (TNRs) were synthesized to serve as efficient electron-collecting scaffolds with high surface area for dye adsorption. One-dimensional (1D) TNRs were prepared via a controlled hydrothermal synthesis to promote direct electron transport, reduce grain-boundary scattering, and enhance charge-collection efficiency.

In a typical synthesis process, a compact TiO_2 layer (c-TiO_2; ~30-50 nm) was first prepared via the spin coating method, as shown in **Figure 2.1(a)**. To do so, we initially prepared two TiO_2 solutions of different molarities, i.e., 0.15 and 0.30 M, by mixing stoichiometric amounts of $Ti(acac)_2OiPr_2$ into 5 mL of butanol. These two different molarity mixtures were further ultrasonicated for 1 hour at room temperature (RT) until the Ti precursor was fully dissolved. FTO substrates were simultaneously washed for 15 minutes each with soap, DI water, acetone, and ethanol, then air-dried. For coating the c-TiO_2 layer, 100 mL of a 0.15 M TiO_2 solution was spin-coated at 3000 rpm and dried at 120 °C for 30 min. After drying, the same process was repeated twice with a 0.30 M TiO_2 solution to achieve the desired thickness of the c-TiO_2 layer. All substrates were annealed at 450°C for 30 minutes at a ramp rate of 5 °C min^{-1} after the compact layer coating.

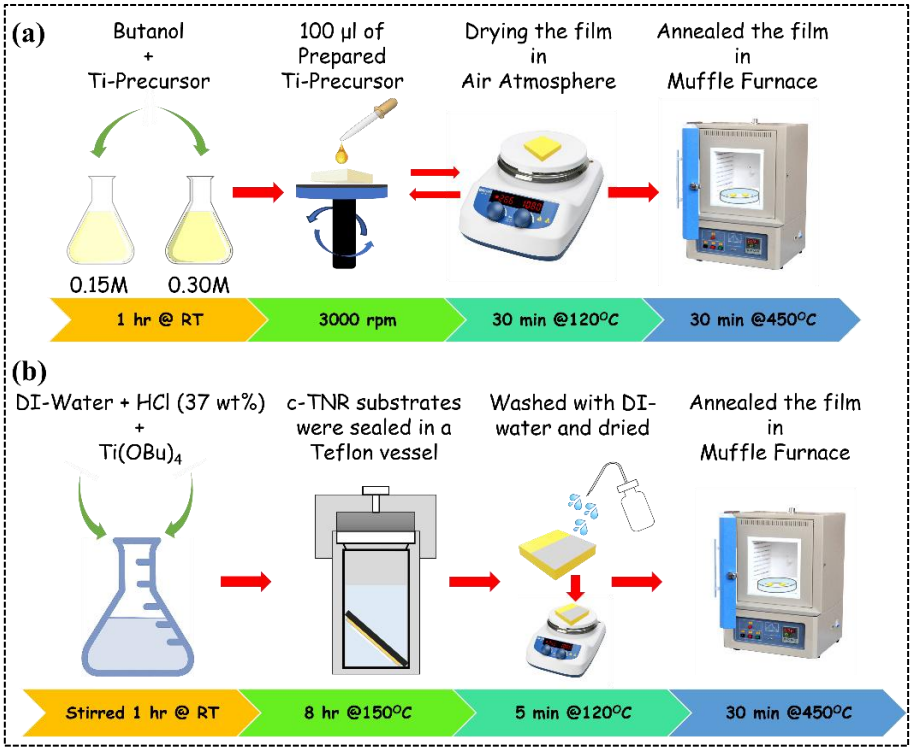

Figure 2.1 Typical schematics of hydrothermal synthesis of 1-D TNRs. (a) a c-TiO_2-coating process on cleaned FTO substrates, and (b) the final step of hydrothermal synthesis of 1-D TNRs on c-TiO_2-coated FTO substrates.

To synthesize 1D-TNRs in the second step, we prepared a solution containing HCl (37 wt.%) and DI water in a (1:1) volume ratio and stirred for 5 mins. After thoroughly mixing HCl and DI water, we added 0.75 mL of $Ti(OBu)_4$ and stirred the solution for 1 hr at RT. Further, the c-TiO_2-coated FTO substrates were placed in a 100 mL Teflon vessel and tilted 45° towards the walls. Remember that the FTO's conducting side or c-TiO_2 coated side must be oriented downwards, as shown in **Figure 2.1(b)**. After pouring the prepared solution into the Teflon vessel, the vessel was sealed in a stainless-steel autoclave and placed in a muffle furnace for further reaction at 150 °C for 8 hours at a ramp rate of 2 °C min^{-1}. After the set reaction, 1-D TNR-grown FTO substrates were removed, rinsed with DI water, and air-dried for 5 min at 120 °C. To increase the crystallinity and remove any remaining organic components, all 1D-TNR samples were finally annealed for 30 min at 450 °C with a ramp rate of 5 °C min^{-1}.[1–3]

2.2.2 Preparation of Dye-Sensitizers

(a) N719 Synthetic dye

The synthetic ruthenium-based dye N719 (cis-bis (isothiocyanato)bis (2,2′-bipyridyl-4,4′-dicarboxylato) ruthenium (II) bis (tetrabutylammonium)), purchased from Sigma-Aldrich, was used as received without further purification. A dye solution was prepared by dissolving an appropriate amount of N719 in 50 mL of anhydrous ethanol to a concentration of 0.3-0.5 mM, ensuring complete dissolution by mild magnetic stirring at room temperature. The freshly prepared N719 dye solution was kept in the dark to prevent photodegradation. A detailed study of an N719-dye-based DSSC is thoroughly discussed in ***Chapter 3***.[1]

(b) Natural Beta Vulgaris (BV) Dye

In various studies, both natural and synthetic dye sensitizers have been prepared for the fabrication of DSSCs. Specifically, for the study in ***Chapter 4***, we chose beetroot (Beta vulgaris: BV) and peeled it to extract betalain pigments. The core of the BV was washed separately with DI water and ethanol and sonicated for 5 minutes each. Then it was dried in air at RT and cut into small pieces, which were later crushed and mixed with lab-grade extra pure ethanol. Thereafter, the extract was centrifuged to remove residual material, then filtered. The extracted liquid dye is heated to 70 °C to evaporate the solvent, yielding the desired viscous liquid dye. Finally, the prepared BV-dye sensitizer was kept in the dark till further use.[4]

2.2.3 Tri-iodide (I^-/I_3^-) Electrolyte Preparation

A 5 mM tri-iodide (I^-/I_3^-) electrolyte solution was prepared by dissolving 42 mg of potassium iodide and 62 mg of iodine crystals in ethylene glycol. This solution was stirred for 1 hour at room temperature in a darkroom, covered with aluminium foil to prevent direct exposure to solar radiation.[5]

2.3 Synthesis Methods for DPSC Materials

The efficiency and stability of DPSC devices are critically dependent on the quality of synthesis and the interfacial compatibility of their constituent materials. In this section, the controlled preparation of electron transport layers (ETLs), the $Cs_2AgBiBr_6$

(CABB) photo-harvester, and carbon electrodes is described, with emphasis on reproducibility, morphology control, and optimization of charge-transport and light-harvesting properties.

2.3.1 Thin Film Synthesis of TiO_2-ETLs

Firstly, a compact/blocking layer of TiO_2 (c-TiO_2) was applied to the 1.5×1 cm^2 FTO substrates. To prepare a c-TiO_2-layer solution, 1.2 mL of $Ti(OCH(CH_3)_2)_4$ was mixed in 20 mL of 2-propanol and 0.4 mL of HCl. After 1 hour of vigorous stirring at room temperature, this c-TiO_2 solution is ready for coating. Before c-TiO_2 layer coating, a 0.5×1.5 cm^2 area on all the FTO substrates was etched and thoroughly cleaned through a series of ultrasonic cleaning. The substrates were first cleaned with deionized (DI) water and a soap solution for 15 minutes, repeated twice, followed by successive rinses in acetone and ethanol for 15 minutes each, performed twice, to ensure thorough removal of all contaminants. Then, the c-TiO_2 solution was spin-coated at 2000 rpm for 30 seconds on the UV-treated FTO substrates, as shown in **Figure 2.2(a)**. Therefore, the c-TiO_2-coated films were annealed at 500 °C for 30 minutes with a 5 °C/min ramp rate to ensure uniformity and density.

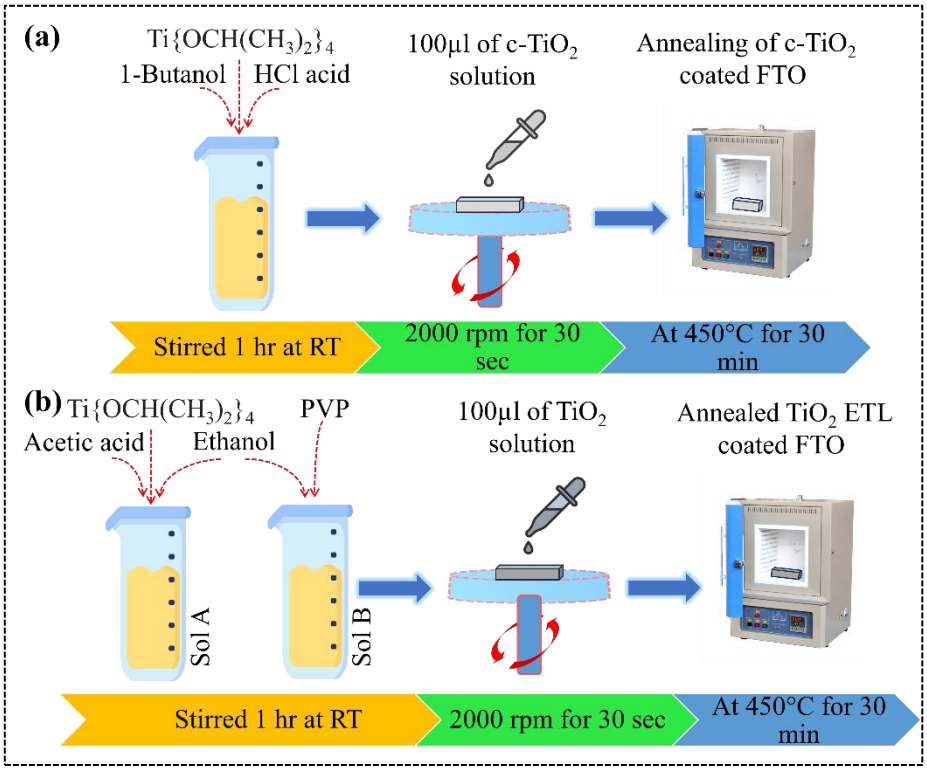

Figure 2.2 Typical spin coating synthesis method of (a) c-TiO_2 layer (blocking layer), and (b) n-type TiO_2 electron transfer layer.

In the second step, the TiO_2-ETL was applied by spin coating. Two solutions, A and B, were separately prepared to form the TiO_2 ETL solution, as shown in **Figure 2.2(b)**. Where solution A contains 3 mL of ethanol, 3 mL of acetic acid, and $Ti(OCH(CH_3)_2)_4$, respectively, and solution B contains 7.5 mL of ethanol and 0.450 g of PVP. After continuous stirring for 30 minutes, solution B was added dropwise to solution A, and the mixture was stirred for an additional 2 hours. The final ETL solution was spin-coated at 2000 rpm for 30 seconds, air-dried at 120 °C for 30 minutes, and annealed at 500 °C for 3 hours to achieve uniform and crystalline TiO_2 ETL.[6,7]

2.3.2 Synthesis of CABB Powder

The CABB powder was synthesized via solution precipitation. In this process, CsBr (0.2 mM) and $BiBr_3$ (0.1 mM) precursors were dissolved in 10 mL of HBr and heated at 110 °C for 1 hour with vigorous stirring. After 1 hour, AgBr (0.1 mM) was added to the solution, which was stirred at 130 °C for 2 hours and cooled overnight. After 12 hours of ageing, the resulting orange powder was filtered using a Whatman™ filter paper, washed with methanol, and dried under reduced pressure. Finally, the collected CABB powder was heated at 250 °C for 10 minutes to improve its crystallinity and phase purity. A schematic process of synthesizing CABB double perovskite is shown in **Figure 2.3**.[6]

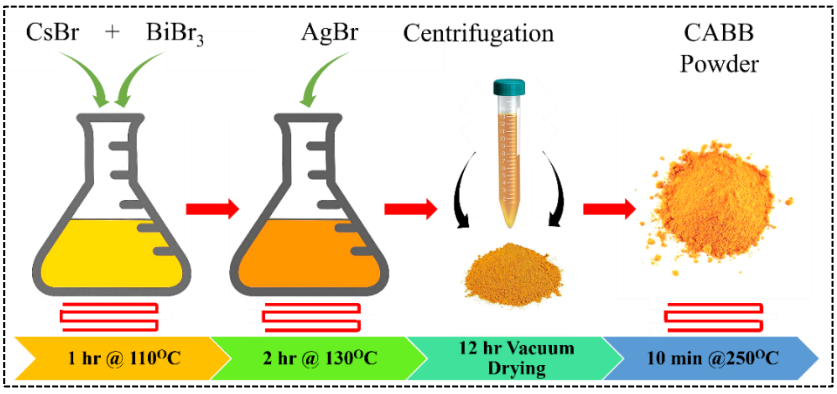

Figure 2.3 Schematic synthesis procedure of CABB powder using the solution precipitation method under open environment conditions.

2.4 Synthesis of Ti_3AlC_2-MAX Phase and $Ti_3C_2T_X$-MXene

The synthesis of MAX phases entails a crucial mechanical activation stage followed by high-temperature heat treatment. Particle size uniformity and improved interfacial contact depend primarily on mechanical stimulation, which affects the final product's overall quality. To date, various techniques have been used for MAX phase synthesis, including spark plasma sintering, hot isostatic pressing, and self-propagating high-temperature synthesis, among others. Herein, we used a high-temperature synthesis method to prepare MAX-phase Ti_3AlC_2 and selectively etched Al with HCl-HF to obtain $Ti_3C_2T_X$-MXene. The schematics of this synthesis process are shown in **Figure 2.4**.[1,8,9]

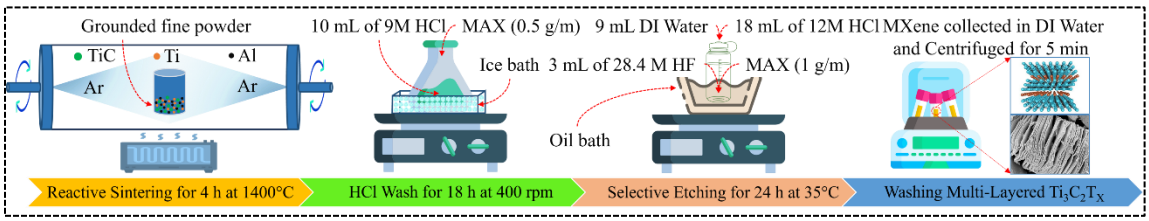

Figure 2.4. Schematic of various steps involved in synthesizing MAX-phase Ti_3AlC_2 and obtaining $Ti_3C_2T_X$ MXene via selective HCl-HF etching.

Step 1: To synthesize the MAX phase Ti_3AlC_2, we first mixed titanium carbide (TiC), titanium (Ti), and aluminium (Al) powders in a molar ratio of 2:1.25:2.2 and grounded into a fine mixture. Later, the mixed powder was removed and transferred to an alumina boat. Thus, this alumina boat was put in a high-temperature tube furnace (HTTF) for reactive sintering after being sealed with graphite tape, where argon gas was purged for 20 minutes at 27 °C. After 20 minutes of argon purging at room temperature, the HTTF was programmed for 4 hours of sintering at 1400 °C and then rapidly cooled to room temperature. After cooling, MAX phase Ti_3AlC_2 was removed from the alumina boat and milled into a fine powder.

Step 2: HCl washing has been performed before selective etching of the Al to dissolve intermetallic impurities. For this, we first took 10 mL of 9 M HCl solution in an ice bath, then added 1 g of MAX-phase Ti_3AlC_2 at a rate of 0.5 g min^{-1}, and left it under vigorous stirring. We monitored this reaction for 20 minutes, removed the ice bath, and then left this reaction for 18 hours under vigorous stirring. After completing this reaction, collect

all the HCl-washed MAX-phase Ti_3AlC_2 via centrifugation (until pH ~ 7) and filter the MAX powder using a vacuum-assisted filter with a 2 μm pore size. Further, the obtained powders were dried under a vacuum at 200 °C for 24 hours.

Step 3: For Selective etching of Al, we took 7 mL of DI water, 14 mL of 12M HCl (37% HCl), and 2.5 mL of 28.4M HF (48% HF) in a plastic bottle and stirred it at 35 °C for 24 hours. After completion of this etching reaction, multilayered $Ti_3C_2T_X$-MXene was obtained by repeated washing with DI water.

Delamination Process: The delamination and thinning mechanism during HCl-HF etching primarily originates from the selective removal of the "A" element (Al layer) from the layered MAX phase structure, followed by weakening of the interlayer interactions between the adjacent sheets. Initially, HF reacts with the Al atomic layers and forms soluble fluoride-based complexes such as AlF_3/H_3AlF_6, while HCl assists in maintaining the acidic environment and promotes continuous etching kinetics. As the Al layers are progressively removed, the interlayer bonding strength decreases significantly, resulting in expansion of the interlayer spacing and gradual separation of the stacked sheets.

With increasing etching duration, more Al atoms are extracted from the structure, leading to further weakening of van der Waals interactions between neighbouring layers. Consequently, the stacked multilayered sheets undergo progressive thinning and partial delamination, ultimately forming few-layer $Ti_3C_2T_X$-MXene nanosheets. Simultaneously, surface termination groups such as –F, –OH, and –O are introduced during the etching process, which further increase interlayer spacing and facilitate exfoliation/delamination of the sheets.

However, excessive etching duration or repeated aggressive etching conditions may lead to structural damage, over-fragmentation, excessive defect generation, oxidation of MXene sheets, and deterioration of electrical conductivity due to disruption of the conductive Ti-C framework. Therefore, an optimized etching duration (24 h in the present work) was selected to achieve sufficient delamination while preserving structural integrity and electrical charge-transport properties of the $Ti_3C_2T_X$-MXene sheets.

2.5 Materials Characterization Techniques

To investigate the structural, morphological, optical, and electronic properties governing the performance of photovoltaic devices, it is essential to characterize the synthesized materials using a range of complementary techniques. Material characterization provides critical insights into crystal structure, phase purity, surface morphology, elemental composition, and interfacial quality, all of which directly influence light absorption, charge transport, and recombination dynamics in solar cells. In this thesis, various advanced characterization techniques have been employed to obtain a comprehensive understanding of the photoanodes, dye sensitisers, perovskite absorbers, and interfacial layers, as discussed in the following sections.

2.5.1 X-ray Diffraction

X-ray diffraction (XRD) is a non-destructive, widely used technique for investigating the crystallographic structure, phase purity, and structural integrity of crystalline materials. It provides essential information on crystal structure, lattice parameters, crystallinity, and phase composition, thereby confirming the successful formation of the intended material phases and identifying any secondary or impurity phases.[10] The working principle of XRD is governed by **Bragg's law** (**equation 2.1**), which describes the constructive interference of X-rays diffracted by periodically arranged atomic planes within a crystal:

$$n\lambda = 2d \sin\theta \qquad 2.1$$

where n is the diffraction order, λ is the X-ray wavelength (1.5406 Å), d is the interplanar spacing, and θ is the diffraction angle. When the Bragg condition is satisfied, constructive interference produces characteristic diffraction peaks (**Figure 2.5(a)**).

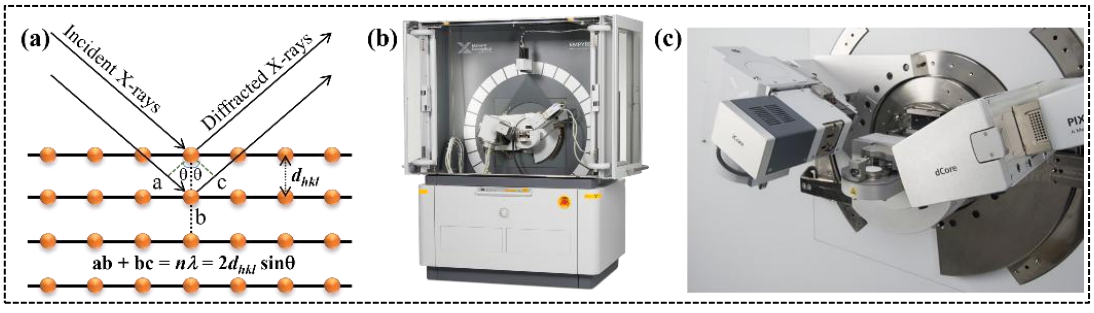

Figure 2.5 Schematic illustration of (a) Bragg's law formulation from crystal planes, (b) Empyrean, Malvern Panalytical X-ray diffractometer, and (c) closer view of XRD stage along with X-ray source and detector.

In an XRD measurement, a monochromatic X-ray beam is incident on the sample, and the diffracted intensity is recorded as a function of the diffraction angle (2θ). The resulting diffraction pattern comprises peaks associated with specific crystallographic planes, whose positions, intensities, and widths provide insights into phase composition, crystallite size, lattice strain, and structural defects. Comparison with standard reference databases enables accurate phase identification and structural analysis of the synthesised materials.

Phase identification was carried out by comparing the experimental XRD patterns with standard data from the Joint Committee on Powder Diffraction Standards (JCPDS) / International Centre for Diffraction Data (ICDD) database, which provides reference information on 2θ positions, d-spacings, relative intensities, and crystal structures. To obtain accurate structural parameters, Rietveld refinement was performed using FullProf software, fitting the experimental patterns to calculated profiles by optimizing lattice parameters, atomic positions, peak broadening factors, and phase fractions. This refinement minimizes the discrepancy between observed and simulated diffraction patterns, enabling the precise determination of crystal structure and phase purity of the synthesized nanomaterials.[10,11]

In this thesis, the third-generation Empyrean Malvern Panalytical X-ray Diffractometer (Cu-Kα source, $\lambda = 1.5406$ Å) is used to perform X-ray diffraction analysis of the developed materials. **Figure 2.5(b-c)** shows the actual image of the Empyrean, Malvern Panalytical X-ray Diffractometer used in this thesis work.

2.5.2 Field Emission Scanning Electron Microscopy/Energy Dispersive X-ray Spectroscopy

Field Emission Scanning Electron Microscopy (FESEM) is a high-resolution imaging technique widely used to investigate the surface morphology, microstructure, and

nanoscale features of advanced materials. Unlike conventional SEM, FESEM employs a field-emission gun (FEG) as the electron source, producing a highly focused, coherent electron beam that enables superior spatial resolution and enhanced image contrast, particularly for nanomaterials (**Figure 2.6(a)**).

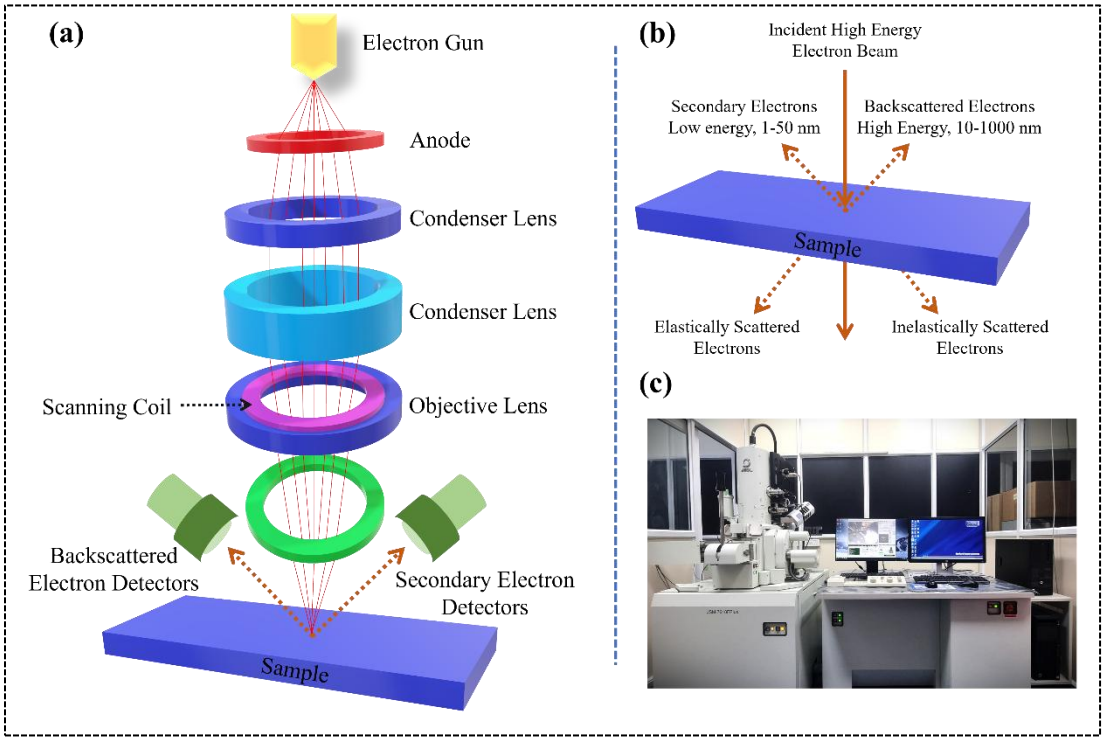

Figure 2.6 (a) Schematic working mechanism and accessories, (b) typical strike and scattering of the high-energy electron beam from the sample's surface, and (c) real-time captured JSM-7610F Plus JEOL FESEM.

FESEM operates by scanning a finely focused electron beam over the sample surface under high-vacuum conditions. Interactions between the incident electrons and the sample generate signals such as secondary electrons (SEs) and backscattered electrons (BSEs), which are detected to provide topographical and compositional contrast, respectively, as shown in **Figure 2.6(b)**. The technique allows detailed examination of particle size, morphology, porosity, and interconnectivity, which are critical parameters influencing charge transport and interfacial properties in photovoltaic materials.[12–14]

In this study, FESEM (JEOL JSM-7610F Plus: **Figure 2.6(c)**) was employed to analyse the surface morphology and microstructure of the synthesised materials. In

addition, energy-dispersive X-ray spectroscopy (EDS) attached to FESEM was used to confirm elemental composition and uniformity, thereby verifying phase purity and the presence of intended elements in the samples.

2.5.3 Transmission Electron Microscopy

Transmission Electron Microscopy (TEM) is a high-resolution characterization technique that enables direct visualization of the internal microstructure, crystallinity, lattice defects, and phase distribution of materials by transmitting a high-energy electron beam through an ultra-thin specimen. Unlike SEM, which primarily probes surface morphology, TEM provides structural information at the nanometre-to-atomic scale, making it indispensable for nanomaterials and photovoltaic research.[15]

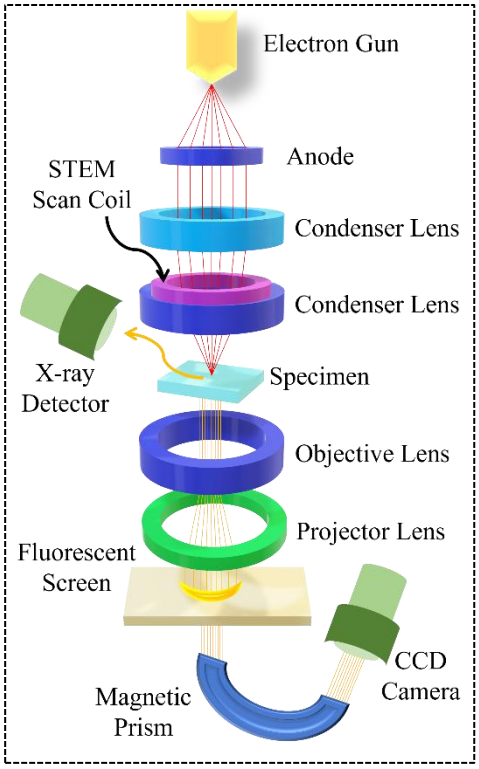

Figure 2.7 Typical schematic working mechanism of Transmission Electron Microscopy and various instrumental components.

TEM operates by directing a focused electron beam (typically 100-300 keV) through a specimen with a thickness below ~100 nm. The transmitted and diffracted electrons are collected and magnified by a series of electromagnetic lenses to form high-

contrast images, as shown in **Figure 2.7**. Image contrast arises from mass-thickness variations, diffraction effects, and phase differences, enabling detailed analysis of internal structure and crystallographic features.[16]

High-resolution TEM (HRTEM) allows direct observation of atomic lattice fringes, providing precise information on interplanar spacing, crystal orientation, and structural defects such as grain boundaries and dislocations. In addition, Selected Area Electron Diffraction (SAED) is used for crystallographic analysis, yielding diffraction patterns that confirm crystal symmetry, phase identity, and lattice parameters, particularly in polycrystalline and nanostructured materials.[17]

In this work, TEM and HRTEM analyses were performed using a JEOL JEM-2100 field-emission transmission electron microscope operated at 200 keV, enabling atomic-scale imaging of nanostructures and detailed assessment of morphology, crystallinity, and lattice structure.

2.5.4 X-Ray Photoelectron Spectroscopy

X-ray Photoelectron Spectroscopy (XPS) is a surface-sensitive analytical technique used to investigate the elemental composition, oxidation states, and surface chemical environment of materials. The technique is based on the photoelectric effect, where irradiation with monochromatic X-rays leads to the emission of core-level electrons whose binding energies are characteristic of specific elements and their chemical states. A typical schematic illustration of the working mechanism is shown in **Figure 2.8**.

In XPS, the binding energy (BE) of the emitted electrons is determined using **equation 2.2** below.

$$\mathrm{BE} = h\upsilon - \mathrm{KE} - \Phi \qquad 2.2$$

where $h\upsilon$ is the photon energy, KE is the measured kinetic energy, and Φ is the spectrometer work function. Survey spectra provide qualitative identification of surface elements (except H and He), while high-resolution spectra enable detailed analysis of chemical states through binding-energy shifts associated with variations in local bonding and electron density.[18,19]

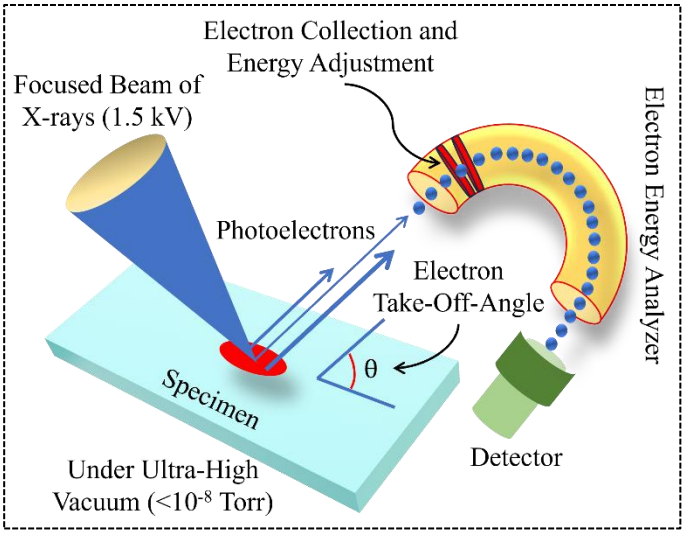

Figure 2.8 Schematic working mechanism illustration of X-ray Photoelectron Spectroscopy.

XPS is particularly effective for identifying mixed oxidation states, surface defects, and interfacial chemistry, which are critical for understanding charge transfer and surface reactions in functional materials. Peak deconvolution of high-resolution spectra allows accurate differentiation of oxidation states and surface species.

In this work, XPS measurements were performed using a Kratos AXIS spectrometer equipped with an Al Kα source (1486.6 eV) to determine the oxidation states, surface composition, and chemical integrity of the synthesized materials.

2.5.5 UV-visible Absorption Spectroscopy

UV-Visible (UV-vis) spectroscopy is a widely used optical characterization technique for investigating the light-absorption behaviour and electronic transitions of functional materials used in photovoltaic devices, including dyes, semiconducting photoanodes, and perovskite absorbers. In solar cell research, UV-vis spectroscopy provides critical information on absorption onset, optical bandgap, light-harvesting capability, and suitability of materials for efficient photon absorption within the solar spectrum.[20]

In this thesis, UV-vis absorption spectra were recorded using a Shimadzu UV-2600 spectrophotometer **(Figure 2.9)** equipped with a dual light-source system, comprising a deuterium lamp for the ultraviolet region (≈190-350 nm) and a tungsten–halogen lamp for the visible to near-infrared region (≈350-1100 nm). This range effectively covers the ultraviolet and visible regions relevant for DSSCs and PSCs. The absorption spectra of natural and synthetic dyes were analysed to identify characteristic absorption peaks, assess spectral coverage, and evaluate their light-harvesting efficiency. Similarly, the optical response of TiO_2 photoanodes and CABB double perovskite absorbers was examined to determine absorption edges and estimate optical band gaps using Tauc plots.[21]

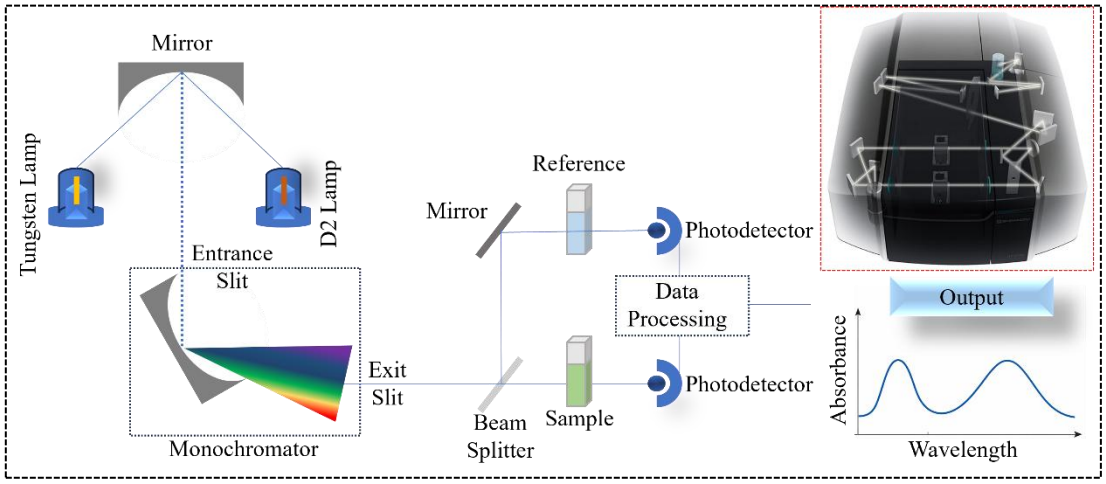

Figure 2.9 Schematic illustration of the UV-visible spectroscopy working principle and instrumental setup.

UV-vis spectroscopy thus plays a crucial role in correlating material optical properties with device performance, enabling a deeper understanding of photon absorption, charge excitation, and overall photoconversion efficiency in third-generation photovoltaic systems.

2.5.6 Atomic Force Microscopy

Atomic Force Microscopy (AFM) is a high-resolution surface characterisation technique that provides three-dimensional topographical information at the nanometre scale. It operates by scanning a sharp probe mounted on a flexible cantilever across the

sample surface, where interatomic forces between the tip and the surface cause deflection of the cantilever. The tip-sample interaction forces (primarily long-range van der Waals forces in non-contact mode) induce variations in the cantilever oscillation amplitude and frequency. These changes are detected by a laser beam reflected from the cantilever onto a position-sensitive photodetector (PSPD), enabling reconstruction of three-dimensional surface topography. In non-contact mode, the cantilever oscillates slightly above the sample surface, minimizing surface damage, preserving delicate nanostructured films, and ensuring accurate roughness evaluation.[22,23]

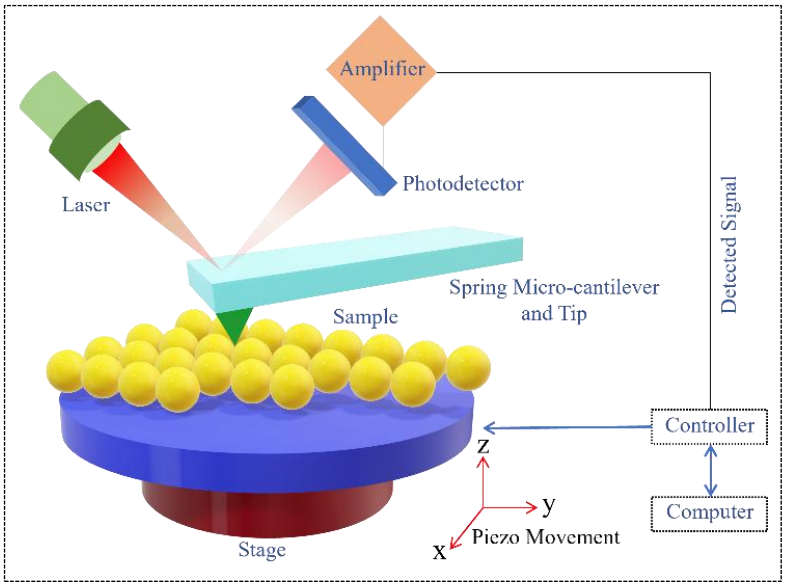

Figure 2.10 Schematic working mechanism of the Atomic Force Microscopy and components.

In this thesis, AFM (PARK NX 10) was employed in non-contact mode to record large-area three-dimensional surface topography and to quantitatively evaluate surface roughness parameters. The technique was systematically used for topological and roughness analysis of TiO_2 nanorods, compact TiO_2 electron transport layers (ETLs), and CABB absorber films. Key parameters, including average roughness (R_a), root-mean-square roughness (R_q), and peak-to-valley height (R_z), were extracted to correlate surface morphology with interfacial contact quality, charge-transport behaviour, and device performance. This analysis played a crucial role in understanding the impact of

nanostructuring and interfacial engineering on recombination dynamics and photovoltaic efficiency.

2.5.7 Electrochemical Impedance Spectroscopy

Electrochemical impedance spectroscopy (EIS) is a powerful frequency-dependent technique used to probe charge-transfer kinetics, recombination behaviour, and interfacial processes in electrochemical and photovoltaic systems. In EIS, a small AC perturbation voltage is applied over a wide frequency range, and the resulting current response is analysed to extract the resistive and capacitive elements associated with charge transport, recombination, and diffusion.[24]

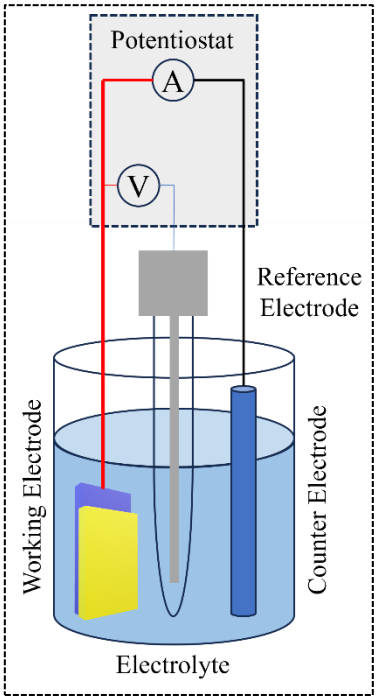

Figure 2.11 Schematic illustration of a three-electrode electrochemical setup for Electrochemical Impedance Spectroscopy analysis.

In this work, EIS measurements were carried out at room temperature under ambient conditions using a Metrohm Autolab (Multichannel-204) workstation controlled by Nova 2.1.4 software. A standard three-electrode configuration was employed, comprising the fabricated photoelectrode as the working electrode, a platinum wire as the counter electrode, and Ag/AgCl (or a suitable reference electrode) as the reference electrode (**Figure 2.11**). For DSSC-related electrochemical studies, 1 M KOH aqueous

electrolyte was utilised, whereas 0.1M $TBAPF_6$ (tetrabutylammonium hexafluorophosphate) in an appropriate organic solvent was used for CABB-based photovoltaic cells to ensure stable, representative charge-transport conditions.[7,25]

The obtained Nyquist and Bode plots were fitted with appropriate equivalent circuit models to extract key parameters, including series resistance (R_S), charge-transfer resistance (R_{Ct}), and recombination resistance (R_{Rec}). These parameters were further used to evaluate fundamental charge-transport properties, including the charge-carrier lifetime (τ_e), electron diffusion length (L_n), and diffusion coefficient (D_e). Such analysis enabled a deeper understanding of interfacial recombination dynamics and carrier transport mechanisms governing the performance and stability of DSSCs and CABB-based photovoltaic devices.

2.5.8 Raman Spectroscopy

Raman analysis is a powerful, non-destructive technique that provides insight into crystal symmetry, bonding characteristics, lattice distortions, and phase purity, which are critically important for understanding charge transport and stability in photovoltaic materials.[26]

The instrument operates on the principle of inelastic light scattering, known as the Raman effect. When the incident laser interacts with the sample, most photons are elastically scattered (Rayleigh scattering), while a small fraction undergoes energy exchange with lattice vibrations (phonons), resulting in a wavelength shift (**Figure 2.12(a)**). These Raman shifts are characteristic of specific vibrational modes of the material.[27] Raman spectroscopy was employed in this thesis to investigate the vibrational, structural, and phase-related properties of TiO_2 electrodes and CABB double perovskite photo absorbers. Raman spectra were recorded using an HJY (Horiba Jobin Yvon) micro-Raman spectrometer equipped with a He-Ne laser excitation source (λ = 633 nm), as shown in **Figure 2.12(b)**.

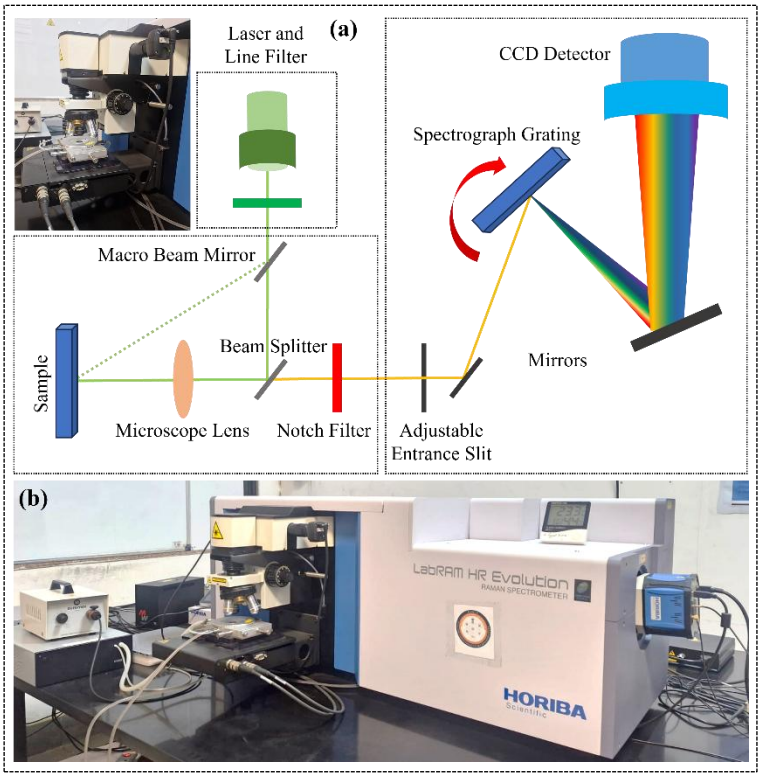

Figure 2.12 (a) Schematic working mechanism of RAMAN Spectroscopy and (b) real-time image of HJY micro-RAMAN spectrophotometer.

2.5.9 Photovoltaic Studies

Solar radiation reaching the Earth's surface is influenced by atmospheric scattering and absorption, resulting in both direct and diffuse components collectively referred to as global radiation. Before entering the atmosphere, solar radiation is defined as Air Mass 0 (AM0). At sea level, when the Sun is positioned directly overhead, the radiation traverses one complete atmospheric path and is termed AM 1.0. For other solar zenith angles and locations, the air mass increases; consequently, AM 1.5 G, corresponding to an irradiance of 1000 W/m^2, is internationally adopted as the standard test condition for photovoltaic performance evaluation.[28,29]

In the present study, device characterization was performed using a class AAA solar simulator that closely matches the terrestrial solar spectrum. The simulator comprises a xenon arc lamp, an AM 1.5 G optical filter, a collimator, and a Keithley source-and-measurement unit (**Figure 2.13**). The emitted spectrum closely resembles that

of a 5800 K blackbody, ensuring uniform and stable illumination of the device. Current-voltage (I-V) characteristics were recorded under AM 1.5 G illumination, from which key photovoltaic parameters, short-circuit current (I_{SC}), open-circuit voltage (V_{OC}), fill factor (FF), and power conversion efficiency (PCE), were extracted for device performance evaluation.



Figure 2.13 PET class AAA solar simulator equipped with Xenon arc (AM 1.5G optical filter) for testing solar cells.

(a) Short circuit current (I_{SC})

The **I_{SC}** represents the maximum current generated by a solar cell under illumination when the applied bias voltage is zero (short-circuit condition). It is governed by the diode **equation 2.3** and can be expressed as:

$$I_{SC} = I_S \left[exp\left(\frac{qV}{k_B T}\right) - 1 \right] - I_L \qquad 2.3$$

where I_S is the diode saturation current (A), q is the elementary charge, V is the applied voltage (V), k_B is the Boltzmann constant (1.38×10^{-23} $m^2Kg.s^{-2}K^{-1}$), T is the absolute temperature (K), and I_L is the photogenerated current (A).

(b) Open-Circuit Voltage (V_{OC})

V_{OC} is defined as the maximum voltage developed across a solar cell under illumination when the external circuit is open and the net current flow is zero, as given in **equation 2.4**:

$$V_{OC} = \frac{k_B T}{q} \ln\left(\frac{I_L}{I_S} + 1\right) \approx \frac{k_B T}{q} \ln\left(\frac{I_L}{I_S}\right) \quad 2.4$$

(c) Fill Factor (FF)

FF is a key performance parameter of a solar cell, defined as the ratio of the maximum extractable power to the product of the V_{OC} and I_{SC}. It is expressed as **equation 2.5**:

$$FF = \frac{V_{MP} \times I_{MP}}{I_{SC} \times V_{OC}} \quad 2.5$$

where V_{MP} and I_{MP} are the voltage (V) and current (A) at the maximum power point, respectively.

(d) Power Conversion efficiency (PCE)

The **PCE** is defined as the ratio of the solar cell's maximum electrical power output to the incident solar power under standard illumination (AM 1.5G, 1000 W/m^2). It is expressed as **equation 2.6**:

$$PCE = \frac{I_{SC} \times V_{OC} \times FF}{P_{in} \times A} \quad 2.6$$

where A (cm^2) is the active area of solar cells.

References

[1] A. Srivastava, Y. Ito, H. Lee, Y. Ohshita, A. Ogura, M. Dhonde, P.M. Shirage, Multilayered 2D $Ti_3C_2T_X$-MXene: Best Interfacial Passivating Agent for Dye-Sensitized Solar Cells with V_{OC} Approaching 1 V, ACS Appl. Electron. Mater. 7 (2025) 1531–1549. https://doi.org/10.1021/acsaelm.4c02107.

[2] R. Chauhan, A. Srivastava, P.M. Shirage, K. Bala, Innovating dye-sensitized solar cells through novel microalgal and cyanobacterial species extricated dyes: A sustainable tack for material scarce earth, Sol. Energy. 270 (2024) 112369. https://doi.org/10.1016/j.solener.2024.112369.

[3] A.S. Teja, A. Srivastava, J. Akash Kumar Satrughna, M. Kumar Tiwari, A. Kanwade, H. Lee, A. Ogura, P.M. Shirage, Synergistic co-sensitization of environment-friendly chlorophyll and anthocyanin-based natural dye-sensitized solar cells: An effective approach towards enhanced efficiency and stability, Sol. Energy. 261 (2023) 112–124. https://doi.org/10.1016/j.solener.2023.06.004.

[4] A. Srivastava, J.A.K. Satrughna, M.K. Tiwari, A. Kanwade, S.C. Yadav, K. Bala, P.M. Shirage, Effect of $Ti_{1-x}Fe_xO_2$ photoanodes on the performance of dye-sensitized solar cells utilizing natural betalain pigments extracted from Beta vulgaris (BV), Energy Adv. 2 (2023) 148–160. https://doi.org/10.1039/D2YA00197G.

[5] A. Srivastava, B. Singh Chauhan, S. Chand Yadav, M. Kumar Tiwari, J. Akash Kumar Satrughna, A. Kanwade, K. Bala, P.M. Shirage, Performance of dye-sensitized solar cells by utilizing Codiaeum Variegatum Leaf and Delonix Regia Flower as natural sensitizers, Chem. Phys. Lett. 807 (2022) 140087. https://doi.org/10.1016/j.cplett.2022.140087.

[6] A. Srivastava, M. Kasliwal, P.M. Shirage, From HTL to HTL-free: Experimental and numerically modelled performance dynamics of $Cs_2AgBiBr_6$ double perovskite solar cells, Sol. Energy. 298 (2025) 113733. https://doi.org/10.1016/j.solener.2025.113733.

[7] A. Srivastava, P.M. Shirage, $Ti_3C_2T_X$-MXene-Assisted Dual-Interfacial Passivation for HTL-Free $Cs_2AgBiBr_6$ Double Perovskite Solar Cells, ACS Appl. Energy Mater. 9 (2026) 2422–2433. https://doi.org/10.1021/acsaem.5c04086.

[8] A. Thakur, N. Chandran B.S., K. Davidson, A. Bedford, H. Fang, Y. Im, V. Kanduri, B.C. Wyatt, S.K. Nemani, V. Poliukhova, R. Kumar, Z. Fakhraai, B. Anasori, Step-by-Step Guide for Synthesis and Delamination of $Ti_3C_2T_x$ MXene, Small Methods. 7 (2023). https://doi.org/10.1002/smtd.202300030.

[9] O.J. Kewate, S. Punniyakoti, Ti_3AlC_2 MAX phase and $Ti_3C_2T_X$ MXene-based composites towards supercapacitor applications: A comprehensive review of

synthesis, recent progress, and challenges, J. Energy Storage. 72 (2023) 108501. https://doi.org/10.1016/j.est.2023.108501.

[10] A.A. Bunaciu, E. gabriela Udriştioiu, H.Y. Aboul-Enein, X-Ray Diffraction: Instrumentation and Applications, Crit. Rev. Anal. Chem. 45 (2015) 289–299. https://doi.org/10.1080/10408347.2014.949616.

[11] M. Borcha, I. Fodchuk, I. Krytsun, Lattice parameter determination by coincidental multi-beam X-ray diffraction, Phys. Status Solidi. 206 (2009) 1699–1703. https://doi.org/10.1002/pssa.200881617.

[12] N. Brodusch, H. Demers, R. Gauvin, Field Emission Scanning Electron Microscopy, Springer Singapore, Singapore, 2018. https://doi.org/10.1007/978-981-10-4433-5.

[13] B. Kämpfe, F. Luczak, B. Michel, Energy Dispersive X-Ray Diffraction, Part. Part. Syst. Charact. 22 (2005) 391–396. https://doi.org/10.1002/ppsc.200501007.

[14] G. Di Domenico, Introduction to Microscopy, in: Electro-Optic Photonic Circuits, Springer, Cham, 2019: pp. 19–31. https://doi.org/10.1007/978-3-030-23189-7_2.

[15] A. Mayeen, L.K. Shaji, A.K. Nair, N. Kalarikkal, Morphological Characterization of Nanomaterials, in: Charact. Nanomater., Elsevier, 2018: pp. 335–364. https://doi.org/10.1016/B978-0-08-101973-3.00012-2.

[16] Z.L. Wang, J.L. Lee, Electron Microscopy Techniques for Imaging and Analysis of Nanoparticles, in: Dev. Surf. Contam. Clean., Elsevier, 2008: pp. 395–443. https://doi.org/10.1016/B978-0-323-29960-2.00009-5.

[17] C.Y. Tang, Z. Yang, Transmission Electron Microscopy (TEM), in: Membr. Charact., Elsevier, 2017: pp. 145–159. https://doi.org/10.1016/B978-0-444-63776-5.00008-5.

[18] A.V. Boryakov, S.I. Surodin, R.N. Kryukov, D.E. Nikolichev, S.Y. Zubkov, Spectral fit refinement in XPS analysis technique and its practical applications, J. Electron Spectros. Relat. Phenomena. 229 (2018) 132–140.

https://doi.org/10.1016/j.elspec.2017.11.004.

[19] P.S. Bagus, E.S. Ilton, C.J. Nelin, The interpretation of XPS spectra: Insights into materials properties, Surf. Sci. Rep. 68 (2013) 273–304. https://doi.org/10.1016/j.surfrep.2013.03.001.

[20] W. Mäntele, E. Deniz, UV–VIS absorption spectroscopy: Lambert-Beer reloaded, Spectrochim. Acta Part A Mol. Biomol. Spectrosc. 173 (2017) 965–968. https://doi.org/10.1016/j.saa.2016.09.037.

[21] J. Klein, L. Kampermann, B. Mockenhaupt, M. Behrens, J. Strunk, G. Bacher, Limitations of the Tauc Plot Method, Adv. Funct. Mater. 33 (2023). https://doi.org/10.1002/adfm.202304523.

[22] F.J. Giessibl, Advances in atomic force microscopy, Rev. Mod. Phys. 75 (2003) 949–983. https://doi.org/10.1103/RevModPhys.75.949.

[23] Y. Seo, W. Jhe, Atomic force microscopy and spectroscopy, Reports Prog. Phys. 71 (2008) 016101. https://doi.org/10.1088/0034-4885/71/1/016101.

[24] B.-Y. Chang, S.-M. Park, Electrochemical Impedance Spectroscopy, Annu. Rev. Anal. Chem. 3 (2010) 207–229. https://doi.org/10.1146/annurev.anchem.012809.102211.

[25] A.C. Lazanas, M.I. Prodromidis, Electrochemical Impedance Spectroscopy─A Tutorial, ACS Meas. Sci. Au. 3 (2023) 162–193. https://doi.org/10.1021/acsmeasuresciau.2c00070.

[26] S.P. Mulvaney, C.D. Keating, Raman Spectroscopy, Anal. Chem. 72 (2000) 145–158. https://doi.org/10.1021/a10000155.

[27] R. Alcántara, J. Navas, C. Fernández-Lorenzo, J. Martín, E. Guillén, J.A. Anta, Synthesis and Raman spectroscopy study of TiO_2 nanoparticles, Phys. Status Solidi C. 8 (2011) 1970–1973. https://doi.org/10.1002/pssc.201000319.

[28] K.A. Emery, Solar simulators and I–V measurement methods, Sol. Cells. 18 (1986)

251–260. https://doi.org/10.1016/0379-6787(86)90124-9.

[29] V. Esen, Ş. Sağlam, B. Oral, Light sources of solar simulators for photovoltaic devices: A review, Renew. Sustain. Energy Rev. 77 (2017) 1240–1250. https://doi.org/10.1016/j.rser.2017.03.062.

Chapter 3

$Ti_3C_2T_X$ Optimized Interfacial Passivation for Dye-Sensitized Solar Cells

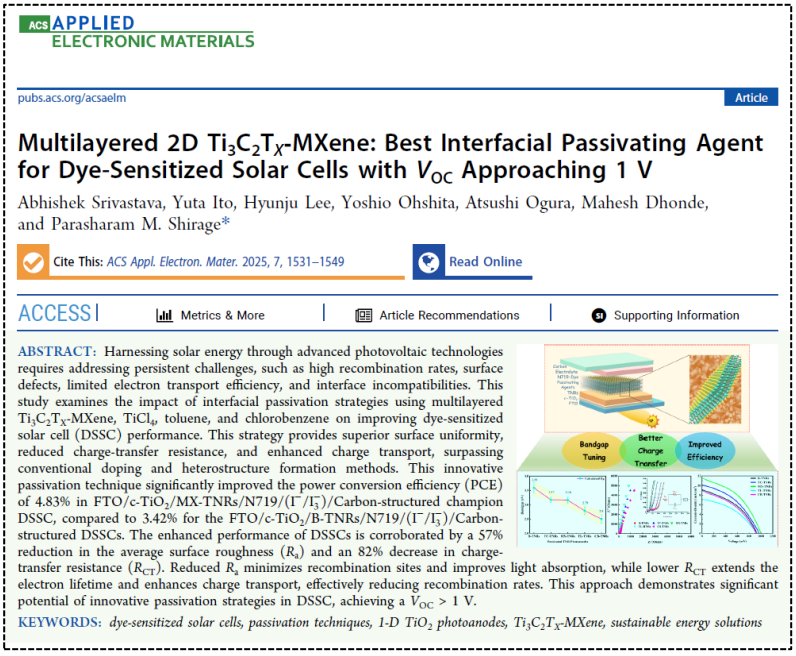

ACS APPLIED ELECTRONIC MATERIALS

pubs.acs.org/acsaelm Article

Multilayered 2D $Ti_3C_2T_X$-MXene: Best Interfacial Passivating Agent for Dye-Sensitized Solar Cells with V_{OC} Approaching 1 V

Abhishek Srivastava, Yuta Ito, Hyunju Lee, Yoshio Ohshita, Atsushi Ogura, Mahesh Dhonde, and Parasharam M. Shirage*

Cite This: *ACS Appl. Electron. Mater.* 2025, 7, 1531−1549 | Read Online

ACCESS | Metrics & More | Article Recommendations | Supporting Information

ABSTRACT: Harnessing solar energy through advanced photovoltaic technologies requires addressing persistent challenges, such as high recombination rates, surface defects, limited electron transport efficiency, and interface incompatibilities. This study examines the impact of interfacial passivation strategies using multilayered $Ti_3C_2T_X$-MXene, $TiCl_4$, toluene, and chlorobenzene on improving dye-sensitized solar cell (DSSC) performance. This strategy provides superior surface uniformity, reduced charge-transfer resistance, and enhanced charge transport, surpassing conventional doping and heterostructure formation methods. This innovative passivation technique significantly improved the power conversion efficiency (PCE) of 4.83% in FTO/c-TiO_2/MX-TNRs/N719/(I^-/I_3^-)/Carbon-structured champion DSSC, compared to 3.42% for the FTO/c-TiO_2/B-TNRs/N719/(I^-/I_3^-)/Carbon-structured DSSCs. The enhanced performance of DSSCs is corroborated by a 57% reduction in the average surface roughness (R_a) and an 82% decrease in charge-transfer resistance (R_{CT}). Reduced R_a minimizes recombination sites and improves light absorption, while lower R_{CT} extends the electron lifetime and enhances charge transport, effectively reducing recombination rates. This approach demonstrates significant potential of innovative passivation strategies in DSSC, achieving a V_{OC} > 1 V.

KEYWORDS: *dye-sensitized solar cells, passivation techniques, 1-D TiO_2 photoanodes, $Ti_3C_2T_X$-MXene, sustainable energy solutions*

This chapter demonstrates that 2D $Ti_3C_2T_X$ MXene is the most effective passivating agent among various conventional treatments, significantly reducing recombination and enhancing charge transport in DSSCs. The optimized device achieves a PCE of 4.83% (vs. 3.42%) with a high V_{OC} > 1 V, supported by reduced surface roughness and charge transfer resistance.

3.1 Introduction

We are living momentously in the world of energy as we enter the third decade of the 21st century. There is a global discussion about the future of our energy sources, driven by the urgent need to address climate change while maintaining economic stability and energy security.[1,2] Renewable energy sources, including solar, wind, hydro, geothermal, and biomass, are essential to steer this global energy transition. These sources represent a significant change in energy production and consumption, demonstrating a broader dedication to resilience, sustainability, and a more harmonious coexistence with nature.[3] As a result, the search for renewable and sustainable energy sources has increased attention on solar energy as a potential replacement for fossil fuels.[4,5] DSSCs have gained significant market share among photovoltaic technologies due to their affordability, flexibility, and potential for high efficiency under low-light conditions. However, problems with charge recombination and ineffective electron transport, which restrict their PCE, frequently prevent the practical use of DSSCs.[6–8]

A typical DSSC consists of an n-type photoanode, a dye sensitizer, a redox mediator, and a counter electrode. The dye absorbs light, injecting excited electrons into the semiconductor conduction band, generating a photocurrent.[9] TiO_2, with a ~ 3.2 eV bandgap, is commonly used in nanostructured forms like nanoparticles,[10] nanorods,[11,12] nanowires,[13] and nanotubes.[14] 1D-TNRs enable anatase-rutile phase synergy, enhancing charge separation, reducing recombination, and improving light harvesting.[15] Surface treatments further optimize TNR morphology and dye interactions, enhancing device efficiency. Efficient electron injection, transport, and dye regeneration are crucial for achieving high PCE. Since the discovery of N719 dye by O'Regan and Grätzel in 1991,[16] DSSCs have garnered significant interest due to their suitable band gaps (E_g), high absorption coefficients (α), long carrier diffusion lengths (L_D), superior mobility (μ), and low trap density (N_t).[17–20] Despite achieving PCEs of ~15%, challenges such as charge extraction and dye stability persist, requiring further innovation.[21–26] Efficient DSSC operation relies on critical interfaces, particularly the TiO_2/dye and FTO/TiO_2 junctions, which facilitate charge separation, transport, and collection.[27–31]

Interfaces in DSSCs, including those between FTO, TiO_2, and the electrolyte, as well as FTO grain boundaries, are critical but also prone to charge recombination, which undermines device performance.[32–35] $TiCl_4$ is widely used in DSSCs to address these challenges by reducing charge recombination, enhancing charge transfer, and passivating surface traps. It improves the TNR layer's uniformity, surface area, and light scattering, boosting dye adsorption and light harvesting. However, precise control is required to prevent excessive layer formation, and its high reactivity, hazards, and long-term stability issues remain concerns.[36–40] Furthermore, toluene and chlorobenzene were investigated as organic passivating agents to improve DSSC performance. Toluene, a non-polar solvent, forms a hydrophobic layer that passivates, traps, and stabilizes the photoactive layer, but may result in incomplete passivation due to its low boiling point. Chlorobenzene, with a higher boiling point and polarity, promotes better dissolution and film formation, enhancing charge transfer, but poses higher toxicity and environmental risks.[41–45] Despite their benefits, both solvents have limitations related to safety, environmental impact, and the need for optimal processing conditions to maximize performance. These limitations motivate the search for alternative passivation materials that offer enhanced stability, safety, and ease of processing.

Additionally, platinum (Pt) counter electrodes are the standard choice for DSSCs due to their superior catalytic activity, conductivity, and stability, which enable efficient triiodide reduction.[46,47] In 2007, Yoon *et al.*[48] fabricated a mesoporous platinum counter electrode via electrochemical deposition on FTO glass using an octaethylene glycol monohexadecyl ether ($C_{16}EO_8$). The resulting DSSC achieved a higher PCE (7.6%) than cells with sputter-deposited or thermally deposited Pt electrodes (6.4%) due to increased active surface area, improved light reflection, and reduced sheet resistance. On the other hand, Bajpai *et al.*[49] used graphene-platinum (G-Pt) nanoparticle composite as a counter electrode, prepared via pulsed laser deposition. The composite with 27% Pt loading outperformed conventional Pt thin-film electrodes, achieving 45% higher PCE (2.9%), greater J_{SC} (6.67 mA cm^{-2}), and V_{OC} (0.74 V) without a loss in fill factor. Enhanced performance is attributed to lower charge-transfer resistance (2.36 $\Omega \cdot cm^2$ vs. 7.73 $\Omega \cdot cm^2$ for standard Pt) and stronger catalytic activity, as confirmed by electrochemical impedance spectroscopy and cyclic voltammetry. However, their high

cost and limited availability drive the need for carbon-based alternatives, which are low-cost, abundant, corrosion-resistant, and tunable for enhanced performance.

Hence, this study focuses on enhancing the performance of carbon-counter-electrode-based DSSCs through innovative interfacial engineering using 1D TiO_2 TNRs and 2D $Ti_3C_2T_X$-MXene. The 2D $Ti_3C_2T_X$-MXene was synthesized via a solid-state synthesis method that included pre-etch HCl washing and HCl-HF etching of the Al layers. Integrating $Ti_3C_2T_X$-MXene as a passivating agent aims to improve charge separation and extraction while reducing interfacial charge recombination. To achieve this, surface passivation of the TiO_2/N719 dye interface was performed using $Ti_3C_2T_X$-MXene and conventional agents, including $TiCl_4$, toluene, and chlorobenzene. By leveraging the unique zero-Eg properties and layered structure of MXene, this approach enhances surface uniformity, lowers charge-transfer resistance (R_{Ct}), and mitigates ion migration, thereby improving interfacial stability and long-term device performance. The study demonstrates the potential of MXene to outperform conventional passivating agents by significantly increasing the V_{OC}, achieving values above 1V, and enhancing the PCE of DSSCs. Additionally, the scalability of this synthesis method ensures the production of high-quality MXene for large-scale applications. This research highlights the transformative potential of $Ti_3C_2T_X$-MXene in addressing critical challenges in DSSC technology, particularly V_{OC} enhancement, charge transport, and device stability, paving the way for next-generation solar technologies.

3.2 Experimental Section

3.2.1 Materials

The chemicals utilized in this work include transparent and conducting fluorine-doped tin oxide (FTO; L×W×T:100×100×2.3 mm^3, Surface Resistivity ~ 7Ω/sq) purchased from Sigma Aldrich, Titanium diisopropoxide bis(acetylacetonate) ($Ti(acac)_2OiPr_2$, 75% in IPA, Sigma Aldrich), 1-butanol (≥ 99.4%, Sigma Aldrich), Titanium Butoxide ($Ti(OBu)_4$, ≥ 97%, Sigma Aldrich), Titanium Tetrachloride ($TiCl_4$, 0.09 M in 20% HCl, Sigma Aldrich), Chlorobenzene (C_6H_5Cl, ≥ 99%, Sigma Aldrich), Toluene ($C_6H_5.CH_3$, ≥ 99%, Thomas Baker), (deionized (DI) water, N719 Ruthenium dye ($C_{58}H_{86}N_8O_8RuS_2$, ≥ 97%, Sigma Aldrich), hydrochloric acid (HCl) at a concentration of

35% w/w, ethylene glycol (≥ 99%, Sigma Aldrich), ethanol (Sigma Aldrich), Carbon cloth as a counter electrode (CE), potassium iodide (KI) (Z99%, Sigma Aldrich), and iodine (I_2) (Z99.8%, Sigma Aldrich). All chemical compounds were used as received without any further purification.

3.2.2 Passivation Protocol

To prepare passivated TNR photoanodes (i.e., TC-TNR, MX-TNR, TL-TNR, and CB-TNR), first, we prepared a 0.5 M passivating solution of each passivating agent in 10 mL of appropriate solvents. After mixing $TiCl_4$, $Ti_3C_2T_X$ MXene, Toluene ($C_6H_5.CH_3$), and Chlorobenzene (C_6H_5Cl) in the solvent, all four passivating solutions were stirred for 60 min at 25 °C till complete dissolution. Once this solution was carefully prepared, the hydrothermally synthesized 1D-TNR photoanodes were soaked in four distinct passivating solutions for 1 hour and heated at 70 °C in an oil bath. After 1 hour, all the passivated photoanodes were taken out from the beaker, rinsed with DI water and ethanol several times, and air dried. Finally, all the passivated photoanodes, namely TC-TNR, MX-TNR, TL-TNR, and CB-TNRs, were annealed at 500 °C for 30 min and then ready for further application. A schematic depiction of the passivation process is shown in **Figure 3.1**.

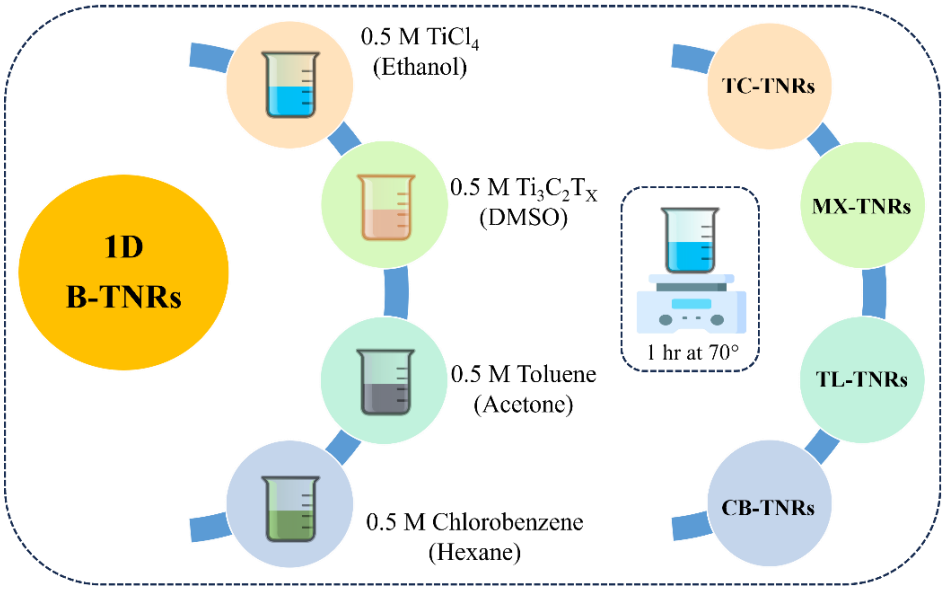

Figure 3.1 Schematics of photoanode passivation strategy used to prepare TC-TNR, MX-TNR, TL-TNR, and CB-TNRs.

3.2.3 DSSC Fabrication and Working Mechanism

As shown in **Figure 3.2(a)**, all the layers were assembled systematically. We first passivated bare 1D-TNRs with four different passivating agents: Titanium tetrachloride, MXene $Ti_3C_2T_X$, Toluene, and Chlorobenzene. Hereafter, these passivated TNRs were referred to as B-TNRs, TC-TNRs, MX-TNRs, TL-TNRs, and CB-TNRs. Following the passivation treatment for 1 hour, all photoanodes were thoroughly rinsed with DI water to remove excess precursor solution and loosely attached residues. Therefore, the passivating agents primarily contribute towards interfacial surface modification and enhancement of the morphological, optical, and electrical properties of the TNR photoanodes without directly affecting the structural integrity of the device and performance.

These passivated TNR photoanodes were soaked overnight in prepared N719 dye. After 24 hours, all passivated TNRs were removed, washed several times with ethanol to remove any residual material on the photoanode surface, and dried. A 5mM (I^-/I_3^-) iodine electrolyte was prepared by mixing 42 mg of KI and 64 mg of I_2 crystals in 5 mL of ethylene glycol and stirring at RT for 30 minutes. The carbon counter electrode of 1.5×1.5 cm^2 was cut from the conducting carbon cloth. Further, the DSSC assembly was sealed with a prepared carbon counter electrode and a 60 μm-thick paraffin spacer. Using a 5 mL medical syringe, 100 μL of the prepared electrolyte was injected between a dye-soaked photoanode and a carbon counter electrode. This step completes the device fabrication, and the fabricated DSSC is now ready for testing. The DSSCs utilize monolayers of dye molecules adsorbed onto high-surface-area photoanodes, such as mesoporous 1D-TiO_2 TNRs, to enhance light absorption. These TNR photoanodes, with porosity around 50% and surface areas hundreds of times larger than flat electrodes, enable significantly higher dye loading and efficient light scattering. Further, chemically bonded dye molecules facilitate optimal device performance by interacting with the redox electrolyte within the mesoporous structure. The counter electrode, positioned parallel to the working electrode, collects positive charges from the redox mediator, completing the charge transport cycle.

The working mechanism of DSSCs (**Figure 3.2(b)**) with B-TNRs and passivated TNRs involves three key steps: (i) photoinduced charge generation via dye excitation (D → D*), (ii) charge injection from dye's excited state (D*) into the TNR conduction band (CB_{TNR}), and (iii) charge transfer through the electrolyte to the counter electrode. Regeneration of the oxidized dye (D^+) by the redox mediator (I^-/I_3^-) minimizes recombination, ensuring efficient charge flow. Effective electron injection requires sufficient energy overlap between the D* and the CB_{TNR}. Achieving a high CB level in TNRs is crucial for maximizing the V_{OC} and device performance.

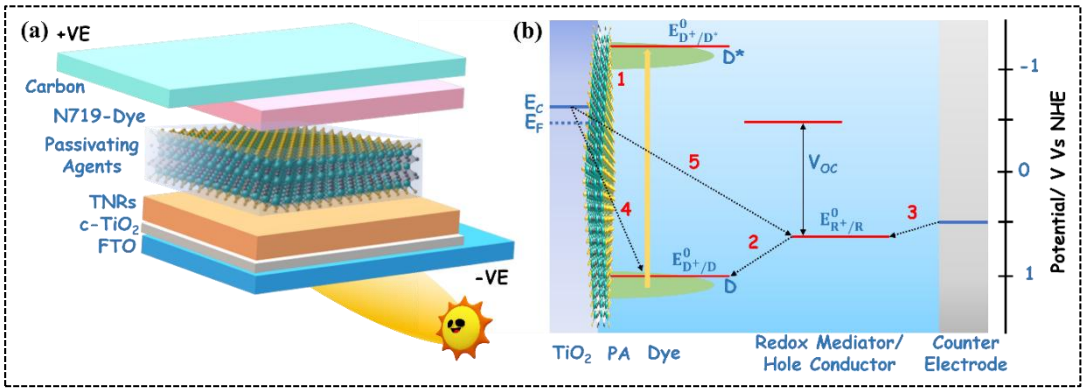

Figure 3.2 (a) Typical schematic of the fabricated DSSC device, and (b) a standard plausible working mechanism of the fabricated DSSC.

3.3 Results and Discussion

3.3.1 Morphological and Structural Analysis of $Ti_3C_2T_X$-MXene

$Ti_3C_2T_X$-MXenes are anticipated to be effective passivating agents due to their unique 2D layered structure, high surface area, high wettability, and surface termination groups (-OH, -F, -O). Also, the metal-like conductivity of $Ti_3C_2T_X$-MXenes is desirable for efficient charge channelization and transfer. As shown in **Figures 3.3(a-b)**, prolonged HCl-HF etching for 24 hours promotes continuous removal of the interlayer Al atoms, resulting in progressive delamination and thinning of the stacked layers, ultimately leading to the formation of multilayered $Ti_3C_2T_X$-MXene sheets with an average interlayer spacing of ~90 nm. The elemental mapping confirms the distribution of elements across the $Ti_3C_2T_X$ layers and shows a layered-like stoichiometric distribution in **Figure 3.3(c-e)**. The visible cracks observed in **Figures 3.3(a-b)** may arise from

intrinsic stresses during synthesis, drying-induced shrinkage, or vacuum conditions during sample preparation. These features are likely the sample preparation or characterization artefacts and do not influence device performance, as the $Ti_3C_2T_X$ MXene treatment preserves the functional integrity of the passivated photoanodes.

The degree of stacking and delamination of $Ti_3C_2T_X$-MXene sheets plays a crucial role in determining their electrical and charge-transport properties. Highly stacked multilayered MXene structures generally provide continuous electron-conduction pathways due to strong interflake connectivity and structural robustness; however, excessive stacking can reduce the accessible active surface area and hinder ion/electrolyte diffusion through the compact interlayer galleries. In contrast, few-layer or partially delaminated MXene sheets exhibit enlarged interlayer spacing and increased exposed surface area, which facilitate enhanced electrolyte penetration, shorter charge-transport pathways, and improved interfacial contact with the surrounding matrix/photoactive material. These features promote efficient charge separation, faster electron transport kinetics, and reduced charge-transfer resistance, thereby improving the overall electrochemical and photovoltaic performance of the MXene-based systems.

XRD analysis was performed to assess the phase purity and structure of $Ti_3C_2T_X$-MXene at room temperature in the 2θ range of 5 to 50°. **Figure 3.3(f)** shows the XRD pattern of bulk Ti_3AlC_2 (black) and $Ti_3C_2T_X$-MXene (red) with all the characteristic peaks of MAX-phase and MXene. The distinctive peaks of MAX-phase Ti_3AlC_2 were (002), (004), (101), (102), (103), (104), (105), and (107), appearing at 2θ of 9.56, 19.14, 34.01, 35.06, 36.74, 39.00, 41.75, and 48.46°, respectively. The refined XRD of bulk MAX-phase Ti_3AlC_2 is shown in **Figure 3.4**, which confirms the formation of $M_{n+1}AX_n$-like (Ti_3AlC_2) MAX phase of space group P 63/*mmc*. The lattice parameters of the MAX-phase Ti_3AlC_2 are $a = b = 3.072 \pm 0.003$, and $c = 18.534 \pm 0.005$ Å with $\alpha = \beta = 90°$ and $\gamma = 120°$.

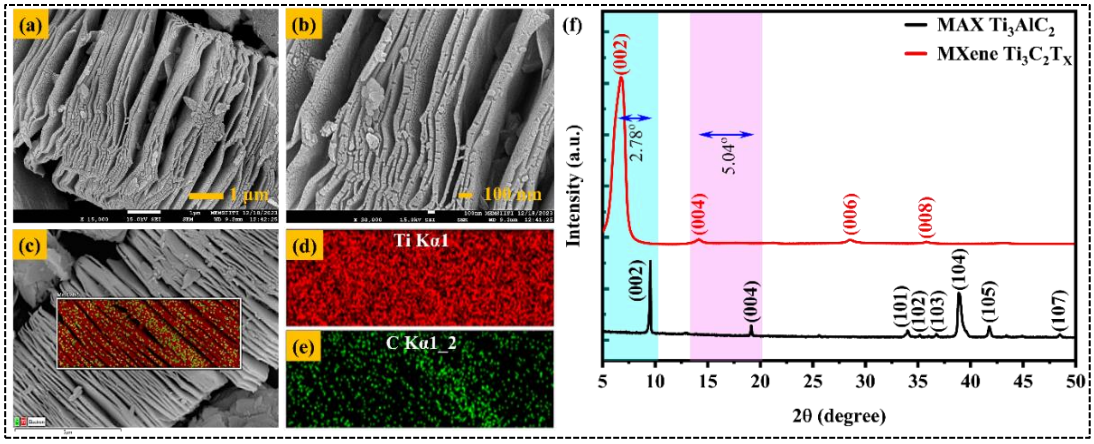

Figure 3.3 (a-b) The morphology of multi-layered $Ti_3C_2T_X$-MXene was obtained at different magnifications from FESEM analysis, (c-e) Elemental mapping confirmed the uniform distribution of Ti and C across the layers, and (f) XRD patterns of MAX-phase Ti_3AlC_2 (black) and multi-layered 2D $Ti_3C_2T_X$-MXene (red).

The peak (104) of MAX-phase Ti_3AlC_2 at 2θ = 39° is diminished with a flat region, suggesting the removal of Al and the formation of laminated 2D $Ti_3C_2T_X$-MXenes following HCl-HF etching. Moreover, three broadened and poorly intense peaks were observed at 14.17, 28.56, and 35.80° in the laminated 2D $Ti_3C_2T_X$-MXenes XRD pattern (red), which correspond to the (004), (006), and (008) peaks related to $Ti_3C_2(OH)_2$. Furthermore, as the etching time increased, the diffraction peak intensity steadily decreased, suggesting that the structure of the $Ti_3C_2T_X$-MXenes was undergoing significant change and that the interlayer gap was increasing. Moreover, as shown in **Figure 3.3(f)**, the (002) peak of $Ti_3C_2T_X$ after HCl-HF etching shifts toward a lower 2θ angle, in agreement with the FESEM image shown in **Figures 3.3(a-b)**. The larger interlayer spacing corresponds to a lower 2θ value in XRD patterns due to Bragg's law, which states that $n\lambda = 2d \sin\theta$, where d is the interlayer distance. In particular, the (002) and (004) peaks of $Ti_3C_2T_X$ after etching for 24 hours at 35 °C shift to 2.78° and 5.04° lower 2θ diffraction angles, respectively. Hence, all these results are in good agreement with the literature and in accordance with Bragg's law.

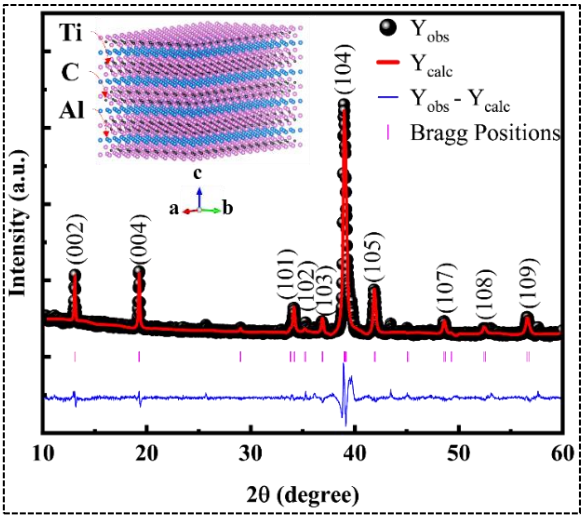

Figure 3.4 Rietveld refined XRD pattern of MAX phase Ti_3AlC_2, and corresponding Bragg's positions.

Further, the stoichiometry and oxidation states of all elements in the laminated 2D-$Ti_3C_2T_X$-MXenes were probed by X-ray photoelectron spectroscopy (XPS). XPS survey-scan spectra (**Figure 3.5(a)**) show the presence of Ti, C, and F, and the atomic composition is mentioned in **Table 3.1**. As shown in **Figures 3.5(b-c)** and **(d)**, the core level XPS spectra of C (1s), Ti (2p), and F (1s) were deconvoluted by Gaussian-Lorenzian mix functions with Shirley's background. The binding energy (BE) values of all the components were found to be in accordance with the available literature. This result confirms the presence of three types of surface functional groups on laminated 2D $Ti_3C_2T_X$-MXenes: oxide (-O-), hydroxyl (-OH), and fluoride (-F).

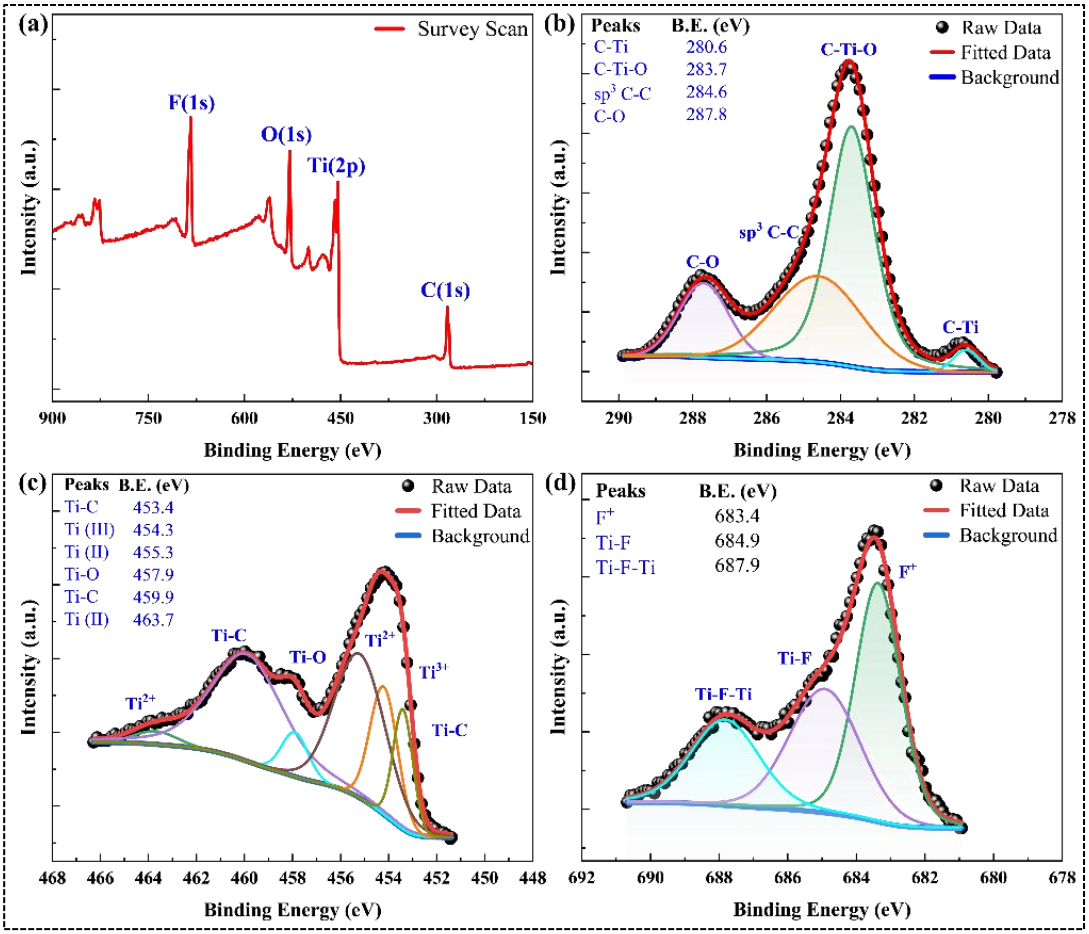

Figure 3.5 (a) XPS Survey-scan spectra of $Ti_3C_2T_X$-MXene in the binding energy range of 900 to 150 eV. Core-level XPS spectra of the multi-layered $Ti_3C_2T_X$-MXene deconvoluted by Gaussian-Lorenzen mix functions with Shirley's background (b) C(1s), (c) Ti(2p), and (d) F(1s).

Table 3.1 Binding energies obtained from XPS fitting of core-level C (1s), Ti (2p), and F (1s) spectra for 2D $Ti_3C_2T_X$-MXene.

Element	Component Name	Binding Energy (eV)
Ti $(2p)_{3/2}$, Ti $(2p)_{1/2}$	Ti-C	453.4, 459.9
	Ti (II)	455.3, 463.7
	Ti (III)	454.3
	Ti-O	457.9
	C-Ti-F_X	460.4
C (1s)	C-Ti-T_X	280.6
	C-Ti-O	283.7

	C-C	284.6
	C-O	287.8
F (1s)	F (I)	683.4
	Ti-F	684.9
	Ti-F-Ti	687.9

3.3.2 Morphological Analysis of Bare and Passivated TiO_2 Photoanodes

To assess the morphology and chemical uniformity of the hydrothermally grown 1D-TNRs on FTO substrates, we performed FESEM and elemental mapping, as shown in **Figure 3.6**. The top-view FESEM of vertically aligned bare-TNRs (B-TNRs) on the FTO substrate, resembling a seagrass-like structure and forming clumps when gathered collectively, is depicted in **Figure 3.6(a)**. Herein, HCl plays a crucial role in improving the morphology and crystallinity of the TNRs. The HCl concentration acts as a decisive factor in controlling the hydrolysis and nucleation kinetics of the highly water-reactive titanium precursor. The acidic environment suppresses rapid hydrolysis and uncontrolled precipitation, thereby promoting uniform nucleation, anisotropic growth, improved crystallinity, and well-aligned rutile TNR formation. Also, the average size of the top facets of grown B-TNRs is 85 nm with a standard deviation (σ) of 5 nm. **Figure 3.6(b-d)** confirms the uniform elemental distribution of Ti and O without any foreign species across the sample. As a result, the produced TNR photoanodes had extremely high structural, morphological, and chemical stability. Every finding demonstrated strong agreement with the readily accessible literature.

The main focus of this study is to understand the effect of interfacial engineering of TNRs on the performance of DSSCs and on changes in the optical/electrical properties of B-TNRs. The passivation of the TNRs was performed with $TiCl_4$ (TC), $Ti_3C_2T_X$ (MX), toluene (TL), and chlorobenzene (CB), and the resulting TNRs will be further attributed

as TC-TNRs, MX-TNRs, TL-TNRs, and CB-TNRs, respectively. **Figure 3.7(a-b)** depicts the top-view FESEM images of the B-TNRs and EDX spectra, confirming the vertical orientation of the nanorods and stoichiometric presence of the Ti and O across the surface. Also, FESEM images of all other passivated TC-, MX-, TL-, and CB-TNRs are shown in **Figure 3.7(c-f)**, respectively. TC passivation of TNRs induces chemical modulation, forming a very thin $TiO_{2-X}Cl_X$ layer that facilitates better electron transport and reduces electron recombination with the electrolyte.

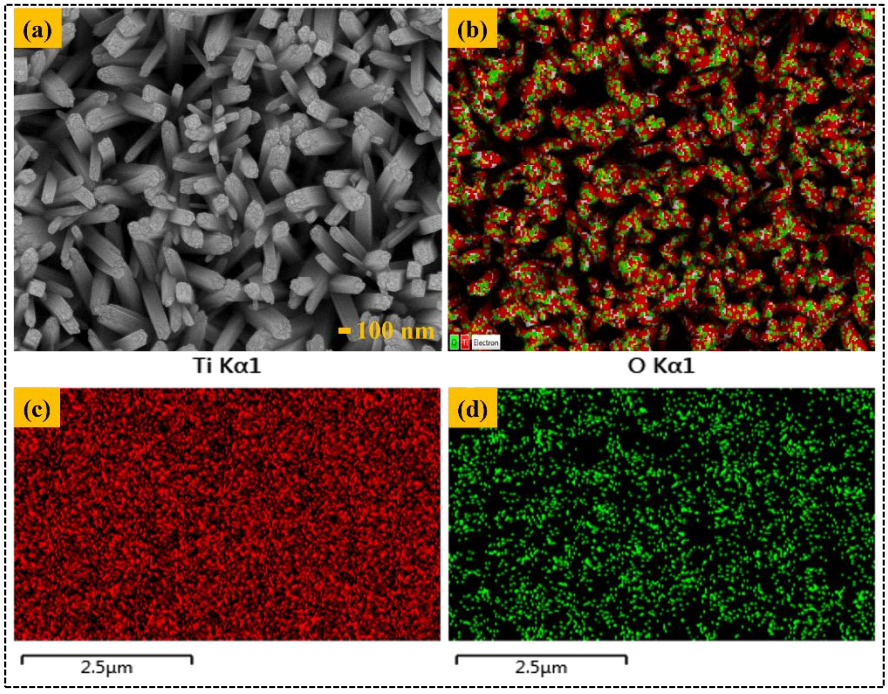

Figure 3.6 Morphological analysis of the hydrothermally grown B-TNRs (8hr @150°C). (a) The top-view FESEM image of the B-TNRs shows vertical growth of the FTO substrate at 30000X magnification, and (b-d) elemental mapping of the respective TNR photoanode confirms the uniform distribution of the Ti and O.

As visible in **Figure 3.7(c)**, TC-TNRs surfaces are comparatively smoother than B-TNRs and provide better sunlight scattering, helping to improve electron injection and light harvesting efficiency. This passivation also tuned the optical properties and acted as an anti-corrosive layer, protecting it under harsh conditions. **Figure 3.7(d)** shows that MX

passivation increases the compactness of the TNRs and the surface area, providing more sites for dye absorption. MX also has a very high surface area and a broad light-absorption spectrum, which reduces recombination losses and accelerates electron transport within the TNRs. Although $Ti_3C_2T_X$-MXene exhibits broad UV-visible-NIR absorption due to its metallic/semi-metallic nature, it does not form a thick continuous coating layer over the photoanode that could significantly suppress photon absorption by the dye sensitizer. This could minimize charge transport losses and improve overall device performance, particularly under low-light conditions. By passivating surface defects and trap sites on TNRs, MX-passivation can mitigate charge-carrier recombination, thereby enhancing the V_{OC} and FF of DSSCs.

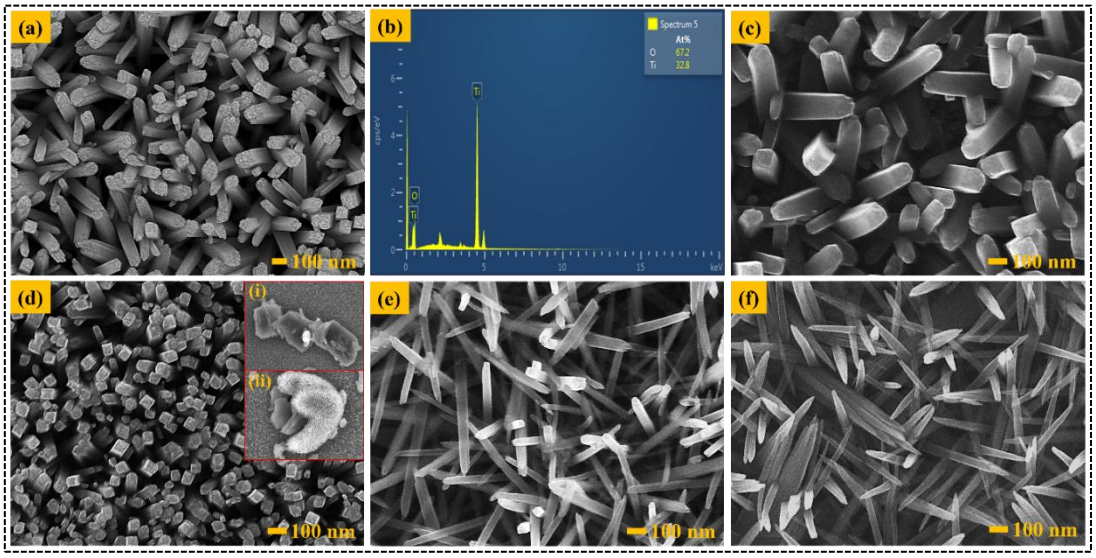

Figure 3.7 Top view of FESEM images of all the passivated TNRs and their elemental composition. (a) B-TNRs, (b) EDX spectra of B-TNRs confirming the stoichiometric presence of Ti and O-atoms across the surface, (c) TC-TNRs, (d) MX-TNRs, (e) TL-TNRs, and (f) CB-TNRs.

To ensure the removal of any excess MXene residues on the surface of the 1D MX-TNR photoanodes, we thoroughly washed the samples with DI water and ethanol prior to annealing. This step was crucial for eliminating unbound or loosely adhered MXene sheets, thereby reducing the prominence of intercalated structures under high-magnification imaging. Nevertheless, we could identify subtle but distinguishable traces

of MXene sheets at lower magnifications. These features were challenging to capture distinctly at higher magnifications because the intercalated MXene sheets are often embedded within the TNR matrix, forming a well-dispersed and conformal coating rather than visible, standalone sheets. To address this, we have included inset images (**Figure 3.7(d-i)** and **3.7(d-ii)**) that specifically highlight these subtle traces, providing clearer visual evidence of the intercalation.

Again, TNRs were passivated using two organic activators, TL and CB, and their FESEM images are shown in **Figure 3.7(e-f)**. Interestingly, the facet sizes and rod thickness decreased drastically in TL- and CB-TNRs, indicating that the surface energy was finitely modulated. It also suggests that TL and CB molecules are adsorbed onto specific TNR facets, forming TNR surface complexes that suppress the growth of larger facets into smaller ones. TL and CB passivation may induce surface reconstruction of TNRs, forming smaller facets with different crystallographic orientations. This can occur when passivating molecules interact with surface atoms, leading to rearrangements that favor the formation of smaller facets. CB passivation acts as an etchant, altering the reactivity of the nanorod's different facets. As a result, when subjected to a CB-etchant solution, certain facets may be more susceptible to etching than others. This selective etching process can remove specific regions of the nanorods, reshaping or reducing their size.

The High-Resolution Transmission Electron Microscopy (HRTEM) image of 1D B-TNRs provides detailed insights into their structural characteristics. **Figure 3.8(a)** displays a low-magnification TEM image of a single TNR, with the scale bar indicating a length of approximately 50 nm for the section shown. This image highlights the overall shape and dimensions of the nanorod, providing context for the higher-magnification images in **Figure 3.8(b-c)**. The high-magnification HRTEM image of a specific section of the TNR, as denoted by the red box in panel **Figure 3.8(a)**, reveals lattice fringes, indicating the nanorod's crystalline structure. The image shows two distinct lattice spacings: the red arrows and text indicate a lattice spacing of $d_{(110)}$ = 0.32±0.01 nm, corresponding to the [001] crystallographic direction, while the green arrows and text indicate a lattice spacing of $d_{(001)}$ = 0.31±0.02 nm, corresponding to the [110]

crystallographic direction. These measurements confirm the crystalline nature of the TNRs and provide detailed insights into their structural properties. **Figure 3.8(c)** displays the Selected Area Electron Diffraction (SAED) pattern of the TNRs. The diffraction spots in this pattern indicate the crystalline nature and orientation of the nanorod, with labelled spots corresponding to different crystallographic planes of rutile TiO_2, such as (001), (101), and (111). The arrangement and intensity of these spots provide information on the crystal lattice's symmetry and orientation, further corroborating the crystalline structure observed in **Figure 3.8(b)**.

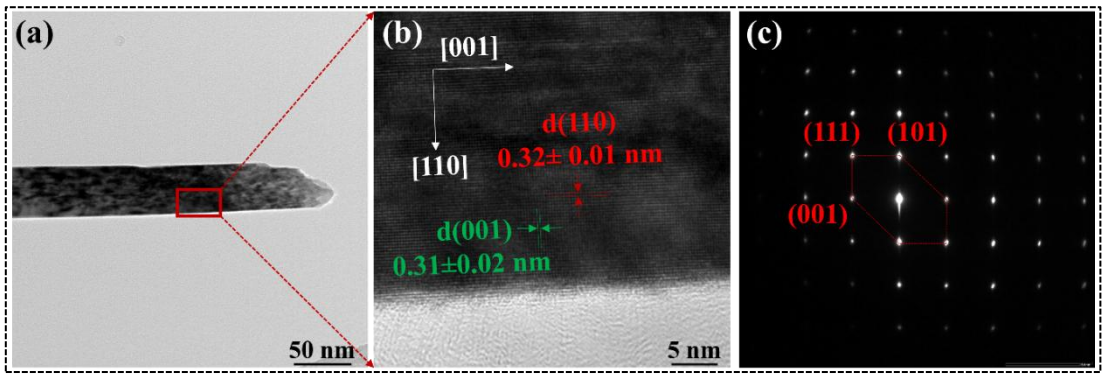

Figure 3.8 High-resolution TEM Analysis. (a) TEM image of a single B-TNR in a resolution scale of 50 nm, (b) HRTEM image of a selected portion of the B-TNR (highlighted in red color box), and estimated lattice spacing of [001] and [110] crystallographic planes, and (c) Respective SAED pattern confirming the crystalline nature and orientation of the TNRs.

In summary, the HRTEM image in **Figure 3.8(b)** reveals the atomic-scale structure of the TNRs, showing distinct lattice fringes corresponding to specific crystallographic planes. The SAED pattern in **Figure 3.8(c)** supports these observations by providing diffraction data that align with the observed lattice spacings. Together, these images confirm the high crystallinity and well-defined structure of the 1D TNRs, which are crucial for their application in DSSCs. The well-defined crystalline structure and orientation can significantly influence the electronic properties and charge-transport mechanisms within nanorods, thereby contributing to the overall efficiency of DSSCs.

3.3.3 Structural Analysis

An XRD study is performed to confirm the crystalline nature, lattice constants, and phase purity of the B-TNRs and other passivated TNRs. To acquire XRD data, we used X-ray diffraction (XRD, Malvern Panalytical, Empyrean) with Cu $K_{\alpha 1}$ radiation (λ = 1.5406 Å) in the 2θ range of 20º-60º with a step size of 0.026º. A diffractogram of rutile phase TNRs and passivated TNRs exhibiting a tetragonal arrangement of TiO_2 octahedra is shown below in **Figure 3.9(a)**. For B-TNRs, all the characteristic 2θ peaks were found at 26.43º, 36.04º, 37.68º, 41.22º, and 54.42º, corresponding to X-ray reflection from the (110), (101), (200), (111), and (211) planes, respectively. All these prominent characteristic peaks are present in the passivated TNRs samples, indicating that passivation does not deform the crystal structure or phase purity of the TNRs. The FTO peaks are marked by asterisks (*) and used as transparent conducting substrates for the hydrothermal growth of the TNRs. In the case of MX-TNRs, one extra diffraction peak was observed at 2θ of 41.69º, which is associated with the (105) diffraction plane of $Ti_3C_2T_X$-MXene.

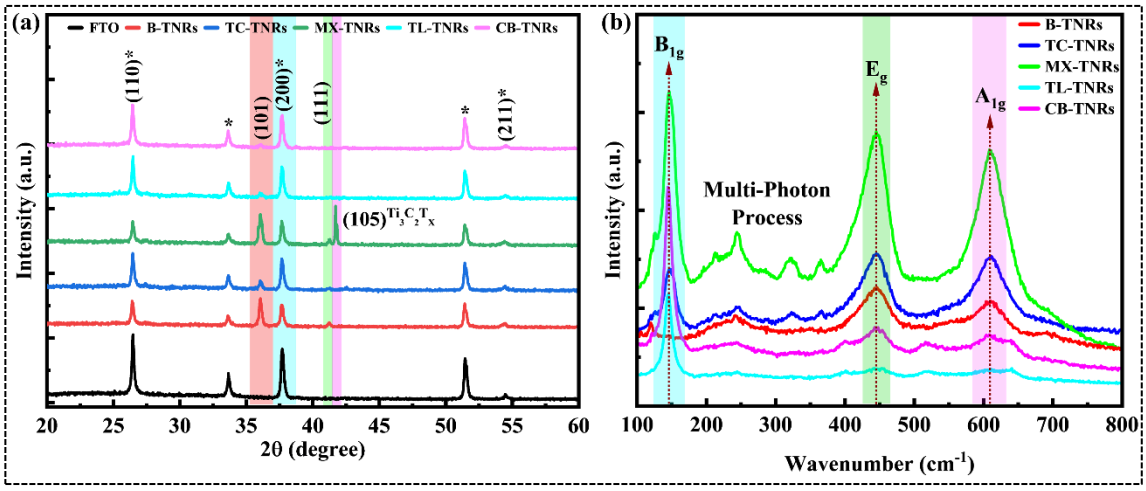

Figure 3.9 (a) XRD pattern of FTO, hydrothermally synthesized B-TNRs, and other passivated (TC-, MX-, TL-, and CB-) TNRs. The continuous XRD scan was performed from 20° to 60° with a step size of 0.026°, using a Cu Kα (1.5406 Å) source.

However, other characteristic peaks of MXene are absent in the diffractogram of passivated MX-TNRs, suggesting a much lower concentration. This peak appeared in the

MX-TNR diffraction pattern, and all peaks were attributed to TNRs, confirming that the crystal structures of both $Ti_3C_2T_X$ and TNRs were maintained. This shows that the two materials do not undergo any chemical or structural changes and coexist in the composite film. The TC-TNR and MX-TNRs possess all the characteristic diffraction peaks of TNR and some passivation diffraction peaks (i.e., MX-peaks). However, when organic passivation was performed with TL- and CB-, structural deformation occurred, resulting in diminished intensities of some diffraction planes. Structural deformation was visible in FESEM images (**Figure 3.7**), consistent with the XRD results. However, other than the (101) and (111) diffraction peaks, all other peaks are uniformly intense without any impurity peaks. As the diffraction peaks diminish or change in intensity, it indicates that the crystal structure of TNRs has been altered. The disintegration or reorganization of the TNRs caused by etching with CB and TL may alter their crystallinity and result in non-uniform intensity distribution. For instance, if the etching process preferentially removes certain crystal facets or induces surface passivation, it can simultaneously affect the intensity of the diffraction peaks and alter the surface morphology. Furthermore, the calculated lattice parameters of the TNR and other passivated TNRs are nearly equal: $a = b = 4.762 \pm 0.005$ Å and $c = 2.863 \pm 0.006$ Å. Lastly, the peak position remains unchanged, suggesting that the crystal lattice parameters of the bare and passivated TNRs remain relatively unchanged. Passivation might alter the surface-state density or the degree of crystallinity, leading to changes in peak intensities without necessarily causing peak shifts.

Additionally, to monitor the molecular vibrations and lattice vibrations in prepared B-TNRs and other passivated TNRs. Surface passivation aims to improve the quality and stability of B-TNR surfaces by minimizing local defects and contaminants. Here, by examining changes in characteristic Raman peaks or vibrational modes, we can estimate the presence of surface defects (vacancies, dislocations, etc.) and contaminants (adsorbed foreign species, impurities, etc.). **Figure 3.9(b)** shows first and second-order multi-phonon modes at room temperature (300K) for B-TNRs and other passivated-TNRs. The RT-Raman peak positions do not vary between B-TNR and other passivated TNR photoanodes, suggesting either no strain across samples or the same strain in all samples. For the bulk rutile phase tetragonal TNRs, three main characteristic stretching Raman

peaks were identified as B_{1g} (symmetric O-Ti-O bending vibrations), E_g (symmetric O-Ti-O stretching vibration), and A_{1g} (symmetric Ti-O stretching vibration) at 145.80, 444.89, and 609.28 cm^{-1}, falling within the range and in good agreement with the literature as given in **Table 3.2**. This confirms that no phonon confinement is taking place and suggests the phase-pure formation of rutile-TNRs. At the same time, an additional broad peak was observed between 240 and 380 cm^{-1}, attributed to a multi-phonon process.

A summary of these second-order vibrations and their corresponding identifications is given in **Table 3.2**. This second-order multi-phonon vibration usually occurs because of the simultaneous absorption or emission of multiple phonons (quantized lattice vibrations) during the electronic transitions within the TNRs. Also, the peak intensities vary across passivated TNR photoanodes, indicating that passivation alters their surface roughness and crystallinity.

Table 3.2 Various Raman Vibration modes of rutile phase tetragonal TNRs and respective frequencies at Γ, X, M, and Z of the Brillouin zone at RT.

Order of scattering	**Mulliken notation**	**Obtained Raman peak positions of TNRs (cm^{-1})**	**Standard frequency range (cm^{-1})**	**Ref.**
First-order	B1g	145	142-145	[50] [51] [52]
	Eg	444	443-447	
	A1g	609	609-613	
Second-order multi-phonon	$X_2^1+X_2^1$	~ 212	-	[53] [54]
	$E_u(2)$-$E_u(1)$	~ 244	-	
	$E_u(3)$-$E_u(1)$	~ 321	-	
	$E_u(2)$-$B_{1u}(1)$	~ 364	-	

3.3.4 UV-visible Absorption and FTIR studies

We performed UV-visible spectroscopy to characterize the absorption spectra of the TNRs and the N719 dye. This study helps us determine the appropriate band gap of the TNRs and the UV-visible light absorption range. As shown in **Figure 3.10(a-b)**, all the TNR and 0.5mM-N719 dye samples were scanned to estimate their absorption in the 300 to 800 nm wavelength range. In **Figure 3.10(a)**, the absorption spectra of B-TNR and other passivated TNRs are depicted, clearly showing that the absorption edges of all TNRs lie between 340 and 450 nm. More interestingly, all the passivated TNR photoanodes

exhibited enhanced visible-light absorption behaviour with a comparatively broadened and slightly redshifted absorption edge in the order of B-TNRs < TC-TNRs < MX-TNRs < TL-TNRs < CB-TNRs. The observed optical behaviour suggests that both organic and inorganic passivation treatments influence the interfacial electronic environment, surface-state distribution, and light-harvesting characteristics of the TNRs. To estimate the optical bandgap behaviour of all TNRs, Tauc plots were analyzed by plotting $(\alpha h\nu)^2$ vs $h\nu$. The estimated optical bandgap values for B-TNRs, TC-TNRs, MX-TNRs, TL-TNRs, and CB-TNRs were found to be 3.59, 3.17, 3.16, 2.79, and 2.50 eV, respectively (**Figure 3.10(a) inset**). The observed variation is attributed to absorption-edge broadening and interfacial electronic interactions arising from passivation rather than significant intrinsic bandgap modification of the TNRs.

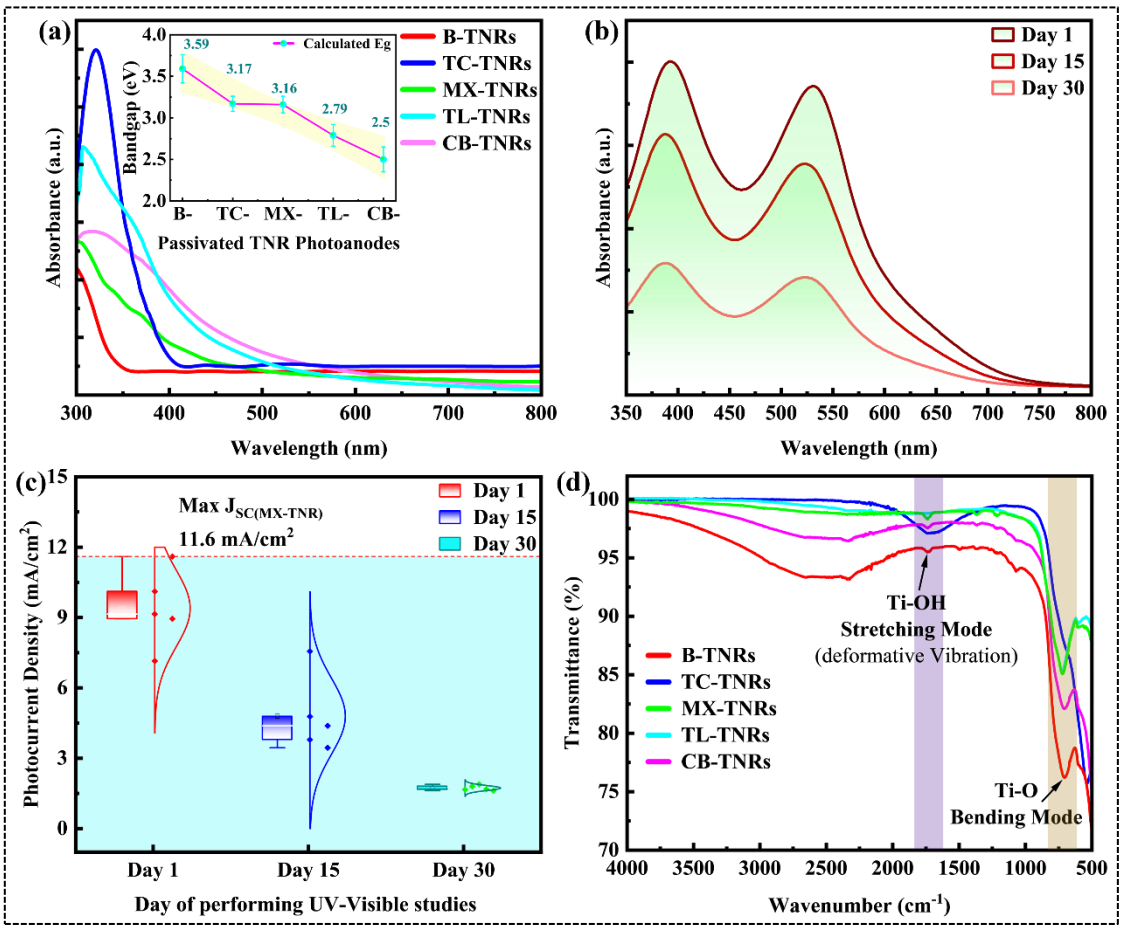

Figure 3.10 UV-vis absorption studies of (a) bare-TNRs and other passivated TNRs, and (b) 0.5mM-N719 dyes tested three times in 30 days and showed their UV-visible

absorption spectra on the 1st, 15th, and 30th day, which were preserved under dark conditions at 25 °C with RH 40%. (c) photocurrent response from all the passivated photoanodes on the testing on day 1st, 15th, and 30th, showing maximum J_{SC} of 11.60 mA cm^{-2}, (d) FTIR Spectra of hydrothermally synthesized B-TNRs and passivated TNRs, where the passivating agents are TC, MX, TL, and CB.

The introduction of passivating agents modifies the interfacial electronic environment and suppresses surface defect states and oxygen-vacancy-related trap centres in TNRs. Such interfacial interactions can slightly influence the electronic structure and optical absorption behaviour, contributing towards improved light harvesting, reduced charge-carrier recombination, and enhanced charge separation efficiency. In MXene-passivated TNRs (MX-TNRs), intimate electronic coupling between conductive $Ti_3C_2T_X$ MXene sheets and TiO_2 induces band-edge shifts through heterojunction formation, surface dipole effects, and interfacial charge transfer. This interaction modifies the density of states near the valence and conduction band edges, resulting in an upward shift of the VBM and/or a downward shift of the CBM, thereby reducing the effective band gap. The experimentally observed redshift in UV-vis absorption spectra confirms this band gap narrowing, highlighting the role of MXene passivation in improving visible-light absorption and overall photoanode performance.

Further, the absorption spectra of N719-dye-soaked TNRs were scanned from 350 nm to 800 nm, and excellent absorption behaviour was observed below 600 nm, as shown in **Figure 3.10(b)**. Also, the dyes' absorption decreased steadily on days 1, 15, and 30, even when they were kept in a dark environment. The possible reasons for this absorption reduction can be (i) dye molecules may degrade over time due to exposure to light, oxygen, moisture, or other environmental factors, (ii) dye molecules may aggregate or form complexes with other species present in the environment, and (iii) changes in environmental conditions, such as temperature, humidity, or pH, can influence the stability and properties of the dye molecules leading to the reduced absorption. Overall, the decrease in the absorption of N719 dye over time could be due to a combination of factors related to the stability, interactions, and environmental conditions affecting the dye molecules.

Moreover, two distinct absorption peaks were found in the absorption spectrum of N719 dye between 350 and 425nm and 500 and 575nm (**Figure 3.10(b)**). These absorption peaks were observed in many ruthenium-based dyes and are associated with the metal-to-ligand charge-transfer (MLCT: 350-425nm) and ligand-to-ligand charge-transfer (LLCT: 500-575nm) transitions. The presence of two absorption peaks allows the N719 dye to absorb a broader range of visible wavelengths. Therefore, by covering a wider spectral range, the N719 dye reduces the likelihood that unabsorbed photons will excite electrons in the semiconductor substrate, thereby reducing electron-hole recombination and photocurrent loss. Moreover, light-harvesting efficiency (LHE) was calculated from UV-visible absorption spectra to assess the photoanode's ability to absorb incident photons and generate charge carriers effectively. The formula for LHE is given as:

$$LHE = 1\text{-}10^{-A(\lambda)} \qquad 3.1$$

where A is the absorbance of the dye at a specific wavelength. Higher absorbance values indicate greater photon capture by the dye molecules, thereby increasing electron generation. All results from the LHE analysis are properly justified by the current density variation shown in **Figure 3.10(c)**. The variations in LHE for MX-TNR photoanodes are influenced by the extent of dye anchoring to the surface and the overall light-absorption characteristics. Effective passivation strategies, such as MXene treatments, will enhance dye loading and optimize surface interactions, thereby maximizing light absorption and improving the device's photoconversion efficiency.

Further, we performed FTIR spectroscopy to confirm the chemical structure, the functional groups present, and the presence of impurities or contamination in the TNRs and passivated TNRs, as shown in **Figure 3.10(d)**. A broad band from 3500 to 2500 cm^{-1} is characteristic of associated hydroxyl groups. These are weakly chemisorbed and usually disappear at temperatures >200 °C. This broad FTIR peak is characteristic of tetrahedral-coordinated vacancies designated for Ti^{4+}-OH. Also, in passivated TNRs, this peak disappeared, indicating that tetrahedrally coordinated vacancies are decreasing. Two other characteristic peaks that belong to the rutile phase TNRs, i.e., Ti-OH stretching mode and Ti-O bending modes, were observed in FTIR spectra at 1736 and 705 cm^{-1},

respectively. The adsorbed water molecules are thought to be the primary reason, given the higher interaction surface area and the lower pore-size distribution. Modest bending vibrations at 1369 cm^{-1}, which might have been caused by the products' absorption during air exposure, verified the existence of water. There were no visible absorption bands at 480 cm^{-1}, which is the absorption band of Ti_2O_3. Additionally, no additional absorption peaks were observed, such as the stretching vibrations of organic residues -CH and -CH_2 at 1400-2900 cm^{-1}, suggesting that the films were not contaminated by carbon or OH groups.

3.3.5 XPS Analysis

To examine the electrical structure, ionic states, and chemical makeup of the hydrothermally produced 1D-TNRs, we performed an XPS analysis. The survey scan of 1D-TNRs grown on the c-TiO_2-coated FTO substrates is shown in **Figure 3.11(a)**. In good agreement with the EDX results, the survey scan verifies the presence of Ti, O, and C, whereas the carbon content is solely due to background contamination and is not present in the produced TNRs sample. The high-resolution core level XPS spectra of C(1s) were deconvoluted by Gaussian-Lorenzian mix functions with Shirley's background, as shown in **Figure 3.11(b)**. This XPS spectrum yielded three distinct peaks at 284.6, 286.1, and 288.2 eV, attributed to the C-C, C-O, and C=O bonds in the bulk. A diamond-like structure or sp^3 C-H bonding is thought to be the cause of the first dominating peak seen at 284.6 eV, which is associated with C-C sp^3 hybridization. The other peak at about 286.1 eV might be a chemical connection between C and O or C and H. The C(O)OH or HO-C-OH bonds are typically associated with the sub-peak at 288.2 eV. Since most sp^3 bonds can be terminated by hydrogen, which cannot be directly detected with the techniques used here, the presence of sp^3 does not indicate that the film is diamond-like carbon (DLC), even though the data cannot be fitted with a sp^2 peak.

Figure 3.11(c-d) displays the core-level XPS spectra of Ti(2p) and O(1s), which were deconvoluted using the Voigt curve fitting within the Shirley background in order to identify the typical behaviour of TNRs precisely. At binding energies (BE) of 457.6 eV and 463.3 eV, respectively, the double peak typical of the $Ti(2p)_{3/2}$ and $Ti(2p)_{1/2}$ core level, which corresponds to the Ti^{4+} cations, is completely fitted. Furthermore, the energy

segregation of the $Ti(2p)_{3/2}$ and $Ti(2p)_{1/2}$ peaks and their area ratios of 5.7 and 2.45 eV, respectively, demonstrate the strong connection between Ti and O atoms. Similarly, O(1s) core level spectra were fitted with a Shirley background, and the Voigt function reveals the deconvolution of two distinct peaks at 528.7 and 530.3 eV. The lower BE peak (528.7 eV) of O(1s) spectra, which is associated with the lattice oxygen of O^{2-} anions, validates the strong Ti-O chemical coupling (O_{1s}^{Ti-O}) in TNRs.

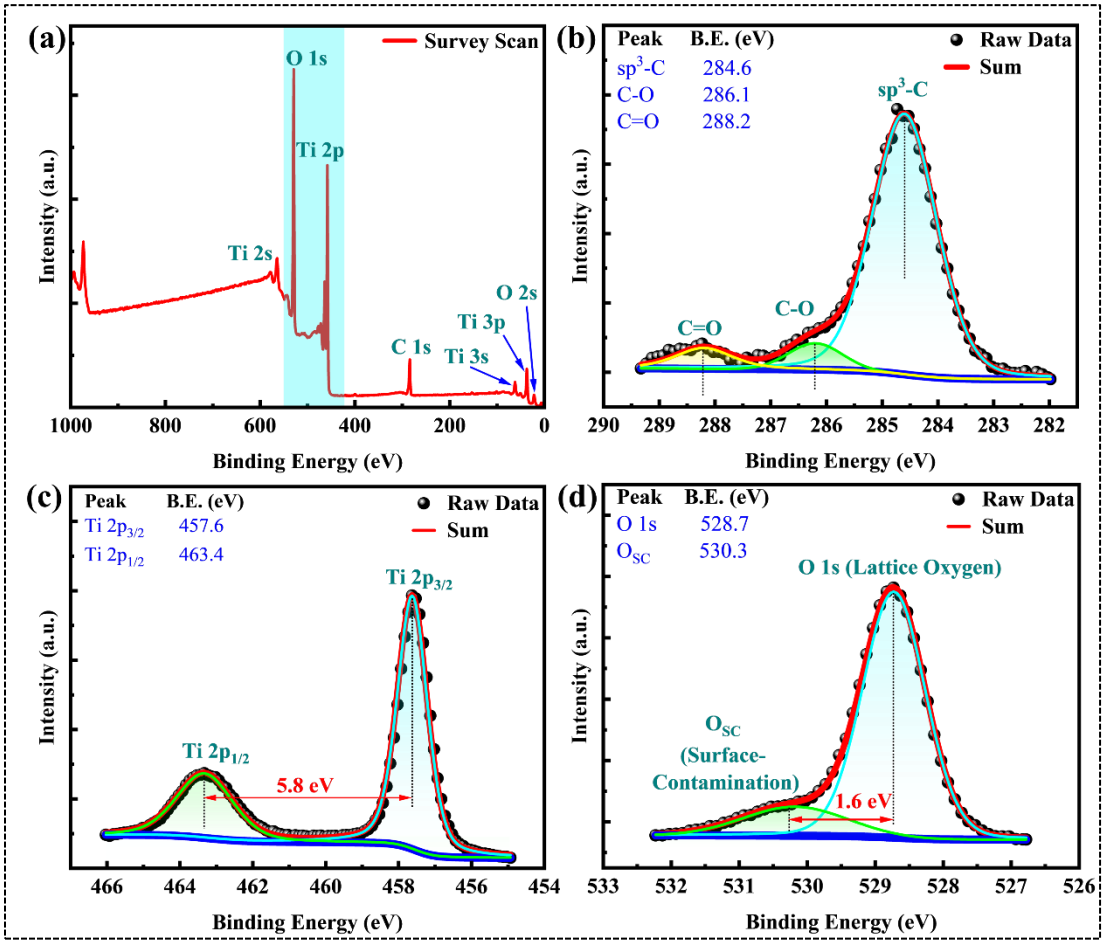

Figure 3.11 (a) XPS survey spectra of Hydrothermally synthesized B-TNR photoanode, (b) core-level C1s spectra used for carbon correction, and (c-d) Typical core-level XPS spectra of Ti(2p) and O(1s) deconvoluted with Shirley background and Voigt function fitting. The distinct characteristic peaks are $Ti(2p)_{3/2}$, $Ti(2p)_{1/2}$, and O(1s): lattice oxygen and O_{SC} (surface contamination) observed at 457.6, 463.4, 528.7, and 530.3 eV, respectively.

Also, due to the presence of carbon oxides or hydroxides, the surface contamination (O_{SC}) peak appears in the O(1s) core spectra at 530.3 eV. This O_{SC} peak shows the O-H chemical bonding, which comes from the surface-adsorbed H_2O. However, the ratio of the two peaks' area (A_{O_L} and $A_{O_{SC}}$) under the curves, the amount of surface-contaminated oxygen is much less. Despite the initial atomic reactant ratio of Ti/Sn being 4:1, no Sn^{4+} peaks were observed, indicating the formation of pure rutile-phase TNRs, consistent with earlier studies. As visible in **Figure 3.11(c-d)**, the $BE_{Ti(2p)_{3/2}-O(1s)}$ is nearly 71.1 eV, which is very close to the BE difference between ($BE_{Ti(2p)_{3/2}-O(1s)}$: 71.5 eV) assigned for the TNRs. Whereas $BE_{Ti(2p)_{3/2}-O(1s)}$ of Ti_2O_3 and TiO are approximately ~73.4 eV and ~75.0 eV, respectively, confirming that the structure formed over the c-TiO_2 is purely oxidized rutile TiO_2 and maintains its stoichiometric ratio.

The relative oxygen vacancy concentration was estimated from the deconvoluted O 1s XPS spectra using the ratio of the oxygen-vacancy-associated peak area to the total O 1s peak area. The calculated oxygen vacancy fraction decreased from 17.6% (B-TNRs) to 13.5% (MX-TNRs) after passivation treatment, confirming the effective suppression of oxygen-vacancy-related defect states and supporting the improved charge-transport and photovoltaic performance of the passivated photoanodes.

3.3.6 J-V Analysis

Finally, FTO/c-TiO_2/p-TNRs/N719/ I^-/I_3^- /Carbon-structured DSSC was fabricated in the open environment and tested under typical operational conditions (25 °C, RH = 40%, and standard 1 Sun illumination). The J-V characteristics of the fabricated DSSC and the variations in PCE, FF, J_{SC}, and V_{OC} with respect to the different passivation TNRs are shown in **Figure 3.12(a, c,** and **e)**. Interface engineering between $Ti_3C_2T_X$ MXene sheets and TNRs significantly suppresses charge recombination and enhances electron transport. Owing to its high electrical conductivity, $Ti_3C_2T_X$ forms an efficient conductive pathway with TNRs, enabling rapid extraction and transport of photogenerated electrons injected from the excited dye into the TiO_2 conduction band. The MXene-TNR interface effectively passivates surface trap states, reduces R_{Ct}, and

minimizes e^--h^+ recombination, thereby improving charge collection efficiency and overall DSSC performance.

$Ti_3C_2T_X$-MXene sheets can effectively passivate surface defects on TNRs. These defects, such as oxygen vacancies ($\mathbf{O}_V$) or undercoordinated titanium atoms, act as recombination centers that trap photogenerated electrons and holes. The terminal functional groups on $Ti_3C_2T_X$-MXene (such as -OH, -O, and -F) will form chemical bonds with undercoordinated titanium or $\mathbf{O}_V$ sites on TNRs, passivating surface defects and minimizing recombination. The conductive nature of $Ti_3C_2T_X$-MXene also alters the energy band alignment at the TNR-MXene interface, creating a favorable energy gradient for charge separation. The MXene-TNR interface ensures that photogenerated electrons in TNRs are more efficiently injected into the MXene sheets, where they experience reduced recombination losses due to MXene's high conductivity. Furthermore, the Fermi-level alignment between MXene and TiO_2 results in a built-in electric field at the interface. This field drives the separation of photogenerated charge carriers, thereby further enhancing the efficiency of charge extraction. For certain $Ti_3C_2T_X$-MXenes, their metallic nature and high carrier density can give rise to surface plasmon resonance (SPR) effects, enhancing the local electric field and increasing light absorption near the TNR-MXene interface. MXene sheets also impart improved chemical stability to the TNR photoanodes. The protective layer formed by $Ti_3C_2T_X$-MXene shields the TNRs from photo-corrosion and degradation under operational conditions. This enhanced stability contributes to a longer operational lifetime and sustained performance of the solar device.

The graph shown in **Figure 3.10(c)** depicting photocurrent variation over time for B-TNR, TC-TNR, MX-TNR, TL-TNR, and CB-TNR photoanodes illustrates a clear correlation with the UV-visible absorption data collected on days 1st, 15th, and 30th. Notably, MX-TNRs exhibit the highest photocurrent density of 11.60 mA cm^{-2}, attributed to their superior light absorption and enhanced charge-transport properties, facilitated by MXene passivation. This high photocurrent performance can be linked to the effective light harvesting by the N719 dye, as observed in the initial UV absorption data, which remains stable over 30 days, indicating minimal degradation. The consistent absorption and improved interfacial charge-transfer efficiency due to MXene's conductive properties

ensure sustained photocurrent generation. In contrast, other photoanodes, such as B-TNR and CB-TNR, exhibit lower and more rapidly declining photocurrents, reflecting higher recombination losses, less effective light absorption, and reduced stability over time.

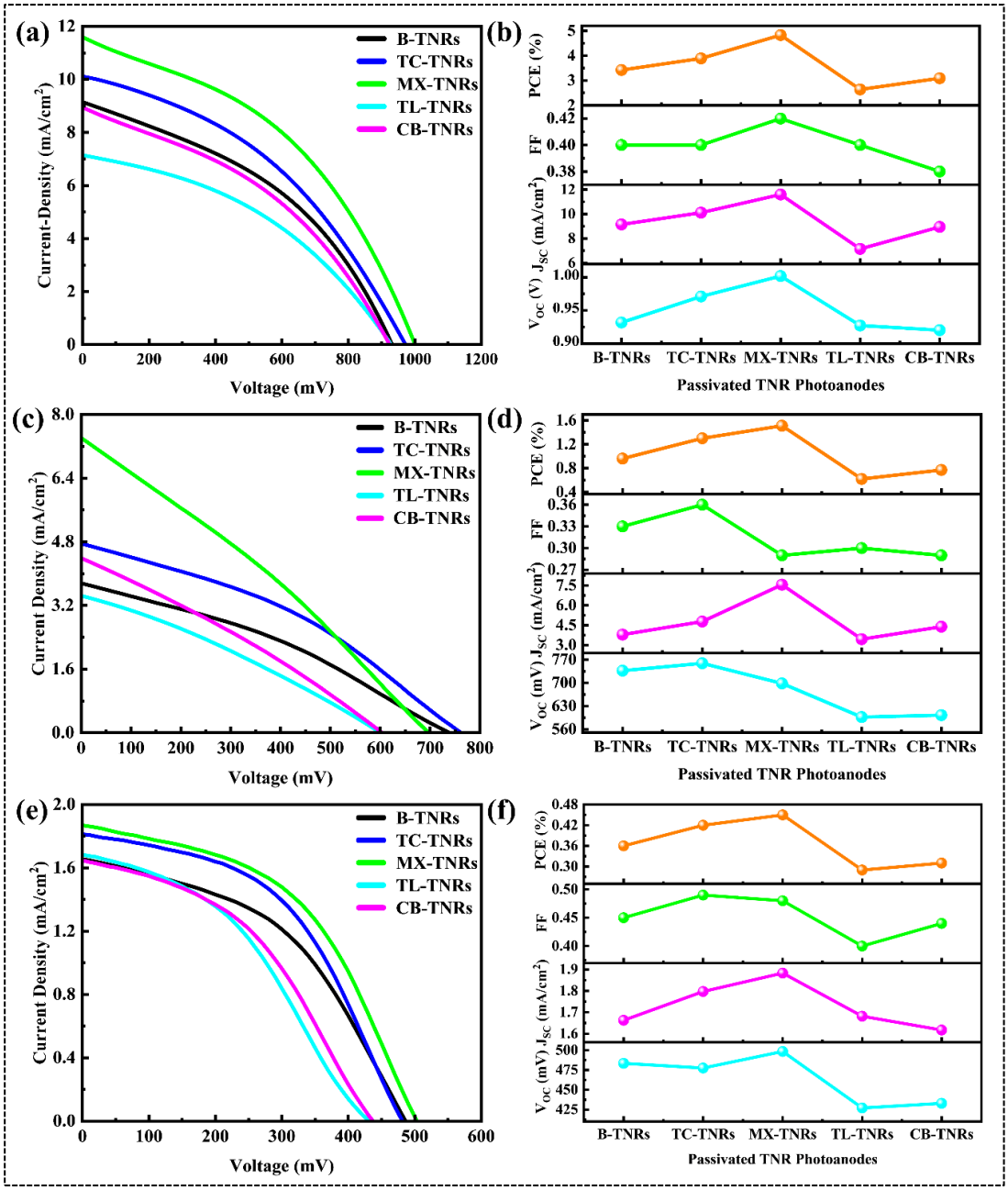

Figure 3.12 J-V analysis of the fabricated FTO/c-TiO_2/TNRs/N719/(I^-/I_3^-)/Carbon-structured DSSC at standard solar irradiance of 100 mW cm^{-2} (AM1.5G), temperature 37

± 6 °C and RH of 47 ± 5%. (a, c, and e) J-V curves were obtained from the DSSC on the 1st day, 15th day, and 30th day, respectively. (b, d, and f) Relative PV parameter variations with respect to the different passivating agents.

The three J-V curves shown in **Figure 3.12(a, c, and e)** are the results of DSSC testing on the very first day, after 15 days, and after 30 days. To test the DSSC device after a specific period, we refilled the I^-/I_3^- electrolyte through the sealant and preserved the DSSC under dark conditions at 25 °C and RH = 40%. Further, the variation in characteristic PV parameters across the various passivated TNRs is shown in **Figure 3.12(b, d, and f)**, which reveals a common trend in the results obtained on the first, 15th, and 30th days. The maximum PCE of 4.83% was obtained on the very first day in the FTO/c-TiO_2/MX-TNRs/N719/I^-/I_3^-/Carbon-structured DSSC device, with V_{OC} approaching ~1V.

Table 3.3 Summary of all the photovoltaic parameters such as V_{OC}, J_{SC}, FF, and PCE obtained from the FTO/c-TiO_2/TNRs/N719/(I^-/I_3^-)/Carbon-structured DSCCs on the 1st, 15th, and 30th day.

Sample Name	Day of Testing	V_{OC} (mV)	J_{SC} (mA cm^{-2})	FF	η (%)
B-TNRs	Day 1	931.720	9.145	0.40	3.42
TC-TNRs		971.090	10.11	0.40	3.89
MX-TNRs		**1001.94**	**11.60**	**0.42**	**4.83**
TL-TNRs		927.200	7.145	0.40	2.64
CB-TNRs		920.180	8.945	0.38	3.09
B-TNRs	Day 15	736.811	3.790	0.33	0.93
TC-TNRs		759.123	4.776	0.36	1.30
MX-TNRs		**698.583**	**7.555**	**0.29**	**1.51**
TL-TNRs		596.915	3.446	0.30	0.62
CB-TNRs		602.634	4.385	0.29	0.77
B-TNRs	Day 30	483.413	1.663	0.45	0.36
TC-TNRs		477.535	1.797	0.49	0.42
MX-TNRs		**498.402**	**1.883**	**0.48**	**0.45**
TL-TNRs		427.098	1.682	0.40	0.29
CB-TNRs		432.858	1.617	0.44	0.31

However, when the same device was tested on the 15th and 30th days, the resulting PCE decreased drastically to 1.51% and 0.45%, respectively, with reduced V_{OC} from ~0.7V to ~0.5V. Also, the J_{SC} for the same DSSC using MX-TNRs changes from 11.6 to 1.88 mA cm^{-2} after 30 days. Similarly, the PCE of FTO/c-TiO_2/B-TNRs/N719/(I^-/I_3^-)/Carbon-structured DSSCs were 3.42% initially, which were reduced to 0.96 and 0.36% after 15 and 30 days, respectively. Between these two DSSCs comprising B- and MX-TNRs, the TC-TNR-based DSSCs also show significant performance enhancements of 14, 35, and 17% on the 1st, 15th, and 30th days of testing, respectively. Although FTO/c-TiO_2/TC-TNRs/N719/(I^-/I_3^-)/Carbon-structured DSSC devices show significant performance improvement compared to the B-TNR-based DSSC, but not as good as the MX-TNR-based DSSCs. On the other hand, DSSCs comprising TNRs passivated with organic agents, such as TL-TNRs and CB-TNRs, exhibit lower PCE than B-TNR-based DSSCs. This drastic reduction in performance may be due to poor dye loading and increased defect states, as the TNRs' thickness and facet sizes have reduced significantly. The number of TNRs per unit area increased significantly after TL- and CB-passivation, leading to higher grain-boundary regions and, consequently, poor performance. To justify the obtained results, we have performed several additional physicochemical characterizations of B- and passivated TNRs, including AFM and EIS, as discussed in more detail. All the characteristic PV parameters obtained for DSSCs with different TNRs as photoanodes on days 1, 15, and 30 were summarized in **Table 3.3**.

The incident photon-to-current efficiency (IPCE) of MX-TNR-based DSSCs, measured on days 1, 15, and 30, exhibits a decreasing trend consistent with the variations observed in J-V performance and UV-visible absorption studies over time. This decline in IPCE highlights the gradual degradation of dye molecules and a possible decrease in overall light-harvesting capability, which affects charge generation and collection, as shown in **Figure 3.13(a)**. The IPCE spectrum of the dye-soaked MX-TNRs clearly shows two prominent humps, corresponding to the MMCT and LLCT absorption peaks of the N719 dye (**Figure 3.10(b)**). These features confirm efficient photon absorption and electron injection processes within the same wavelength range, providing strong evidence of the photoanode's effective interaction with the dye. Thus, the IPCE data validate the UV-visible absorption characteristics and underscore the stability and photoactivity of the

dye-functionalized MX-TNRs over the observed period. A comparative study of TiO_2 and passivated TiO_2 is summarized in **Table 3.4**, along with a detailed comparison with MXene-passivated photoanodes for DSSCs.

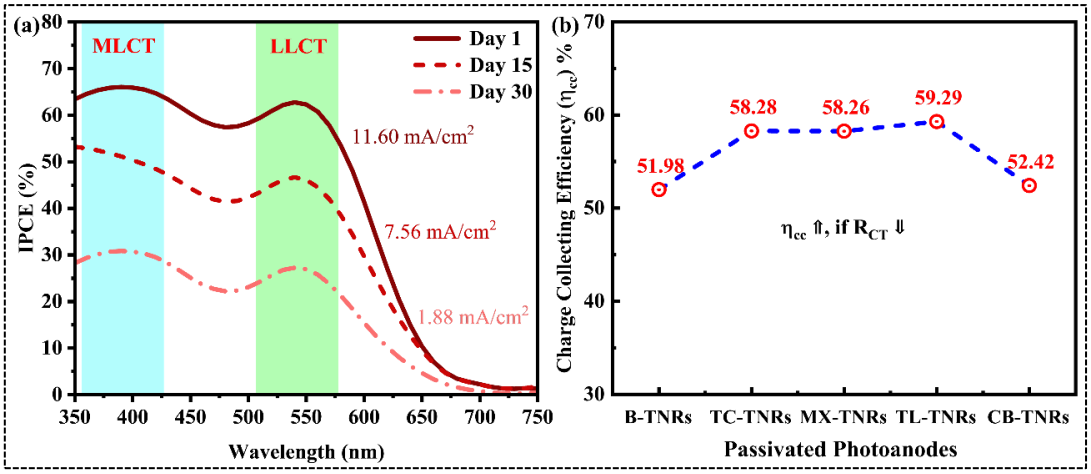

Figure 3.13 (a) IPCE obtained from MX-TNRs-based DSSC on the measurement days 1st, 15th, and 30th, and (b) Calculated charge collection efficiency variation for different passivated photoanode-based DSSC.

Table 3.4 Comparison of different photoanode passivating agents used to date and possible performance enhancement mechanisms in DSSCs.

Sr. No.	PCE (%)		Properties of Passivating Agents Used to Improve the PCE	Ref.
	With TiO_2	With Passivating Agent		
1.	0.32 (J_{SC}=1.95 mA cm^{-2}, V_{OC}=0.52 V, and FF=0.31)	1.68 (J_{SC}=6.67 mA cm^{-2}, V_{OC}=0.56 V, and FF=0.45)	i. GO was prepared from graphite and exfoliated on a single sheet via sonication. ii. 0.01-0.05 mg/ml GO used in TiO_2 suspension.	[55]
2.	4.2 (J_{SC}=10.75 mA cm^{-2},	5.5 (J_{SC}=12.16 mA cm^{-2},	i. GO prepared using the modified Hummers method.	[56]

	V_{OC}=0.68 V, and FF=0.56)	V_{OC}=0.66 V, and FF=0.67)	ii. 0.75 wt% of GO used in TiO_2.	
3.	1.79 (J_{SC}=4.96 mA cm^{-2}, V_{OC}=0.66 V, and FF=0.54)	2.78 (J_{SC}=7.6 mA cm^{-2}, V_{OC}=0.67 V, and FF=0.54)	i. Modified Hummers method for GO preparation. ii. 0.21 wt% GO with TiO_2.	[57]
4.	6.3 (TiO_2 Fibers) (J_{SC}=13.90 mA cm^{-2}, V_{OC}=0.71 V, and FF=0.63)	7.6 (J_{SC}=16.20 mA cm^{-2}, V_{OC}=0.71 V, and FF=0.66)	i. rGO purchased from Sigma Aldrich. ii. Electrospinned TiO_2 fibers-rGO composite in PVP carrier solution.	[58]
5.	6.08 (J_{SC}=14.88 mA cm^{-2}, V_{OC}=0.70 V, and FF=0.57)	8.03 (J_{SC}=17.91 mA cm^{-2}, V_{OC}=0.66 V, and FF=0.67)	i. rGO was prepared using a chemical reduction method. ii. Spin-coated rGO/TiO_2 heterostructure.	[59]
6.	3.42 (J_{SC}=9.145 mA cm^{-2}, V_{OC}=0.93 V, and FF=0.40)	4.83 (J_{SC}=11.60 mA cm^{-2}, V_{OC}=1.0 V, and FF=0.42)	i. $Ti_3C_2T_X$-MXene was prepared via solid state synthesis method. ii. Dip-doated passivation to prepare MX-TNRs.	**This Work**

3.3.7 AFM Analysis

To understand how passivation affects the surface roughness of TNR photoanodes, we probed all passivated TNR photoanodes using atomic force microscopy (AFM), and all characterization was performed in non-contact mode (NCM). In non-contact mode, the AFM tip does not physically contact the sample surface. Instead, it oscillates near the surface at a frequency slightly above its resonance frequency.

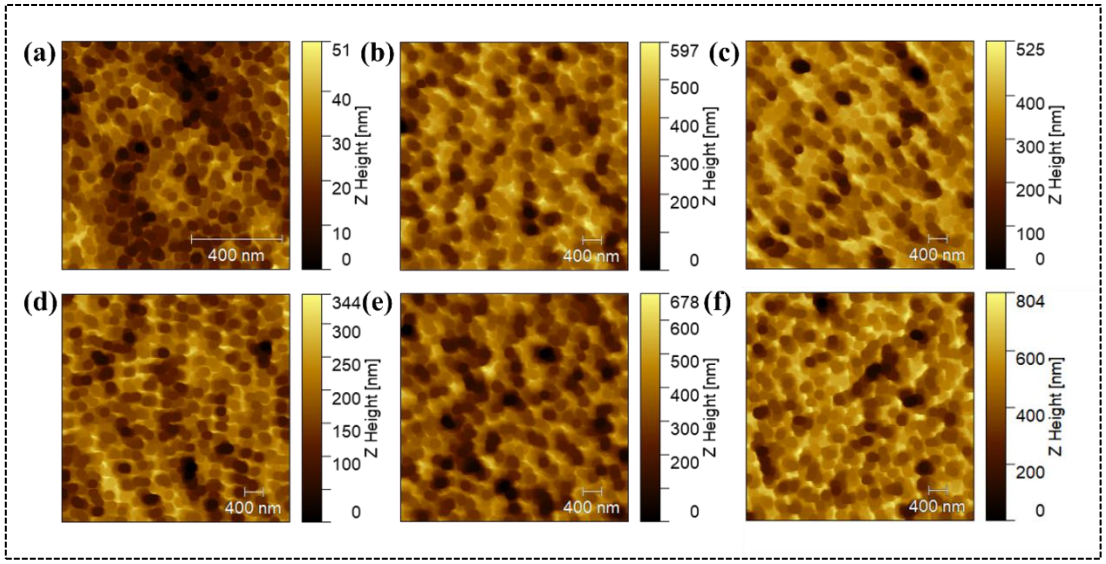

Figure 3.14 Atomic force microscopy (AFM) analysis of (a) c-TiO_2, (b) B-TNR, (c) TC-TNR, (d) MX-TNR, (e) TL-TNR, and (f) CB-TNR photoanodes.

The tip-sample interaction in this mode is dominated by long-range Van Der Waals forces rather than the significant short-range repulsive forces in contact mode. In all three contacts, tapping, and no-contact modes, NCM modes offer several key advantages, including high resolution, non-destructive operation, and minimal tip wear. The high-resolution 2D topographical AFM images of c-TiO_2 and B-TNRs are shown in **Figure 3.14(a-b)**, with root-mean-square roughness ($\mathbf{R}_q$) values of 9.84 and 121.08 nm, respectively. Furthermore, AFM images of passivated photoanodes, such as TC-TNR, MX-TNR, TL-TNR, and CB-TNR, are shown in **Figure 3.14(c- f)**, respectively. After analyzing all these AFM results with XEI data processing and Analysis (Park systems), we estimated the root mean square roughness ($\mathbf{R}_q$), average roughness ($\mathbf{R}_a$), peak-to-valley height ($\mathbf{R}_z$), surface skewness ($\mathbf{R}_{sk}$), and surface kurtosis ($\mathbf{R}_{ku}$) values for all the passivated TNRs, which are reported in **Table 3.5**. From the surface roughness results, it is clear that different passivating agents help achieve a comparatively smoother surface with reduced surface defect states. The minimum $\mathbf{R}_q$, $\mathbf{R}_a$, $\mathbf{R}_z$, $\mathbf{R}_{sk}$, and $\mathbf{R}_{ku}$ values were obtained in MX-TNRs, which showed a maximum efficiency of 4.83% on the 1st day. Moreover, even after 15 and 30 days, FTO/c-TiO_2/MX-TNRs/N719/(I^-/I_3^-)/Carbon-structured DSSCs delivered the maximum PCE of 1.51 and 0.45%.

Table 3.5 Different surface roughness parameters were analyzed using AFM analysis of the passivated TNR photoanodes.

Passivated Photoanodes	R_q (nm)	R_a (nm)	R_z (nm)	R_{sk}	R_{ku}
c-TiO_2	9.84	7.38	86.7	-1.083	5.824
B-TNRs	121.08	96.22	829.9	-0.032	2.93
TC-TNRs	78.89	61.98	653.4	0.342	3.49
MX-TNRs	51.73	41.17	352.7	0.043	2.94
TL-TNRs	124.833	100.67	874.4	0.468	3.123
CB-TNRs	111.31	89.121	737.7	-0.047	2.79

Surface roughness parameters critically influence defect density, charge recombination, and electron transport in DSSCs. High values of $\mathbf{R}_q$ and $\mathbf{R}_a$ indicate pronounced height variations and surface defects, which act as recombination centres and reduce device efficiency. A large $\mathbf{R}_z$ reflects severe surface irregularities that hinder electron transport and compromise structural integrity. The $\mathbf{R}_{sk}$ describes peak-valley asymmetry: positive values indicate sharp, degradation-prone peaks, while negative values indicate valleys that may trap impurities and induce local defects. High $\mathbf{R}_{ku}$ signifies extreme surface features associated with increased defect formation. Overall, lower values of $\mathbf{R}_q$, $\mathbf{R}_a$, $\mathbf{R}_z$, and $\mathbf{R}_{ku}$ are desirable for achieving high photovoltaic performance, as observed for MX-TNRs. Although precise control over $\mathbf{R}_{sk}$ is challenging, it can be moderated through careful optimization of fabrication and surface engineering processes.

3.3.8 EIS Analysis

We performed EIS over a 0.1 Hz to 100 kHz frequency range using a 1 M KOH aqueous electrolyte, which is particularly useful for understanding the role of passivation in DSSCs. The Nyquist plot obtained is shown in **Figure 3.15(a)**, and a magnified view of semicircular arcs in the mean frequency region is shown in the inset. The TNR/electrolyte interfacial electron transport resistance and recombination are attributed to this semicircular arc. Nonetheless, the mechanics of electrolyte diffusion are linear at low frequencies, as shown in the inset of **Figure 3.15(a)**. Finally, the MX-TNRs exhibit the lowest $\mathbf{R}_{Ct}$ of 7.79 Ω-cm^2, indicating a significant decrease in charge trapping and

excellent charge transportation. Consequently, it leads to higher conductivity, showing compatibility with previous findings.

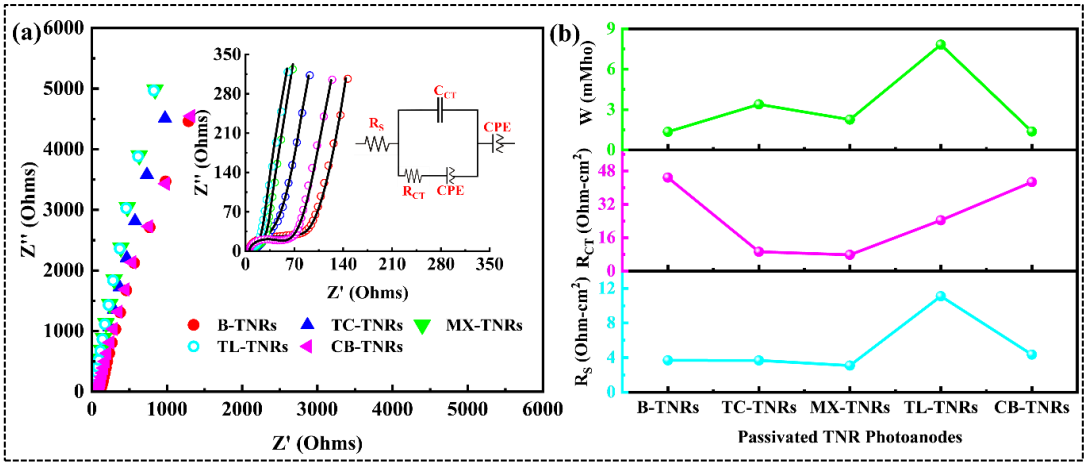

Figure 3.15 (a) EIS analysis of the bare TNR and all other passivated TNRs performed in 1M KOH aqueous electrolyte in the frequency range of 0.1 Hz to 100 kHz. A High-resolution Nyquist plot and equivalent electrical circuit are shown in the inset for passivated TNR photoanodes, (b) Variation of $\mathbf{R}_S$, $\mathbf{R}_{Ct}$, and W with respect to different passivated TNRs, depicting TC and MX as the best-performing passivation agents.

The inset image in **Figure 3.15(a)** depicts an equivalent electrical circuit for bare and passivated TNRs, and the values of the various resistances are given in **Table 3.6**. As mentioned in **Table 3.6**, $\mathbf{R}_S$ significantly decreases with TC and MX passivation from 3.7 to 3.1 Ω-cm^2, indicating that the uncompensated solution and contact resistance of the electrochemical system remain nearly unchanged after passivation treatment. However, $\mathbf{R}_S$ increases when TNRs are passivated with organic agents such as TL and CB, confirming that passivation forms an insulating layer and reduces conductivity. On the other hand, a clear reduction in $\mathbf{R}_{Ct}$ was observed when passivated with TC and MX, from 44.8 to 7.8 Ω-cm^2, but it increased again to 42.7 Ω-cm^2 from 24.3 Ω-cm^2 with TL and CB passivation, respectively. Lower $\mathbf{R}_{Ct}$ values, i.e., successful passivation, often reduce charge transfer resistance by minimizing surface defects and providing better electronic pathways. A lower $\mathbf{R}_{Ct}$ indicates efficient electron injection and reduced recombination. Meanwhile, increased $\mathbf{R}_{Ct}$ might suggest that passivation has introduced barriers to charge transfer or increased surface states that trap electrons.

Charge collection efficiency (CCE) is a vital metric that reflects the efficacy of photogenerated charge carrier collection at the electrodes while minimizing recombination losses. The CCE varies inversely with $\mathbf{R}_{Ct}$. This relationship shows that reducing charge-flow resistance enhances electron transport from the photoanode to the electrode, thereby improving the device's overall performance. In our study, various passivation strategies were employed on TNRs, yielding distinct improvements in CCE: B-TNR (51.98%), TC-TNR (58.28%), MX-TNR (58.26%), TL-TNR (59.29%), and CB-TNR (52.42%) (**Figure 3.13(b)**). These results offer critical insights into how different passivation techniques influence charge carrier dynamics and, consequently, device performance. The bare B-TNR exhibits the lowest CCE of 51.98%, attributed to significant charge recombination at surface and bulk defect sites, which hampers electron extraction. $TiCl_4$ treatment (TC-TNR) enhances the CCE to 58.28% by forming a uniform TiO_2 passivation layer, reducing surface recombination, and improving electron transport. Similarly, $Ti_3C_2T_X$-MXene passivation (MX-TNR) achieves a comparable CCE of 58.26%, leveraging MXene's high conductivity to form a conductive bridge and chemically interact with the TNRs surface, mitigating recombination and stabilizing the electronic structure.

Although TL-TNRs and CB-TNRs exhibit similar CCE, their performance is hindered by significantly higher surface roughness and increased $\mathbf{R}_{Ct}$. The elevated surface roughness in both cases leads to increased scattering of charge carriers, resulting in inefficient electron transport and higher recombination losses. Additionally, the high $\mathbf{R}_{Ct}$ further impedes the flow of charge carriers from the TNRs to the electrode, thereby reducing the overall device efficiency. Consequently, despite similar CCE values, suboptimal surface morphology and charge-transfer dynamics limit the performance of TL-TNRs and CB-TNRs. Further, **Figure 3.15(b)** confirms that, across all bare and passivated photoanodes, TC and MX-TNRs are the best-performing, with the lowest ohmic and charge-transfer resistances.

Table 3.6 All the corresponding EIS circuit parameters for different passivated-TNR photoanodes were studied in 1M KOH electrolyte.

Passivated Photoanodes	R_S (Ω-cm^2)	R_{CT} (Ω-cm^2)	C_{CT} (μF cm^{-2})
B-TNRs	3.686	44.81	85.5
TC-TNRs	3.676	9.26	106.8
MX-TNRs	3.081	7.79	133.1
TL-TNRs	11.1	24.32	74.6
CB-TNRs	4.346	42.66	62.5

Chemical capacitance ($\mathbf{C}_{Ct}$) has mixed effects on DSSCs, which is crucial in understanding the impact of passivation on their performance. A $\mathbf{C}_{Ct}$ relates to the storage of charge at the interface and the material's ability to accommodate electronic states. Higher $\mathbf{C}_{Ct}$ improves the dye's ability to inject electrons into the TNRs and facilitates excellent charge separation, which becomes an essential factor for the enhanced performance of DSSCs. Also, with more charges stored, the effective light-harvesting efficiency might improve overall device performance. However, lower $\mathbf{C}_{Ct}$ values were associated with enhanced stability, as they reduced the number of reactive surface sites that could degrade over time. It also exhibits reduced electron-hole recombination rates, improving the V_{OC} and overall efficiency. Therefore, an optimal balance between high and low $\mathbf{C}_{Ct}$ is often desired. While high $\mathbf{C}_{Ct}$ can enhance charge storage and dye loading, excessively high capacitance might introduce more recombination centers. Conversely, low $\mathbf{C}_{Ct}$ can reduce recombination but might limit charge storage capacity. So, passivation strategies should be tailored to achieve the desired capacitance levels, ensuring that the benefits of increased charge storage and reduced recombination are balanced to maximize device efficiency and stability.

The CPE accounts for the frequency-dependent nature of the interface capacitance, providing a more accurate representation of interfacial processes. The last CPE in the circuit represents the diffusion-related impedance of the redox species in the electrolyte. This element captures the Warburg-like impedance, reflecting the diffusion limitations of the redox couple. The diffusion impedance becomes crucial at lower

frequencies, where ion transport in the electrolyte can limit overall charge regeneration efficiency. Therefore, understanding these parameters is essential for evaluating the impact of passivation in DSSC. Overall, passivated photoanodes exhibit more efficient charge transfer and reduced recombination, driven by the combined effects of surface passivation, improved conductivity, and better interfacial engineering. This leads to higher photocurrent densities, enhanced light-harvesting efficiency, and improved overall PCE in DSSCs.

3.4 Conclusion

In summary, the incorporation of multi-layered $Ti_3C_2T_X$-MXene into DSSCs as an interfacial passivating agent significantly enhances performance, achieving a V_{OC} above 1V with a 7.52% enhancement. Its superior conductivity, high surface area, and effective interfacial engineering improve charge transfer, reduce recombination, and boost PCE by 41.23%, complemented by a 26.85% increment in J_{SC}. Compared to conventional passivation methods such as $TiCl_4$, chlorobenzene, and toluene, MXene offers improved surface uniformity, enhanced dye adsorption, and stronger interaction with electrolytes. $TiCl_4$ smooths TNR surfaces by filling defects, while MXene's conductivity and functional groups improve charge transport. This leads to a 57% reduction in $\mathbf{R}_q$ and 82% in R_{Ct}, highlighting MXene's potential for scalable, high-efficiency DSSC applications.

References

[1] G. Holmes, J. Clemoes, K. Marriot, S. Wynne-Jones, The politics of the rural and relational values: Contested discourses of rural change and landscape futures in west wales, Geoforum. 133 (2022) 153–164. https://doi.org/10.1016/j.geoforum.2022.05.014.

[2] M. Kallio, J.Y. Chen, Energy Security in the EU Solar Energy Strategy, (2023) 83.

[3] A. Srivastava, J.A.K. Satrughna, M.K. Tiwari, A. Kanwade, S.C. Yadav, K. Bala, P.M. Shirage, Lead metal halide perovskite solar cells: Fabrication, advancement strategies, alternatives, and future perspectives, Mater. Today Commun. 35 (2023)

105686. https://doi.org/10.1016/j.mtcomm.2023.105686.

[4] Q. Hassan, S. Algburi, A.Z. Sameen, T.J. Al-Musawi, A.K. Al-Jiboory, H.M. Salman, B.M. Ali, M. Jaszczur, A comprehensive review of international renewable energy growth, Energy Built Environ. (2024). https://doi.org/10.1016/j.enbenv.2023.12.002.

[5] Q. Hassan, P. Viktor, T. J. Al-Musawi, B. Mahmood Ali, S. Algburi, H.M. Alzoubi, A. Khudhair Al-Jiboory, A. Zuhair Sameen, H.M. Salman, M. Jaszczur, The renewable energy role in the global energy Transformations, Renew. Energy Focus. 48 (2024) 100545. https://doi.org/10.1016/j.ref.2024.100545.

[6] A. Srivastava, P.M. Shirage, Overcoming Intrinsic and Extrinsic Challenges in Perovskite Solar Cells: A Pathway Toward Advancement, in: Perovskite Sol. Cells Fundam. Approaches Mater. Process. Sustain. Futur., 1st ed., Springer Singapore, 2024: pp. 55–89. https://doi.org/10.1007/978-981-97-7624-5_2.

[7] A. Srivastava, P.M. Shirage, Possible Perovskite Substitutes, Advances, and Future Prospects, in: Perovskite Sol. Cells Fundam. Approaches Mater. Process. Sustain. Futur., 1st ed., Springer Singapore, 2024: pp. 141–175. https://doi.org/10.1007/978-981-97-7624-5_4.

[8] A. Srivastava, P.M. Shirage, Pioneering the Path: Unveiling Exciting Applications for Integrated Perovskite Solar Cells, in: Perovskite Sol. Cells Fundam. Approaches Mater. Process. Sustain. Futur., 1st ed., Springer Singapore, 2024: pp. 177–203. https://doi.org/10.1007/978-981-97-7624-5_5.

[9] I.C. Emeji, O.M. Ama, U.O. Aigbe, K. Khoele, P.O. Osifo, S.S. Ray, Electrochemical Cells, Eng. Mater. 414 (2020) 65–84. https://doi.org/10.1007/978-3-030-43346-8_4.

[10] X. Xin, M. He, W. Han, J. Jung, Z. Lin, Low-cost copper zinc tin sulfide counter electrodes for high-efficiency dye-sensitized solar cells, Angew. Chemie - Int. Ed. 50 (2011) 11739–11742. https://doi.org/10.1002/anie.201104786.

[11] B. Liu, E.S. Aydil, Growth of oriented single-crystalline rutile TiO_2 nanorods on transparent conducting substrates for dye-sensitized solar cells, J. Am. Chem. Soc. 131 (2009) 3985–3990. https://doi.org/10.1021/ja8078972.

[12] P. V. Kamat, Quantum dot solar cells. Semiconductor nanocrystals as light harvesters, J. Phys. Chem. C. 112 (2008) 18737–18753. https://doi.org/10.1021/jp806791s.

[13] J.B. Baxter, E.S. Aydil, Nanowire-based dye-sensitized solar cells, Appl. Phys. Lett. 86 (2005) 1–3. https://doi.org/10.1063/1.1861510.

[14] J.R. Jennings, A. Ghicov, L.M. Peter, P. Schmuki, A.B. Walker, Dye-sensitized solar cells based on oriented TiO_2 nanotube arrays: Transport, trapping, and transfer of electrons, J. Am. Chem. Soc. 130 (2008) 13364–13372. https://doi.org/10.1021/ja804852z.

[15] A. Srivastava, P.M. Shirage, Operational Stability Management Approaches for Perovskite Solar Cells, in: Perovskite Sol. Cells Fundam. Approaches Mater. Process. Sustain. Futur., 1st ed., Springer Singapore, 2024: pp. 91–139. https://doi.org/10.1007/978-981-97-7624-5_3.

[16] Brian O'Regan & Michael Grätzel, A low-cost, high-efficiency solar cell based on dye-sensitized colloidal TiO_2 films, Nature. 353 (1991) 737–740.

[17] A.S. Teja, A. Srivastava, J.A.K. Satrughna, M.K. Tiwari, A. Kanwade, S. Chand Yadav, P.M. Shirage, Optimal processing methodology for futuristic natural dye-sensitized solar cells and novel applications, Dye. Pigment. 210 (2023) 110997. https://doi.org/10.1016/j.dyepig.2022.110997.

[18] D. Parasuraman, M. Ramakrishnan, A Review on Dye-Sensitized Solar Cells (DSSCs), Materials and Applications, Iran. J. Mater. Sci. Eng. 20 (2023) 1–23. https://doi.org/10.22068/ijmse.2994.

[19] K.T. Asmaa Soheil Najm, Sara Ali Alwash, Noor Humam Sulaiman, M. S. Chowdhury, N719 dye as a sensitizer for dye-sensitized solar cells (DSSCs): A

review of its functions and certain rudimentary principles, Environ. Prog. Sustain. Energy. 42 (2023). https://doi.org/https://doi.org/10.1002/ep.13955.

[20] R. Chauhan, A. Srivastava, P.M. Shirage, K. Bala, Innovating dye-sensitized solar cells through novel microalgal and cyanobacterial species extricated dyes: A sustainable tack for material scarce earth, Sol. Energy. 270 (2024) 112369. https://doi.org/10.1016/j.solener.2024.112369.

[21] S.N. Tamilselvan, S. Shanmugan, Towards sustainable solar cells: unveiling the latest developments in bio-nano materials for enhanced DSSC efficiency, Clean Energy. 8 (2024) 238–257. https://doi.org/10.1093/ce/zkae031.

[22] William Shockley; Hans J. Queisser, Detailed Balance Limit of Efficiency of p-n Junction Solar Cells, J. Appl. Phys. 32 (1961) 510–519. https://doi.org/https://doi.org/10.1063/1.1736034.

[23] U. Mahajan, A. Srivastava, M. Dhonde, K. Sahu, P. Ghosh, P.M. Shirage, Zinc-modified barium stannate micro-rods: Investigating structural, morphological, and optical features, Chem. Phys. Impact. 8 (2024) 100622. https://doi.org/10.1016/j.chphi.2024.100622.

[24] F. Babar, U. Mehmood, H. Asghar, M.H. Mehdi, A.U.H. Khan, H. Khalid, N. ul Huda, Z. Fatima, Nanostructured photoanode materials and their deposition methods for efficient and economical third generation dye-sensitized solar cells: A comprehensive review, Renew. Sustain. Energy Rev. 129 (2020) 109919. https://doi.org/10.1016/j.rser.2020.109919.

[25] A. Surya Teja, Abhishek Srivastava, Jena Akash Kumar Satrughna, Manish Kumar Tiwari, Archana Kanwade, Hyunju Lee, Atsushi Ogura, Parasharam M. Shirage, Synergistic co-sensitization of environment-friendly chlorophyll and anthocyanin-based natural dye-sensitized solar cells: An effective approach towards enhanced efficiency and stability, Sol. Energy. 261 (2023) 112–124. https://doi.org/https://doi.org/10.1016/j.solener.2023.06.004.

[26] A. Srivastava, B.S. Chauhan, S.C. Yadav, M.K. Tiwari, J.A.K. Satrughna, A.

Kanwade, K. Bala, P.M. Shirage, Performance of dye-sensitized solar cells by utilizing Codiaeum Variegatum Leaf and Delonix Regia Flower as natural sensitizers, Chem. Phys. Lett. 807 (2022) 140087. https://doi.org/10.1016/j.cplett.2022.140087.

[27] A. Srivastava, J.A.K. Satrughna, M.K. Tiwari, A. Kanwade, S.C. Yadav, K. Bala, P.M. Shirage, Effect of $Ti_{1-x}Fe_xO_2$ photoanodes on the performance of dye-sensitized solar cells utilizing natural betalain pigments extracted from Beta vulgaris (BV), Energy Adv. 2 (2023) 148–160. https://doi.org/10.1039/d2ya00197g.

[28] C.S. Lee, J.K. Kim, J.Y. Lim, J.H. Kim, One-step process for the synthesis and deposition of anatase, two-dimensional, disk-shaped TiO_2 for dye-sensitized solar cells, ACS Appl. Mater. Interfaces. 6 (2014) 20842–20850. https://doi.org/10.1021/am505217k.

[29] S.M. Amir-Al Zumahi, N. Arobi, M. Mahbubur Rahman, M. Kamal Hossain, M. Ara Jahan Rozy, M.S. Bashar, A. Amri, H. Kabir, M. Abul Hossain, F. Ahmed, Understanding the optical behaviours and the power conversion efficiency of novel organic dye and nanostructured TiO_2 based integrated DSSCs, Sol. Energy. 225 (2021) 129–147. https://doi.org/10.1016/j.solener.2021.07.024.

[30] V. Madurai Ramakrishnan, M. Natarajan, S. Pitchaiya, A. Santhanam, D. Velauthapillai, A. Pugazhendhi, Microwave assisted solvothermal synthesis of quasi cubic F doped TiO_2 nanostructures and its performance as dye sensitized solar cell photoanode, Int. J. Energy Res. 45 (2021) 17259–17268. https://doi.org/10.1002/er.5882.

[31] H. Sayahi, K. Aghapoor, F. Mohsenzadeh, M. Mohebi Morad, H.R. Darabi, TiO_2 nanorods integrated with titania nanoparticles: Large specific surface area 1D nanostructures for improved efficiency of dye-sensitized solar cells (DSSCs), Sol. Energy. 215 (2021) 311–320. https://doi.org/10.1016/j.solener.2020.12.060.

[32] M. Freitag, J. Teuscher, Y. Saygili, X. Zhang, F. Giordano, P. Liska, J. Hua, S.M.

Zakeeruddin, J.E. Moser, M. Grätzel, A. Hagfeldt, Dye-sensitized solar cells for efficient power generation under ambient lighting, Nat. Photonics. 11 (2017) 372–378. https://doi.org/10.1038/nphoton.2017.60.

[33] X. Liu, B. Li, M. Han, X. Zhang, J. Chen, S. Dai, Research Progress of Self-assembled Hole-transporting Monolayers in Inverted Perovskite Solar Cells, Acta Chim. Sin. 82 (2024) 348–366. https://doi.org/10.6023/A24010026.

[34] T.R. Naveen Kumar, S. Yuvaraj, P. Kavitha, V. Sudhakar, K. Krishnamoorthy, B. Neppolian, Aromatic amine passivated TiO_2 for dye-sensitized solar cells (DSSC) with ~9.8% efficiency, Sol. Energy. 201 (2020) 965–971. https://doi.org/10.1016/j.solener.2020.03.077.

[35] D.F.S.L. Rodrigues, F. Santos, C.M.R. Abreu, J.F.J. Coelho, A.C. Serra, D. Ivanou, A. Mendes, Passivation of the TiO_2 Surface and Promotion of N719 Dye Anchoring with Poly(4-vinylpyridine) for Efficient and Stable Dye-Sensitized Solar Cells, ACS Sustain. Chem. Eng. 9 (2021) 5981–5990. https://doi.org/10.1021/acssuschemeng.1c00842.

[36] U. Mahajan, K. Prajapat, K. Sahu, P. Ghosh, P.M. Shirage, M. Dhonde, Unveiling the impact of $TiCl_4$ surface passivation on dye-sensitized solar cells: enhancing charge transfer kinetics and power conversion efficiency, J. Mater. Sci. Mater. Electron. 34 (2023) 1–11. https://doi.org/10.1007/s10854-023-11555-8.

[37] N.F. M. Sharif, S. Shafie, M.Z.A. Ab. Kadir, W.Z.W. Hasan, M.N. Mustafa, B. Samaila, The effect of titanium (IV) chloride surface treatment to enhance charge transport and performance of dye-sensitized solar cell, Results Phys. 15 (2019) 1–7. https://doi.org/10.1016/j.rinp.2019.102725.

[38] S.G. Adhikari, A. Shamsaldeen, G.G. Andersson, The effect of TiCl4 treatment on the performance of dye-sensitized solar cells, J. Chem. Phys. 151 (2019). https://doi.org/10.1063/1.5125996.

[39] A.P. Amalathas, L. Landová, T. Huminiuc, L. Horák, B. Conrad, T. Polcar, J. Holovský, Elucidating the role of $TiCl_4$ post-treatment on percolation of TiO_2

electron transport layer in perovskite solar cells, J. Phys. D. Appl. Phys. 53 (2020). https://doi.org/10.1088/1361-6463/ab938c.

[40] Z. Wu, Y. Wang, L. Li, R. Zhang, J. Hong, R. Huang, L. Che, G. Yang, H. Rao, Z. Pan, X. Zhong, Improving the Electron Transport Performance of TiO_2 Film by Regulating $TiCl_4$ Post-Treatment for High-Efficiency Carbon-Based Perovskite Solar Cells, Small. 19 (2023) 1–9. https://doi.org/10.1002/smll.202300690.

[41] M.N.E. Alam, M.A. Islam, Y.B. Kar, Anti-solvent materials enhanced structural and optical properties on ambiently fabricated perovskite thin films, Sci. Rep. 14 (2024) 19995. https://doi.org/10.1038/s41598-024-70344-3.

[42] S. Hyun, I. Su, J. Woong, Green solvent engineering for environment-friendly fabrication of high-performance perovskite solar cells, Chem. Eng. J. 425 (2021) 131475. https://doi.org/10.1016/j.cej.2021.131475.

[43] D. Gedamu, I.M. Asuo, D. Benetti, M. Basti, I. Ka, S.G. Cloutier, F. Rosei, R. Nechache, Solvent-Antisolvent Ambient Processed Large Grain Size Perovskite Thin Films for High- Performance Solar Cells, Sci. Rep. 8 (2018) 12885. https://doi.org/10.1038/s41598-018-31184-0.

[44] S. Zhang, L. Ye, H. Zhang, J. Hou, Green-solvent-processable organic solar cells, Biochem. Pharmacol. 19 (2016) 533–543. https://doi.org/10.1016/j.mattod.2016.02.019.

[45] S. Tian, J. Li, S. Li, T. Bu, Y. Mo, S. Wang, W. Li, A facile green solvent engineering for up-scaling perovskite solar cell modules, Sol. Energy. 183 (2019) 386–391. https://doi.org/10.1016/j.solener.2019.03.038.

[46] M.Y. Song, K.N. Chaudhari, J. Park, D.S. Yang, J.H. Kim, M.S. Kim, K. Lim, J. Ko, J.S. Yu, High efficient Pt counter electrode prepared by homogeneous deposition method for dye-sensitized solar cell, Appl. Energy. 100 (2012) 132–137. https://doi.org/10.1016/j.apenergy.2012.06.017.

[47] C.C. Yang, H.Q. Zhang, Y.R. Zheng, DSSC with a novel Pt counter electrodes

using pulsed electroplating techniques, Curr. Appl. Phys. 11 (2011) S147–S153. https://doi.org/10.1016/j.cap.2010.11.012.

[48] C.H. Yoon, R. Vittal, J. Lee, W.S. Chae, K.J. Kim, Enhanced performance of a dye-sensitized solar cell with an electrodeposited-platinum counter electrode, Electrochim. Acta. 53 (2008) 2890–2896. https://doi.org/10.1016/j.electacta.2007.10.074.

[49] R. Bajpai, S. Roy, P. Kumar, P. Bajpai, N. Kulshrestha, J. Rafiee, N. Koratkar, D.S. Misra, Graphene supported platinum nanoparticle counter-electrode for enhanced performance of dye-sensitized solar cells, ACS Appl. Mater. Interfaces. 3 (2011) 3884–3889. https://doi.org/10.1021/am200721x.

[50] S.P.S. Porto, P.A. Fleury, T.C. Damen, Raman spectra of TiO_2, MgF_2, ZnF_2, FeF_2, and MnF_2, Phys. Rev. 154 (1967) 522–526. https://doi.org/10.1103/PhysRev.154.522.

[51] T. Mazza, E. Barborini, P. Piseri, P. Milani, D. Cattaneo, A. Li Bassi, C.E. Bottani, C. Ducati, Raman spectroscopy characterization of TiO_2 rutile nanocrystals, Phys. Rev. B - Condens. Matter Mater. Phys. 75 (2007) 1–5. https://doi.org/10.1103/PhysRevB.75.045416.

[52] G.A. Samara, P.S. Peercy, Pressure and temperature dependence of the static dielectric constants and raman spectra of TiO_2 (Rutile), Phys. Rev. B. 7 (1973) 1131–1148. https://doi.org/10.1103/PhysRevB.7.1131.

[53] O. Frank, M. Zukalova, B. Laskova, J. Kürti, J. Koltai, L. Kavan, Raman spectra of titanium dioxide (anatase, rutile) with identified oxygen isotopes (16, 17, 18), Phys. Chem. Chem. Phys. 14 (2012) 14567–14572. https://doi.org/10.1039/c2cp42763j.

[54] J.H. Nicola, C.A. Brunharoto, M. Abramovich, C.E.T. Conçalves da Silva, Second order Raman spectrum of rutile TiO_2, J. Raman Spectrosc. 8 (1979) 32–34. https://doi.org/10.1002/jrs.1250080108.

[55] Y.B. Tang, C.S. Lee, J. Xu, Z.T. Liu, Z.H. Chen, Z. He, Y.L. Cao, G. Yuan, H. Song, L. Chen, L. Luo, H.M. Cheng, W.J. Zhang, I. Bello, S.T. Lee, Incorporation of graphenes in nanostructured TiO_2 films via molecular grafting for dye-sensitized solar cell application, ACS Nano. 4 (2010) 3482–3488. https://doi.org/10.1021/nn100449w.

[56] W. Shu, Y. Liu, Z. Peng, K. Chen, C. Zhang, W. Chen, Synthesis and photovoltaic performance of reduced graphene oxide-TiO_2 nanoparticles composites by solvothermal method, J. Alloys Compd. 563 (2013) 229–233. https://doi.org/10.1016/j.jallcom.2013.02.086.

[57] H. Wang, S.L. Leonard, Y.H. Hu, Promoting Effect of Graphene on Dye-Sensitized Solar Cells, Ind. Eng. Chem. Res. 51 (2012) 10613–10620.

[58] A. Anish Madhavan, S. Kalluri, D.K. Chacko, T.A. Arun, S. Nagarajan, K.R.V. Subramanian, A. Sreekumaran Nair, S. V. Nair, A. Balakrishnan, Electrical and optical properties of electrospun TiO_2-graphene composite nanofibers and its application as DSSC photo-anodes, RSC Adv. 2 (2012) 13032–13037. https://doi.org/10.1039/c2ra22091a.

[59] S. Bhand, P.K. Jha, N. Ballav, Unusual enhancement in efficiency of DSSCs upon modifying photoanodes with reduced graphene oxide, RSC Adv. 12 (2022) 30041–30044. https://doi.org/10.1039/d2ra05375f.

Chapter 4

$Ti_{1-x}Fe_xO_{2-\delta}$ Photoanodes for Natural Dye-Sensitized Solar Cells

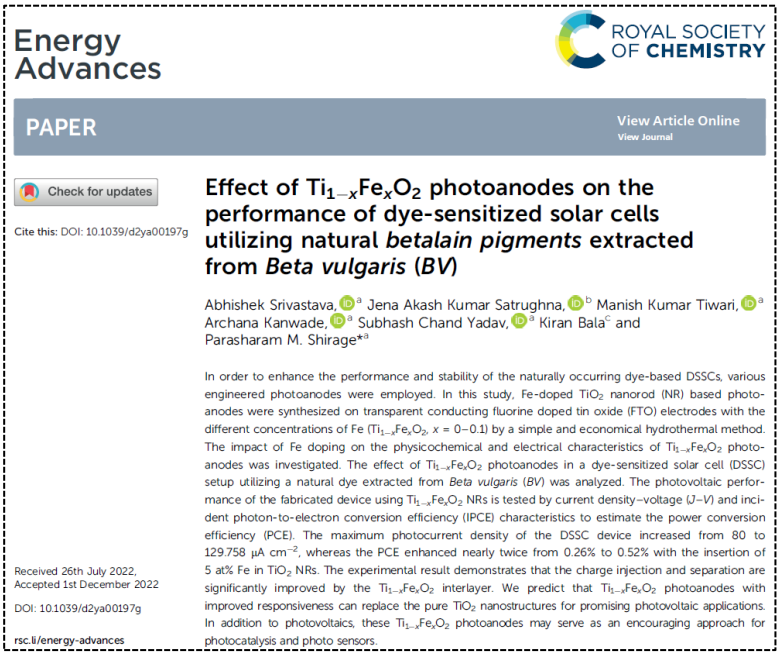

Energy Advances

ROYAL SOCIETY OF CHEMISTRY

PAPER

View Article Online
View Journal

Check for updates

Cite this: DOI: 10.1039/d2ya00197g

Effect of $Ti_{1-x}Fe_xO_2$ photoanodes on the performance of dye-sensitized solar cells utilizing natural *betalain pigments* extracted from *Beta vulgaris* (*BV*)

Abhishek Srivastava,[a] Jena Akash Kumar Satrughna,[b] Manish Kumar Tiwari,[a] Archana Kanwade,[a] Subhash Chand Yadav,[a] Kiran Bala[c] and Parasharam M. Shirage*[a]

In order to enhance the performance and stability of the naturally occurring dye-based DSSCs, various engineered photoanodes were employed. In this study, Fe-doped TiO_2 nanorod (NR) based photoanodes were synthesized on transparent conducting fluorine doped tin oxide (FTO) electrodes with the different concentrations of Fe ($Ti_{1-x}Fe_xO_2$, x = 0–0.1) by a simple and economical hydrothermal method. The impact of Fe doping on the physicochemical and electrical characteristics of $Ti_{1-x}Fe_xO_2$ photoanodes was investigated. The effect of $Ti_{1-x}Fe_xO_2$ photoanodes in a dye-sensitized solar cell (DSSC) setup utilizing a natural dye extracted from *Beta vulgaris* (*BV*) was analyzed. The photovoltaic performance of the fabricated device using $Ti_{1-x}Fe_xO_2$ NRs is tested by current density–voltage (J–V) and incident photon-to-electron conversion efficiency (IPCE) characteristics to estimate the power conversion efficiency (PCE). The maximum photocurrent density of the DSSC device increased from 80 to 129.758 μA cm^{-2}, whereas the PCE enhanced nearly twice from 0.26% to 0.52% with the insertion of 5 at% Fe in TiO_2 NRs. The experimental result demonstrates that the charge injection and separation are significantly improved by the $Ti_{1-x}Fe_xO_2$ interlayer. We predict that $Ti_{1-x}Fe_xO_2$ photoanodes with improved responsiveness can replace the pure TiO_2 nanostructures for promising photovoltaic applications. In addition to photovoltaics, these $Ti_{1-x}Fe_xO_2$ photoanodes may serve as an encouraging approach for photocatalysis and photo sensors.

Received 26th July 2022,
Accepted 1st December 2022

DOI: 10.1039/d2ya00197g

rsc.li/energy-advances

This chapter replaces the synthetic N719 dye with eco-friendly beetroot-derived dye and employs Fe-doped TiO_2 nanorod photoanodes to enhance performance. Optimal 5 at% Fe doping nearly doubles the PCE (0.26% to 0.52%) by improving charge injection and transport, highlighting its potential for sustainable photovoltaic and photosensing applications.

4.1 Introduction

In 1991, the first DSSC was developed by O'Regan and Gratzel at UC Berkeley, and since then, intensive research has been conducted to improve the device's performance.[1] It also grabs the researcher's attention because of its low production cost and very low environmental and health impact. Production of DSSCs is very fast, easy, and economical compared to other emerging and conventional photovoltaics, and their performance has exceeded 14%.[2] Moreover, DSSCs based on natural dyes, such as extracts from leaves, flowers, and fruit peels, are also attracting researchers' attention. However, the performance of such DSSCs is directly influenced by charge collection efficiency, photo-scattering, and recombination rates.[3,4] Apart from this, the effective operation of natural dye-based DSSCs is still under investigation and is lower than that of conventional photovoltaic technologies, such as silicon solar cells, which hinders their wide application. To achieve higher PCE, the design of photoanodes with optimal dye loading, improved sunlight scattering, efficient charge-carrier transport, and reduced charge-carrier recombination is crucial.[5] Generally, metal oxides are preferred for the photoanodes, and mesoporous nanostructures of TiO_2, ZnO, SnO_2, Nb_2O_5, etc., are widely investigated.[6–8] Among metal oxide-based photoanodes, TiO_2 has gained the most popularity because of its high surface area, greater chemical stability, lower toxicity, a significantly higher catalyst band edge, and very low charge recombination. Superior photo-charge separation and transport in the photoanode; the interface between the photoanode and electrolyte is important for device performance, which is substantially morphology- and structure-dependent. In contrast, due to the availability of large surface sites in the mesoporous structures, the recombination rate shoots up.[9] To overcome this, 1D nanostructures such as nanowires,[10] nanorods,[11] and nanotubes[12] have been explored for photoanodes, effectively shortening the charge-transport path. Previous studies have suggested that transition-metal doping alters electronic properties, provides structural stability, and tunes light absorption.[13–16]

In most previously reported works on BV-dye-based DSSCs, photoanode structures were examined to investigate device performance and stability. Although many nanostructured photoanodes were investigated, they were unable to significantly enhance

DSSC performance due to insufficient charge-collection efficiency, low photo-scattering, and increased interfacial charge recombination. Therefore, in addition to nanostructure dimensions, doping is an interesting approach to tune the absorption edge in the visible spectrum, thereby improving photo-charge scattering and collection and reducing recombination rates. Here, the absorption-edge tuning is driven by charge-carrier transitions between the d electrons of the doped transition metal (Fe^{3+}) and the TiO_2 NRs.[17] A new electron state is created within the TiO_2 electronic structure due to Fe doping, thereby reducing charge recombination by capturing photo-generated electrons in the TiO_2 valence band.[18,19] Fe(III) doping in TiO_2 photoanodes is an attractive perspective since: (i) Fe^{3+} doping will empower the TiO_2 crystal structure and comfortably accommodate within the TiO_2 lattice because of nearly similar ionic radii,[20] (ii) Fe^{3+} doped TiO_2 will also assist the improved interfacial charge transportation mediated by shallow charge trapping site originated at deep inside and on the surface of the grown nanostructures as well,[21,22] Fe^{3+} doping will also allow photonic excitation with low energy level because of new energy state formation in the TiO_2 bandgap,[23] (iv) Surface adsorption is also improved by Fe^{3+} doping and gives rise to surface hydroxyl groups and OH^- radicals which is ascribed to the extra oxygen vacancy within the lattice and on the surface.[24]

In general, the valence band (VB) of TiO_2 is composed of hybrid O(2p) and Ti(3d) orbitals, while the conduction band (CB) consists of Ti(3d) orbitals, and transition metal doping will significantly alter the electronic and optical properties. Metal ion dopants can change TiO_2 electron transport characteristics, enhance the separation of photo-generated charge carriers, and shift the absorption edge of the material to the visible spectrum. More carriers can move to the surface because the dopant energy level, which lies beneath the CB of TiO_2, acts as an electron or hole entrapment. The absorption spectra of TiO_2 shift to higher wavelengths upon transition-metal doping, which alters the material's electronic energy levels and narrows the band gap.[25]

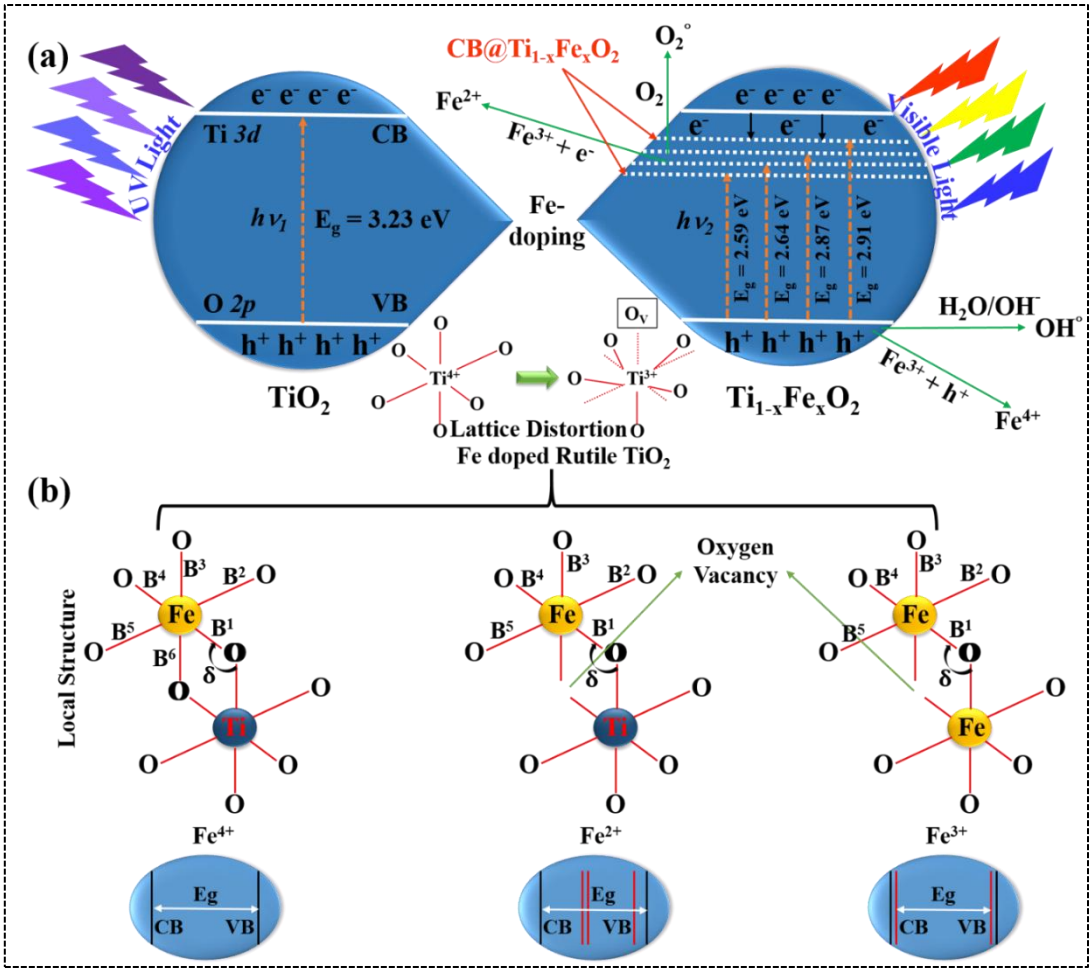

Figure 4.1 (a) The process of charge transport involving elevated electrons and VBs of the TiO_2 nanorods with Fe^{3+} ions of $Ti_{1-x}Fe_xO_2$ (x=0-0.1), and (b) Schematics of the local topologies of Fe-dopants in the different Fe^{4+}, Fe^{2+}, and Fe^{3+} doped TiO_2 models, respectively. B^{1-6} are the bond lengths of Fe-O bonds, and the bond angle between Fe-O-Ti and Fe-O-Fe is denoted by δ.

Figure 4.1(a) illustrates the typical charge transport reactions involved in Fe-doped TiO_2 photo anodes for DSSC applications. Additionally, Fe^{3+} ions in TiO_2 can serve as electron and hole trapping centers, preventing electron-hole recombination and increasing the production of reactive oxygen species. This led to the absorption red shift and therefore enhances photovoltaic activity. When the doping concentration is raised to 5 mM, the bandgap decreases for two reasons. The first step is the doping of TiO_2 with Fe^{3+}, which produces surface states and oxygen-vacancy sites. The second aspect is the crystallization of hematite (Fe_2O_3), whose particles have a narrower energy band gap than

TiO_2, and the reduction of the band gap by forming a heterojunction between Fe_2O_3 and TiO_2.[26] This will further increase visible light absorption. According to the mechanistic theory, electrons produced upon light absorption are confined in the Ti^{3+} state below the conduction band minimum, making it easier to separate charges at a heterojunction. With the synthesis of Ti-O_2^- and its subsequent binding as peroxide, those trapped electrons are relocated to O_2 species. During the chemical pathway, surface Fe^{3+} sites stabilize -OH via hydrogen bonding. Even at higher Fe concentrations, the crystal structure of $Ti_{1-x}Fe_xO_2$ is not dramatically affected, but the local structure around the Fe atoms can be severely deformed, particularly when oxygen vacancies are present.[27]

Figure 4.1(b) presents three distinct Fe dopant models to explain the $Fe^{2+/3+/4+}$ oxidation states in the rutile TiO_2 lattice. It is found from the literature that the configuration of Fe^{3+} is the most stable energy structure in which two adjacent Ti-atoms are replaced by Fe, and will create an O-vacancy in between. As a result, Fe doping introduces mid-gap states, drastically reducing the band gap. In all the possible arrangements of the Fe dopants, the most stable structure prefers an antiferromagnetic ordering. Moreover, the formation of a hybrid Fe-TiO_2 crystal comprising hematite and rutile phases is energetically unfavorable under all the mechanisms discussed herein. It can therefore be inferred that the spontaneous formation of pure metal oxides is unlikely under an oxygen-rich environment. Nevertheless, predicting the feasibility of synthesizing such mixed-phase structures remains challenging.[28]

Li *et al.*[29] conducted a detailed atomistic investigation and concluded that, for Fe^{4+} doping, the formation energy was 1.23 eV per Fe atom, which decreased with increasing Fe concentration. One O-atom acts as a bridge between two Fe dopants in the lowest energy form. With the lowest formation energy of approximately 3 eV per Fe, the integration of Fe^{2+} into the TiO_2 matrix is even less stable. In this case, Fe prefers to be integrated into the TiO_2 crystal lattice adjacent to the O vacancy. The most likely Ti substituent in the rutile phase is Fe^{3+}, with a formation energy of roughly 1 eV per Fe-atom. Similar to Fe^{2+}, the lowest-energy arrangement in this instance has two nearest neighbours, both Fe substituents, situated close to the O-vacancy.

The lattice angles are essentially unaltered in either situation. But the neighbourhood architecture near the Fe dopants might change considerably. The most noticeable structural modification is the expansion of the Fe-O-Ti or Fe-O-Fe bond angle (δ), which is a frequent outcome when an O-vacancy is present. B^2 and B^5 (apex) Ti-O bond lengths are varied from B^1, B^3, B^4, and B^6 (basal). The Fe-O bond lengths B^2 and B^5 increase for Fe-interstitial doping, whereas the basal ones decrease. Due to the induced O-vacancy, the dopant atom only forms bonds with five O-atoms in the Fe^{2+} and Fe^{3+} models. It's crucial to remember that the O-vacancy tends to pop up near the Fe-octahedron's basal plane. Only B^2 and B^5 of these five Fe-O bond lengths remain comparable to one another, with the other three turning inequivalent. These findings demonstrate that the O-vacancy distorts the TiO_6 octahedral more significantly than the dopant atom alone.[29]

The first DSSC was fabricated using a platinum (Pt) counter electrode (CE) and nano-crystalline TiO_2 as the photoanode, achieving a PCE of 7.9%. Rawling *et al.*[30] fabricated a DSSC using a Ruthenium-Based Dye (N719) and reported a PCE of ~12%. In 2011, Lin and his group reported 12.3% PCE with a DSSC using a cobalt (II/III)-based electrolyte, a Pt-CE, and TiO_2 as the photoanode. However, the corrosive nature of Pt by electrolytes having I^-/I_3^- ions and the very high price hinder its applicability.[31] Record 14.2% PCE is achieved with a novel Thieno[3,2-b]indole-type organic dye having a suitable porphyrin sensitizer, whereas the used redox electrolyte is $[Co(bpy)_3]^{2+/3+}$.[32] To add a modified layer over the FTO, advanced coating techniques such as Chemical vapor deposition,[33] sputtering,[34] spray pyrolysis,[35] and dip coating[36] are preferred.

In this work, we preferred an easy, cost-effective spin-coating deposition method to make DSSCs more affordable and efficient. An ideal dye for DSSC will have a broad light-absorption range, a large number of oxygen functional groups, a high molar extinction coefficient, and be highly stable. Also, for effective photo-electron injection, the energy levels of the dyes should align with the conduction band of the photo-anode.[37–39] However, disadvantages associated with the inorganic dyes, such as low capacitance, hazardous nature, and long extraction process, hinder their applicability.[40]

To overcome this, natural dyes are generally preferred for their cost-effectiveness, ease of biodegradation, and wide availability. Natural dyes are generally extracted from the various parts of plants, such as fruits, flower petals, peels, and leaves.[41] Continuous progress in the field of natural and metal complex dye-based DSSCs has revealed a significant performance of ~ 0.1-10.3%.[42–44] The most common pigments that are found in these dyes are (i) betalains, (ii) flavonoids, (iii) chlorophyll, and (iv) carotenoids. DSSCs support the development of high-conversion-efficiency, low-cost photovoltaic components for a system that converts pure and non-conventional solar radiation into electricity. When assessing DSSC performance, the role of the dyes as sensitizers is crucial. Due to their low cost, high availability, and biodegradability, natural dyes (organic dyes) have become a worthwhile alternative to the typical and expensive inorganic sensitizers.

Herein, we used betalain pigments as a natural photosensitizer to investigate DSSCs. The group of red-violet (betacyanins) and yellow (betaxanthins) pigments known as betalains is found within the Caryophyllales plants. Red beetroot is one of the propitious sources of the betalain pigments, which belong to the subfamily Betoideae of the family Amaranthaceae. Red beetroots altogether restrain two major soluble pigments, betanin (red) and vulgaxanthine I (yellow). Depending on the cultivar, red beetroots contain betacyanin and betaxanthin at 0.04-0.21% and 0.02-0.14%, respectively. To avoid degradation, we immediately used the extracted dyes and kept them at 4 °C throughout the dye-loading process. In addition to the non-toxicity, low cost, and ease of synthesis of TiO_2 photoanodes, we aimed to develop a very economical, efficient, and stable DSSC utilizing BV dyes and $Ti_{1-x}Fe_xO_2$ photoanodes. After carefully investigating the properties of hydrothermally grown novel $Ti_{1-x}Fe_xO_2$ nanobrushes, this study aims to reveal the performance enhancement of the DSSC utilizing natural betalain pigments extracted from BV.

4.2 Experimental Section

4.2.1 Materials

Transparent and conducting fluorine doped tin oxide (FTO) (Sigma Aldrich), $Ti(acac)_2OiPr_2$ (75%in Isopropanol, Sigma Adrich), 1-butanol (≥ 99.4%, Sigma Aldrich), $Ti(OBu)_4$ (≥ 97%, Sigma Aldrich), Iron nitrate nano-hydrate (≥ 98%, Sigma Aldrich), DI water, Beta Vulgaris Dye, HCl (35% w/w), Ethylene Glycol (≥ 99%, Sigma Aldrich), Ethanol (Sigma Aldrich), Ni-based CE, KI (≥ 99%, Sigma Aldrich), and I_2 (≥99.8%, Sigma Aldrich). All chemical compounds were used as purchased without further purification.

4.2.2 DSSC Fabrication

The fabricated bare and Fe-doped TiO_2 photo-anodes (as discussed in **Chapter 2**) and Nickel (Ni) CE were sandwiched together to form a DSSC module. All the photo-anodes were dipped overnight in the red BV extract for dye sensitization, and a slight colour change from milky white to reddish was observed. Ni-foam was pressed under hydraulic pressure, sonicated in DI water for 5 minutes, and then dried in air at room temperature. DSSC is assembled with the dye-sensitized photoanode and Ni-CE on top of each other, so that only the coated part of the substrates is covered with the CE. So that there will be some space left for the outer circuit connection. Between the photoanode and Ni-CE, two drops of the prepared electrolyte were added. This assembly of the photoanode and CE was held in place by two binder clips to gently secure the device. The negative and positive terminals of the fabricated device were the dye-sensitized $Ti_{1-x}Fe_xO_2$ (photo-anode) on FTO and Ni-CEs, respectively, which were used to connect the external circuit.

4.2.3 Working Mechanism

The working mechanisms of a DSSC are mainly based on four pillars: photoabsorption, electron injection, charge-carrier transport, and current collection. The schematic shown in **Figure 4.2** addresses these attributes and illustrates the photoconversion of light into current. At first, photons were absorbed by the betalain pigments used as the photosensitizer, leading to electron excitation from the valence state

(S^+/S) to the conduction state (S^+/S^*). **Figure 4.7(c)** shows the highest absorption peak of the dye near 457 nm, while the minimum photo energy required for electron excitation is nearly 3.79 eV. The excited electrons, with lifetimes of nanoseconds, were injected into the TiO_2 NRs' conduction band, which is generally lower in energy than the excited state of the dye. There is also some UV photon absorption by TiO_2 NRs, as reported in the literature.[45] This will result in oxidation of the dye and can be represented by the equation given below,

$$S^+/S + hv \rightarrow S^+/S^* \qquad 4.1$$

$$S^+/S^* \rightarrow S^+/S + e^-(TiO_2\ NRs) \qquad 4.2$$

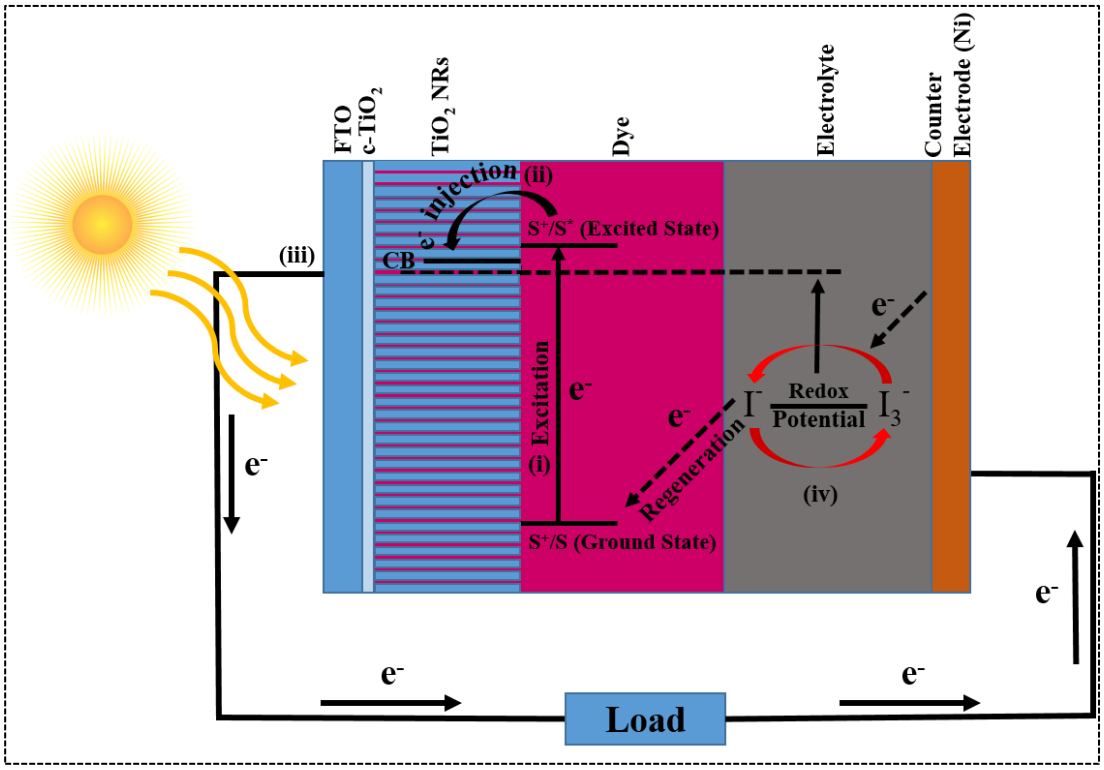

Figure 4.2 Typical schematics and working mechanism of the Dye Sensitized Solar Cells.

Now these injected charge carriers (electrons) were transported via TiO_2 NRs and diffused to the transparent conducting electrode (FTO). Later, the electrons were extended to the CE via external circuitry. At CE, the electrons were reduced from I_3^- to $I^-$and due

to the electron acceptance from I^- ion redox mediator, dye regeneration takes place. Subsequently oxidation of I^-into I_3^- (oxidized state) takes place (**equation 4.3**).

$$S^+/S^* + e^- \rightarrow S^+/S \quad 4.3$$

$$I_3^- + 2e^- \rightarrow 3I^- \quad 4.4$$

Further, diffusion of I_3^- oxidation mediator at the CE takes place and reduces into I^- ions (**equation 4.4**). Hence, as explained, dye sensitization occurs when sunlight is incident, and the formation of HOMO and LUMO levels takes place. If the sunlight radiation has sufficiently high energy, the e-charges are excited and injected into the CB of $Ti_{1-x}Fe_xO_2$ (x=0-0.1) NRs, and the dye is simultaneously oxidized. The outer circuitry helps these injected charges reach the CE. Electrolytes having I^- and I_3^- redox ions, which get reduced by the injected electron, will lead to the regeneration of the dye molecules.

4.3 Results and Discussion

4.3.1 Structural Analysis

Figure 4.3 displays the XRD patterns of $Ti_{1-x}Fe_xO_2$ (*x=0-0.1*) NRs grown on the FTO substrate. Bare TiO_2 NRs results of XRD match with the JCPDS card No. 21-1276, designated as tetragonal rutile phase. Diffraction peaks are observed at 26.69°, 27.61°, 36.25°, 37.90°, 41.41°, 54.60°, and 61.66°are assigned to (110), (121), (101), (200), (111), (211), and (002) planes, respectively, in pure TiO_2 NRs showing crystalline nature.[46] The absence of an extra diffraction peak for Fe in the XRD pattern suggests that the Fe content is below the detection limit. Because Fe and Ti have nearly equal ionic radii, the Fe^{3+} ions are well substituted in the TiO_2 crystal lattice, either as interstitials or on Ti^{4+} lattice sites. This indicates that Fe^{3+} ions were homogeneously incorporated into the NR matrix and that no Fe oxide is present on the surface, as reported in the literature.[47,48]

The (100) and (200) plane domination over other planes indicates that NRs preferentially grow in directions perpendicular to the substrate. The lattice constant for undoped TiO_2 NRs is *a*=*b*=4.864±0.003 Å and *c*=3.078±0.005 Å, which has good agreement with the available literature. **Table 4.1** presents the lattice constants for $Ti_{1-x}Fe_xO_2$ NRs, and clear variations are observed. A very small, low-angle peak shift at

61.66º has been observed with increasing Fe^{3+} concentration, indicating that substitutional Ti^{4+} sites in the TiO_2 crystal were occupied by Fe^{3+} ions. This is in good agreement with the lattice expansion observed as the 2θ angle increases, ascribed to the larger ionic radius of Fe^{3+} (0.79 Å) compared to that of Ti^{4+} (0.75 Å).[49]

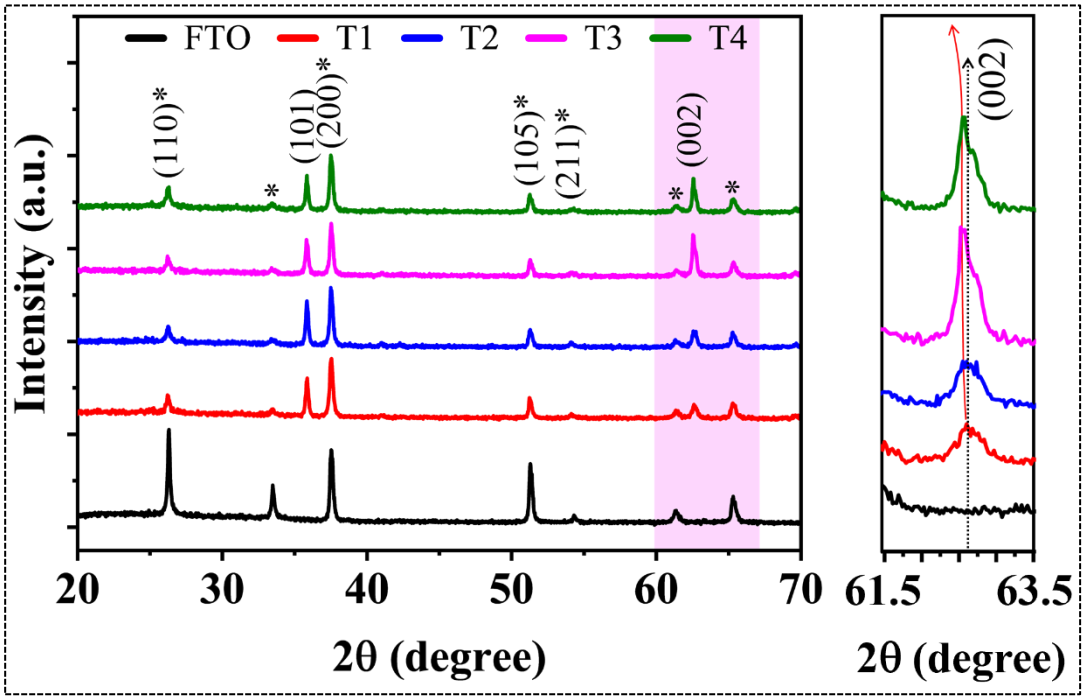

Figure 4.3 XRD pattern of FTO, bare TiO_2 (T1), $Ti_{0.975}Fe_{0.025}O_{2-\delta}$ (T2), $Ti_{0.95}Fe_{0.05}O_{2-\delta}$ (T3), and $Ti_{0.925}Fe_{0.075}O_{2-\delta}$ (T4) photoanodes. The asterisk (*) represents FTO diffraction peaks.

Table 4.1 Variation in the Lattice constant values with different concentrations of Fe-doping in TiO_2 NRs.

Composition	***a* = *b* (Å)**	***c* (Å)**
TiO_2	4.864±0.003	3.078±0.005
$Ti_{0.975}Fe_{0.025}O_2$	4.87±0.007	3.08±0.004
$Ti_{0.95}Fe_{0.05}O_2$	4.874±0.004	3.084±0.002

$Ti_{0.925}Fe_{0.075}O_2$	4.881±0.006	3.085±0.001
$Ti_{0.9}Fe_{0.1}O_2$	4.890±0.002	3.086±0.003

4.3.2 Morphological Analysis

Figure 4.4 represents the FESEM images of $Ti_{1-x}Fe_xO_2$ (*x=0-0.1*) NRs prepared at 150 °C for 8 h. On top of the FTO substrate, a uniform compact-TiO_2 layer had been coated, and then $Ti_{1-x}Fe_xO_2$ NRs were grown vertically on the FTO substrate. **Figure 4.4(a)** shows the top view of bare TiO_2 NRs, where the sides of the NRs are very smooth, but there are a few step edges mounted on the top. The growth of TiO_2 NRs may be due to additional Ti nucleation sites at the top step edges.[50] As expected, these NRs have a tetragonal crystal structure with square facets, as shown in **Figure 4.4(a)**. Also, **Figure 4.4(a-e)** validates the porous structure formation with interlinked TiO_2 NRs. The diffraction concentration of Fe-doping will drastically change the morphology, as shown in **Figure 4.4(b-e)**.

As observed, a hierarchical nano-dot-like structure was grown on the top of the TiO_2 NRs. These nano-dot-like structures on the top of NRs will significantly increase surface area and enhance charge transfer. The average calculated length and diameter of the $Ti_{1-x}Fe_xO_2$ NRs from **Figure 4.4(a-e)** are in the range of 350±10 to 370±10 nm and 80±10 to 90±10 nm, respectively, for *x=0-0.1.* In **Figure 4.4(f)**, a cross-sectional view of the photoanode is shown, and it is found that the average width of $Ti_{1-x}Fe_xO_2$ NRs and *c*-TiO_2 layer is nearly 1.4-1.9 μm and 250 nm, respectively. Reports are well-suited and already explain the advantages of the semiconducting nanoscale NRs, such as: (i) high surface to volume ratio;[51] (ii) very low grain boundaries, which directly alter the charge carrier trapping and scattering;[52] and (iii) suitable charge carrier transportation.[53] To increase dye loading, amply packed, large, and lean NRs can act as a dye scaffold while maintaining sufficient charge-carrier collection. With Fe doping, the rod-like morphology altered to a highly porous surface consisting of nanorods cum dot-like morphology, which indicated the increase in surface area, which may significantly change the charge conversion/extraction efficiency.

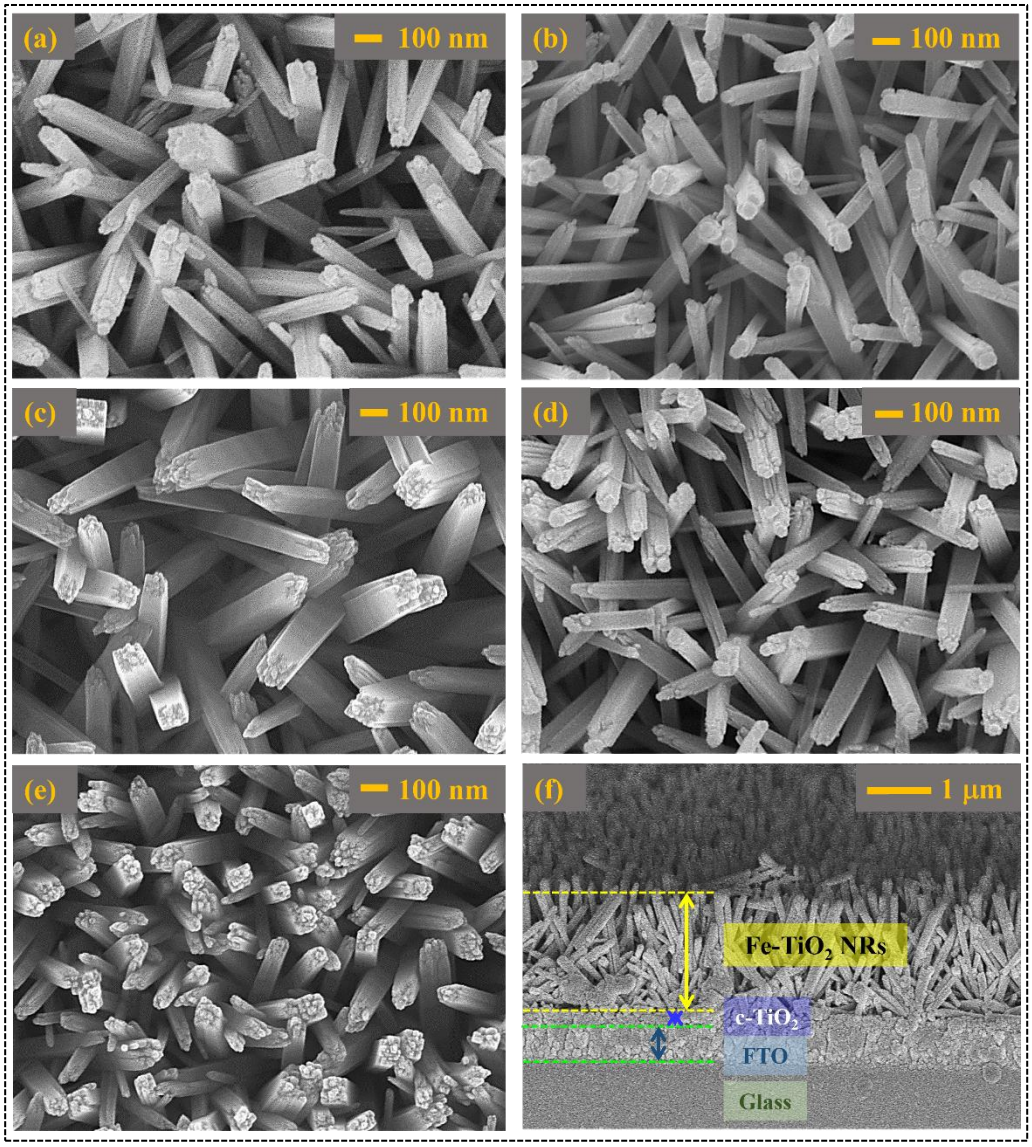

Figure 4.4 (a-e) FESEM top view image of $Ti_{1-x}Fe_xO_2$ (*x=0-0.1*) NRs grown. (a) Undoped (*x=0*) TiO_2 NRs, (b) *x=0.025*, (c) *x=0.05*, (d) *x=0.075*, (e) *x=0.1*, and (f) Cross-sectional image of undoped TiO_2 NR arrays.

To confirm the elemental composition and the efficacy of Fe doping, EDX analysis is performed on TiO_2 and $Ti_{0.95}Fe_{0.05}O_2$ photoanodes. As shown in **Figure 4.5(a)**, the **T1** has a stoichiometric distribution of Ti and O atoms, matching well with the literature. However, the Fe signal could not be distinctly resolved in $Ti_{0.95}Fe_{0.05}O_2$ photoanodes, which may be attributed to the low Fe concentration approaching the detection limit of the EDX system, along with instrumental constraints such as detector sensitivity,

interaction volume, and working-distance-dependent signal collection efficiency during FESEM-EDX measurements (**Figure 4.5(b)**). Therefore, further elemental mapping (**Figures 4.5(c-e)**) confirms the presence of Fe content and detects nanodot-like traces of it across the photoanode surface.

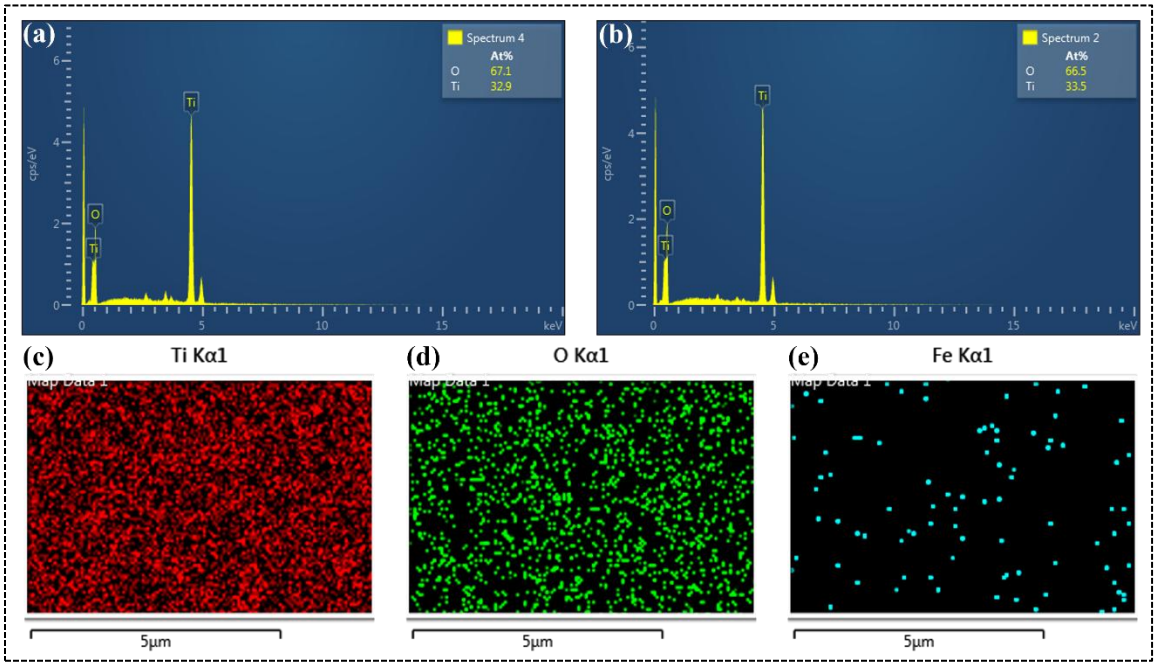

Figure 3.5 EDX spectra of (a) TiO_2 and (b) $Ti_{0.95}Fe_{0.05}O_2$ confirm the stoichiometric presence of Ti and O atoms. As no traces of Fe were found in EDX, elemental mapping (c-e) was done to confirm the presence of Fe and the uniform distribution of Ti and O.

Transmission electron microscopy (TEM) investigation was performed to analyze the crystal structure of TiO_2 NRs. Low-resolution TEM images of single TiO_2 NRs are represented in **Figure 4.6(a)**. Surprisingly, numerous step edges are present on the top facet of each NR, as shown in **Figure 4.6(a)**. These step edges served as nucleation sites, leading to axial growth of TiO_2 NRs at different rates. Further, such step edges may serve as substrates for the secondary growth of TiO_2 NRs. The relative HRTEM image of a single TiO_2 NR is depicted in **Figure 4.6(b)**, which confirms the single crystalline behaviour of these TiO_2 NRs having a lattice spacing of 0.32 nm along (101) planes of tetragonal rutile TiO_2 NRs. Additionally, the growth direction of TiO_2 NRs was parallel to the normal of the (001) plane. Therefore, the rutile TiO_2 NR arrays grown predominantly along the [001] plane show good agreement with the XRD pattern.

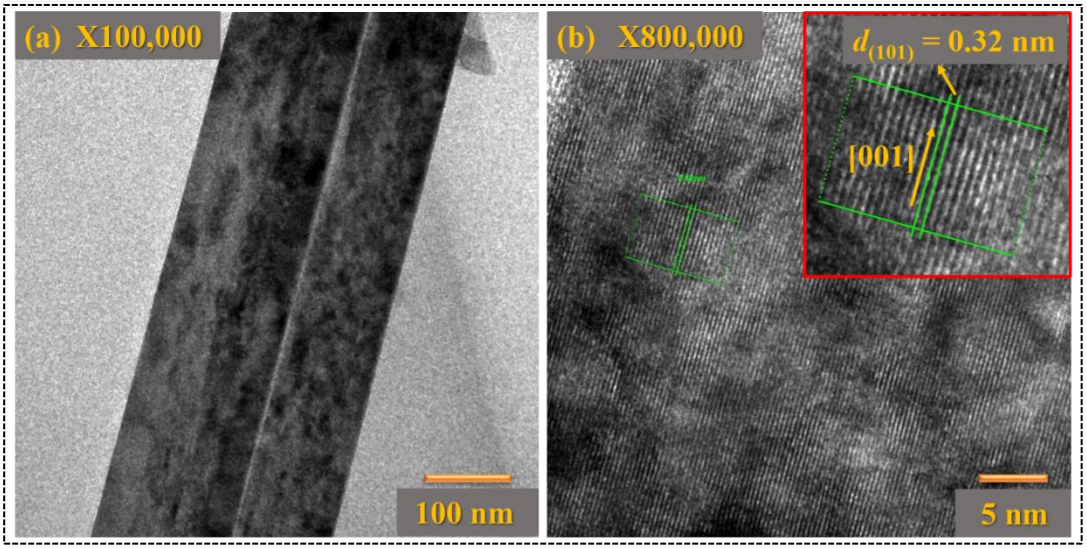

Figure 4.6 (a) TEM images of a single TiO_2 NR, and (b) Corresponding HRTEM image of a single TiO_2 NR. The inset image of (b) displays the lattice spacing between (101) planes of the rutile phase TiO_2.

4.3.3 XPS Analysis

TiO_2 has garnered significant interest worldwide, as it has been well proven and is an excellent photoanode for DSSCs. On the other hand, TiO_2 is a wide-band-gap (~3.2 eV) semiconductor that readily absorbs UV light. Numerous researchers claim that metal cations and non-metal anions can successfully dope titanium dioxide to prevent this UV-sensitization. In this work, simple, inexpensive hydrothermal fabrication of Fe-doped TiO_2 produced excellent photoanodic characteristics for DSSC applications. Therefore, X-ray photoelectron spectroscopy (XPS) was employed to fully understand the doping processes. Basically, XPS is a technique that was used to investigate the elemental composition, chemical state, and ionic states of iron in $Ti_{1-x}Fe_xO_2$ (x=*0-0.1*) photoanodes.

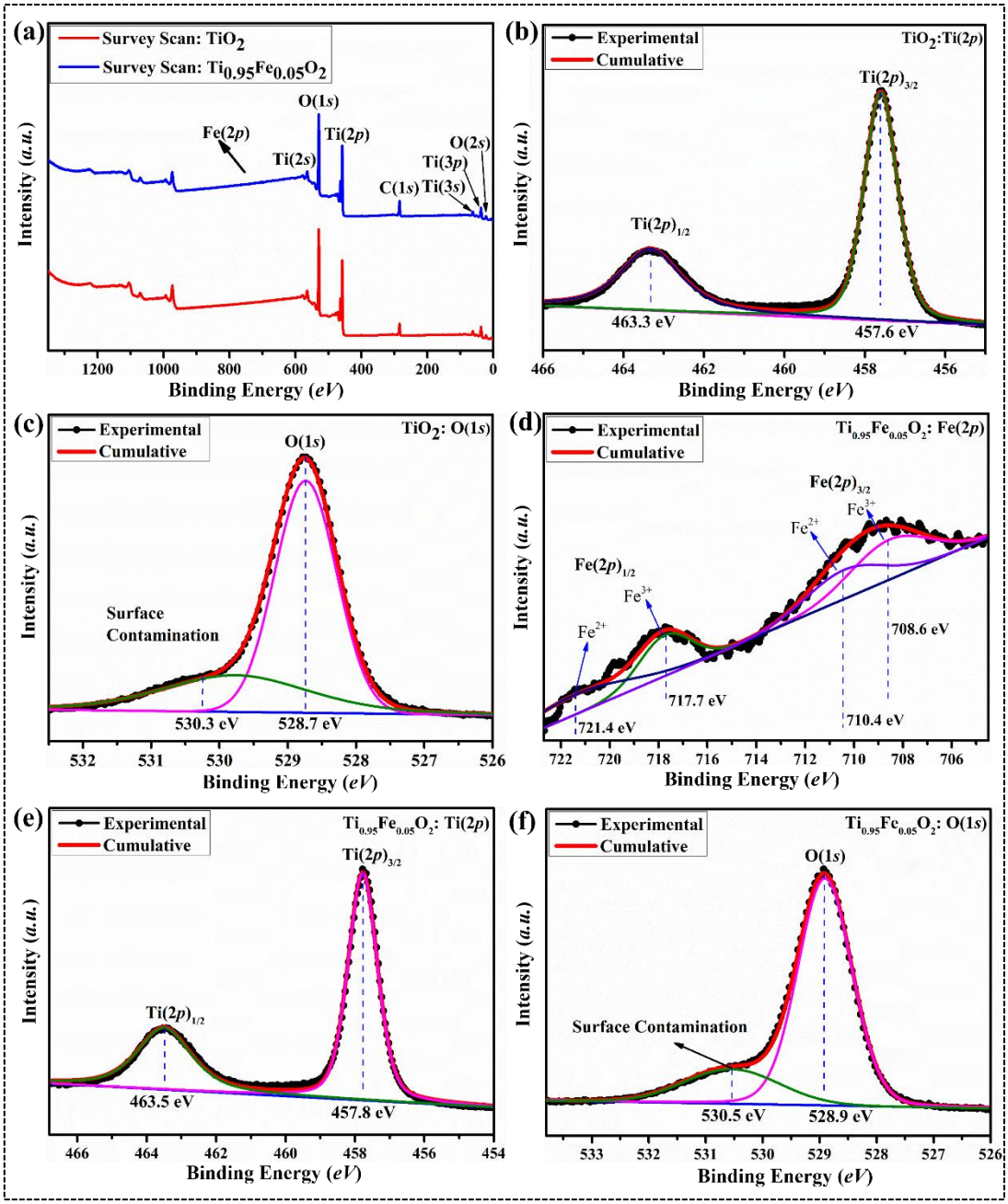

Figure 4.7 The XPS spectra of bare TiO_2 and $Ti_{0.95}Fe_{0.05}O_2$ photoanodes. (a) Comparison of XPS survey scan spectra, (b) TiO_2: Ti(2*p*) core-level XPS spectra, (c) TiO_2: O(1*s*) core-level XPS spectra, (d) $Ti_{0.95}Fe_{0.05}O_2$: Fe(2*p*) XPS spectra, (e) $Ti_{0.95}Fe_{0.05}O_2$: Ti(2*p*) core-level XPS spectra, and (f) $Ti_{0.95}Fe_{0.05}O_2$: O(1*s*) core-level XPS spectra.

Survey spectra of bare TiO_2 and $Ti_{0.95}Fe_{0.05}O_2$ photoanodes are displayed in **Figure 4.7(a)**. From the survey scan, the presence of Ti, O, C, and Fe elements was

identified, whereas no Fe content was detected in bare TiO_2 photoanodes. Here, C is detected in the survey scan only due to background or Adventitious carbon contamination and is not present in the synthesized samples. Further high-resolution XPS spectra of Ti(2p) and O(1s) core levels from bare TiO_2 and $Ti_{0.95}Fe_{0.05}O_2$ photoanodes are shown in **Figure 4.7(b-c)** and **Figure 4.7(e-f)**, respectively.

Figure 4.7(b and **e)** reveals that the XPS spectrum of Ti(2*p*) core consists of two major peaks, namely $Ti(2p)_{3/2}$ and $Ti(2p)_{1/2}$, whereas the Ti(2*p*) spectrum mostly present in Ti^{4+} oxidation with minor composition of Ti^{3+} (because of O-inadequacy in TiO_2 lattice) for both bare TiO_2 and $Ti_{0.95}Fe_{0.05}O_2$ photoanodes, respectively. In bare TiO_2 photoanodes, the binding energies of dominant $Ti(2p)_{3/2}$ and minor $Ti(2p)_{1/2}$ were observed at 457.8 and 463.3 eV (**Figure 4.7(b)**). However, both these Ti(2*p*) spectrum peaks were shifted positively by 0.2 eV in $Ti_{0.95}Fe_{0.05}O_2$ photoanodes (**Figure 4.7(e)**). This peak shift is ascribed to reduced Ti coordination and shorter Ti-O bond lengths, i.e., a decrease in Ti^{4+} content. Additionally, this peak shift led to the formation of Fe-O-Ti bonds attributed to TiO_2/Fe_2O_3 binary oxide formation.

High-resolution XPS spectra of O(1*s*) for bare TiO_2 and $Ti_{0.95}Fe_{0.05}O_2$ photoanodes are shown in **Figure 4.7(c** and **f)**, respectively. Here, in the case of bare TiO_2, the binding energy of the ruling O(1s) peak is 528.7 eV, which later shows a minor positive shift of 0.2 eV in $Ti_{0.95}Fe_{0.05}O_2$ derivatives, ascribed to the oxygen signals in the TiO_2 lattice. Moreover, the O(1s) peaks are reduced in $Ti_{0.95}Fe_{0.05}O_2$ photoanodes, as Fe-O bond formation occurs on the TiO_2 surface. At both 530.3 and 530.5 eV binding energies, in both cases, another peak is observed, which is due to surface contamination, i.e., OH^- adsorption on the TiO_2 surface.

At last, XPS spectra of Fe(2p) were investigated to understand the electronic behaviour of Fe in $Ti_{0.95}Fe_{0.05}O_2$ photoanodes, and the Fe(2p) core spectrum is shown in **Figure 4.7(d)**. The binding energy of the two dominant $Fe(2p)_{3/2}$ and $Fe(2p)_{1/2}$ doubled peaks were found at 708.6 and 717.7 eV, respectively, which are associated with Fe^{3+} oxides. Along with these main peaks, there are some shake-up satellite peaks, and weak peaks are also observed at 710.4 and 721.4 eV, which are identified as minor contributions from Fe^{2+} oxidation states. However, these Fe^{2+} ions on the TiO_2 surface may become less

mobile and convert to the Fe^{3+} state, leading to the formation of Ti^{3+} defect states. The collected information will be very helpful for future transition-metal-doping processes of TiO_2.

4.3.4 UV-Visible Absorption Analysis

Below 400nm, absorption spectra (**Figure 4.8(a)**) of $Ti_{1-x}Fe_xO_2$ (*x=0-0.1*) NRs show a sudden increase in absorption, assigned to stable rutile TiO_2 with the bandgap of 3.2 eV (x=0, TiO_2 NRs).[54] In visible light, a nearly non-zero baseline is observed, which matches the previously reported work of Zhao *et al.*[55] This may be due to low film thickness or pinholes in the film. The absorbance of iron ions is present in the spectra of Fe-doped TiO_2 NRs.

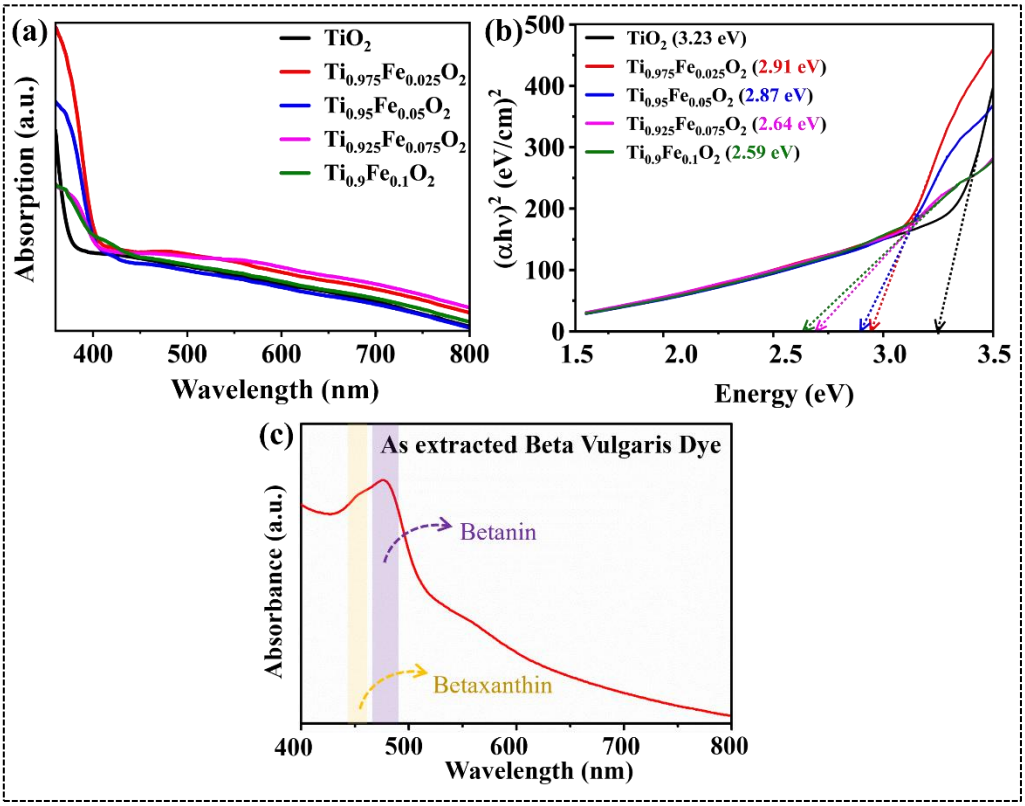

Figure 4.8 Absorption spectra of (a) $Ti_{1-x}Fe_xO_2$ *(*x=*0-0.1)* NRs, (b) Tauc's plot of the $Ti_{1-x}Fe_xO_2$ *(*x=*0-0.1)* NRs, and (c) UV-visible spectra of extracted BV dye.

In **Figure 4.8(b)**, optical bandgap estimation has been shown from the Tauc's plot, and the observed bandgap values for $Ti_{1-x}Fe_xO_2$ *(x = 0-0.1)* NRs are 3.23, 2.91, 2.87, 2.64,

and 2.59 eV, respectively. A gradual redshift was observed in all Fe-doped samples, which may be attributed to Fe-related intermediate electronic states and oxygen-vacancy-associated shallow trap states introduced within the TiO_2 band structure. These states facilitate lower-energy electronic transitions and contribute towards enhanced visible-light absorption and apparent bandgap reduction with increasing Fe concentration.[56] The UV-Visible analysis of the prepared dye from BV is represented in **Figure 4.8(c)**. In fact, dyes control both photocharge generation and transport, which, in turn, affect device performance. To investigate the light capture ability of the used dye, UV-vis absorption spectra were recorded. Broad absorption band at 427-523 nm, and the maximum absorption is found at ~457 nm. The maximum absorption peak (~457 nm) attributed to the purple-red betanin, while a small hump at ~451 nm, confirms the presence of yellow betaxanthin pigments and is in good agreement with the available literature. Functional groups present in the dye, namely –O=H and –C (=O) OH, will enhance charge transfer at the dye-photoanode interface. Approximately 3.79 eV of photo energy is required to excite the electron from the HOMO to the LUMO states of the BV dye.

4.3.5 FTIR Analysis

The presence of functional groups in the dye extracted from natural resources is necessary for its adsorption onto the TiO_2 NR photoanode. FTIR spectrum of dye extracted from BV is shown in **Figure 4.9(a)**, which confirms the presence of betalain pigments.

Optimized FT-IR results have shown a sharp peak at 3346 cm^{-1} because of -OH stretching vibration, whereas the peak at 2978 cm^{-1} is assigned to C−H stretching vibration of alkanes. At 1637 cm^{-1}, the amide bond (carbonyl stretching mode) is observed. Peak at 1376 cm^{-1} is attributed to either the C−N stretching or –OH vibrational bond, while the C−O bond is assigned at 1272 cm^{-1} for carboxylic acid stretching vibration mode. In addition to these modes, symmetric stretching vibration (C−O−C), C−H bond deformation, and C−COOH stretching vibration absorption bands are observed at 1086, 1042, and 876 cm^{-1}, respectively. All these observed vibrational and stretching modes corresponding to the different functional groups are associated with the red-purple betanin pigments and effectively bind with the photoanode surface.

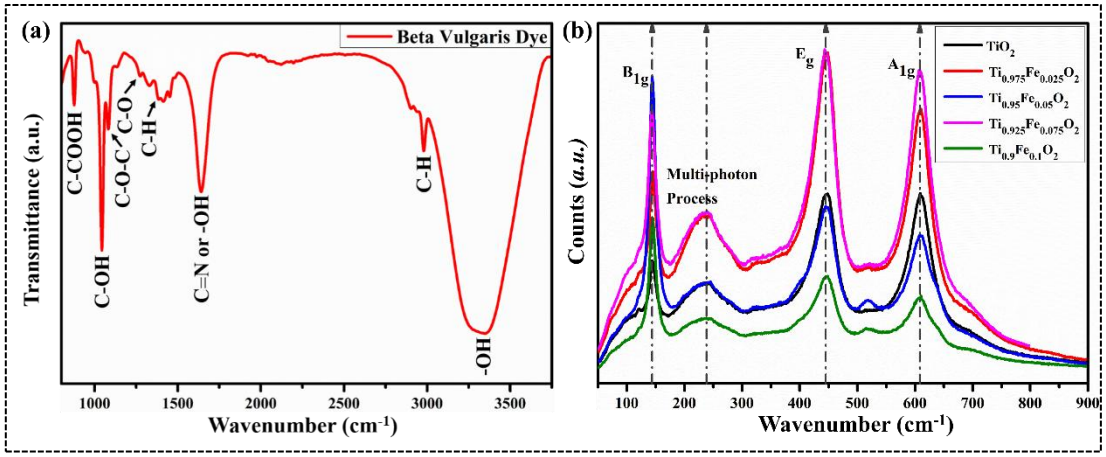

Figure 4.9 (a) FT-IR spectrum of the dye extracted from the BV, (b) Raman spectra for tetragonal rutile phase $Ti_{1-x}Fe_xO_2$ *(*x=*0-0.1)* NRs grown hydrothermally on FTO substrate.

Generally, Raman spectroscopy (**Figure 4.9(b)**) is preferred to investigate the structural properties of the hydrothermally grown $Ti_{1-x}Fe_xO_2$ (*x=0-0.1*) NRs. All the first-order three active Raman modes A_{1g} (609.18 cm^{-1}), B_{1g} (143.65 cm^{-1}), and the most prominent second-order scattering mode E_g (446.37 cm^{-1}) validate the formation of rutile phase TiO_2 NRs. At nearly 140 cm^{-1}, a sharp peak arises from the O-Ti-O symmetric bending vibration, which gives rise to the B_{1g} mode. Another intense characteristic peak at 446 cm^{-1} was observed, which may be assisted by symmetric O-Ti-O stretching vibration. All the results are in good agreement with previously reported literature.

4.3.6 J-V Analysis

The photovoltaic properties of the DSSC device prepared using $Ti_{1-x}Fe_xO_2$ (*x=0-0.1*) NRs grown on the FTO substrate having a TiO_2 blocking layer sandwiched in between have been shown in **Figure 4.10(a).** Betalain pigments extracted from BV (red beetroot) were used as photo-sensitizers. For its real-world applications, the device's stability is a priority alongside performance. After 300 hours of testing, 70% PCE retention was observed in DSSCs comprising the most effective $Ti_{0.95}Fe_{0.05}O_2$ photoanodes and BV dyes. Further, the PCE retention of the DSSCs having TiO_2, $Ti_{0.975}Fe_{0.025}O_2$, $Ti_{0.925}Fe_{0.075}O_2$, and $Ti_{0.9}Fe_{0.1}O_2$ photoanodes was 50, 67, 60, and 45%, respectively, after 300 hours under the standard 1 Sun (AM 1.5G) illumination, as shown in **Figure 4.10(b)**.

The incident-photon conversion efficiency (IPCE) of the corresponding DSSCs is shown in **Figure 4.10(c)** over the wavelength range from 350 to 750 nm. The highest IPCE value, 54.6%, was observed for the $Ti_{0.95}Fe_{0.05}O_2$ photoanodes at ~560 nm. However, for the $Ti_{0.925}Fe_{0.075}O_2$, $Ti_{0.9}Fe_{0.1}O_2$, $Ti_{0.975}Fe_{0.025}O_2$, and pure TiO_2 photoanodes, the maximum obtained IPCE peak values are 48.3, 43.5, 39.9, and 34.6 %. The IPCE value and J_{SC} had a favourable correlation. Consequently, the results of the J-V study and the overall IPCE investigation were consistent. The absorbance of the betalain dye occurred between 400 and 600 nm, where the IPCE value was maximum. On the other hand, absorption of $Ti_{1-x}Fe_xO_2$ (*x=0-0.1*) photoanodes varied between 350 and 450 nm, related to the bandgap of 2.59-3.23 eV, which were properly compatible with the IPCE study findings.

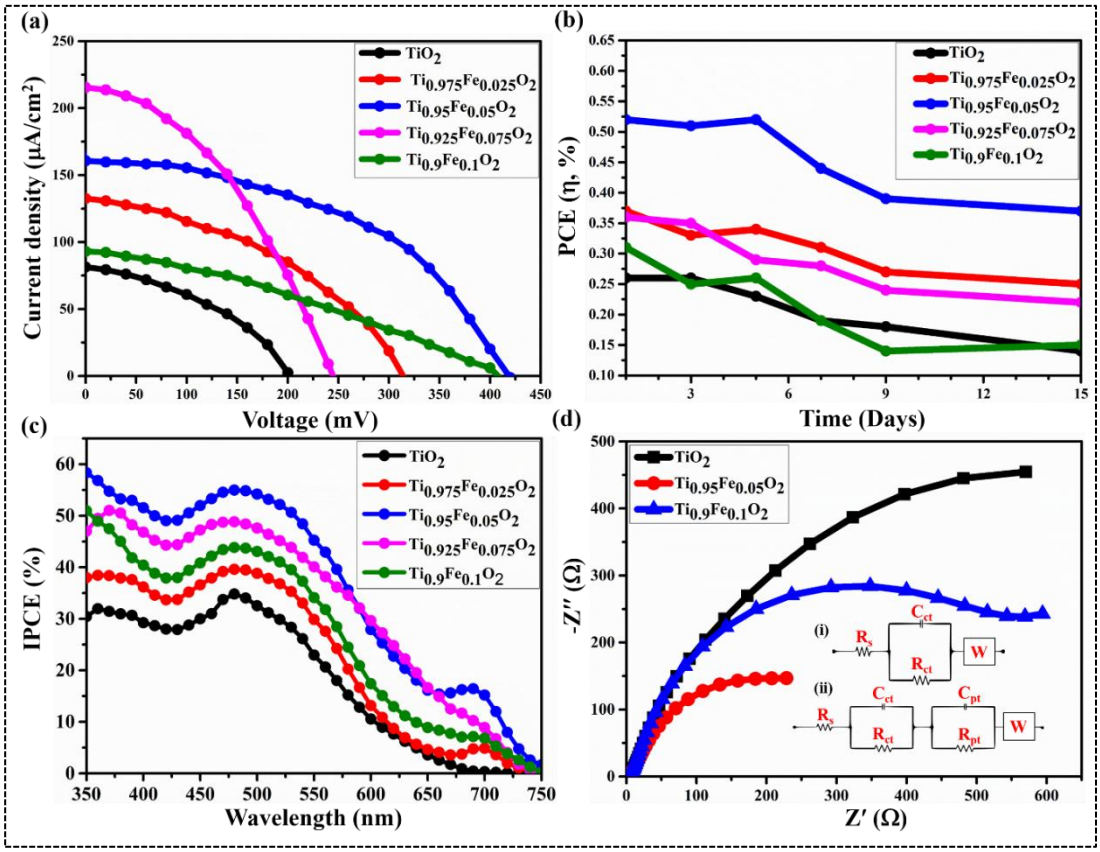

Figure 4.10 (a) *J-V* characteristics of the $Ti_{1-x}Fe_xO_2$ *(x=0-0.1)* NRs-based DSSC utilizing BV dyes as sensitizers, (b) Stability analysis on the fabricated DSSCs consists of $Ti_{1-x}Fe_xO_2$ *(x=0-0.1)* photoanodes and BV dyes, (c) IPCE spectra of $Ti_{1-x}Fe_xO_2$ *(x=0-0.1)* NR

photoanodes-based DSSCs, and (d) EIS Nyquist plots of undoped and doped TiO_2 photoanodes at a bias of $V=V_{OC}$.

The large IPCE values for $Ti_{0.95}Fe_{0.05}O_2$ photoanode-based DSSCs across a wide spectrum will increase light-harvesting capacity, ascribed to the high dye loading and maximum reflectance. Additionally, IPCE analysis reveals that $Ti_{0.95}Fe_{0.05}O_2$ photoanode-based DSSCs exhibit a clear red-shift in the absorption spectrum compared to others, due to their efficient light-scattering properties. The extended EQE response observed in the 650-700 nm region for Fe-doped TiO_2 nanorods may be attributed to Fe-induced intermediate electronic states and oxygen-vacancy-related defect levels introduced within the TiO_2 band structure. These defect-assisted sub-bandgap transitions enable lower-energy photon absorption and extend the photoresponse towards the visible-red region. Additionally, the porous nanorod cum dot-like morphology may further enhance photon trapping and light interaction within the photoanode structure.

The Electron Impedance Spectroscopy (EIS) investigation of $Ti_{1-x}Fe_xO_2$ (*x=0-0.1*) photoanode-based DSSCs in the frequency range 0.1 Hz to 100 kHz is shown in **Figure 4.10(d)**. EIS evaluates the charge transfer mechanisms in DSSCs, such as series resistance R_s, related to resistance offered by FTO and CE, high frequency impedance responses R_{ct} and C_{pt} associated with the events happening at Ni/electrolyte interface, mean frequency responses R_{pt} and C_{pt} related to the electron transport and recombination at TiO_2/electrolyte interface, and low frequency response W designated as electrolyte diffusion impedance.

As depicted in **Figure 4.10(d)**, in the mean frequency region, the Nyquist plots contain a semicircle, which is ascribed to the TiO_2/electrolyte interfacial electron transport resistance and recombination. However, a very small, straight-line, low-frequency component is associated with the diffusion mechanics. The diameters of the semicircles in the Nyquist plots of $Ti_{1-x}Fe_xO_2$ (x=0-0.1) photoanodes varied with the Fe concentration. Equivalent circuits for bare TiO_2 and $Ti_{0.9}Fe_{0.1}O_2$ photoanodes are represented by the inset circuit (i) drawn. However, the equivalent circuit for $Ti_{0.95}Fe_{0.05}O_2$ photoanodes is represented by the inset circuit (ii). All the values of R_s, R_{ct}, C_{ct}, R_{pt}, C_{pt}, and W for $Ti_{1-x}Fe_xO_2$ (*x=0-0.1*) photoanodes based DSSCs are summarized in **Table 4.2**. Finally,

$Ti_{0.95}Fe_{0.05}O_2$ photoanodes exhibit two impedance components with a lower electron transport resistance (R_{ct} = 660 Ω), indicating decreased electron recombination and enhanced electron transport, leading to higher conductivity, consistent with the previous findings.

Table 4.2 Corresponding circuit parameters of $Ti_{1-x}Fe_xO_2$ (*x=0-0.1*) photoanodes in 1M KOH electrolyte.

Composition	R_s (Ω)	R_{ct} (Ω)	C_{ct} (mF)	R_{pt} (Ω)	C_{pt} (mF)	W (mMho)
TiO_2	21.27	1376	37.69	-	-	-
$Ti_{0.95}Fe_{0.05}O_2$	3.653	659.3	21.86	96.05	27.74	27.82
$Ti_{0.9}Fe_{0.1}O_2$	9.236	991	42.98	-	-	22.43

This study is aimed at checking the role of $Ti_{1-x}Fe_xO_2$ (*x=0-0.1*) photoanodes on the DSSC performance. Various solar cell performance parameters such as power conversion efficiency (η %), open circuit voltage (V_{OC}), short circuit current density (J_{SC}), and fill factor (FF) for $Ti_{1-x}Fe_xO_2$ (*x=0-0.1*) based DSSC are given in **Table 4.3**. Performance escalation directly depends on (i) a large contact area between FTO and *c*-TiO_2 and (ii) the blocking ability of the *c*-TiO_2. A large contact area will significantly reduce the charge transport resistance and simultaneously increase the charge collection efficiency, while the blocking ability of *c*-TiO_2 will help reduce charge recombination. The Choice of CEs also plays an important role in the device performance.

Table 4.3 Photovoltaic studies of $Ti_{1-x}Fe_xO_2$ (*x=0-0.1*) photoanode-based DSSC utilizing BV dyes as light harvester.

Composition	J_{SC} (mA cm^{-2})	V_{OC} (mV)	FF	η (%)
TiO_2	0.080	203	0.97	0.26
$Ti_{0.975}Fe_{0.025}O_2$	0.151	420	0.36	0.37
$Ti_{0.95}Fe_{0.05}O_2$	0.130	312.3	0.79	0.52
$Ti_{0.925}Fe_{0.075}O_2$	0.210	246	0.43	0.36
$Ti_{0.9}Fe_{0.1}O_2$	0.092	419	0.50	0.31

In this study, we preferred Ni-based CE for its cost-effectiveness, ease of processing, and superior performance. However, Ni has a lower conductivity of 1.43 × 10^7 S m^{-1} as compared to conventional CEs such as gold (4.10 × 10^7 S m^{-1}), silver (6.30 × 10^7 S m^{-1}), copper (5.96 × 10^7 S m^{-1}), etc., attributed to the lower performance (as compared to some reports given in **Table 4.4**) of the Fe-doped TiO_2 NR photoanode and Ni-CE based DSSC where BV dye has been used as the photosensitizer. Apart from the lower conductivity of Ni-CE, photo-generated charge recombination at the FTO and *c*-TiO_2 interface will result in a significant but lower efficiency of only 0.52%. Although Ni-CE-based DSSCs are cost-effective and have comparable PCE, they are eco-friendly and affordable solar cells.

Table 4.3 confirms the substantial variation across samples, especially in J_{SC}. As J-V results show that there is a significant increase in J_{SC}, accompanied by enhanced V_{OC}. Undoped samples have shown lower J_{SC} due to rapid photocharge recombination, as reported in the literature.[20] As Fe concentration increases, J_{SC} values increase as well. This may have occurred due to enhanced absorption and energy transfer from the Fe^{3+} band to the CB of the TiO_2 NRs. The PCE and J_{SC} were nevertheless inhibited when too much Fe content was introduced because potential barriers stopped the electrons from flowing to the external circuit. Also, because of reduced grain-boundary resistance, recombination losses are greatly reduced during charge transportation. Hence, based on the observed photovoltaic properties, Fe-doping results in an increase.

A comparative study of BV-dye-based DSSCs is presented in **Table 4.4**. Herein, we also reported the performance of $Ti_{1-x}Fe_xO_2$ NRs-based DSSC by using betalain pigments extracted from BV. BV dyes were examined by Sinha *et al.*[57] for DSSCs with a combination of carbon and ZnO electrodes, yielding a PCE of 0.17%. In the same report, mixed dye (chlorophyll and betalains) successfully boosted the device performance by 0.38%. In another report, Bashar *et al.*[58] used $TiCl_4$-treated TiO_2 photoanodes in a DSSC with the BV photosensitizer and achieved 0.49% PCE, whereas mixing red and green dyes (4:1) notably improved performance to 0.99%. Salinas *et al.*[59] investigated

combined BV and orange Bougainville extracts on a TiO_2 photoanode for DSSC and obtained 0.274% PCE, while bare BV dye showed a better PCE of 0.467%. This decrease in PCE with the mixed dye was attributed to reduced photoabsorption. Increased lifetime and a slightly lower PCE (0.89% to 0.68%) have been reported with a mixed BV dye and tetraethylorthosilicate.[60]

In summary, the limited charge-transfer capability and surface area coverage of TiO_2 photoanodes, when combined with conventional CEs, need to be modified to improve performance. To address these gaps, we doped TiO_2 NRs with Fe, which shifted the absorption edge into the visible region and reduced charge recombination at the FTO/*c*-TiO_2 interface. Because of their nearly equal ionic radii, Fe doping will maintain the crystal structure. Enhanced surface adsorption and low-energy-level photonic excitation will be achieved with Fe doping. Moreover, we replaced costly conventional CE with Ni, which delivers notable performance despite its lower conductivity.

Table 4.4 Comparative study of the BV dyes-based DSSC performance from the available literature.

Dye	**CE**	**Photoanode**	**J_{SC} (mA cm^{-2})**	**V_{OC} (mV)**	**FF (%)**	**η (%)**	**Ref.**
BV	Carbon	ZnO	0.72	460	0.54	0.179	[57]
Purple cabbage and BV	Carbon	ZnO	1.12	560	0.60	0.382	
BV	Carbon	$TiCl_4$ treated TiO_2	2.23	407.6	0.54	0.49	[58]
80% BV + 20% spinach	Carbon	$TiCl_4$ treated TiO_2	4.65	386.7	0.55	0.99	
BV		TiO_2	2.71	576	0.57	0.89	[60]
BV + Tetraethylorthosilicate	carbon	TiO_2	2.08	609	0.54	0.68	

BV	Pt	TiO_2	1.295	380	0.32	0.15	[61]
BV	Graphite	TiO_2	1.7	0.46	-	1.3	[62]
BV	Pt	TiO_2	0.055	470	-	0.03	[63]
BV	Nickel	TiO_2 NRs	0.080	203	0.97	0.26	**This work**
BV	Nickel	$Ti_{0.975}Fe_{0.025}O_2$ NRs	0.151	420	0.36	0.37	**This work**
BV	Nickel	$Ti_{0.95}Fe_{0.05}O_2$ NRs	0.130	312.3	0.79	0.52	**This work**
BV	Nickel	$Ti_{0.925}Fe_{0.075}O_2$ NRs	0.210	246	0.43	0.36	**This work**
BV	Nickel	$Ti_{0.9}Fe_{0.1}O_2$ NRs	0.092	419	0.50	0.31	**This work**

4.4 Conclusions

In conclusion, we have prepared a very economical DSSC using $Ti_{1-x}Fe_xO_2$ nanorods and BV dyes. To understand the role of Fe-doped TiO_2 photoanodes and the performance of BV dye-based DSSCs, various physicochemical characterizations and photovoltaic analyses were performed. This Fe-doping will reduce photocharge recombination, while *c*-TiO_2 helps minimize interfacial charge-transfer resistance and is a very effective approach to resolving the low PCE of DSSCs. On the other hand, the economically prepared Ni-CEs will enhance the charge collection. Here, this combination of photoanodes, dyes, and CEs was explored for the first time, yielding a notable PCE. However, pinholes on the photoanode's surface and dye degradation may lead to device failure later. Furthermore, ease of fabrication, cost-effectiveness, eco-friendliness, and the remarkable performance of DSSCs with Fe-doped TiO_2 NR photoanodes, Ni-CEs, and betalain pigment-based photosensitizers make it an effective and feasible approach for commercial fabrication. In addition, such DSSCs may become a game changer for novel applications, such as wearables, thermochromics, and laser drilling.

References

[1] Brian O'Regan & Michael Grätzel et al., A low-cost, high-efficiency solar cell based on dye-sensitized colloidal TiO_2 films, Nature. 35 (1991) 737–740. https://doi.org/10.1038/353737a0.

[2] K. Kakiage, Y. Aoyama, T. Yano, K. Oya, J.I. Fujisawa, M. Hanaya, Highly-efficient dye-sensitized solar cells with collaborative sensitization by silyl-anchor and carboxy-anchor dyes, Chem. Commun. 51 (2015) 15894–15897. https://doi.org/10.1039/c5cc06759f.

[3] L. Song, P. Du, J. Xiong, F. Ko, C. Cui, Efficiency enhancement of dye-sensitized solar cells by optimization of electrospun ZnO nanowire/nanoparticle hybrid photoanode and combined modification, Electrochim. Acta. 163 (2015) 330–337. https://doi.org/10.1016/j.electacta.2015.02.093.

[4] C.-T. Wu, W.-P. Liao, J.-J. Wu, Three-dimensional ZnO nanodendrite/nanoparticle composite solar cells, J. Mater. Chem. 21 (2011) 2871. https://doi.org/10.1039/c0jm03481a.

[5] W. Ahmad, U. Mehmood, A. Al-Ahmed, F.A. Al-Sulaiman, M.Z. Aslam, M.S. Kamal, R.A. Shawabkeh, Synthesis of zinc oxide/titanium dioxide (ZnO/TiO_2) nanocomposites by wet incipient wetness impregnation method and preparation of ZnO/TiO_2 paste using poly(vinylpyrrolidone) for efficient dye-sensitized solar cells, Electrochim. Acta. 222 (2016) 473–480. https://doi.org/10.1016/j.electacta.2016.10.200.

[6] C.-P. Lee, C.-T. Li, K.-C. Ho, Use of organic materials in dye-sensitized solar cells, Mater. Today. 20 (2017) 267–283. https://doi.org/10.1016/j.mattod.2017.01.012.

[7] S. Chand Yadav, A. Srivastava, V. Manjunath, A. Kanwade, R.S. Devan, P.M. Shirage, Properties, performance and multidimensional applications of stable lead-free $Cs_2AgBiBr_6$ double perovskite, Mater. Today Phys. 26 (2022) 100731. https://doi.org/10.1016/j.mtphys.2022.100731.

[8] A. Kanwade, S. Gupta, A. Kankane, A. Srivastava, S.C. Yadav, P.M. Shirage, Phosphate-based cathode materials to boost the electrochemical performance of sodium-ion batteries, Sustain. Energy Fuels. 6 (2022) 3114–3147. https://doi.org/10.1039/d2se00475e.

[9] S.C. Yadav, V. Manjunath, A. Srivastava, R.S. Devan, P.M. Shirage, Stable lead-free $Cs_4CuSb_2Cl_{12}$ layered double perovskite solar cells yielding theoretical efficiency close to 30%, Opt. Mater. (Amst). 132 (2022) 112676. https://doi.org/10.1016/j.optmat.2022.112676.

[10] X. Feng, K. Shankar, O.K. Varghese, M. Paulose, T.J. Latempa, C.A. Grimes, Vertically Aligned Single Crystal TiO_2 Nanowire Arrays Grown Directly on Transparent Conducting Oxide Coated Glass: Synthesis Details and Applications, Nano Lett. 8 (2008) 3781–3786. https://doi.org/10.1021/nl802096a.

[11] B. Liu, E.S. Aydil, Growth of Oriented Single-Crystalline Rutile TiO_2 Nanorods on Transparent Conducting Substrates for Dye-Sensitized Solar Cells, J. Am. Chem. Soc. 131 (2009) 3985–3990. https://doi.org/10.1021/ja8078972.

[12] Q. Kang, J. Cao, Y. Zhang, L. Liu, H. Xu, J. Ye, Reduced TiO_2 nanotube arrays for photoelectrochemical water splitting, J. Mater. Chem. A. 1 (2013) 5766. https://doi.org/10.1039/c3ta10689f.

[13] Y. Zhang, X. Xiong, Y. Han, X. Zhang, F. Shen, S. Deng, H. Xiao, X. Yang, G. Yang, H. Peng, Photoelectrocatalytic degradation of recalcitrant organic pollutants using TiO_2 film electrodes: An overview, Chemosphere. 88 (2012) 145–154. https://doi.org/10.1016/j.chemosphere.2012.03.020.

[14] D. Zhang, F. Zeng, Photocatalytic oxidation of organic dyes with visible-light-driven codoped TiO_2 photocatalysts, Russ. J. Phys. Chem. A. 85 (2011) 1077–1083. https://doi.org/10.1134/S0036024411060367.

[15] A. Kanwade, S. Gupta, A. Kankane, M.K. Tiwari, A. Srivastava, J.A. Kumar Satrughna, S. Chand Yadav, P.M. Shirage, Transition metal oxides as a cathode for indispensable Na-ion batteries, RSC Adv. 12 (2022) 23284–23310.

https://doi.org/10.1039/d2ra03601k.

[16] M.K. Tiwari, S.C. Yadav, A. Srivastava, A. Kanwade, J.A.K. Satrughna, S.S. Mali, J. V. Patil, C.K. Hong, P.M. Shirage, Enhancement of CO gas sensing performance by Mn-doped porous $ZnSnO_3$ microspheres, RSC Adv. 12 (2022) 32249–32261. https://doi.org/10.1039/D2RA06785D.

[17] C.M. Teh, A.R. Mohamed, Roles of titanium dioxide and ion-doped titanium dioxide on photocatalytic degradation of organic pollutants (phenolic compounds and dyes) in aqueous solutions: A review, J. Alloys Compd. 509 (2011) 1648–1660. https://doi.org/10.1016/j.jallcom.2010.10.181.

[18] S. Kment, H. Kmentova, P. Kluson, J. Krysa, Z. Hubicka, V. Cirkva, I. Gregora, O. Solcova, L. Jastrabik, Notes on the photo-induced characteristics of transition metal-doped and undoped titanium dioxide thin films, J. Colloid Interface Sci. 348 (2010) 198–205. https://doi.org/10.1016/j.jcis.2010.04.002.

[19] A. Di Paola, E. García-López, S. Ikeda, G. Marcì, B. Ohtani, L. Palmisano, Photocatalytic degradation of organic compounds in aqueous systems by transition metal doped polycrystalline TiO_2, Catal. Today. 75 (2002) 87–93. https://doi.org/10.1016/S0920-5861(02)00048-2.

[20] M. Asiltürk, F. Sayılkan, E. Arpaç, Effect of Fe^{3+} ion doping to TiO_2 on the photocatalytic degradation of Malachite Green dye under UV and vis-irradiation, J. Photochem. Photobiol. A Chem. 203 (2009) 64–71. https://doi.org/10.1016/j.jphotochem.2008.12.021.

[21] M.I. Litter, J.A. Navío, Photocatalytic properties of iron-doped titania semiconductors, J. Photochem. Photobiol. A Chem. 98 (1996) 171–181. https://doi.org/10.1016/1010-6030(96)04343-2.

[22] B. Wang, Q. Li, W. Wang, Y. Li, J. Zhai, Preparation and characterization of Fe^{3+}-doped TiO_2 on fly ash cenospheres for photocatalytic application, Appl. Surf. Sci. 257 (2011) 3473–3479. https://doi.org/10.1016/j.apsusc.2010.11.050.

[23] A. Zaleska, Doped-TiO_2: A Review, Recent Patents Eng. 2 (2008) 157–164. https://doi.org/10.2174/187221208786306289.

[24] A. Neren Ökte, Ş. Akalın, Iron (Fe^{3+}) loaded TiO_2 nanocatalysts: characterization and photoreactivity, React. Kinet. Mech. Catal. 100 (2010) 55–70. https://doi.org/10.1007/s11144-010-0168-0.

[25] Y. Hu, Y. Pan, Z. Wang, T. Lin, Y. Gao, B. Luo, H. Hu, F. Fan, G. Liu, L. Wang, Lattice distortion induced internal electric field in TiO_2 photoelectrode for efficient charge separation and transfer, Nat. Commun. 11 (2020) 2129. https://doi.org/10.1038/s41467-020-15993-4.

[26] Y. Kim, S. Yang, E.H. Jeon, J. Baik, N. Kim, H.S. Kim, H. Lee, Enhancement of Photo-Oxidation Activities Depending on Structural Distortion of Fe-Doped TiO_2 Nanoparticles, Nanoscale Res. Lett. 11 (2016) 41. https://doi.org/10.1186/s11671-016-1263-6.

[27] S. George, S. Pokhrel, Z. Ji, B.L. Henderson, T. Xia, L. Li, J.I. Zink, A.E. Nel, L. Mädler, Role of Fe Doping in Tuning the Band Gap of TiO_2 for the Photo-Oxidation-Induced Cytotoxicity Paradigm, J. Am. Chem. Soc. 133 (2011) 11270–11278. https://doi.org/10.1021/ja202836s.

[28] W. Li, A. Kuc, C.F.J. Walther, T. Heine, Detailed Atomistic Investigation of Fe-Doped Rutile Phases, J. Phys. Chem. A. 119 (2015) 5742–5748. https://doi.org/10.1021/acs.jpca.5b01599.

[29] Y. Wang, R. Zhang, J. Li, L. Li, S. Lin, First-principles study on transition metal-doped anatase TiO_2, Nanoscale Res. Lett. 9 (2014) 46. https://doi.org/10.1186/1556-276X-9-46.

[30] T. Rawling, F. Buchholz, A.M. McDonagh, Convenient Synthesis and Purification of [Bu4N]2[Ru(4-carboxy-4-carboxylate-2,2'-bipyridine)2(NCS)2]: a Landmark DSC Dye, Aust. J. Chem. 61 (2008) 405–408. https://doi.org/10.1071/CH08037.

[31] M. Ye, X. Wen, M. Wang, J. Iocozzia, N. Zhang, C. Lin, Z. Lin, Recent advances

in dye-sensitized solar cells: from photoanodes, sensitizers and electrolytes to counter electrodes, Mater. Today. 18 (2015) 155–162. https://doi.org/10.1016/j.mattod.2014.09.001.

[32] J. Ji, H. Zhou, Y.K. Eom, C.H. Kim, H.K. Kim, 14.2% Efficiency Dye-Sensitized Solar Cells by Co-sensitizing Novel Thieno[3,2- b]indole-Based Organic Dyes with a Promising Porphyrin Sensitizer, Adv. Energy Mater. 10 (2020). https://doi.org/10.1002/aenm.202000124.

[33] M. Thelakkat, C. Schmitz, H.-W. Schmidt, Fully Vapor-Deposited Thin-Layer Titanium Dioxide Solar Cells, Adv. Mater. 14 (2002) 577. https://doi.org/10.1002/1521-4095(20020418)14:8<577::AID-ADMA577>3.0.CO;2-S.

[34] S. Ito, P. Liska, P. Comte, R. Charvet, P. Péchy, U. Bach, L. Schmidt-Mende, S.M. Zakeeruddin, A. Kay, M.K. Nazeeruddin, M. Grätzel, Control of dark current in photoelectrochemical (TiO_2/I^-–I_3^-) and dye-sensitized solar cells, Chem. Commun. 14 (2005) 4351–1453. https://doi.org/10.1039/b505718c.

[35] B. Peng, G. Jungmann, C. Jäger, D. Haarer, H.-W. Schmidt, M. Thelakkat, Systematic investigation of the role of compact TiO_2 layer in solid state dye-sensitized TiO_2 solar cells, Coord. Chem. Rev. 248 (2004) 1479–1489. https://doi.org/10.1016/j.ccr.2004.02.008.

[36] W.Y. Gan, S.W. Lam, K. Chiang, R. Amal, H. Zhao, M.P. Brungs, Novel TiO_2 thin film with non-UV activated superwetting and antifogging behaviours, J. Mater. Chem. 17 (2007) 952. https://doi.org/10.1039/b618280a.

[37] M.-E. Ragoussi, T. Torres, New generation solar cells: concepts, trends and perspectives, Chem. Commun. 51 (2015) 3957–3972. https://doi.org/10.1039/C4CC09888A.

[38] T. Horiuchi, H. Miura, K. Sumioka, S. Uchida, High Efficiency of Dye-Sensitized Solar Cells Based on Metal-Free Indoline Dyes, J. Am. Chem. Soc. 126 (2004) 12218–12219. https://doi.org/10.1021/ja0488277.

[39] F. Bella, N. Vlachopoulos, K. Nonomura, S.M. Zakeeruddin, M. Grätzel, C. Gerbaldi, A. Hagfeldt, Direct light-induced polymerization of cobalt-based redox shuttles: an ultrafast way towards stable dye-sensitized solar cells, Chem. Commun. 51 (2015) 16308–16311. https://doi.org/10.1039/C5CC05533D.

[40] D. Ganta, J. Jara, R. Villanueva, Dye-sensitized solar cells using Aloe Vera and Cladode of Cactus extracts as natural sensitizers, Chem. Phys. Lett. 679 (2017) 97–101. https://doi.org/10.1016/j.cplett.2017.04.094.

[41] H. Zhou, L. Wu, Y. Gao, T. Ma, Dye-sensitized solar cells using 20 natural dyes as sensitizers, J. Photochem. Photobiol. A Chem. 219 (2011) 188–194. https://doi.org/10.1016/j.jphotochem.2011.02.008.

[42] F. Kabir, M.M.H. Bhuiyan, M.S. Manir, M.S. Rahaman, M.A. Khan, T. Ikegami, Development of dye-sensitized solar cell based on combination of natural dyes extracted from Malabar spinach and red spinach, Results Phys. 14 (2019) 102474. https://doi.org/10.1016/j.rinp.2019.102474.

[43] T. Jalali, P. Arkian, M. Golshan, M. Jalali, S. Osfouri, Performance evaluation of natural native dyes as photosensitizer in dye-sensitized solar cells, Opt. Mater. (Amst). 110 (2020) 110441. https://doi.org/10.1016/j.optmat.2020.110441.

[44] L. Xu, C. Aumaitre, Y. Kervella, G. Lapertot, C. Rodríguez-Seco, E. Palomares, R. Demadrille, P. Reiss, Increasing the Efficiency of Organic Dye-Sensitized Solar Cells over 10.3% Using Locally Ordered Inverse Opal Nanostructures in the Photoelectrode, Adv. Funct. Mater. 28 (2018) 1706291. https://doi.org/10.1002/adfm.201706291.

[45] H. Kusama, H. Orita, H. Sugihara, TiO_2 Band Shift by Nitrogen-Containing Heterocycles in Dye-Sensitized Solar Cells: a Periodic Density Functional Theory Study, Langmuir. 24 (2008) 4411–4419. https://doi.org/10.1021/la703696f.

[46] N.S. Allen, N. Mahdjoub, V. Vishnyakov, P.J. Kelly, R.J. Kriek, The effect of crystalline phase (anatase, brookite and rutile) and size on the photocatalytic activity of calcined polymorphic titanium dioxide (TiO_2), Polym. Degrad. Stab.

150 (2018) 31–36. https://doi.org/10.1016/j.polymdegradstab.2018.02.008.

[47] M. Ismael, Enhanced photocatalytic hydrogen production and degradation of organic pollutants from Fe (III) doped TiO_2 nanoparticles, J. Environ. Chem. Eng. 8 (2020) 103676. https://doi.org/10.1016/j.jece.2020.103676.

[48] M. Khan, S. Woo, O. Yang, Hydrothermally stabilized Fe(III) doped titania active under visible light for water splitting reaction, Int. J. Hydrogen Energy. 33 (2008) 5345–5351. https://doi.org/10.1016/j.ijhydene.2008.07.119.

[49] W. Chakhari, J. Ben Naceur, S. Ben Taieb, I. Ben Assaker, R. Chtourou, Fe-doped TiO_2 nanorods with enhanced electrochemical properties as efficient photoanode materials, J. Alloys Compd. 708 (2017) 862–870. https://doi.org/10.1016/j.jallcom.2016.12.181.

[50] A. Pottier, C. Chanéac, E. Tronc, L. Mazerolles, J.-P. Jolivet, Synthesis of brookite TiO_2 nanoparticles by thermolysis of $TiCl_4$ in strongly acidic aqueous media, J. Mater. Chem. 11 (2001) 1116–1121. https://doi.org/10.1039/b100435m.

[51] A.I. Hochbaum, P. Yang, Semiconductor Nanowires for Energy Conversion, Chem. Rev. 110 (2010) 527–546. https://doi.org/10.1021/cr900075v.

[52] M. Law, L.E. Greene, J.C. Johnson, R. Saykally, P. Yang, Nanowire dye-sensitized solar cells, Nat. Mater. 4 (2005) 455–459. https://doi.org/10.1038/nmat1387.

[53] S. Li, Y. Wang, C. Gao, S. Ge, J. Yu, M. Yan, "Signal-off" photoelectrochemical DNA sensing strategy based on target dependent DNA probe conformational conversion using CdS quantum dots sensitized TiO_2 nanorods array as photoactive material, J. Electroanal. Chem. 759 (2015) 38–45. https://doi.org/10.1016/j.jelechem.2015.06.007.

[54] P. Soundarrajan, K. Sankarasubramanian, T. Logu, K. Sethuraman, K. Ramamurthi, Growth of rutile TiO_2 nanorods on TiO_2 seed layer prepared using facile low cost chemical methods, Mater. Lett. 116 (2014) 191–194. https://doi.org/10.1016/j.matlet.2013.11.026.

[55] W. Zhao, Y. Li, M. Zhang, J. Chen, L. Xie, Q. Shi, X. Zhu, Direct microwave–hydrothermal synthesis of Fe-doped titania with extended visible-light response and enhanced H_2-production performance, Chem. Eng. J. 283 (2016) 105–113. https://doi.org/10.1016/j.cej.2015.07.064.

[56] A. Singh, S. Kumari, R. Shrivastav, S. Dass, V. Satsangi, Iron doped nanostructured TiO_2 for photoelectrochemical generation of hydrogen, Int. J. Hydrogen Energy. 33 (2008) 5363–5368. https://doi.org/10.1016/j.ijhydene.2008.07.041.

[57] D. Sinha, D. De, D. Goswami, A. Mondal, A. Ayaz, ZnO and TiO_2 Nanostructured Dye sensitized Solar Photovoltaic Cell, Mater. Today Proc. 11 (2019) 782–788. https://doi.org/10.1016/j.matpr.2019.03.043.

[58] H. Bashar, M.M.H. Bhuiyan, M.R. Hossain, F. Kabir, M.S. Rahaman, M.S. Manir, T. Ikegami, Study on combination of natural red and green dyes to improve the power conversion efficiency of dye sensitized solar cells, Optik (Stuttg). 185 (2019) 620–625. https://doi.org/10.1016/j.ijleo.2019.03.043.

[59] M.J. García-Salinas, M.J. Ariza, Optimizing a Simple Natural Dye Production Method for Dye-Sensitized Solar Cells: Examples for Betalain (Bougainvillea and Beetroot Extracts) and Anthocyanin Dyes, Appl. Sci. 9 (2019) 2515. https://doi.org/10.3390/app9122515.

[60] A. Hernández-Martínez, M. Estévez, S. Vargas, R. Rodríguez, Stabilized Conversion Efficiency and Dye-Sensitized Solar Cells from Beta vulgaris Pigment, Int. J. Mol. Sci. 14 (2013) 4081–4093. https://doi.org/10.3390/ijms14024081.

[61] M.A. Almutairi, W.A. Farooq, M.S. AlSalhi, Photovoltaic and impedance properties of dye-sensitized solar cell based on nature dye from beetroot, Curr. Appl. Phys. 40 (2022) 119–125. https://doi.org/10.1016/j.cap.2021.07.010.

[62] S. Sathyajothi, R. Jayavel, A.C. Dhanemozhi, The Fabrication of Natural Dye Sensitized Solar Cell (DSSC) based on TiO_2 Using Henna And Beetroot Dye Extracts, Mater. Today Proc. 4 (2017) 668–676.

https://doi.org/10.1016/j.matpr.2017.01.071.

[63] C. Pathak, K. Surana, V. Kumar Shukla, P.K. Singh, Fabrication and characterization of dye sensitized solar cell using natural dyes, Mater. Today Proc. 12 (2019) 665–670. https://doi.org/10.1016/j.matpr.2019.03.111.

Chapter 5

HTL and HTL-free $Cs_2AgBiBr_6$ Double Perovskite Solar Cells



Solar Energy 298 (2025) 113733

Contents lists available at ScienceDirect

Solar Energy

journal homepage: www.elsevier.com/locate/solener

From HTL to HTL-free: Experimental and numerically modelled performance dynamics of $Cs_2AgBiBr_6$ double perovskite solar cells

Abhishek Srivastava, Manas Kasliwal, Parasharam M. Shirage *

Advanced Functional Materials Research Group (AFMRG), Department of Metallurgical Engineering and Materials Science, Indian Institute of Technology Indore 453552, India

ARTICLE INFO

Keywords:
$Cs_2AgBiBr_6$
Double perovskite solar cells
HTL-free PVs
Lead-free PV solutions
SCAPS-1D
($ZnO/TiO_2/WO_3/SnO_2$)-ETLs

ABSTRACT

For addressing the global energy crisis, this experimental and numerical study investigates HTL-free $Cs_2AgBiBr_6$ (CABB) double perovskite solar cells (DPSCs), highlighting their lead-free, non-toxic, and thermally stable properties. The FTO/TiO_2/CABB/Carbon-structured DPSCs showed >95 % PCE retention (1.63 % to 1.57 %) after 200 h. The underlying charge transport dynamics reveal a high R_{Rec} (1625 Ω), long τ_e (0.226 s), and efficient η_{cce} (89.65 %). Additionally, the estimated L_n (3.86 μm) and D_{eff} (27.33 $\mu m^2/s$) support the observed retention in device performance, confirming that interfacial stability and minimal charge recombination govern the long-term durability of the HTL-free DPSCs. However, the low photovoltaic (PV) performance (J_{SC} = 9.41 mA/cm^2, V_{OC} = 456.13 mV, FF = 0.38, and PCE = 1.63 %) is concerning for the futuristic technological development. Therefore, numerical simulations for optimizing the HTL and HTL-free DPSCs consisting of four different ETLs (TiO_2, SnO_2, WO_3, and ZnO) were conducted using SCAPS-1D, revealing ZnO as the optimal ETL for both HTL and HTL-free DPSCs. For HTL-DPSCs, ZnO achieved the highest performance (PCE: 27.30 %, J_{SC}: 23.83 mA/cm^2, V_{OC}: 1.29 V, FF: 0.89), followed by TiO_2 (25.48 %), WO_3 (25.42 %), and SnO_2 (22.63 %). Additionally, the HTL-free DPSCs showed overall ~4 % reduced efficiency due to higher interfacial recombination and limited charge extraction, with ZnO again leading (PCE: 23.09 %, J_{SC}: 23.00 mA/cm^2, V_{OC}: 1.15 V, FF: 0.85). This study highlights the optimization strategy that could bridge the simulation-experiment performance gap, positioning CABB as a leading lead-free double perovskite material for efficient and sustainable PV solutions.

This chapter demonstrates highly stable HTL-free CABB DPSCs (>95% PCE retention) having long carrier lifetime, and efficient charge collection, but with low efficiency. SCAPS-1D simulations identify ZnO as the optimal ETL, achieving up to 27.30% (HTL) and 23.09% (HTL-free), highlighting interfacial recombination as the key limitation. These challenges can be mitigated through device optimization, highlighting the potential of CABB as a stable lead-free perovskite absorber.

5.1 Introduction

As global energy demand continues to escalate, transitioning to renewable energy sources has become imperative to meet these needs sustainably while mitigating the environmental impacts associated with conventional fossil fuels.[1,2] Solar energy emerges as a driving force in the transition to sustainable energy, renowned for its limitless abundance and ease of access.[3,4] Single-junction organic-inorganic lead halide perovskites have rapidly attracted attention as promising alternatives to crystalline silicon solar cells, with an impressive power conversion efficiency (PCE) of 26.95%.[5] Their exceptional optoelectronic properties, such as a high absorption coefficient (α), extended carrier diffusion lengths (L_n), and a tunable bandgap (E_g), position them as frontrunners in the quest for high-performance photovoltaic technologies.[6–9] Despite their remarkable efficiency, the widespread commercialization of perovskite solar cells (PSCs) is hindered by significant challenges, including the high toxicity of lead and their susceptibility to environmental stressors such as elevated temperatures, moisture, and UV radiation. Although efforts to develop efficient lead-free perovskites continue, these alternatives currently lack the performance needed for widespread application.[10–14]

Various low-toxicity metal halides have been explored as alternatives to lead (Pb)-based perovskites, with tin (Sn^{2+}) receiving considerable attention due to its isoelectronic configuration and high carrier mobility ($\sim 200\,cm^2/V\cdot s$).[15–17] However, the rapid oxidation of Sn^{2+} to Sn^{4+} in ambient conditions severely limits device stability and performance longevity.[18] To overcome this, research has shifted toward lead-free double perovskites by replacing Pb^{2+} with heterovalent cation pairs (e.g., $M(I)^+$ and $M(III)^{3+}$), leading to the formation of $A_2M(I)M(III)X_6$-type structures. These materials, commonly referred to as elpasolite, offer structural and chemical versatility with over 350 known compositions.[19,20] First-principles studies have identified eleven such compounds with suitable E_g for photovoltaic applications, among which $Cs_2AgBiBr_6$ (CABB), $Cs_2AgBiCl_6$, and $(CH_3NH_3)_2AgBiBr_6$ have been successfully synthesized, demonstrating promising optoelectronic properties and ambient stability.[21,22]

Among these, CABB stands out due to its superior thermodynamic stability, high decomposition energy (~ 1.9-2.0 eV/atom), and 3D perovskite-like framework, which

contrasts with the 0D/2D structures and low dimensionality of other non-toxic alternatives such as $Cs_3Bi_2I_9$ or $Cs_3Sb_2Br_9$.[19] CABB also exhibits a relatively moderate exciton binding energy (~100-150 meV), lower defect density (~10^{15}-10^{16} cm^{-3}), and improved resistance to halide/cation vacancies compared to its bismuth or antimony-based counterparts. The substitution of Pb^{2+} with Ag^{+} and Bi^{3+} not only enhances lattice stability through increased Coulombic interactions but also contributes to better charge delocalization and suppressed non-radiative recombination. Despite its wider, indirect bandgap (~2 eV), CABB's robust environmental and thermal stability (>280 °C) and compatibility with bandgap-tuning strategies make it one of the most promising Pb-free candidates for stable, environmentally benign solar cell applications.

Although promising, CABB-based DPSCs exhibit modest efficiencies, capped at 4.23%, primarily due to inherent challenges, including large effective carrier masses, indirect Eg nature, and inefficient charge transport. In 2022, Zhang *et al.*[23] demonstrated that hydrogenation can reduce the E_g from 2.18 eV to 1.64 eV and improve carrier lifetime (τ_e) from 18.85 ns to 41.86 ns, leading to 6.37% PCE with good stability. This method enhances carrier mobility (μ) and energy level alignment, offering a solution to the performance limitations of CABB-based DPSCs. Some other studies have achieved PCEs of around 2.5% with FTO/TiO_2/CABB/Spiro-OMeTAD/Au configurations, 2.23% with an inverted planar heterojunction, and 1.44% with ITO/SnO_2/CABB/P3HT/Au.[24–26] Efforts to optimize alternative ETLs have led to efficiencies of up to 4.23%.[27] Despite these advancements, CABB-based DPSCs still underperform traditional lead-based PSCs, mainly due to their wide bandgap (~2 eV), which limits light absorption, and their high defect density, which reduces the carrier lifetime to about 13.7 ns.[28]

Recently, Yang *et al.*[29] developed an HTL-free gradient-structured FTO/TiO_2/IDL/CABB/Carbon-DPSC, achieving a high defect tolerance (~10^{16} cm^{-3}) and enhanced built-in electric field for efficient charge separation. Compared to conventional HTL-based CABB-DPSCs (V_{OC} = 1.09 V, J_{SC} = 3.80 mA cm^{-2}, FF = 0.40, PCE = 1.67%), the numerically optimized gradient HTL-free structure demonstrated significantly improved performance with V_{OC} = 1.69 V, J_{SC} = 12.11 mA cm^{-2}, FF = 0.89, and PCE = 18.21%. Shen *et al.*[30] enhanced HTL-free FTO/c-TiO_2/mesoporous-

TiO_2/CABB/Carbon-DPSCs by incorporating plasmonic Ag nanoparticles, leveraging far-field scattering and near-field enhancement to boost light absorption and increase V_{OC} via improved Fermi level alignment at the TiO_2/CABB interface. The optimized device achieved a PCE of 2.69% (vs 2.04% control) and retained 98% of its efficiency after 32 days under ambient conditions, marking one of the highest reported efficiencies for carbon-based HTL-free PSCs. Further, Ihtisham *et al.*[31] enhance the efficiency of CABB-DPSCs by incorporating 15% $MAPbBr_3$ via a sol-gel method. The modification induces compressive strain, reduces dislocation density by 38%, and increases crystallite size (27 to 33 nm), improving crystallinity. This $MAPbBr_3$ introduction also narrows the E_g from 1.94 to 1.90 eV, enhancing light absorption and dielectric properties. As a result, the DPSC's efficiency improves by 25% (5.05% vs. 4.04%) due to higher J_{SC} (6.91 vs. 5.81 mA cm^{-2}) and reduced recombination, as confirmed by EIS, which shows enhanced charge transport.

The wide E_g nature of CABB restricts light absorption to the high-energy region of the visible spectrum, thereby limiting photocurrent generation. Furthermore, the indirect E_g nature results in lower α compared to direct E_g materials, requiring thicker absorber layers that compromise charge extraction. CABB also suffers from low μ and short τ of the charge carriers due to high effective masses and prevalent trap-assisted recombination. These issues are compounded by a high density of intrinsic defects and grain boundaries, which contribute to non-radiative losses and reduced V_{OC} and FF. In addition, inefficient energy-level alignment and poor interfacial contact with commonly used ETLs and HTLs lead to suboptimal charge transport and increased recombination. Consequently, the PCE of CABB-based devices remains below 6%, significantly lower than their Pb-based counterparts. Processing challenges, such as achieving phase-pure, high-quality films with uniform morphology, further affect device reproducibility and scalability. Moreover, limited options for doping and band engineering constrain efforts to optimize the material's optoelectronic properties. Addressing these limitations is essential to unlocking the full potential of CABB in Pb-free PSCs.

Henceforth, simulations are crucial for understanding material properties and performance in CABB-based DPSC. Device simulations, particularly using software such

as wXAMPS[32] and SCAPS-1D[33], enable the optimization of physical parameters, leading to enhanced PCE and stability. Recent studies have simulated a maximum PCE of 11.69% and 11.32% for ITO/SnO_2/CABB/P_3HT/Au and ITO/SnO_2/CABB/P_3HT/Au-DPSCs, demonstrating the effectiveness of numerical modeling in improving device performance.[32] In a recent simulation of FTO/ZnO/CABB/NiO/Au structured DPSC, the PCE plummeted from 21.88% to a mere 1.58%, as the minority carrier lifetime was drastically shortened from 1 μs to 0.1 ns, highlighting the critical role of charge carrier dynamics in performance.[33] Ezema *et al.*[34] modelled a CABB-DPSC with an optimal architecture (FTO/ZnO/CABB/CFTS/Au). Initial device parameters yielded a PCE of 15.65%, which improved to 25.56% after systematic optimization of t_{layers}, N_a/N_d, N_{if}, and χ. Key optimized values included an ETL thickness of 0.04 μm, an absorber thickness of 0.4 μm, and defect densities of 10^{14}-10^{10} cm^{-2}. The optimized DPSC achieved a 38.8% improvement in PCE.

This study investigates the experimental study of FTO/TiO_2/CABB/Carbon-DPSC, followed by numerical studies of HTL- and HTL-free CABB-based DPSCs incorporating diverse electron transport layers (ETLs) such as TiO_2, SnO_2, ZnO, and WO_3, which play a key role in advancing sustainable PV technologies. Moreover, investigating HTL-free DPSC architectures simplifies device fabrication, reducing production complexity and cost. Evaluating different ETL materials provides insights into optimizing charge transport and reducing recombination losses, ultimately improving the overall PCE and stability. The novelty lies in the comprehensive numerical approach using SCAPS-1D to systematically analyze and compare ETL performance, paving the way for sustainable, affordable, and efficient DPSCs.

5.2 Experimental Section

5.2.1 Materials

The chemicals used to carry out this research work were as follows: fluorine-doped tin oxide (FTO, surface resistivity ~7 Ω/sq) sheets, cesium bromide (CsBr, ≥ 99%), silver bromide (AgBr, ≥ 99%), bismuth bromide ($BiBr_3$, ≥ 99%), hydrobromic acid (HBr, ≥ 98%), hydrochloric acid (HCl, ≥ 98%), dimethyl sulfoxide (DMSO, ≥ 99%), 2-propanol

(> 98%), extra-pure ethanol (> 99%), titanium isopropoxide ($Ti(OCH(CH_3)_2)_4$, ≥ 99%), polyvinylpyrrolidone (PVP, ≥ 99%), chlorobenzene (C_6H_5Cl, ≥ 99%), carbon black (≥ 99%), graphite powder (≥ 98%), ethyl cellulose ($C_{20}H_{38}O_{11}$, ≥ 99%), and terpineol ($C_{10}H_{18}O$, ≥ 98%). All chemicals were purchased from Sigma Aldrich and employed directly as received without undergoing additional purification.

5.2.2 HTL-free DPSC Fabrication

The DPSC fabrication process began with the deposition of the TiO_2-ETL (**Section 2.3.1**). For the absorber layer coating, the prepared CABB powder (**Section 2.3.2**) was used to make the CABB ink. The CABB ink was prepared by dissolving 319 mg (0.3 M) of CABB powder in 1 mL of DMSO and stirring at 80 °C for 4 hours until complete dissolution. Once the ETL deposition was complete, 100 µL of CABB absorber layer ink was spin-coated at 1000 rpm for the first 10 seconds, followed by 70 seconds at 3000 rpm, with an additional 150 µL of C_6H_5Cl added at the 30-second mark to improve film formation and larger grain sizes. This layer was dried at 250 °C for 5 minutes to ensure proper crystallization (**Figure 5.1(a)**). Finally, a carbon electrode was prepared using 1.5 g of conductive carbon, 0.5 g of graphite powder, and 0.2 g of ethyl cellulose ($C_{10}H_{18}O$), stirred at 1000 rpm for 24 hours to ensure uniformity, and applied using the doctor blade technique, followed by drying at 100 °C for 20 minutes. The complete schematic assembly of all the 16 fabricated HTL-free CABB-based DPSC (FTO/c-TiO_2/TiO_2 ETL/CABB/Carbon) is shown in **Figure 5.1(b)**.

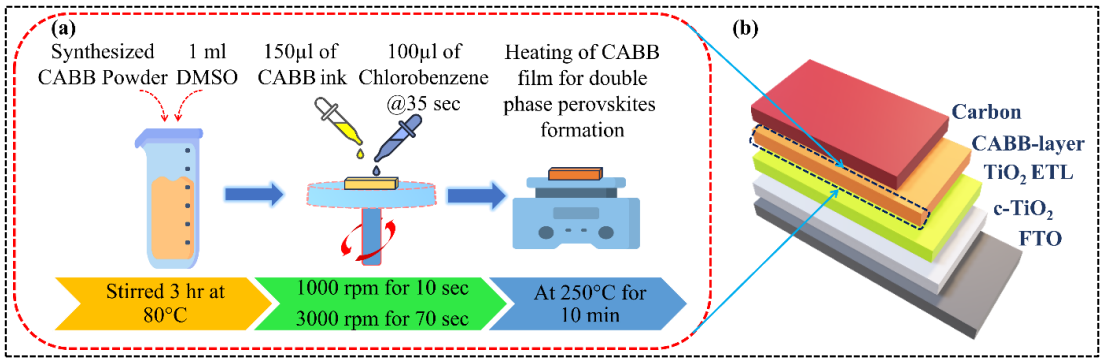

Figure 5.1 (a) Schematic of CABB-ink preparation and coating on TiO_2-ETL-coated FTO substrates. (b) HTL-free DPSC (FTO/c-TiO_2/TiO_2 ETL/CABB/Carbon) fabricated in the open environment.

5.3 SCAPS-1D Simulation Details

A lot of experimental research is underway to improve the performance and stability of planar n-i-p-structured CABB-based DPSCs, but it still lags behind commercially available solar cells.[35–37] This study examined four different ETLs-based DPSCs (FTO/(TiO_2/SnO_2/ZnO/WO_3)/CABB/spiro-OMeTAD/Au) using SCAPS-1D software. Additionally, HTL and HTL-free DPSCs were also examined to understand the role of the spiro-OMeTAD layer and its consequences. Spiro-OMeTAD was consistently used as the HTL in n-i-p-structured DPSC devices to evaluate its impact on device performance. Key parameters, including absorber thickness (t_{CABB}), interfacial defect density ($N_{if\ (ETL/CABB)}$ and $N_{if\ (CABB/HTL)}$), doping concentration (N_a/N_d), the HTL thickness (t_{HTL}), and ETL thickness (t_{ETL}), were systematically optimized. In this configuration, FTO serves as the front contact material, while Au is employed as the rear contact. The SCAPS-1D simulation software, developed by Marc Burgelman at the Department of Electronics and Information Systems (ELIS) at the University of Gent, Belgium, was used for the modeling studies.[38] This software usually simulates heterojunction and 1D multijunction solar cells based on their operational parameters and produces results that are comparable to experimental results.

SCAPS-1D is a powerful tool for simulating multi-layered solar cells, capable of modeling up to 7 layers. Within this simulation framework, we meticulously calculated key electrical properties, including power conversion efficiency (PCE), open-circuit voltage (V_{OC}), short-circuit current density (J_{SC}), quantum efficiency (QE), current density distribution, and fill factor (FF). To obtain these results, custom algorithms were developed and solved, ensuring precise simulations of the device's performance. SCAPS-1D employs a distinctive method to solve these algorithms, primarily relying on Poisson's equation (**equation 5.1**) and the continuity equations for both holes and electrons under steady-state conditions $\left(\frac{dp_n}{dt} = \frac{dn_p}{dt} = 0\right)$, as outlined in **equations 5.2** and **5.3**. This approach ensures accurate modeling of charge carrier dynamics within the device.

$$\frac{d}{dx}\left(-\varepsilon(x)\frac{d\psi}{dx}\right) = q[p(x) - n(x) + N_d^+(x) - N_a^-(x) + p_t(x) - n_t(x)] \quad 5.1$$

$$\frac{dp_n}{dt} = G_p - \frac{p_n - p_{n0}}{\tau_p} + p_n\mu_p\frac{d\xi}{dx} + \mu_p\xi\frac{dp_n}{dx} + D_p\frac{d^2p_n}{dx^2} \quad 5.2$$

$$\frac{dn_p}{dt} = G_n - \frac{n_p - n_{p0}}{\tau_n} + n_p \mu_n \frac{d\xi}{dx} + \mu_n \xi \frac{dn_p}{dx} + D_n \frac{d^2 n_p}{dx^2} \quad 5.3$$

Also, as we know, charge transport occurs due to drift and diffusion, and the electron (e^-) and hole (h^+) current densities can be written as **equations 5.4** and **5.5**, respectively.

$$J_n = n\mu_n \frac{\partial E_{Fn}}{\partial x} = q\left[n\mu_n E + D_n \frac{\partial n}{\partial x}\right] \quad 5.4$$

$$J_p = p\mu_p \frac{\partial E_{Fp}}{\partial x} = q\left[p\mu_p E - D_p \frac{\partial p}{\partial x}\right] \quad 5.5$$

where ε: permittivity of the photo harvester; ψ: electrostatic potential; N_d: donor density; N_a: acceptor density; n_t/p_t: trapped e^-/h^+; G_n/G_p: generation rate of e^-/h^+; τ_n/τ_p: e^-/h^+ lifetime; D_n/D_p: diffusion coefficient of e^-/h^+; μ_n/μ_p: mobility of e^-/h^+; E_{Fn}/E_{Fp}: quasi-Fermi level of e^-/h^+; and J_n/J_p: current density of e^-/h^+, respectively.

The e^-/h^+ generation rate, which is dependent on the distance (x), is described in **equation 5.6**. The recombination processes of electrons and holes were thoroughly examined, accounting for both radiative recombination and deep-trap mechanisms. The deep-trap recombination was modeled using the Shockley-Read-Hall (SRH) mechanism, with the bulk recombination rate represented by Equation (7) and the minority carrier τ varying with N_t, as shown in Equation (8). Additionally, interfacial recombination rates were estimated using the Pauwels-Vanhoutte model. [39]

$$G_{n,p}(x) = \int_0^{\infty} G_{n,p}(\lambda, x)d\lambda = \int_{\lambda 1}^{\lambda 2} \alpha(\lambda)\big(1 - r(\lambda)\big)N(\lambda, 0)Q(\lambda)e^{[-\alpha(\lambda)x]}d\lambda \quad 5.6$$

$$R_{RSH} = \frac{(np - n_i^2)}{\tau\left(p + n + 2n_i \cosh\left(\frac{E_i - E_t}{k_B T}\right)\right)} \quad 5.7$$

where r (λ): reflection coefficient; Q (λ): internal quantum efficiency; N (λ, 0): incident photon flux (Photons/s.m^2); E_i: intrinsic energy level; E_t: trap energy level.

Further, all simulation parameters, including optoelectronic properties, defect densities, and interfacial defect properties for the different layers used in the SCAPS-1D software to obtain the best-performing DPSC, are listed in **Tables 5.1**, **5.2**, and **5.3**. Specifically, **Tables 5.1** and **5.2** summarize various optoelectrical parameters of the FTO, ETL, CABB, and Spiro-OMeTAD layers, including thickness, bandgap, electron affinity, permittivity, band densities, mobility, and acceptor/donor densities.

Table 5.1 Typical optoelectrical properties of FTO, CABB, and Spiro-OMeTAD-HTL layer for SCAPS-1D simulation.

Parameters	**FTO** [33,40]	**$Cs_2AgBiBr_6$** [32,41]	**Spiro-OMeTAD** [41–43]
t_{layers} (nm)	300	100-1000	10-100
E_g (eV)	3.5	1.61	2.9
Electron affinity χ (eV)	4	3.72	2.2
Dielectric permittivity	9	5.8	3
CB effective density of states N_c (cm^{-3})	2.2×10^{18}	2×10^{18}	2.5×10^{19}
VB effective density of states N_v (cm^{-3})	1.8×10^{18}	1×10^{18}	1.8×10^{19}
μ_n (cm^2/V. s)	20	9.28	2×10^{-4}
μ_p (cm^2/V. s)	10	9.28	2×10^{-4}
N_d (cm^{-3})	2.0×10^{19}	0	1×10^{7}
N_a (cm^{-3})	0	1×10^{16}	1×10^{18}

Moreover, a neutral defect type was assumed to be located at the center of the E_g. For the CABB layer, a Gaussian energy distribution with a characteristic energy of 0.1 eV was selected to model the defect states. The 1.29 V of trap-filled limit voltage (V_{TFL}) for the CABB absorber was estimated by Wu *et al.*[26] with a $\tau_{n,p}$ of 843.6 ns, where the t_{ETL} and t_{HTL} are 5.1 µm and 1 µm, respectively. Additionally, it was assumed that the optical reflectance of FTO (front contact) is ~40%. With all these assumptions and values, the e^-/h^+ conductivity (σ_n/σ_p) is estimated using the formula given in **equation 5.8**. Further N_t can be calculated from **equation 5.9**, as shown below:

$$\sigma_{n,p} = \frac{1}{N_t V_{th} \tau_{n,p}} \tag{5.8}$$

$$N_t = \frac{2\varepsilon_0 \varepsilon V_{TFL}}{qt^2} \tag{5.9}$$

where V_{th} is known as the thermal velocity of electrons and holes, ε_0 is the vacuum permittivity, t is the thickness, and q is the elementary charge of the CABB layer.

Table 5.2 Typical optoelectrical properties of distinct ETL layers (TiO_2, SnO_2, WO_3, and ZnO) for SCAPS-1D simulation.

Parameters	**TiO_2** [44,45]	**SnO_2** [41,46,47]	**WO_3**	**ZnO** [48,49]
t_{ETL} (nm)	25-250	25-250	25-250	25-250
Eg (eV)	3.26	3.6	2.7	3.3
χ (eV)	4	4	3.8	3.72
Dielectric permittivity	32	8	4.8	9
N_c (cm^{-3})	2.2×10^{18}	2.2×10^{18}	2.2×10^{21}	2.2×10^{18}
N_v (cm^{-3})	1.8×10^{19}	1.8×10^{19}	2.2×10^{21}	1.8×10^{19}
μ_n (cm^2/V. s)	20	15	30	100
μ_p (cm^2/V. s)	10	15	30	25
N_d (cm^{-3})	1×10^{20}	1×10^{19}	6.35×10^{19}	1×10^{18}
N_a (cm^{-3})	0	0	0	0

Table 5.3 Defect parameters for different layers and interfaces of ETL/CABB and CABB/HTL.[32,50,51]

Parameters	**ETLs**	**HTL**	**CABB**	**CABB/HTL**	**ETL/CABB**
Defect Type	Neutral	Neutral	Neutral	Neutral	Neutral
σ_n (cm^{-2})	1×10^{-15}	1×10^{-15}	1×10^{-15}	1×10^{-18}	1×10^{-15}
σ_p (cm^{-2})	1×10^{-15}	1×10^{-15}	1×10^{-15}	1×10^{-16}	1×10^{-15}
Energetic Distribution	Single	Single	Gaussian	Single	Single
Energy level w.r.t E_v (above E_v) (eV)	0.6	0.650	0.6	0.6	0.6
Characteristic Energy (eV)	0.1	0.1	0.1	0.1	0.1
N_t (cm^{-3})	1×10^{15}	1×10^{15}	1×10^{14}	1×10^{10}	1×10^{12}

5.4 Results and Discussion

5.4.1 Experimental Results

As shown in **Figure 5.2(a)**, the XRD analysis of synthesized CABB powder was performed and refined using Fullprof Suite software. The XRD pattern was scanned over

2θ from 10 to 60 with a Cu $K_{\alpha 1}$ X-ray source (1.5406 Å). The obtained XRD diffraction peaks match well with JCPDS card No. 01-084-8699, confirming the phase purity of the CABB octahedra and good agreement with its cubic crystal structure in the Fm-3m (225) space group. All the lattice parameters and other details obtained from the refinement are mentioned in **Table 5.4**. All the characteristics XRD diffraction peaks (111), (200), (220), (311), (222), (400), (331), (420), (422), (511), (440), (531), (600), (620), (622), (444), and (640) are found at 2θ of 13.59º, 15.17º, 22.29º, 26.20º, 27.39º, 31.73º, 34.66º, 35.59º, 39.12º, 41.60º, 45.49º, 47.70º, 48.42º, 51.22º, 53.92º, 56.52º, and 59.06º, respectively and matching well with the available literature.

Table 5.4 Crystal type, space group, and lattice parameters obtained from refined p-XRD of CABB.

Crystal Structure	**Space Group**	**Lattice Parameters**		**Position Parameters**					
		a = b = c (Å)	Cell Volume ($Å^3$)	Atom	Occupancy	x	y	z	Multiplicity
Cubic	Fm-3m (225)	11.27	1429.73	Cs	0.043	0.75	0.25	0.25	8
		α = β = γ		Ag	0.021	1.00	0.50	0.50	4
		90°		Bi	0.021	0.50	0.50	0.50	4
				Br	0.130	0.75	0.50	0.50	24

The famous Debye-Scherrer equation was used to calculate the crystallite size (D), which is given in **equation 5.10**.

$$D = \frac{0.9\lambda}{\beta_{hkl} \cos\theta} \quad 5.10$$

$$\delta = \frac{1}{D^2} \quad 5.11$$

$$\varepsilon_m = \frac{\beta}{4 \tan\theta} \quad 5.12$$

where λ: wavelength of Cu-$K_{\alpha 1}$ source, β_{hkl}: full-width half maxima (FWHM), δ: dislocation density (**equation 5.11**), ε_m: micro strain (**equation 5.12**), and θ: half of the corresponding Bragg's angle.

Table 5.5 Estimated values of β, D, δ, and ε for (220), (400), and (440) highly intense diffraction peaks.

Diffraction Planes	β (Radians)	D (nm)	δ (nm^{-2})	ε
(220)	2.43×10^{-3}	58.18	2.95×10^{-4}	3.09×10^{-3}
(400)	2.83×10^{-3}	51.11	3.82×10^{-4}	2.49×10^{-3}
(440)	3.55×10^{-3}	42.51	5.53×10^{-4}	2.09×10^{-3}

Furthermore, the dislocation density (δ) and micro strains (ε) of the synthesized CABB powder were estimated according to Equations (11) and (12). All the estimated values for diffraction peaks (220), (400), and (440) are summarized in **Table 5.5**.

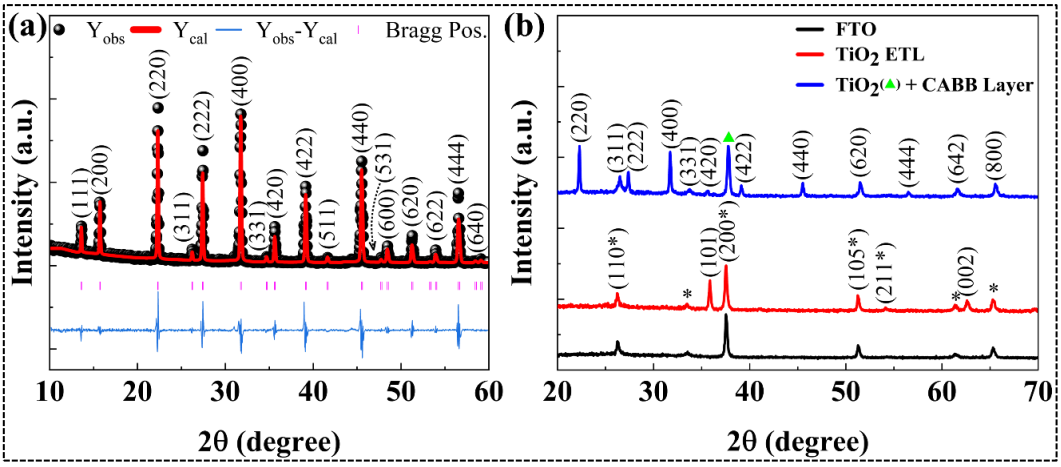

Figure 5.2 (a) Rietveld refined XRD pattern of as-synthesized CABB powder, (b) layer-by-layer XRD pattern of FTO, TiO_2 ETL, and TiO_2 + CABB layer comprising CABB-based HTL-free DPSC.

Additionally, layer-by-layer XRD patterns of bare FTO, TiO_2 Layer, and TiO_2 + CABB layer have been shown in **Figure 5.2(b)**. These results confirm the formation of

rutile phase TiO_2 ETL film on the FTO substrates, along with the good quality CABB film deposited on TiO_2 ETL.

X-ray photoelectron spectroscopy (XPS) was employed to gain deeper insights into the exceptional crystallinity and morphological characteristics of the solution-processed CABB powder, enabling a comprehensive understanding of its structural properties. **Figure 5.3(a)** represents the survey scan confirming the presence of all the characteristic elements, Cs, Ag, Bi, and Br. The core-level XPS spectra of carbon (**Figure 5.3(b)**) also arise from the background and the carbon tape used to mount the sample. Additionally, the core-level XPS spectra for Cs, Ag, Bi, and Br are presented in **Figure 5.3(c-f)**, with the stoichiometric compositional ratios detailed in **Table 5.6**, providing valuable insights into the material's elemental composition. It can be seen that the as-synthesized CABB closely matches the 2:1:1:6 atomic ratio of Cs/Ag/Bi/Br expected for CABB-double perovskite formation.

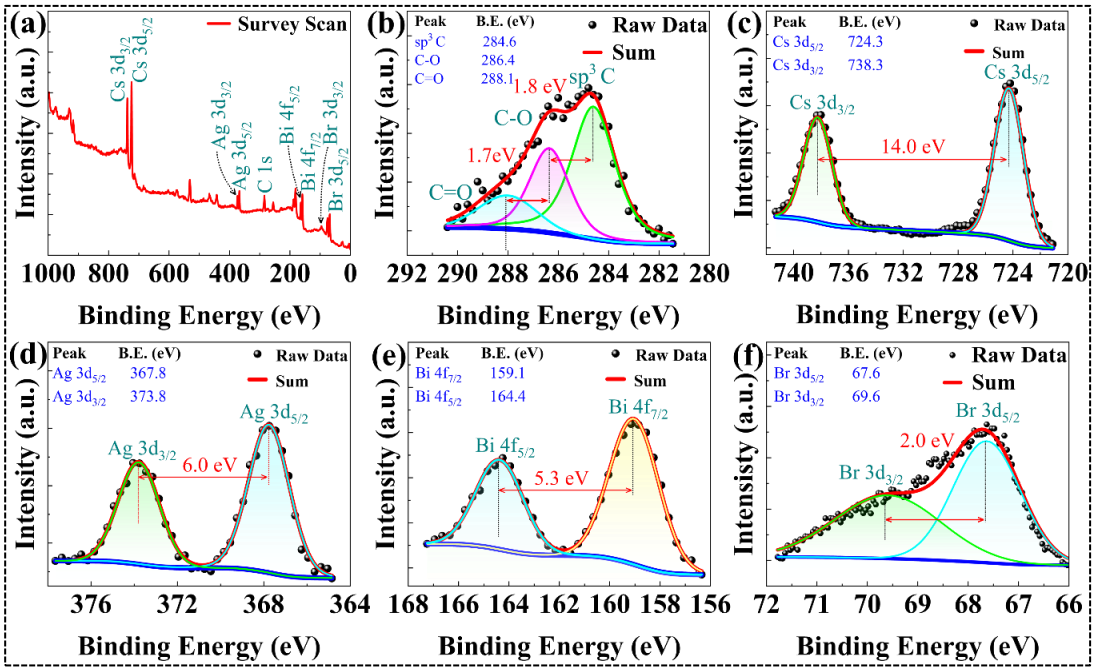

Figure 5.3 Detailed XPS patterns of (a) survey scan of CABB in the range 0 to 1000 eVs and characteristic core level XPS spectra of (b) C (1s), (c) Cs (3d), (d) Ag (3d), (e) Bi (4f), and (f) Br (3d).

Table 5.6 Summary of stoichiometric compositional data, including binding energy, FWHM, area, and at%, obtained from different core-level XPS spectra of CABB.

Elements	Core level	Binding Energy (eV)	FWHM (eV)	Area	Atomic (%)
Cs	Cs $(3d)_{3/2}$	738.3	2.82	1547.02	7.42
	Cs $(3d)_{5/2}$	724.3	2.99	1800.22	8.63
Ag	Ag $(3d)_{3/2}$	373.8	2.64	623.88	2.99
	Ag $(3d)_{5/2}$	367.8	2.67	675.38	3.24
Bi	Bi $(4f)_{5/2}$	164.4	2.56	563.21	2.7
	Bi $(4f)_{7/2}$	159.1	2.68	737.77	3.54
Br	Br $(3d)_{3/2}$	69.6	2.84	3209.75	15.39
	Br $(3d)_{5/2}$	67.6	2.82	4695.33	17.07

Crucially, maintaining the stoichiometric balance of Br within the chemical composition is vital for regulating the quality and consistency of the final compound. Bromine loss during vacuum processing and annealing is a challenge, which can be mitigated by annealing in a Br-rich atmosphere.

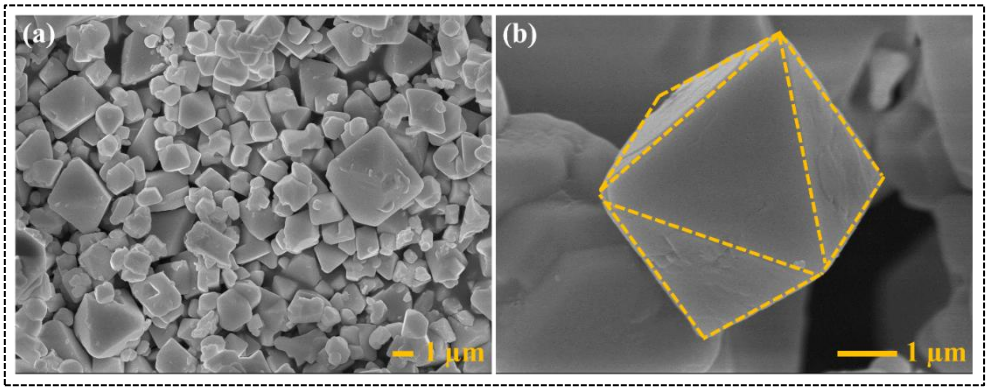

Figure 5.4 (a-b) FESEM images of as-synthesized CABB powder showing octahedral crystals having edges larger than 3 µm.

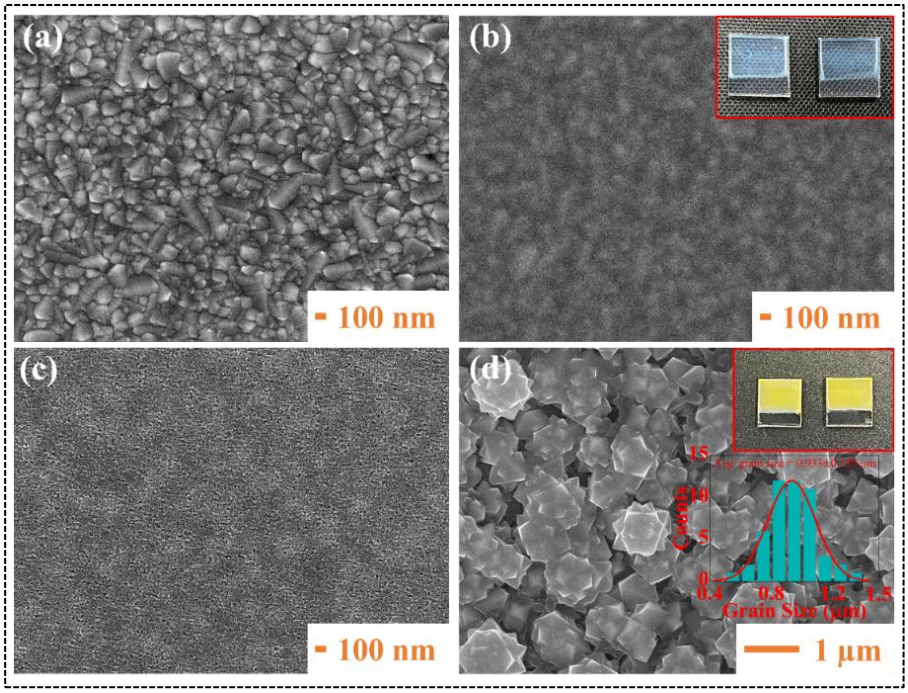

Figure 5.5 Top-view FESEM images of (a) FTO, (b) c-TiO_2, (c) TiO_2 ETL, and (d) CABB layer. Inset images attached (b) and (d) are the real-time images of opaque TiO_2 ETL and CABB absorber layers along with the grain size distribution.

However, conflicting reports on ideal growth conditions (Br-poor/Bi-rich vs. Br-rich/Bi-poor) highlight the need for deeper insights to optimize Br stoichiometry and minimize defect formation for high-quality films. As per Pauling's ionic radius rule, the ionic radius of Br^- is ideally compatible with octahedral coordination alongside Ag^+ within the double perovskite crystal framework. Halogens influence the bandgap of halide double perovskites, with larger halide ionic radii reducing the bandgap. Br^- provides optimal stability and bandgap suitability for CABB in photovoltaic applications. However, Br deficiency can lead to point defects, such as bromine vacancies (V_{Br}), which act as deep electron traps, adversely affecting photophysical properties.

The morphological studies of CABB powder and prepared films were carried out using FESEM. **Figure 5.4(a-b)** represents the octahedral formation of CABB crystals with an edge size of roughly 3 μm. Further, top-view FESEM images of FTO, c-TiO_2, TiO_2 ETL, and CABB layers are shown in **Figure 5.5(a-d)**. All the top-view FESEM images confirm the uniform deposition of TiO_2 ETL and CABB layer, along with the

attached real-time images (inset of **Figure 5.5(b)** and **(d)**). The grain size distribution analysis shown in the inset image of **Figure 5.5(d)** confirms the average grain size of 0.933±0.155 µm. Also, the EDX and elemental mapping shown in **Figure 5.6(a-b)** for TiO_2 ETL and CABB layer confirm the stoichiometric formation of the corresponding layers with uniform distribution of the elements across the film.

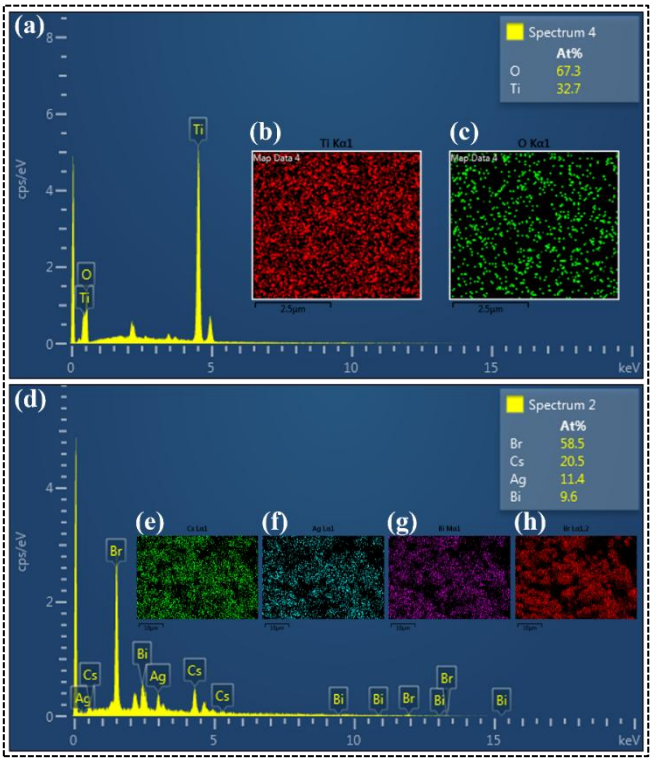

Figure 5.6 EDX and elemental mapping of (a-c) TiO_2 ETL and (d-h) as-synthesized CABB powder.

The photophysical properties of CABB films, critical for photovoltaic applications, were investigated using UV-vis absorption spectroscopy. **Figure 5.7(a-b)** depicts the UV-vis absorption spectra and Tauc's plot for TiO_2 ETL in the range of 300 to 800 nm. Absorption spectra of TiO_2 ETL show a clear absorption onset near 360 nm, reflecting the E_g of 3.59 eV. This reflects the suitability of TiO_2 ETLs for PV applications, given their excellent UV-light-blocking capabilities. Similarly, **Figure 5.7(c)** shows UV-vis absorption spectra with sharp peaks nearly at 600 nm for the CABB film. As no monotonic variations have been seen in crystallite size and peak shape, these peaks are not attributed to quantum-confined excitonic transitions.

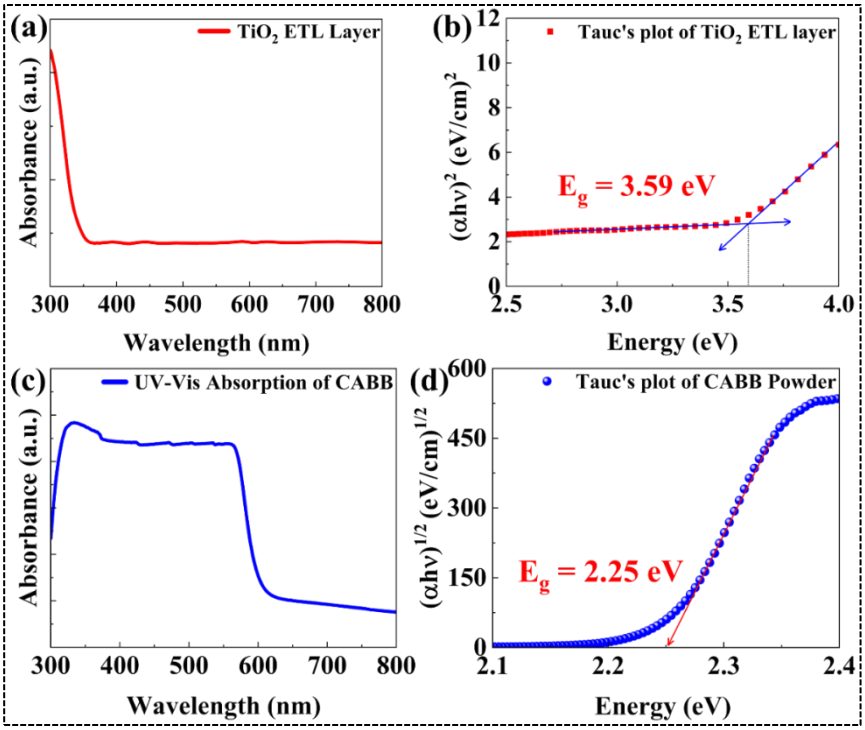

Figure 5.7 Photophysical properties of TiO_2 ETL and CABB absorber layer. (a-b) UV-vis absorption and Tauc's plot of TiO_2 ETL, and (c-d) UV-vis absorption and Tauc's plot of CABB photo absorber layer.

Thus, the resultant absorption peaks occur due to the s-p transition in Bi. Also, the estimated E_g for CABB (**Figure 5.7(d)**) shows the indirect nature of the bandgap, which is 2.25 eV. However, the resulting $E_{g(CABB)}$ is much higher and indirect in nature as compared to the traditional perovskite absorbers ($MAPbI_3$: 1.55 eV, $FAPbI_3$: 1.47 eV).[52] Therefore, by controlling factors such as synthesis method, doping engineering, structural modeling, and atomic arrangement disorder, one can minimize Eg and improve the nature of CABB for superior PV suitability.

Finally, an HTL-free planar lead-free CABB-based solar cell with the structure FTO/TiO_2/CABB/Carbon was fabricated and evaluated for photovoltaic performance. The J-V performance of the champion DPSCs, tested immediately after fabrication (**DT0**) and after 200 hours (**DT200**) in open air, is shown in **Figure 5.8(a)**. Herein, the annealing temperature of the solution-processed CABB film was optimized at 250°C for 5 minutes. The champion **DT0** and **DT200** show the best PCEs of 1.63% and 1.57%, respectively,

among all 16 devices. More interestingly, in **DT200**, the PCE decreases by ~3.68% (**Figure 5.8(b)**), with reduced J_{SC} (~17%) and enhanced V_{OC} (~6%). Also, a very small change (~10%) in the FF has been observed, leading to self-healing in the CABB layer arrangement.

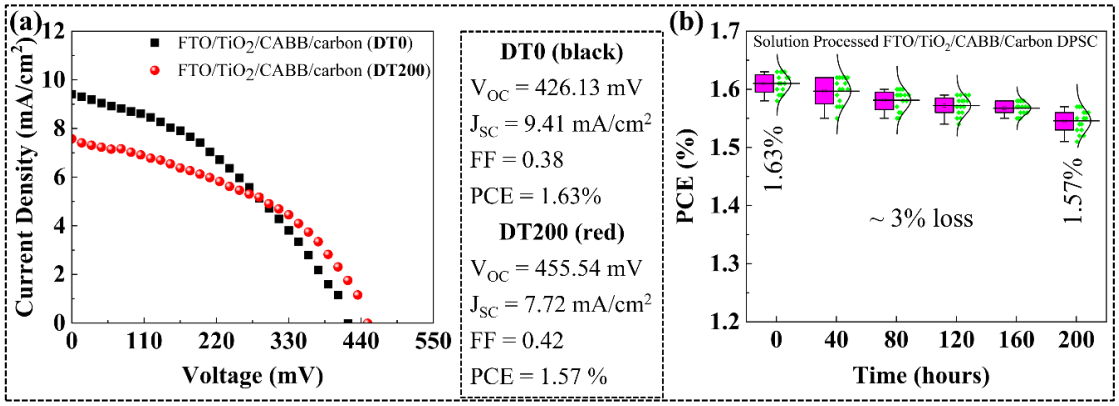

Figure 5.8 (a) J-V analysis of the DPSCs (**DT0** and **DT200**) structured as FTO/TiO_2/CABB/Carbon, (b) Open-air stability of all the 16 fabricated DPSCs with optimized solution-processed CABB absorber ink.

The decline in J_{SC} is likely due to degradation of the CABB active layer or the TiO_2 interface, leading to reduced carrier generation or increased recombination losses. On the other hand, the increased V_{OC} suggests excellent interfacial contact or lower trap-assisted recombination, while the marginal rise in FF indicates possible improvements in series or shunt resistance over time due to self-healing of the absorber layer. These findings highlight J_{SC}'s sensitivity to material or interfacial degradation, which accounts for the majority of the overall efficiency loss. Post-aging characterization, such as photoluminescence and impedance spectroscopy, along with stability testing under controlled conditions, is recommended to better understand and address the observed degradation. To further investigate charge-carrier dynamics and support the stability analysis, electrochemical impedance spectroscopy (EIS) was performed on the FTO/TiO_2/CABB-based electrodes in 0.1 M $TBAPF_6$ electrolyte in 100 mL DCM under dark conditions. This analysis summarized in **Figure 5.9(a-b)** and **Table 5.7** enabled the estimation of critical parameters such as electron lifetime (τ_e), diffusion length (L_n), effective electron diffusion coefficient (D_{eff}), charge collection efficiency (η_{cce}), effective

electron diffusion length (L_{eff}), effective electron diffusion lifetime (τ_d) offering a comprehensive understanding of carrier transport and recombination mechanisms.

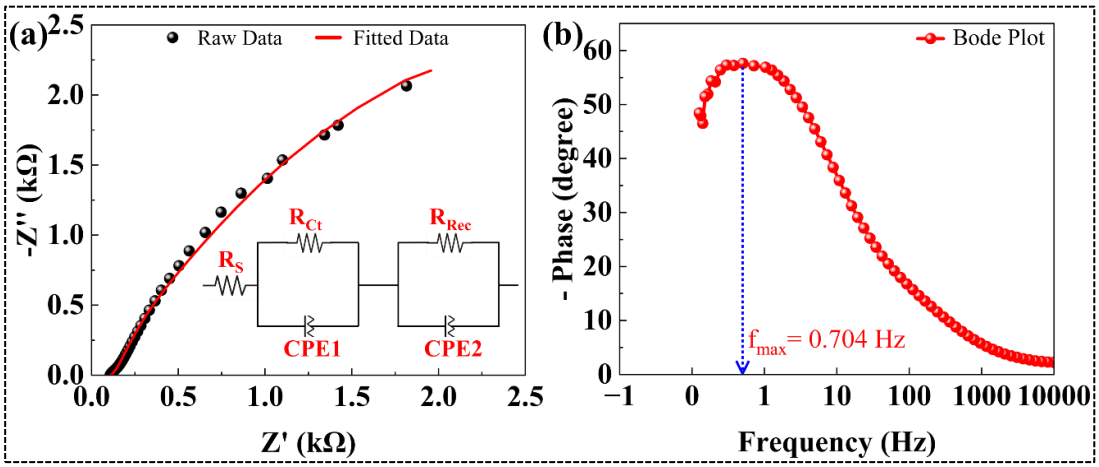

Figure 5.9 (a) Nyquist and (b) Bode plot of FTO/TiO_2/CABB electrodes in 0.1 M $TBAPF_6$ electrolyte in DCM solution for diffusion-recombination model. The inset image shows the equivalent electrical circuit model used to fit the Nyquist plot.

The visible smaller and larger semicircular arcs in **Figure 5.9(a)** represent the interfacial resistance of the counter electrode/electrolyte (R_{Ct}) and recombination of electrons at TiO_2/CABB/electrolyte (R_{Rec}). Also, the solution resistance is denoted as R_S, which further elucidates the interfacial kinetics and confirms the excellent stability and lower recombination losses in the fabricated HTL-free DPSCs. The Bode plot shown in **Figure 5.9(b)** was used to identify the peak frequency (f_{max}) and further calculate $\tau_e = 1/2\pi f_{max}$. Additionally, the DPSC exhibited a relatively long τ_e = 0.226 s, high D_{eff} = 27.33 $\mu m^2/s$, and substantial L_n = 3.86 µm, all of which support efficient carrier mobility and extraction. The η_{cce} = 89.65%, along with a L_{eff} = 3.09 µm and τ_d = 0.023 s, further shows strong agreement with the J-V result that the DPSC has excellent interfacial quality, minimal recombination losses, and is suitable for long-term application.

The high R_{Rec} and long τ_e strongly corroborate the improved V_{OC} (426 mV to 455 mV) observed in the J-V results. Moreover, the high η_{cce} (~90%) and well-maintained Leff indicate efficient charge collection even after prolonged exposure, validating minimal efficiency degradation. The relatively stable FF and elevated R_{Rec} also suggest

suppressed interfacial recombination, in agreement with the EIS-derived kinetics. These complementary insights from J-V and EIS measurements confirm that the HTL-free planar CABB-based DPSC retains excellent interfacial integrity and charge-transport stability, making it a viable candidate for sustainable, low-toxicity, and air-stable perovskite solar technologies.

Table 4.7 Summary of fitted EIS circuit parameters and deduced electrical parameters such as τ_e, L_n, D_{eff}, η_{cce}, L_{eff}, and τ_d.

R_S (Ω)	R_{Ct} (Ω)	R_{Rec} (Ω)	τ_e (s)	L_n (μm)	D_{eff} ($\mu m^2/s$)	η_{cce} (%)	L_{eff} (μm)	τ_d (s)
107.7	168.2	1625	0.226	3.86	27.33	89.65	3.09	0.023

However, to address the limitations observed in the experimental J-V performance, numerical simulations were conducted to optimize the device architecture and photophysical parameters. Four different ETLs were evaluated, focusing on their impact on charge transport and recombination dynamics. The simulations also accounted for the influence of bulk and interfacial defects, providing insights into defect-induced performance losses. Furthermore, the study explored HTL-free configurations with various counter electrodes to simplify the device structure while maintaining efficiency. These comprehensive simulations provide a deeper understanding of defect-mitigation strategies and design optimization to enhance device stability and performance.

5.4.2 Simulation Results

In this section, we optimized various ETLs by varying thickness, defect density, and HTL materials, including HTL-free devices, to identify the ideal photophysical parameters for efficient, stable DPSCs. One of the most critical factors affecting the performance of a DPSC is the band alignment across its interfaces, characterized by the conduction band offset (CBO: ETL/CABB) and valence band offset (VBO: CABB/HTL). High PCEs are typically observed at the ETL/CABB interface, particularly when a spike-like positive CBO is present. The CBO, defined as the difference between the electron

affinities of the CABB absorber and the ETL (**equation 5.13**), plays a pivotal role in shaping charge carrier dynamics and overall device efficiency.

$$CBO = \chi_{CABB} - \chi_{ETL} \quad 5.13$$

For small positive CBO values, charge carrier flow remains efficient, favouring bulk recombination in the absorber, which is desirable. However, a large positive CBO creates a barrier that impedes electron transport. Conversely, a negative CBO leads to a cliff-type junction, reducing the activation energy (E_A) below the absorber E_g, thereby enhancing interface recombination and degrading performance.

Additionally, a high α is one of the prominent factors influencing efficient light harvesting and photogeneration, which can be estimated using **equation 5.14**.

$$A = \left(A + \frac{B}{h\nu}\right)\left(\sqrt{h\nu - E_g}\right) \quad 5.14$$

where A, B, h, and ν are referred to the optical absorption parameters, Planck's constant, and frequency of the incoming light, respectively.

In this study, a standard absorption coefficient (~10^5 cm^{-1}) compatible with SCAPS-1D was used, based on the experimentally determined absorption onset of the CABB photo absorber layer (~600 nm). Furthermore, we optimized critical parameters of the ETL, CABB, and HTL layers, including thickness, R_S and R_{Sh}, interfacial defect densities (N_a and N_d), to achieve the best PV performance and maximize PCE.

5.4.2.1 FTO/ETLs/CABB/Spiro-OMeTAD/Au Simulations

Herein, we examined Spiro-OMeTAD-HTL-based DPSCs comprising four different metal oxide ETLs: TiO_2, SnO_2, WO_3, and ZnO. To make this study more reliable, the thicknesses of the other layers are kept constant and optimal. All the characteristic PV parameters (J_{SC}, V_{OC}, FF, and η) obtained by varying the thickness of distinguished layers are shown in **Figure 5.10(a-c)**. The thicknesses of the t_{ETL}, t_{CABB}, and t_{HTL} layers are scanned over 25-250 nm, 100-1000 nm, and 10-100 nm, respectively. Consequently, increasing the t_{CABB} enabled absorption of photons at longer wavelengths, thereby

enhancing ηcce (i.e., J_{SC}). According to **equation 5.15**, the V_{OC} depends on both the J_{SC} and the saturation current density (J_0), both of which are significantly influenced by t_{CABB}.

$$V_{OC} = \frac{kT}{q} \ln\left(\frac{J_{SC}}{J_0} + 1\right) \quad 5.15$$

Moreover, as t_{CABB} increases, R_S increases as well, further reducing the FF of DPSCs. Once the t_{CABB} matches the electrical diffusion length, the DPSCs saturate and further reduce the PCE for t_{CABB} values above 1000 nm. Also, a long minority carrier L is essential for efficient photogenerated carrier collection, as defined by **equation 5.16**:

$$L = \sqrt{\frac{kT}{q}\mu\tau} \quad 5.16$$

Therefore, the t_{CABB} and L in CABB-based DPSCs must be carefully balanced to optimize the performance. If $L << t_{CABB}$, carriers are likely to recombine before reaching the contacts, whereas overly thin absorbers limit photon absorption. For efficient operation, t_{CABB} should be sufficient but not exceed L, to achieve higher photon absorption with minimal recombination. Further, **equation 5.17** shows that reduced defect density increases carrier lifetimes, thereby increasing diffusion lengths. Consequently, minimizing defect density is critical, as higher values adversely affect cell performance. A concurrent analysis of absorber thickness and defect density is essential due to their interdependence.

$$\sigma_{n,p} = \frac{1}{N_t V_{th} \tau_{n,p}} \quad 5.17$$

where V_{th} is known as the thermal velocity of electrons and holes.

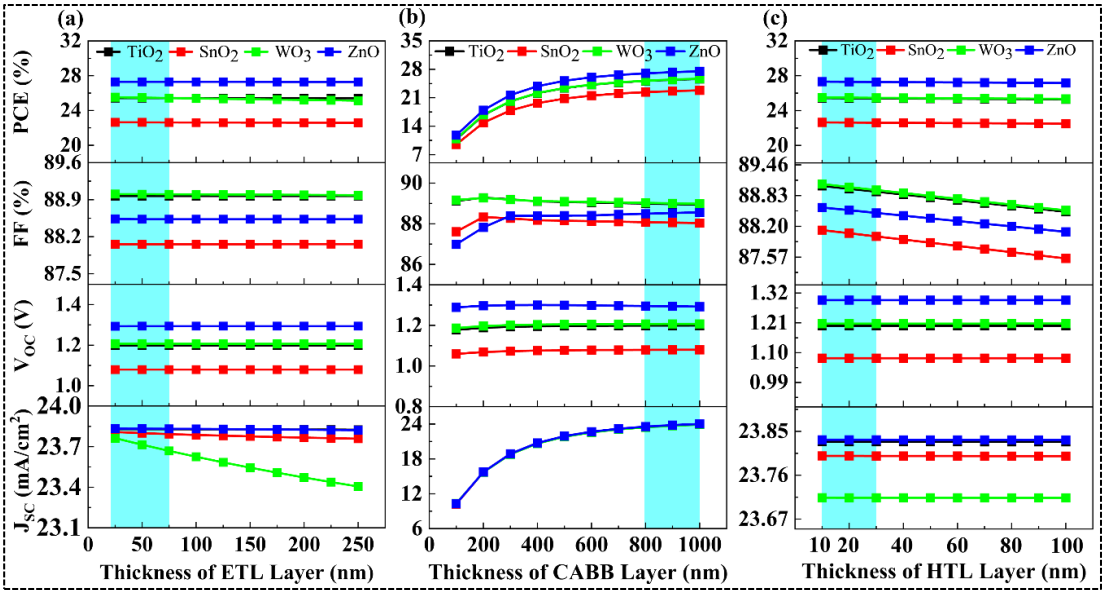

Figure 5.10 Comparative PV performances were obtained from DPSCs by varying the thickness of (a) ETL layers (25-250 nm), (b) CABB photo absorber layer (100-1000 nm), and (c) Spiro-OMeTAD HTL layer (10-100 nm). The portion highlighted in cyan is the optimal thickness range for each layer.

Additionally, PCE remains unchanged, with varying thicknesses across the four distinct ETLs. The observed flat PCE response with increasing t_{ETL} can be attributed to saturation of the electrical and interfacial benefits beyond a threshold. Initially, a moderate increase in t_{ETL} improves electron extraction and reduces surface recombination, but once the ETL becomes sufficiently thick (> 50-100 nm), further increases do not enhance performance due to limited contribution to light absorption and increased series resistance. Moreover, the V_{bi} becomes insufficient to drive electrons efficiently through the deeper ETL regions, potentially increasing recombination losses without any gain in V_{OC} and FF. As a result, the efficiency response flattens due to the trade-off between diminishing electrical improvements and increasing transport limitations. However, transmission of visible light decreases sharply with increasing t_{ETL} (> 250 nm), suggesting that lower t_{ETL} (25 to 75 nm) is best for DPSCs. Therefore, the t_{ETL}, t_{CABB}, and t_{HTL} layers are fixed at 50 nm, 800 nm, and 10 nm, respectively, for further optimization of the DPSCs. Also, it confirms that ZnO is the best ETL with a maximum PCE of 27.30%, along with J_{SC} = 23.83 mA cm^{-2}, V_{OC} = 1.29 V, and FF = 0.89.

The t_{HTL} is a critical determinant of DPSC performance. An ultra-thin HTL may leave portions of the absorber layer exposed, compromising device integrity, whereas an overly thick HTL introduces longer charge carrier paths, elevating recombination and resistance. Achieving the optimal t_{HTL} is essential to ensure complete coverage of the perovskite layer while minimizing series resistance. **Figure 5.10(c)** highlights how t_{HTL} impacts the FF and, by extension, the overall efficiency of the DPSC. As t_{HTL} increases from 10 nm to 100 nm, the V_{OC} remains unchanged, while J_{SC} shows a slight enhancement. Conversely, a substantial and consistent decrement is observed in FF, leading to a marginal improvement in PCE to 27.30% with a 75 nm ZnO-ETL, a 900 nm CABB photo absorber layer, and a 10 nm HTL. Therefore, a thinner HTL enhances transparency, improving photoabsorption, J_{SC}, and FF while reducing R_S. Moreover, it shortens charge transport distance, minimizing losses and boosting FF and η_{cce}.

Optimizing the thickness of distinct layers is crucial for efficient DPSC design, but the roles of N_t and N_a are equally important. Higher N_t creates additional recombination sites, increasing carrier losses and reducing overall device performance. In contrast, increasing the Na concentration enhances charge-carrier mobility and collection, thereby improving photovoltaic efficiency. As shown in **Figure 5.11(a-c)**, all the characteristic PV parameters are analyzed as a function of $N_{a\,(CABB)}$, $N_{t\,(CABB)}$, and $N_{a\,(HTL)}$ for CABB and HTL. Here, $N_{a\,(CABB)}$ and $N_{t\,(CABB)}$ range from 10^{12} to 10^{17} cm^{-3} and 10^{10} to 10^{19} cm^{-3}, along with $N_{a\,(HTL)}$ scanned in the 10^{14} to 10^{23} cm^{-3} range. Maintaining $N_{t\,(CABB)}$ below 10^{14} cm^{-3} ensures stable performance (**Figure 5.11(b)**), irrespective of the $N_{a\,(CABB)}$ level. However, exceeding this threshold leads to DPSC degradation, as defects in the absorber layer function as recombination centers and trap states, significantly diminishing carrier availability for photocurrent generation. These defects also reduce carrier lifetimes, induce material instability, and result in voltage losses, thereby lowering overall efficiency. Minimizing $N_{t\,(CABB)}$ is therefore critical for enhancing both efficiency and device stability.

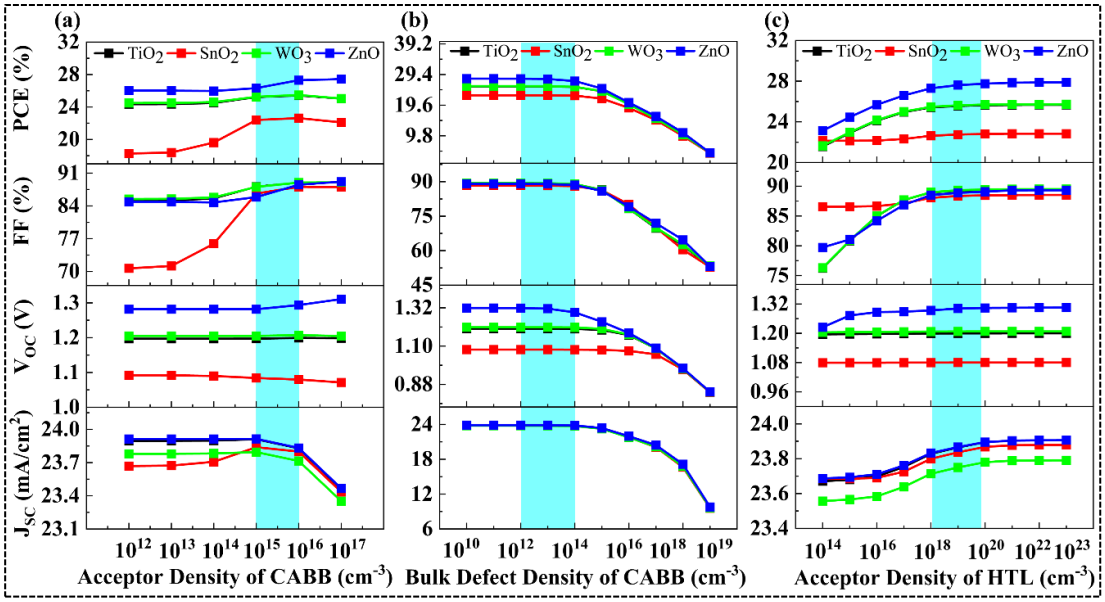

Figure 5.11 Variation in characteristic PV parameters with respect to the changes in (a) N_a of the CABB layer, (b) N_t of the CABB layer, and (c) N_a of the Spiro-OMeTAD HTL layer.

Figure 5.11(a) shows that the highest PCE values are achieved at a doping concentration of 10^{15}-10^{16} cm^{-3}, reflecting the opposing influences of V_{OC}, J_{SC}, and FF on device performance. Also, it indicates that V_{OC} and J_{SC} remain stable up to $N_{a\,(CABB)} = 10^{15}$ cm^{-3}, then increase slightly to 10^{16} cm^{-3}, beyond which they begin to decline. In contrast, a marginal increase in FF with rising doping concentration leads to overall performance improvements. Increasing $N_{a\,(CABB)}$ increases the charge-carrier density, improving charge separation and contributing to higher V_{OC} and J_{SC}. However, as the $N_{a\,(CABB)}$ concentration approaches the $N_{d\,(ETL)}$ level of the ETL, charge recombination increases, reducing V_{OC} and J_{SC}. While doping improves FF by enhancing conductivity and reducing series resistance and shunt leakage, the trade-off between increased conductivity and recombination impacts the overall PCE.

In this study, a fixed $N_{a\,(HTL)} = 10^{19}$ cm^{-3} for Spiro-OMeTAD HTL was explored for overall optimization. However, this numerical study investigated the effects of varying $N_{a\,(HTL)}$ from 10^{14} to 10^{23} cm^{-3} while keeping t_{HTL} constant at 10 nm. The results, presented in **Figure 5.11(c)**, showed similar trends in PV performance, consistent with the available literature. As $N_{a\,(HTL)}$ increased, J_{SC}, FF, and PCE showed an upward trend, in contrast to

the behavior observed when t_{HTL} was increased. Notably, V_{OC} remained constant in both cases, indicating stability across different $N_{a\ (HTL)}$ concentrations (**Figure 5.11(c)**) and t_{HTL} (**Figure 5.10(c)**). Beyond $N_{a\ (HTL)}=10^{19}$ cm^{-3}, further increases in doping concentration up to $N_{a\ (HTL)}=10^{23}$ cm^{-3} resulted in constant PCE as performance metrics approached saturation. This enhancement in DPSC performance can be attributed to HTL doping, which increases hole mobility, reduces resistive losses, improves overall device conductivity, minimizes recombination by neutralizing traps, and ensures proper energy-level matching for better charge-transfer efficiency.

Also, careful optimization of ETL parameters, including CBO and $N_{d\ (ETL)}$, is crucial for enhancing charge separation and minimizing recombination in DPSCs. The $N_{d\ (ETL)}$ level modifies the charge-carrier concentration and conductivity, thereby influencing the built-in electric field (E_{bi}), which is essential for efficient charge separation and transport in CABB-based DPSCs. Here, four ETLs (TiO_2, SnO_2, WO_3, and ZnO) were selected and analyzed for their roles in designing a highly efficient DPSC, providing insights into their impact on PV matrices and underlying mechanisms. As shown in **Figure 5.12(a)**, PCE values saturate at $N_{d\ (ZnO)}>10^{18}$ cm^{-3}, with consistent FF, J_{SC}, and V_{OC}, indicating an optimal doping level at which charge-carrier collection and transport are balanced.

However, the observed decrease in J_{SC} when $N_{d\ (ZnO)}$ exceeds 10^{19} cm^{-3} can be attributed to several factors. Excessive doping may introduce a higher density of trap states or defect sites, thereby facilitate non-radiative recombination and reducing current density. Additionally, high doping levels can lead to increased ionized impurity scattering, lowering carrier μ, and adversely affecting charge collection. Overdoping can also alter the conduction band alignment between the ZnO-ETL and the CABB layer, potentially creating energy barriers that hinder electron transport. Furthermore, changes in the optical properties of ZnO at high N_d levels, such as increased free-carrier absorption, may reduce the light available for photoelectric conversion. Thus, maintaining an optimal doping concentration is critical for balancing conductivity and recombination, ensuring maximum device performance.

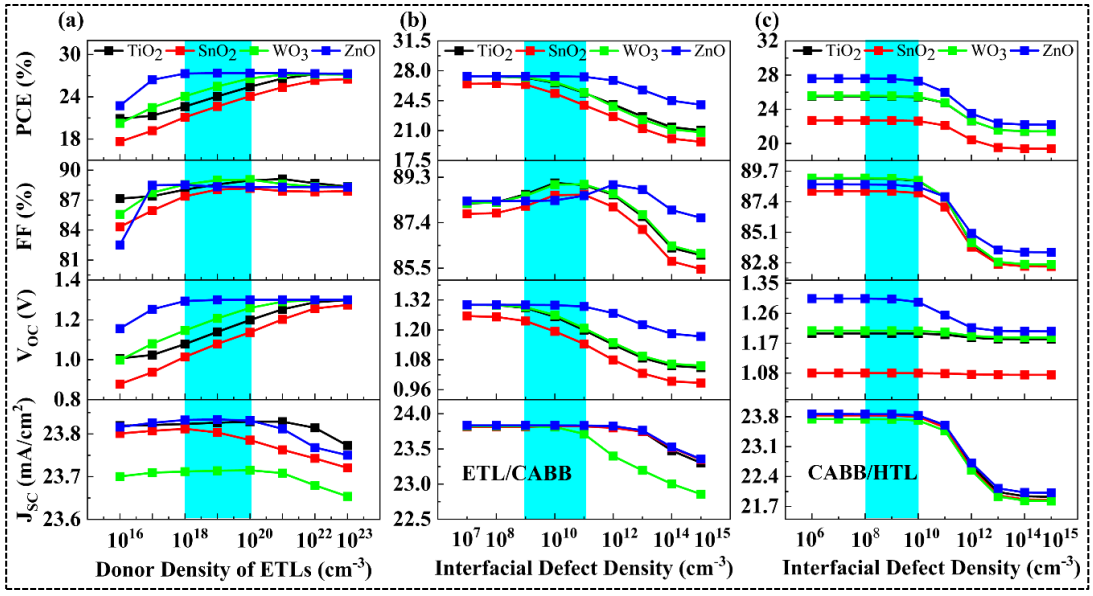

Figure 5.12 Comparative PV-performance analysis by varying (a) N_d of all ETL layers, (b) N_{if} between ETL/CABB layers, and (c) N_{if} between CABB/HTL layers.

Further, the N_{if} level has been optimized for the ETL/CABB and CABB/HTL interfaces. The interface band offset between CABB and HTL or ETL significantly impacts carrier recombination and affects V_{OC}/J_{SC}. Further, **Figure 5.12(b-c)** illustrates the PCE variation with N_{if} level for ETL/CABB (10^7-10^{15} cm^{-3}) and CABB/HTL (10^6-10^{15} cm^{-3}). The consistency of J_{SC}, V_{OC}, and PCE values for $N_{if\,(ETL/CABB)}$ in the range of 10^7 to 10^{11} cm^{-3} can be attributed to the minimal impact of interface defect density on charge transport and recombination within this range. The defect density should be low enough to maintain efficient charge extraction and suppress recombination. However, as $N_{if\,(ETL/CABB)}$ exceeds 10^{11} cm^{-3}, the increasing density of defect states at the ETL/CABB interface introduces trap-assisted recombination and hinders charge transfer, leading to significant reductions in J_{SC}, V_{OC}, and PCE. On the other hand, the drastic decrease in all PV parameters when $N_{if\,(CABB/HTL)}$ exceeds 10^{10} cm^{-3} is likely due to the introduction of significant interface defects, which increase recombination rates and disrupt charge transport. These defects create trap states that reduce the η_{cce} and the overall performance of the DPSC. However, the consistent V_{OC} for TiO_2, SnO_2, and WO_3 across the entire $N_{if\,(CABB/HTL)}$ range suggests that these materials maintain stable band alignment and effective

electron extraction even with increasing defect density, thus preventing significant changes in the V_{bi} and maintaining V_{OC}.

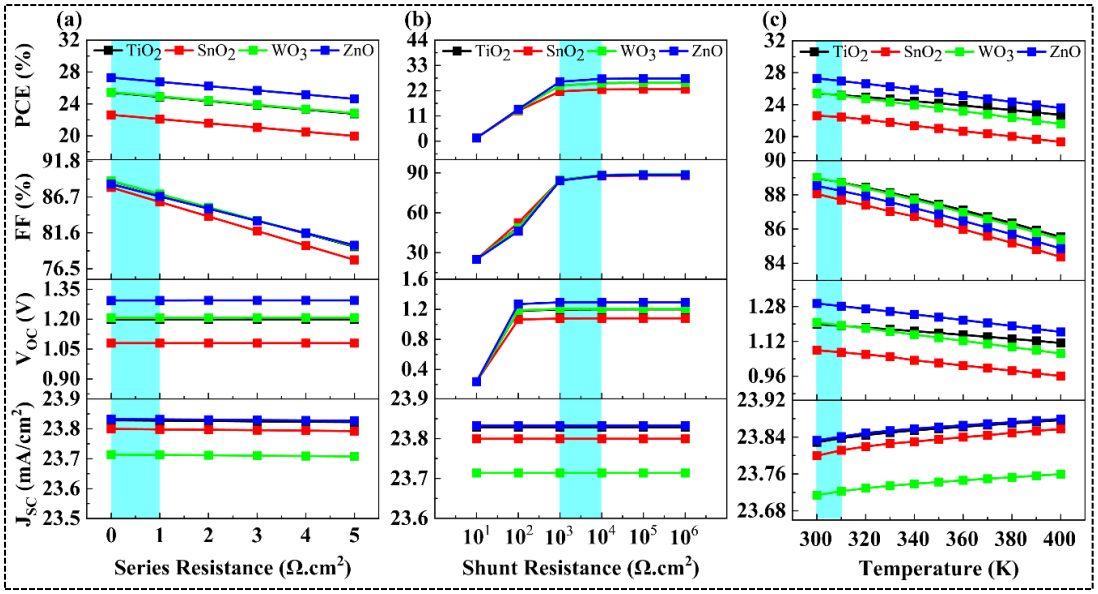

Figure 5.13 Variation of characteristic PV parameters by changing the (a) R_S, (b) R_{Sh}, and (c) T_{opt} of the DPSCs consisting of four distinct ETLs.

Along with t_{layers}, $N_{if(ETL/CABB\ and\ CABB/HTL)}$, and N_d/N_a densities, the performance of DPSCs is significantly influenced by R_S and R_{Sh}, primarily arising from contact resistance and interfacial resistance between the HTL, absorber, and ETL. **Figure 5.13(a)** shows the variation in R_S from 0 to 5 Ω.cm^2, revealing that the highest PCE values are achievable only at R_S = 0 Ω.cm^2. For all DPSCs consisting of different ETLs, J_{SC}, and V_{OC} remain unaffected, while the FF and PCE are reduced linearly due to increased ohmic losses. The linear decrease in PCE with increasing R_S (0-5 Ω·cm^2) is due to the direct impact of R_S on the FF, which in turn proportionally affects PCE. As R_S increases, it causes voltage drops within the device under operating conditions, limiting current flow and reducing FF without significantly altering J_{SC} or V_{OC} at low R_S values. This results in nearly linear degradation of PCE within this moderate RS range, where resistive losses are dominant but not yet severe enough to cause non-linear effects such as diode distortion or charge accumulation. Conversely, R_{Sh} improves DPSC performance by mitigating leakage currents caused by pinholes in the film. As R_{Sh} varies from 10 to 10^6 Ω·cm^2, maximum PCE values for all ETLs are observed at $R_{Sh} > 10^3$ Ω·cm^2 (**Figure 5.13(b)**) and

saturate later. Increased R_{Sh} enhances FF and V_{OC}, leading to improved PCE. While J_{SC} shows consistent behaviour for the whole range of R_{Sh}, which has a negligible impact on the DPSC's PCE, underscoring the role of parasitic resistances in determining DPSCs' efficiency.

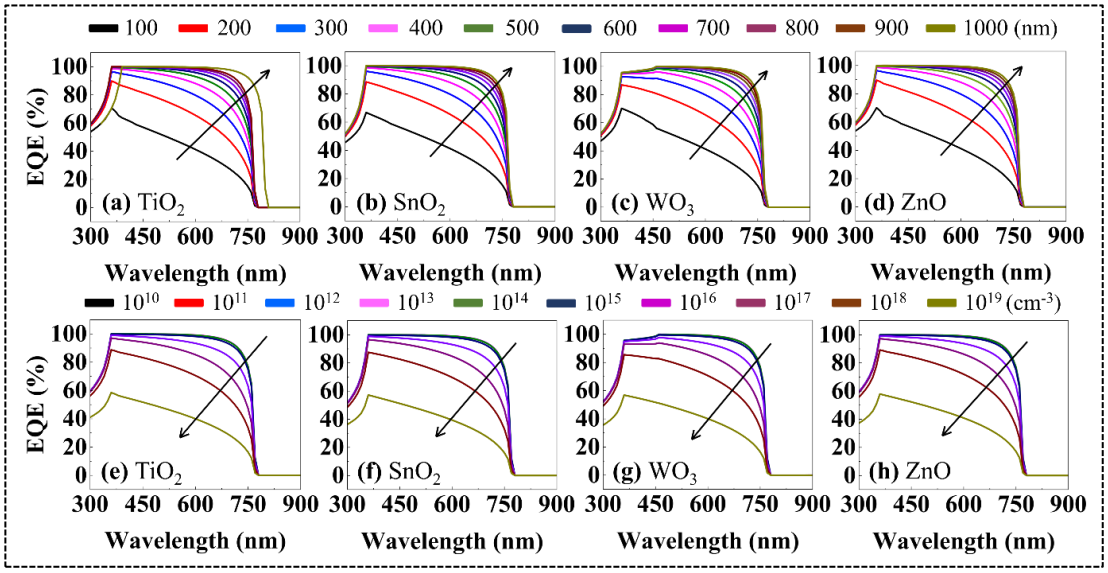

Figure 5.14 EQE variation for distinct ETL-based DPSCs by changing (a-d) t_{CABB}, and (e-h) $N_{t\,(CABB)}$.

Interestingly, the impact of varying operating temperature (T_{opt}) from 300 to 400 K on DPSC's performance highlights their adaptability to diverse environmental conditions. As shown in **Figure 5.13(c)**, the maximum PCEs for all ETLs are obtained at room temperature (i.e., 300 K). As the T_{opt} increases, the enhanced charge-carrier velocity boosts J_{SC} due to greater carrier excitation. However, elevated temperatures lead to higher internal resistance and a higher reverse saturation current, which diminishes FF, V_{OC}, and overall PCE. Therefore, T_{opt} analysis underscores the critical need for efficient thermal management in solar cell designs.

Further, the simulated external quantum efficiency (EQE) for FTO/(TiO_2/SnO_2/WO_3/ZnO)/CABB/HTL/Au devices was obtained by systematically varying t_{CABB} from 100 to 1000 nm and $N_{t\,(CABB)}$ from 10^{10} to 10^{19} cm^{-3}. The results shown in **Figure 5.14(a-d)** confirm a consistent increase in EQE with increasing t_{CABB} up to ~800 nm, attributable to enhanced photon absorption and increased charge-carrier generation.

Beyond 800 nm, however, EQE begins to saturate for all ETLs. This is due to the limited penetration depth of high-energy photons and the onset of recombination losses deeper within the absorber, which limit the collection of photogenerated carriers, consistent with trends observed in thickness-dependent J-V analysis (**Figure 5.10(b)**).

Conversely, when the $N_{t\,(CABB)}$ exceeds 10^{14} cm^{-3}, a significant decline in EQE is observed shown in **Figure 5.14(e-h)**. This behaviour is consistent with the trends observed in the J-V characteristics (**Figure 5.11(b)**), where higher $N_{t\,(CABB)}$ degrades η_{cce} and overall device performance. The EQE trends thus serve as corroborative metrics that confirm the adverse effects of bulk recombination and insufficient carrier extraction under suboptimal material conditions. In **Table 5.8**, we summarize the optimized parameters for the best-performing HTL- and HTL-free DPSCs with distinct ETLs.

Table 5.8 Summary of the various optimized parameters such as thickness, $N_{d(ETL)}$, $N_{a\,(CABB\ and\ HTL)}$, $N_{t\,(CABB)}$, $N_{if\,(ETL/CABB\ and\ CABB/HTL)}$, R_S, R_{Sh}, and T_{opt} for best performing HTL and HTL-free DPSCs.

Optimized Parameters	**Layers and Interfaces**	**FTO/ETLs/CABB/HTL/Au or FTO/ETLs/CABB/Au**
t_{layers} (nm)	ETLs	25-75
	CABB	800-1000
	HTL	10-20
N_d (cm^{-3})	ETLs	10^{18}-10^{20}
N_a (cm^{-3})	CABB	10^{15}-10^{16}
	HTL	10^{18}-10^{20}
N_t (cm^{-3})	CABB	10^{12}-10^{14}
N_{if} (cm^{-3})	ETL/CABB	10^{9}-10^{11}
	CABB/HTL	10^{8}-10^{10}
R_S ($\Omega.cm^2$)	DPSC	As low as possible (~ 0)
R_{Sh} ($\Omega.cm^2$)		~ 10^{3}-10^{4}
T_{opt} (K)		Room temperature (300 K)

In summary, the simulation results provide critical insights into optimizing solar cell parameters to enhance performance. The analyses revealed the importance of balancing key factors such as t_{CABB}, $N_{t\ (CABB)}$, $N_{if\ (ETL/CABB\ and\ CABB/HTL)}$, and $N_{d\ (ETL)}/N_{a\ (CABB/HTL)}$ to achieve efficient charge transport and minimize recombination losses. The interplay between R_S and R_{Sh} significantly influenced the FF and overall DPSC's efficiency, highlighting the role of precise material engineering in reducing parasitic losses. Additionally, the impact of T_{opt} demonstrated the sensitivity of performance metrics such as J_{SC}, V_{OC}, and FF to thermal variations, underscoring the need for robust thermal management strategies. Overall, the findings emphasize the need for a holistic approach to solar cell design that accounts for both intrinsic material properties and external environmental conditions.

5.4.2.2 FTO/ETLs/CABB/Au Simulations

Alternatively, HTL-free DPSCs (FTO/ETLs/CABB/Au) offer a simplified design, reduced fabrication costs, and improved stability by leveraging the perovskite absorber's inherent hole-transport properties. Eliminating the HTL avoids degradation issues, minimizes interfacial losses, and reduces reliance on expensive organic materials, making these devices more scalable and sustainable for industrial applications. Simulations with SCAPS-1D provide insights into optimizing performance for cost-effective, efficient solar energy solutions. HTL-free DPSCs rely on the CABB layer's dual role as a light absorber and hole transporter, eliminating the need for an additional HTL. The high μ_p of CABB-perovskite enables efficient charge extraction directly at the electrode interface, supported by effective energy band alignment that minimizes losses and ensures smooth hole transfer. The reduced number of interfaces lowers recombination losses by minimizing defect sites, while the absence of organic HTL materials enhances stability under environmental stresses such as moisture, oxygen, and heat. This streamlined architecture offers a cost-effective and robust solution for efficient solar energy conversion.

As the efficiency of hole extraction at the back contact is very important for HTL-free DPSCs, the valence-band energy (E_v) of CABB must align appropriately with the work function ($\Phi_{contact}$) of the back electrode, following **equation 5.18**.

$$E_v = \Phi_{contact} - \text{electron affinity of CABB} \qquad 5.18$$

Additionally, the PCE of DPSC can be tuned by adjusting the work function of the rear metal electrode, which influences the built-in potential (V_{bi}). As shown in **Figure 5.15(a-b)**, the efficiency of HTL-free DPSC follows a similar trend to that of HTL-based DPSCs but is lower than that of its counterparts, primarily due to inefficient hole extraction at the CABB/Au interface. Therefore, for a fixed t_{ETL} (50 nm), increasing t_{CABB} enhances PCE by improving J_{SC} and FF, driven by higher photogeneration in thicker double-perovskite films. Notably, V_{OC} decreases initially, then increases to saturation, reflecting variable band offsets between the CABB absorber and the ETLs.

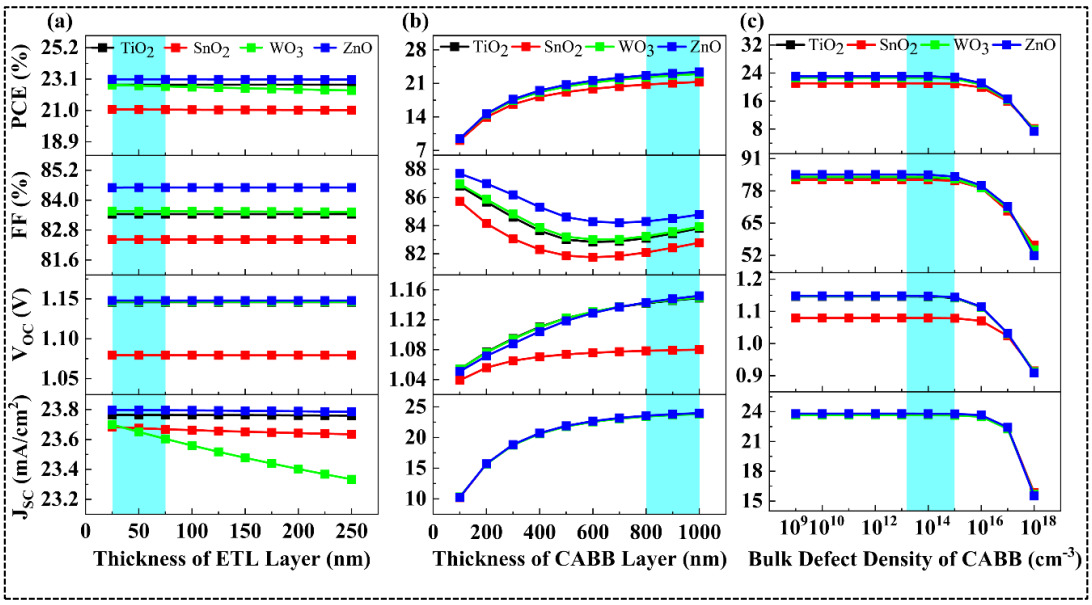

Figure 5.15 Comparative performance analysis of HTL-free CABB-based DPSCs with varying (a) t_{ETL}, (b) t_{CABB}, and (c) N_t of the CABB layer.

Optimizing the $N_{t\,(CABB)}$ and $N_{d\,(ETL)}$ in distinct ETLs significantly impacts the performance of HTL-free DPSCs, as illustrated in **Figure 5.15(c)** and **5.16(a)**. A reduction in the $N_{t\,(CABB)}$ films improves PCE, though it remains lower (~23% for ZnO) than that of devices incorporating the Spiro-OMeTAD-HTL layer (~27% for ZnO). Increasing the $N_{d\,(ETL)}$ concentration raises PCE from ~17% to >23% and saturates at $N_{d\,(ETL)} > 10^{18}$ cm^{-3}. Reduced bulk $N_{t\,(CABB)}$ ($<10^{14}$ cm^{-3}) yields consistent J_{SC} by minimizing recombination losses, while V_{OC} remains relatively constant, with FF primarily controlling PCE. Enhanced μ_n/μ_p, resulting from increased N_d concentration ($>10^{18}$ cm^{-3}) in ETLs, further

improves FF. The best PCEs achieved with optimized $N_{t\,(CABB)}$ and $N_{d\,(ETL)}$ for TiO_2, SnO_2, WO_3, and ZnO ETLs are 22.72%, 21.06%, 22.66%, and 23.09%, respectively.

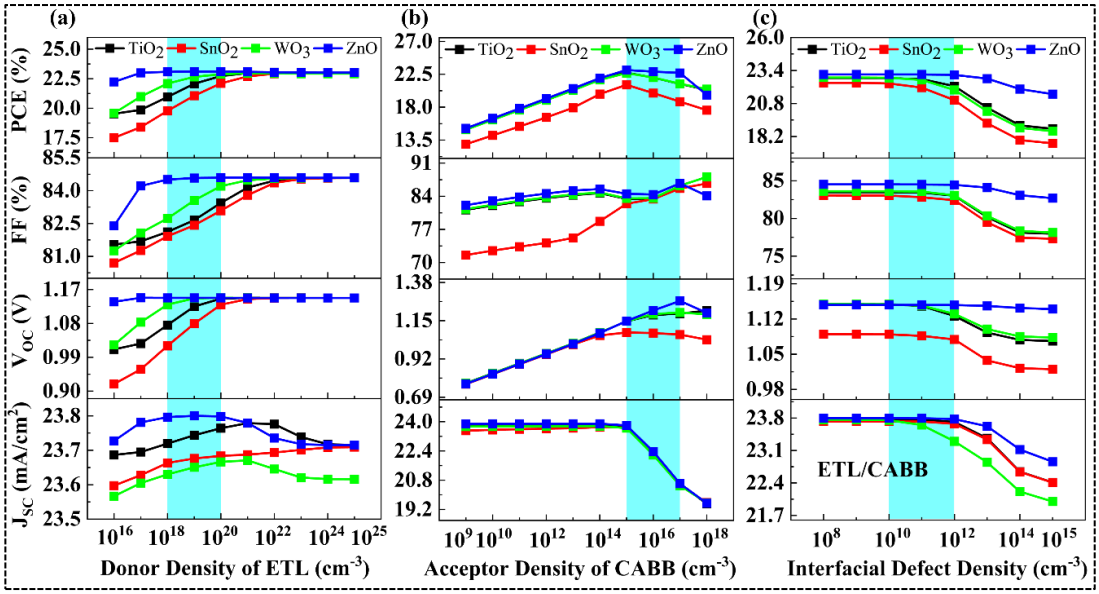

Figure 5.16 Variational analysis of PV parameters in HTL-free DPSCs by varying (a) N_d of ETL, (b) N_a of CABB, and (c) N_{if} at the ETL/CABB interface.

Further, optimizing the Na concentration in the CABB layer and the $N_{if\,(ETL/CABB)}$ interfacial defect density are equally important. As shown in **Figure 5.16(b-c)**, the PV parameters obtained from HTL-free DPSCs followed a similar trend as the DPSC with Spiro-OMeTAD-HTL but reduced average PCE by 4%. The optimum acceptor level concentration obtained from the simulation study is 10^{15}-10^{17} cm^{-3}, followed by maximum FF and V_{OC}. Also, the CBO at the ETL/CABB interface is crucial, as it manages charge-carrier recombination and can influence V_{OC}. Again, **Figure 5.16(c)** suggests that as $N_{t\,(ETL/CABB)}$ increases from 10^8 to 10^{15} cm^{-3}, all PV parameters exhibit constant behaviour up to 10^{12} cm^{-3} and then decrease sharply thereafter.

This is primarily because higher N_{if} at the ETL/CABB interface acts as non-radiative recombination centres, which facilitate the loss of photogenerated charge carriers before they can contribute to the photocurrent. Such defects can arise from lattice mismatches, poor interface passivation, or incomplete processing, leading to increased charge trapping and reduced charge transfer efficiency. Additionally, higher $N_{if\,(ETL/CABB)}$

disrupts the energy band alignment, impeding the effective extraction and transport of electrons from the CABB layer to the ETL. This degradation in interfacial properties not only lowers V_{OC} by introducing sub-bandgap recombination pathways but also reduces the J_{SC} due to suppressed carrier extraction.

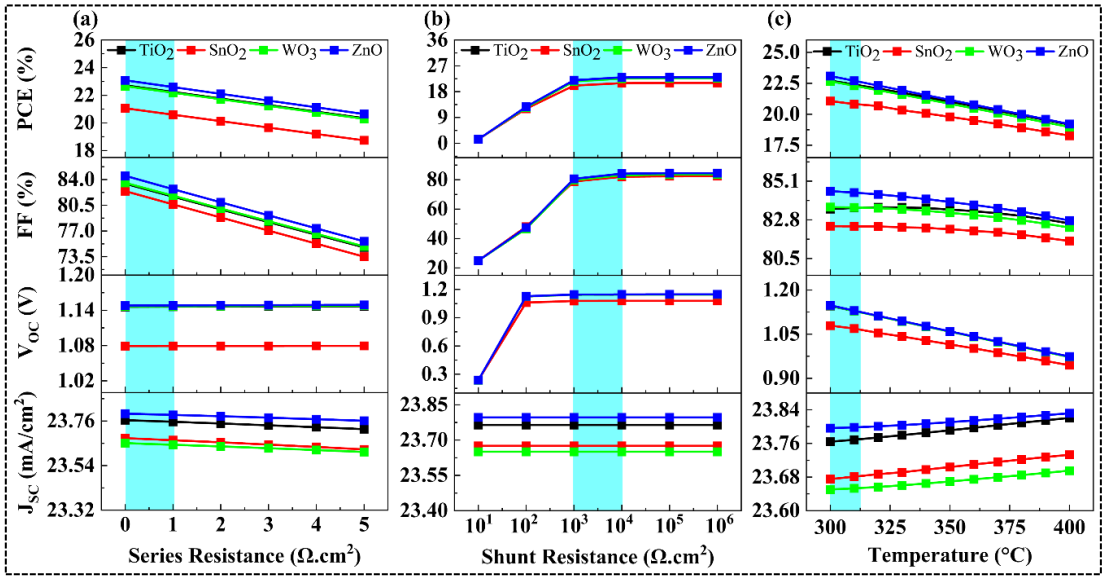

Figure 5.17 Comparative PV parameter analysis for HTL-free DPSCs by varying (a) R_S, (b) R_{Sh}, and (c) T_{opt} of the device.

The trends in R_S, R_{Sh}, and T_{opt} variations in HTL-free DPSCs closely resemble those in DPSCs with Spiro-OMeTAD layer because the underlying physical mechanisms governing charge transport and recombination are similar, as shown in **Figure 5.17(a-c)**. However, the absence of the HTL leads to a ~ 4% reduction in performance due to several interrelated factors. In HTL-free DPSCs, the Au electrode (often a catalytic surface) directly collects the photogenerated holes from the CABB photo absorber layer. This bypasses the selective charge extraction facilitated by the HTL in conventional DPSCs, leading to less effective hole transport and an increased probability of recombination at the CABB/Au interface. Consequently, the R_S increases slightly, indicating suboptimal charge-transfer pathways. Similarly, R_{Sh} decreases marginally because the absence of the HTL reduces the blocking effect that prevents leakage currents. Additionally, the EQE response for HTL-free DPSCs shown in **Figure 5.18(a-h)** followed a trend analogous to that observed in HTL-based devices, exhibiting a rise with increasing t_{CABB} up to ~ 800

nm, followed by saturation beyond 800 nm, due to limited photon absorption and increased carrier recombination in deeper layers. Likewise, a significant drop in EQE was observed when $N_{t\ (CABB)}$ exceeded 10^{14} cm^{-3}, attributed to enhanced trap-assisted recombination in the bulk CABB layer. This decline aligns closely with the corresponding J-V characteristics (**Figure 5.15(b-c)**), confirming the role of the HTL in facilitating efficient hole extraction and suppressing recombination losses at the back contact interface.

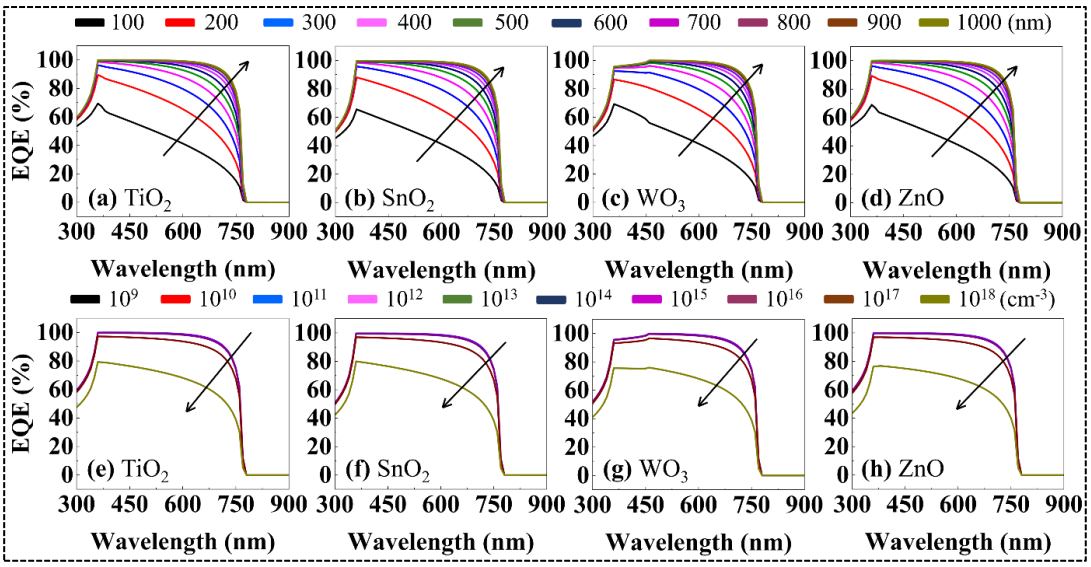

Figure 5.18 EQE variation for distinct ETL-based HTL free DPSCs by changing (a-d) t_{CABB}, and (e-h) $N_{t\ (CABB)}$.

Moreover, the lack of an HTL exacerbates thermal instability under ambient T_{opt} conditions. The HTL typically provides a thermal barrier and structural stability to the device. Without it, the interfacial quality between the CABB and other layers degrades faster under thermal stress, further lowering the device's performance. Collectively, these factors contribute to a comparable trend in resistances and temperature responses, but with a consistent reduction in performance (~4%) due to compromised charge selectivity, increased recombination, and reduced thermal stability. Further, the final optimized J-V curves for both HTL-based and HTL-free DPSCs are shown in **Figure 5.19(a-b)**. The J-V characteristics clearly show distinct J-V onsets for different ETLs. Among the tested ETLs, ZnO consistently exhibits superior performance, emerging as one of the most

effective ETLs due to its favourable conduction band alignment and μ_e. Interestingly, in both HTL-based and HTL-free configurations, the J_{SC} remains nearly constant at approximately ~23.5 mA cm^{-2}, suggesting efficient light absorption and charge generation across architectures.

However, a significant drop in V_{OC} is observed upon the removal of the HTL, which can be attributed to increased interfacial recombination at the CABB/Carbon interface due to the absence of selective hole extraction and blocking capabilities provided by HTLs. The HTL acts as a barrier to suppress back-electron transfer and ensures proper energy-level alignment for efficient hole extraction. Therefore, its absence leads to higher recombination losses and reduced V_{OC}. Interestingly, in HTL-free DPSCs, with all three photoanodes except SnO_2, the V_{OC} remains consistently high at around 1.1 V, which indicates that these ETLs (ZnO, WO_3, and TiO_2) possibly form favourable band alignments and surface energetics with the CABB layer, enabling sufficient V_{bi} for charge separation even without an HTL. In contrast, SnO_2 may introduce more interfacial traps or mismatched band alignment, thereby failing to maintain high V_{OC} in the HTL-free structure.

Moreover, to validate the simulation results and improve their reliability, the simulated external quantum efficiency (EQE) curves are shown in **Figure 5.19(c-d)**. The EQE analysis reveals that the optimized structural, optical, and electrical parameters of ETLs, CABB, and interfaces enhance charge-carrier generation, thereby improving EQE. However, beyond the optimized parameters listed in **Table 5.8**, the limited penetration of incident photons results in EQE saturation, indicating the device's optical absorption limit. The EQE spectra exhibit two distinct onset points: the first near 780 nm, attributed to the optical E_g of the CABB absorber, and the second below 400 nm, associated with the absorption range of distinct ETLs. These features confirm the spectral contributions of both layers and support the validity and physical consistency of the simulated results.

Finally, all the best-performing PV results are summarized in **Table 5.9**, confirming that ZnO is the best ETL for achieving high-performance CABB-based DPSCs. For DPSC structured as FTO/ETLs/CABB/Spiro-OMeTAD/Au, the maximum PCE trend obtained for different ETLs is as ZnO (27.30%) > TiO_2 (25.48%) > WO_3

(25.42%) > SnO_2 (22.63%). Although the overall performance in HTL-free DPSCs reduced substantially, following a similar trend as ZnO (23.09%) > TiO_2 (22.72%) > WO_3 (22.66%) > SnO_2 (21.06%).

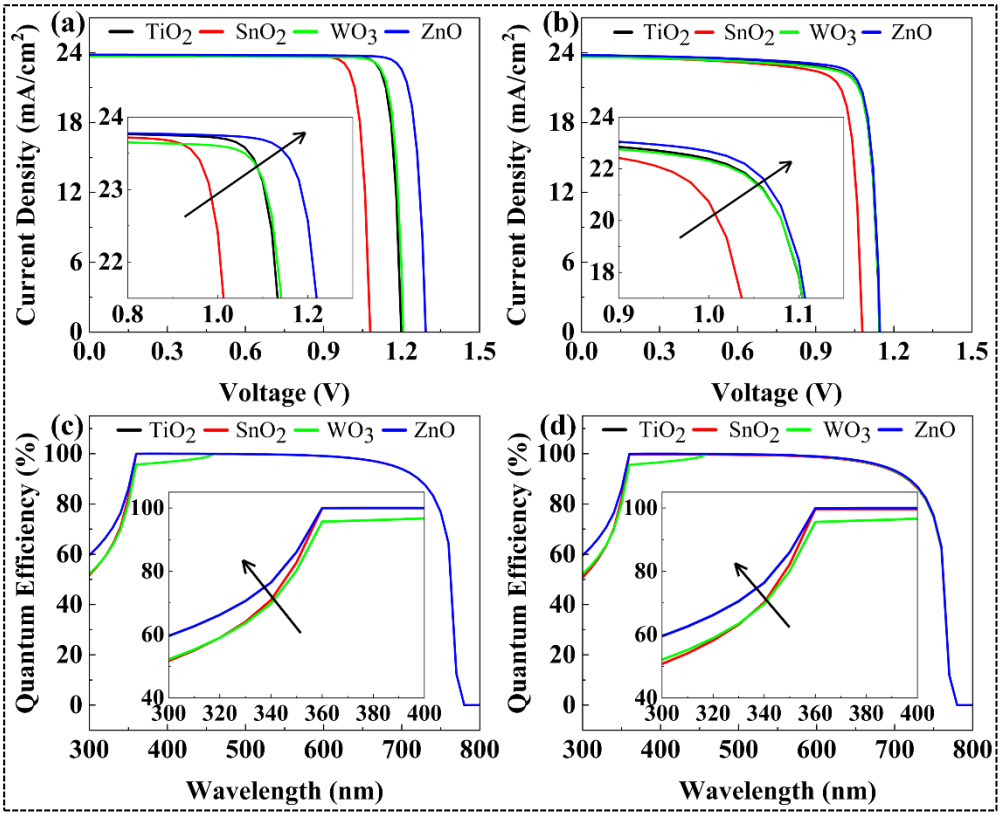

Figure 5.19 Final J-V variation of (a) FTO/ETLs/CABB/Spiro-OMeTAD/Au, and (b) HTL-free FTO/ETLs/CABB/Au-based DPSCs. (c-d) corresponding EQE for FTO/ETLs/CABB/Spiro-OMeTAD/Au and HTL-free FTO/ETLs/CABB/Au-DPSCs.

Table 5.9 Summary of the PV parameters obtained from best-performing CABB-based DPSCs, including experimental (FTO/TiO_2/CABB/Carbon) and simulation (FTO/ETLs/CABB/Spiro-OMeTAD/Au & FTO/ETLs/CABB/Au) results.

DPSC Structure	V_{OC} (V)	J_{SC} (mA cm^{-2})	FF	PCE (%)	Ref.
FTO/TiO_2/CABB/Carbon	0.426	9.41	0.38	1.63	**This Work**
FTO/TiO_2/CABB/Carbon	0.456	7.72	0.42	1.57	

FTO/c-TiO_2/mp-TiO_2/CABB/spiro-OMeTAD/Au	0.98	3.93	0.63	2.43	[24]
ITO/Cu-NiO/CABB/C_{60}/BCP/Ag	1.01	3.19	0.69	2.23	[25]
FTO/c-TiO_2/m-TiO_2/CABB-Indoline/Spiro-OMeTAD/Ag	0.73	8.24	0.70	4.23	[27]
FTO/TiO_2/CABB/Spiro-OMeTAD/Au	1.09	3.80	0.40	1.67	[29]
FTO/c-TiO_2/mp-TiO_2/CABB/carbon	1.12	3.41	0.70	2.69	[30]
FTO/TiO_2/CABB/Spiro-OMeTAD/Au	1.20	23.83	0.89	25.48	**This Work**
FTO/SnO_2/CABB/Spiro-OMeTAD/Au	1.08	23.80	0.88	22.63	
FTO/WO_3/CABB/Spiro-OMeTAD/Au	1.21	23.71	0.88	25.42	
FTO/ZnO/CABB/Spiro-OMeTAD/Au	1.29	23.83	0.89	27.30	
FTO/TiO_2/CABB/Au	1.15	23.76	0.83	22.72	
FTO/SnO_2/CABB/Au	1.08	23.68	0.82	21.06	
FTO/WO_3/CABB/Au	1.15	23.65	0.84	22.66	
FTO/ZnO/CABB/Au	1.15	23.80	0.85	23.09	
ITO/SnO_2/CABB/P_3HT/Au	2.03	6.39	0.90	11.69	[32]
FTO/ZnO/CABB/NiO/Au	1.29	20.69	0.82	21.88	[33]
FTO/ZnO/CABB/CFTS/Au	1.4	19.98	0.90	25.56	[34]

Therefore, to design efficient and stable CABB-based DPSCs, advancements in interface engineering and material optimization are essential. The observed efficiency

trends (ZnO > TiO_2 > WO_3 > SnO_2) suggest the need for tailored ETLs with improved band alignment and reduced recombination. In HTL-free configurations, strategies like ETL doping and passivation can enhance charge transport, while carbon-based electrodes require modification with conductive additives or catalytic nanoparticles to improve performance (currently 1.63%) and stability (up to 200 h). Additionally, advanced encapsulation techniques are critical to minimizing degradation. Combining these approaches can significantly enhance efficiency and operational durability for CABB-based DPSCs, making them viable for practical applications.

5.5 Conclusion

This work presents a comprehensive approach for designing highly efficient and stable lead-free CABB-DPSCs by combining experimental and numerical studies. Initially, an HTL-free FTO/TiO_2/CABB/Carbon-structured DPSC was fabricated under open-air conditions, which achieved a champion PCE (DT0) of 1.63% (J_{SC} = 9.41 mA cm^{-2}, V_{OC} = 0.43 V, FF = 0.38) and retained > 95% PCE (DT200) after 200 hours. The underlying charge-transport dynamics reveal a high R_{Rec} (1625 Ω), a long τ_e (0.226 s), and efficient η_{cce} (89.65%). Additionally, the estimated L_n (3.86 μm) and D_{eff} (27.33 $\mu m^2\ s^{-1}$) support the observed retention in device performance, confirming that interfacial stability and minimal charge recombination govern the long-term durability of the HTL-free DPSCs. Although the obtained performance of **DT0** and DT200-DPSCs is relatively low compared to conventional commercial PV systems, their excellent stability under ambient conditions holds significant promise for real-world applications.

To further study the performance improvement, we designed a systematic numerical approach to optimize HTL- and HTL-free DPSCs, incorporating four ETLs: TiO_2, SnO_2, WO_3, and ZnO. The optimization considered various parameters, including t_{layers}, $N_{d\ (ETL)}$, $N_{a\ (CABB/HTL)}$, $N_{t\ (CABB)}$, $N_{if\ (ETL/CABB\ and\ CABB/HTL)}$, R_S, and R_{Sh}, and T_{opt}, with the best-performing results summarized in **Table 5.8**. The simulation results identify ZnO as the most effective ETL for both HTL- and HTL-free DPSCs, showing superior performance metrics (PCE = 27.30%, J_{SC} = 23.83 mA cm^{-2}, V_{OC} = 1.29 V, FF = 0.89) in HTL-DPSCs. ZnO outperforms TiO_2 (PCE = 25.48%, J_{SC} = 23.83 mA cm^{-2}, V_{OC} = 1.20

V, FF = 0.89), WO_3 (PCE = 25.42%, J_{SC} = 23.71 mA cm^{-2}, V_{OC} = 1.21 V, FF = 0.88), and SnO_2 (PCE = 22.63%, J_{SC} = 23.80 mA cm^{-2}, V_{OC} = 1.08 V, FF = 0.88).

For HTL-free DPSCs, a ~ 4% reduction in PCE was observed, primarily due to increased interfacial recombination and limited charge extraction, which are more pronounced in the absence of an HTL. The physical origin of this reduction is the absence of an HTL, which typically helps reduce recombination and improve charge extraction. Despite this, ZnO still achieved the highest performance (PCE = 23.09%, J_{SC} = 23.80 mA cm^{-2}, V_{OC} = 1.15 V, FF = 0.85), owing to its superior electronic properties. Specifically, ZnO exhibits a suitable band alignment with CABB, facilitating efficient electron extraction and reducing recombination losses at the ETL/CABB interface. This optimal band alignment minimizes the energy barrier for electron transfer, enhancing the η_{cce}, particularly in the absence of an HTL. Furthermore, ZnO's high μ_e and low Φ contribute significantly to its high performance by enabling faster electron transport and improving overall charge extraction. These factors make ZnO an ideal ETL for both HTL- and HTL-free DPSCs, effectively mitigating the challenges posed by interfacial recombination and limited charge transport.

Future advancements in DPSCs should prioritize reducing interface recombination, optimizing transport layers, and exploring advanced ETLs, such as ZnO, to improve charge extraction. These efforts could help bridge the gap between simulated and experimental performance, reinforcing CABB as a promising candidate for lead-free, high-efficiency, and sustainable photovoltaic applications.

References

[1] S. Chand Yadav, A. Srivastava, V. Manjunath, A. Kanwade, R.S. Devan, P.M. Shirage, Properties, performance and multidimensional applications of stable lead-free $Cs_2AgBiBr_6$ double perovskite, Mater. Today Phys. 26 (2022) 100731. https://doi.org/10.1016/j.mtphys.2022.100731.

[2] A.S. Teja, A. Srivastava, J.A.K. Satrughna, M.K. Tiwari, A. Kanwade, S. Chand Yadav, P.M. Shirage, Optimal processing methodology for futuristic natural dye-sensitized solar cells and novel applications, Dye. Pigment. 210 (2023) 110997.

https://doi.org/10.1016/j.dyepig.2022.110997.

[3] A. Surya Teja, Abhishek Srivastava, Jena Akash Kumar Satrughna, Manish Kumar Tiwari, Archana Kanwade, Hyunju Lee, Atsushi Ogura, Parasharam M. Shirage, Synergistic co-sensitization of environment-friendly chlorophyll and anthocyanin-based natural dye-sensitized solar cells: An effective approach towards enhanced efficiency and stability, Sol. Energy. 261 (2023) 112–124. https://doi.org/https://doi.org/10.1016/j.solener.2023.06.004.

[4] A. Srivastava, B. Singh Chauhan, S. Chand Yadav, M. Kumar Tiwari, J. Akash Kumar Satrughna, A. Kanwade, K. Bala, P.M. Shirage, Performance of Dye-Sensitized Solar Cells by utilizing Codiaeum Variegatum Leaf and Delonix Regia Flower as Natural Sensitizers, Chem. Phys. Lett. 807 (2022) 140087. https://doi.org/10.1016/j.cplett.2022.140087.

[5] NREL, the National Renewable Energy Laboratory, best research-cell efficiency chart, 2025. www.nrel.gov/pv/cell-efficiency.html.

[6] A. Srivastava, J.A.K. Satrughna, M.K. Tiwari, A. Kanwade, S.C. Yadav, K. Bala, P.M. Shirage, Lead metal halide perovskite solar cells: Fabrication, advancement strategies, alternatives, and future perspectives, Mater. Today Commun. 35 (2023) 105686. https://doi.org/10.1016/j.mtcomm.2023.105686.

[7] S.S. Chougule, A. Srivastava, G.G. Bolegave, B.A. Gaikwad, P.M. Shirage, C.N. Markides, Next-generation solar technologies: Unlocking the potential of Ag-ZnO hybrid nanofluids for enhanced spectral-splitting photovoltaic-thermal systems, Renew. Energy. 236 (2024) 121405. https://doi.org/10.1016/j.renene.2024.121405.

[8] R. Chauhan, A. Srivastava, P.M. Shirage, K. Bala, Innovating dye-sensitized solar cells through novel microalgal and cyanobacterial species extricated dyes: A sustainable tack for material scarce earth, Sol. Energy. 270 (2024) 112369. https://doi.org/10.1016/j.solener.2024.112369.

[9] W.A. Zahid, W. Akram, M.F. Ahmad, S. Iqbal, S.A.M. Abdelmohsen, M.M.

Alanazi, A. Elmushyakhi, I. Hossain, J. Iqbal, Designing of phenothiazine-based hole-transport materials with excellent photovoltaic properties for high-efficiency perovskite solar cells (PSCs), Spectrochim. Acta Part A Mol. Biomol. Spectrosc. 298 (2023) 122774. https://doi.org/10.1016/j.saa.2023.122774.

[10] A. Srivastava, P.M. Shirage, Overcoming Intrinsic and Extrinsic Challenges in Perovskite Solar Cells: A Pathway Toward Advancement, in: Perovskite Sol. Cells Fundam. Approaches Mater. Process. Sustain. Futur., 1st ed., Springer Singapore, 2024: pp. 55–89. https://doi.org/10.1007/978-981-97-7624-5_2.

[11] A. Srivastava, P.M. Shirage, Operational Stability Management Approaches for Perovskite Solar Cells, in: Perovskite Sol. Cells Fundam. Approaches Mater. Process. Sustain. Futur., 1st ed., Springer Singapore, 2024: pp. 91–139. https://doi.org/10.1007/978-981-97-7624-5_3.

[12] A. Srivastava, P.M. Shirage, Pioneering the Path: Unveiling Exciting Applications for Integrated Perovskite Solar Cells, in: Perovskite Sol. Cells Fundam. Approaches Mater. Process. Sustain. Futur., 1st ed., Springer Singapore, 2024: pp. 177–203. https://doi.org/10.1007/978-981-97-7624-5_5.

[13] A. Srivastava, P.M. Shirage, Perovskite Solar Cells: Futuristic Reliable Renewable Energy Technology, in: Perovskite Sol. Cells Fundam. Approaches Mater. Process. Sustain. Futur., 1st ed., Springer Singapore, 2024: pp. 1–53. https://doi.org/10.1007/978-981-97-7624-5_1.

[14] Y. Hu, S. Zhao, L. Chen, Prediction of Ruddlesden–Popper Antiperovskites K_4OBr_2 and K_4OI_2 for Potential Thermoelectric Application, J. Phys. Chem. C. 129 (2025) 4656–4663. https://doi.org/10.1021/acs.jpcc.4c07834.

[15] A. Srivastava, P.M. Shirage, Possible Perovskite Substitutes, Advances, and Future Prospects, in: Perovskite Sol. Cells Fundam. Approaches Mater. Process. Sustain. Futur., 1st ed., Springer Singapore, 2024: pp. 141–175. https://doi.org/10.1007/978-981-97-7624-5_4.

[16] Z. Omarova, D. Yerezhep, A. Aldiyarov, N. Tokmoldin, In Silico Investigation of

the Impact of Hole-Transport Layers on the Performance of $CH_3NH_3SnI_3$ Perovskite Photovoltaic Cells, Crystals. 12 (2022) 699. https://doi.org/10.3390/cryst12050699.

[17] A.S. Shaikh, S.C. Yadav, A. Srivastava, A.R. Kanwade, M.K. Tiwari, S.M. Rajore, J.A.K. Satrughna, M. Dhonde, P.M. Shirage, Dynamic synergy of tin in the electron-transfer layer and absorber layer for advancing perovskite solar cells: a comprehensive review, Energy Adv. 3 (2024) 1505–1552. https://doi.org/10.1039/d4ya00204k.

[18] J. Chen, Z. Luo, Y. Fu, X. Wang, K.J. Czech, S. Shen, L. Guo, J.C. Wright, A. Pan, S. Jin, Tin(IV)-Tolerant Vapor-Phase Growth and Photophysical Properties of Aligned Cesium Tin Halide Perovskite ($CsSnX_3$; X = Br, I) Nanowires, ACS Energy Lett. 4 (2019) 1045–1052. https://doi.org/10.1021/acsenergylett.9b00543.

[19] A.H. Slavney, T. Hu, A.M. Lindenberg, H.I. Karunadasa, A Bismuth-Halide Double Perovskite with Long Carrier Recombination Lifetime for Photovoltaic Applications, J. Am. Chem. Soc. 138 (2016) 2138–2141. https://doi.org/10.1021/jacs.5b13294.

[20] E.T. McClure, M.R. Ball, W. Windl, P.M. Woodward, Cs_2AgBiX_6 (X = Br, Cl): New Visible Light Absorbing, Lead-Free Halide Perovskite Semiconductors, Chem. Mater. 28 (2016) 1348–1354. https://doi.org/10.1021/acs.chemmater.5b04231.

[21] F. Wei, Z. Deng, S. Sun, F. Zhang, D.M. Evans, G. Kieslich, S. Tominaka, M.A. Carpenter, J. Zhang, P.D. Bristowe, A.K. Cheetham, Synthesis and Properties of a Lead-Free Hybrid Double Perovskite: $(CH_3NH_3)_2AgBiBr_6$, Chem. Mater. 29 (2017) 1089–1094. https://doi.org/10.1021/acs.chemmater.6b03944.

[22] X. Yang, Y. Chen, P. Liu, H. Xiang, W. Wang, R. Ran, W. Zhou, Z. Shao, Simultaneous Power Conversion Efficiency and Stability Enhancement of $Cs_2AgBiBr_6$ Lead-Free Inorganic Perovskite Solar Cell through Adopting a Multifunctional Dye Interlayer, Adv. Funct. Mater. 30 (2020).

https://doi.org/10.1002/adfm.202001557.

[23] Z. Zhang, Q. Sun, Y. Lu, F. Lu, X. Mu, S.-H. Wei, M. Sui, Hydrogenated $Cs_2AgBiBr_6$ for significantly improved efficiency of lead-free inorganic double perovskite solar cell, Nat. Commun. 13 (2022) 3397. https://doi.org/10.1038/s41467-022-31016-w.

[24] E. Greul, M.L. Petrus, A. Binek, P. Docampo, T. Bein, Highly stable, phase pure $Cs_2AgBiBr_6$ double perovskite thin films for optoelectronic applications, J. Mater. Chem. A. 5 (2017) 19972–19981. https://doi.org/10.1039/C7TA06816F.

[25] W. Gao, C. Ran, J. Xi, B. Jiao, W. Zhang, M. Wu, X. Hou, Z. Wu, High-Quality $Cs_2AgBiBr_6$ Double Perovskite Film for Lead-Free Inverted Planar Heterojunction Solar Cells with 2.2 % Efficiency, ChemPhysChem. 19 (2018) 1696–1700. https://doi.org/10.1002/cphc.201800346.

[26] C. Wu, Q. Zhang, Y. Liu, W. Luo, X. Guo, Z. Huang, H. Ting, W. Sun, X. Zhong, S. Wei, S. Wang, Z. Chen, L. Xiao, The Dawn of Lead-Free Perovskite Solar Cell: Highly Stable Double Perovskite $Cs_2AgBiBr_6$ Film, Adv. Sci. 5 (2018) 1700759. https://doi.org/10.1002/advs.201700759.

[27] B. Wang, N. Li, L. Yang, C. Dall'Agnese, A.K. Jena, T. Miyasaka, X.-F. Wang, Organic Dye/$Cs_2AgBiBr_6$ Double Perovskite Heterojunction Solar Cells, J. Am. Chem. Soc. 143 (2021) 14877–14883. https://doi.org/10.1021/jacs.1c07200.

[28] P. Fan, H.-X. Peng, Z.-H. Zheng, Z.-H. Chen, S.-J. Tan, X.-Y. Chen, Y.-D. Luo, Z.-H. Su, J.-T. Luo, G.-X. Liang, Single-Source Vapor-Deposited $Cs_2AgBiBr_6$ Thin Films for Lead-Free Perovskite Solar Cells, Nanomaterials. 9 (2019) 1760. https://doi.org/10.3390/nano9121760.

[29] W. Yang, W. Li, Q. Liu, Y. Jin, Design and simulation of gradient-structured $Cs_2AgBiBr_6$ carbon-based double perovskite solar cell for boosting photovoltaic performance, Sol. Energy. 290 (2025) 113347. https://doi.org/10.1016/j.solener.2025.113347.

[30] Y. Duan, J. Li, B. Wang, Q. Li, Z. Wu, J. Mao, W. Zhang, G. Shao, Y. Shen, Enhanced light harvesting in lead-free $Cs_2AgBiBr_6$ double perovskite solar cells with plasmonic Ag nanoparticles, J. Mater. Chem. C. 13 (2025) 4974–4982. https://doi.org/10.1039/D4TC05218H.

[31] Ihtisham-ul-haq, M.I. Khan, M. Li, O.A. Ali, S.F. Mahmoud, Enhancing the efficiency and stability of $Cs_2AgBiBr_6$ solar cells via MAPbBr3 decoration, Mater. Res. Bull. 190 (2025) 113501. https://doi.org/10.1016/j.materresbull.2025.113501.

[32] A. Mohandes, M. Moradi, H. Nadgaran, Numerical simulation of inorganic $Cs_2AgBiBr_6$ as a lead-free perovskite using device simulation SCAPS-1D, Opt. Quantum Electron. 53 (2021) 319. https://doi.org/10.1007/s11082-021-02959-z.

[33] H.I. Alkhammash, M. Mottakin, M.M. Hossen, M. Akhtaruzzaman, M.J. Rashid, Design and defect study of $Cs_2AgBiBr_6$ double perovskite solar cell using suitable charge transport layers, Semicond. Sci. Technol. 38 (2023) 015005. https://doi.org/10.1088/1361-6641/aca42b.

[34] E. Danladi, E.E. Oguzie, F.I. Ezema, Highly efficient 25.562% $Cs_2AgBiBr_6$ double perovskite solar cell with copper barium tin sulfide and ZnO as charge transport channels: an intuition from a theoretical study using SCAPS-1D, J. Photonics Energy. 15 (2025) 024501. https://doi.org/10.1117/1.JPE.15.024501.

[35] M.S.S. Basyoni, M.M. Salah, M. Mousa, A. Shaker, A. Zekry, M. Abouelatta, M.T. Alshammari, K.A. Al-Dhlan, C. Gontrand, On the Investigation of Interface Defects of Solar Cells: Lead-Based vs Lead-Free Perovskite, IEEE Access. 9 (2021) 130221–130232. https://doi.org/10.1109/ACCESS.2021.3114383.

[36] S.A. Moiz, S.A. Albadwani, M.S. Alshaikh, Towards Highly Efficient Cesium Titanium Halide Based Lead-Free Double Perovskites Solar Cell by Optimizing the Interface Layers, Nanomaterials. 12 (2022) 3435. https://doi.org/10.3390/nano12193435.

[37] Q. Chen, Y. Ni, X. Dou, Y. Yoshinori, The Effect of Energy Level of Transport Layer on the Performance of Ambient Air Prepared Perovskite Solar Cell: A

SCAPS-1D Simulation Study, Crystals. 12 (2022) 68. https://doi.org/10.3390/cryst12010068.

[38] M. Burgelman, P. Nollet, S. Degrave, Modelling polycrystalline semiconductor solar cells, Thin Solid Films. 361–362 (2000) 527–532. https://doi.org/10.1016/S0040-6090(99)00825-1.

[39] H.J. Pauwels, G. Vanhoutte, The influence of interface state and energy barriers on the efficiency of heterojunction solar cells, J. Phys. D. Appl. Phys. 11 (1978) 649–667. https://doi.org/10.1088/0022-3727/11/5/009.

[40] N. Rai, S. Rai, P.K. Singh, P. Lohia, D.K. Dwivedi, Analysis of various ETL materials for an efficient perovskite solar cell by numerical simulation, J. Mater. Sci. Mater. Electron. 31 (2020) 16269–16280. https://doi.org/10.1007/s10854-020-04175-z.

[41] Z. Zhang, Q. Sun, Y. Lu, F. Lu, X. Mu, S.-H. Wei, M. Sui, Hydrogenated $Cs_2AgBiBr_6$ for significantly improved efficiency of lead-free inorganic double perovskite solar cell, Nat. Commun. 13 (2022) 3397. https://doi.org/10.1038/s41467-022-31016-w.

[42] S.R. Hosseini, M. Bahramgour, P. Yardani Sefidi, A. Tabatabaei Mashayekh, A. Moradi, N. Delibas, M.G. Hosseini, A. Niaei, Investigating the effect of non-ideal conditions on the performance of a planar $CH_3NH_3PbI_3$-based perovskite solar cell through SCAPS-1D simulation, Heliyon. 8 (2022) e11471. https://doi.org/10.1016/j.heliyon.2022.e11471.

[43] S.M. Seyed-Talebi, M. Mahmoudi, C.-H. Lee, A Comprehensive Study of $CsSnI_3$-Based Perovskite Solar Cells with Different Hole Transporting Layers and Back Contacts, Micromachines. 14 (2023) 1562. https://doi.org/10.3390/mi14081562.

[44] H.-J. Du, W.-C. Wang, J.-Z. Zhu, Device simulation of lead-free $CH_3NH_3SnI_3$ perovskite solar cells with high efficiency, Chinese Phys. B. 25 (2016) 108802. https://doi.org/10.1088/1674-1056/25/10/108802.

[45] M.D. Stamate, On the dielectric properties of dc magnetron TiO_2 thin films, Appl. Surf. Sci. 218 (2003) 318–323. https://doi.org/10.1016/S0169-4332(03)00624-X.

[46] J.P. Correa Baena, L. Steier, W. Tress, M. Saliba, S. Neutzner, T. Matsui, F. Giordano, T.J. Jacobsson, A.R. Srimath Kandada, S.M. Zakeeruddin, A. Petrozza, A. Abate, M.K. Nazeeruddin, M. Grätzel, A. Hagfeldt, Highly efficient planar perovskite solar cells through band alignment engineering, Energy Environ. Sci. 8 (2015) 2928–2934. https://doi.org/10.1039/C5EE02608C.

[47] S.K. Vasheghani Farahani, T.D. Veal, J.J. Mudd, D.O. Scanlon, G.W. Watson, O. Bierwagen, M.E. White, J.S. Speck, C.F. McConville, Valence-band density of states and surface electron accumulation in epitaxial SnO2 films, Phys. Rev. B. 90 (2014) 155413. https://doi.org/10.1103/PhysRevB.90.155413.

[48] C. Doroody, K.S. Rahman, H.N. Rosly, M.N. Harif, F. Haque, S.K. Tiong, N. Amin, Impact of high resistivity transparent (HRT) layer in cadmium telluride solar cells from numerical simulation, J. Renew. Sustain. Energy. 12 (2020). https://doi.org/10.1063/1.5132838.

[49] R.L.Z. Hoye, B. Ehrler, M.L. Böhm, D. Muñoz-Rojas, R.M. Altamimi, A.Y. Alyamani, Y. Vaynzof, A. Sadhanala, G. Ercolano, N.C. Greenham, R.H. Friend, J.L. MacManus-Driscoll, K.P. Musselman, Improved Open-Circuit Voltage in ZnO–PbSe Quantum Dot Solar Cells by Understanding and Reducing Losses Arising from the ZnO Conduction Band Tail, Adv. Energy Mater. 4 (2014) 1301544. https://doi.org/10.1002/aenm.201301544.

[50] H. Sabbah, Z. Abdel Baki, R. Mezher, J. Arayro, SCAPS-1D Modeling of Hydrogenated Lead-Free $Cs_2AgBiBr_6$ Double Perovskite Solar Cells with a Remarkable Efficiency of 26.3%, Nanomaterials. 14 (2023) 48. https://doi.org/10.3390/nano14010048.

[51] T.I. Alanazi, Design and Device Numerical Analysis of Lead-Free $Cs_2AgBiBr_6$ Double Perovskite Solar Cell, Crystals. 13 (2023) 267. https://doi.org/10.3390/cryst13020267.

[52] Q. Wei, W. Zi, Z. Yang, D. Yang, Photoelectric performance and stability comparison of $MAPbI_3$ and $FAPbI_3$ perovskite solar cells, Sol. Energy. 174 (2018) 933–939. https://doi.org/10.1016/j.solener.2018.09.057.

Chapter 6

$Ti_3C_2T_X$ Assisted Dual Interfacial Passivation for $Cs_2AgBiBr_6$ Double Perovskite Solar Cells

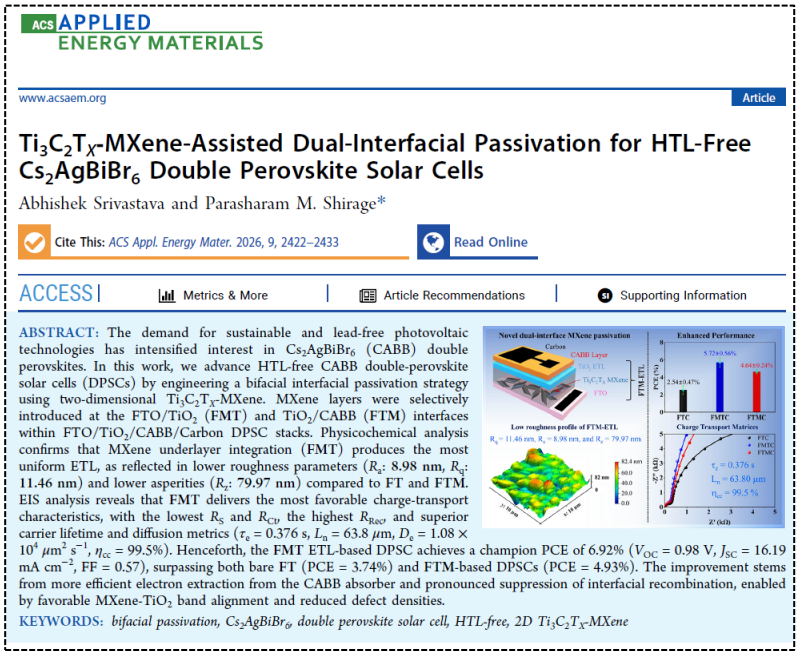

ACS APPLIED ENERGY MATERIALS

www.acsaem.org Article

$Ti_3C_2T_X$-MXene-Assisted Dual-Interfacial Passivation for HTL-Free $Cs_2AgBiBr_6$ Double Perovskite Solar Cells

Abhishek Srivastava and Parasharam M. Shirage*

Cite This: *ACS Appl. Energy Mater.* 2026, 9, 2422−2433 Read Online

ACCESS | Metrics & More | Article Recommendations | Supporting Information

ABSTRACT: The demand for sustainable and lead-free photovoltaic technologies has intensified interest in $Cs_2AgBiBr_6$ (CABB) double perovskites. In this work, we advance HTL-free CABB double-perovskite solar cells (DPSCs) by engineering a bifacial interfacial passivation strategy using two-dimensional $Ti_3C_2T_X$-MXene. MXene layers were selectively introduced at the FTO/TiO_2 (FMT) and TiO_2/CABB (FTM) interfaces within FTO/TiO_2/CABB/Carbon DPSC stacks. Physicochemical analysis confirms that MXene underlayer integration (FMT) produces the most uniform ETL, as reflected in lower roughness parameters (R_s: **8.98 nm**, R_q: **11.46 nm**) and lower asperities (R_z: **79.97 nm**) compared to FT and FTM. EIS analysis reveals that FMT delivers the most favorable charge-transport characteristics, with the lowest R_S and R_{CT}, the highest R_{Rec}, and superior carrier lifetime and diffusion metrics (τ_e = 0.376 s, L_n = 63.8 μm, D_e = 1.08 × 10^4 μm^2 s^{-1}, η_{cc} = 99.5%). Henceforth, the FMT ETL-based DPSC achieves a champion PCE of 6.92% (V_{OC} = 0.98 V, J_{SC} = 16.19 mA cm^{-2}, FF = 0.57), surpassing both bare FT (PCE = 3.74%) and FTM-based DPSCs (PCE = 4.93%). The improvement stems from more efficient electron extraction from the CABB absorber and pronounced suppression of interfacial recombination, enabled by favorable MXene-TiO_2 band alignment and reduced defect densities.

KEYWORDS: *bifacial passivation, $Cs_2AgBiBr_6$, double perovskite solar cell, HTL-free, 2D $Ti_3C_2T_X$-MXene*

This chapter demonstrates MXene-based dual interfacial passivation in HTL-free CABB DPSCs, with the FMT configuration yielding the best performance. Enhanced charge transport and reduced recombination provide a champion PCE of 6.92%, outperforming other configurations, enabled by favourable FTO-MXene-TiO_2 band alignment and defect passivation.

6.1 Introduction

The accelerating global energy crisis, coupled with the rapid depletion of fossil fuels and worsening environmental concerns, has intensified the need for clean, sustainable, and high-efficiency photovoltaic (PV) technologies.[1] Metal-halide perovskite solar cells (PSCs) have emerged as a transformative PV platform due to their exceptional power conversion efficiencies (>26%), solution-processability at low temperatures, and highly tunable optoelectronic characteristics.[2,3] However, despite these advantages, the dominance of lead (Pb) in state-of-the-art PSCs presents severe environmental and health hazards, while intrinsic instability under heat, moisture, and illumination further limits their commercial viability.[4–6] These persistent concerns have prompted the scientific community to explore non-toxic and stable alternatives to conventional Pb-based perovskites.[7–10]

To overcome these limitations, several Pb-free perovskite families, including Sn-based, Cu-based, and vacancy-ordered double perovskites, have been extensively investigated.[11–15] Among these, heterovalent Pb substitution with Ag^{+}/Bi^{3+} to form double perovskites such as $Cs_2AgBiBr_6$ (CABB) and $Cs_2AgBiCl_6$ (CABC) has shown exceptional promise owing to its superior air/moisture stability, wide optical bandgap (~1.9-2.3 eV), and intrinsic environmental benignity.[16–21] Early work by Greul *et al.*[22] demonstrated the first CABB-based double perovskite solar cell (DPSC), which resulted in poor mesostructured film crystallinity, large grain agglomeration, low carrier mobility, and pronounced hysteresis, limiting device efficiency up to 2.43%. Subsequent advancements have focused on improving CABB film morphology, crystallinity, and defect tolerance through solvent engineering, compositional tuning, and surface passivation strategies, yet DPSCs still lag significantly behind their Pb-based counterparts, with efficiencies commonly up to 6% due to severe interfacial recombination and inefficient charge extraction at the ETL/CABB interface.[23–26]

The efficiency of CABB-DPSCs is limited by poor interfacial contacts between the FTO/electron transport layer (ETL), the ETL/CABB interface, and the CABB/hole transport layer (HTL).[27] Commonly used ETL and HTL materials, such as titanium dioxide (TiO_2) and spiro-OMeTAD, exhibit mismatched Fermi energy levels (E_f) with the

conduction band minima (CBM) and valence band maxima (VBM) of CABB, creating significant energy barriers that hinder electron and hole extraction, thus reducing DPSCs' performance.[28,29] Additionally, hydrophilic lithium salts in spiro-OMeTAD contribute to device degradation while the ETL plays a decisive role in dictating charge extraction, recombination kinetics, and overall device performance.[30] Therefore, optimizing these interface contacts is crucial for enhancing the performance and stability of CABB-based DPSCs.

To optimize the DPSC architecture, Abhishek *et al.*[31] systematically investigated the device architecture using SCAPS simulation, with FTO/TiO_2/CABB/HTL(CuI, CuSCN, Cu_2O, Spiro-OMeTAD)/Au. Among the HTLs studied, Cu_2O-based devices exhibited the best performance, achieving a V_{OC} of 1.33 V, J_{SC} of 8.78 mA cm^{-2}, FF of 0.65, and PCE of 7.60%. Detailed capacitance-voltage (C-V), conductance-voltage (G-V), capacitance-frequency (C-f), and conductance-frequency (G-f) analysis revealed that the enhanced performance originates from reduced interfacial defect density, attributed to favourable band alignment between Cu_2O and CABB. In another report, Saifee, M.A. *et al.* investigated the graphene quantum dot HTL in FTO/TiO_2/$Cs_2AgBiBr_6$/GQD/Au architecture with varying absorber thickness, doping density, and total defect density. In addition, a machine learning (ML) model was developed to predict key photovoltaic parameters. The optimised device achieved a V_{OC} of 0.814 V, J_{SC} of 24.55 mA cm^{-2}, FF of 0.77, and a PCE of 15.33%, while the ML model predicted device performance with an accuracy of 96.03%. These results demonstrate the strong potential of CABB-based PSCs and highlight the effectiveness of ML-assisted optimization, with further improvements expected through advanced interface engineering and materials optimization.

Recent studies have shown that 2D materials, particularly $Ti_3C_2T_X$ MXene, can significantly enhance interfacial electronic properties through their high conductivity, tunable surface terminations, and excellent passivation capabilities.[32–35] However, most reported studies are limited to modifying a single interface, and a systematic understanding of where MXene should be strategically positioned, either at the FTO/TiO_2 interface or the TiO_2/CABB interface, to maximize interfacial passivation and charge

transport remains largely unexplored.[36,37] Motivated by these critical gaps, we designed a dual-interface MXene passivation strategy with $Ti_3C_2T_X$-MXene for HTL-free CABB DPSC to systematically engineer the electronic landscape. By integrating ultrathin $Ti_3C_2T_X$ layers at the FTO/TiO_2 interface (**FMT**) and TiO_2/CABB interfaces (**FTM**), we investigate how interfacial energetics, morphology, carrier dynamics, and recombination pathways are collectively modified. Through comprehensive physicochemical analysis, we demonstrate that the strategic incorporation of MXene, especially at the FTO/TiO_2 interface, substantially enhances electron extraction, suppresses deep-level traps, and improves device performance, culminating in a champion PCE (6.92%) for **FMT**/CABB/Carbon-structured DPSCs.

6.2 Experimental Section

6.2.1 Materials

The materials utilized in this study include transparent and conducting fluorine-doped tin oxide (FTO; surface resistivity ~7 Ω/sq) purchased from Sigma Aldrich, Titanium (IV) Isopropoxide ($Ti[OCH(CH_3)_2]_4$; TTIP, 75% in IPA, Sigma Aldrich), Acetic Acid Glacial ($CH_3COOH(C_2H_4O_2)$; ≥ 99.5%, SRL), Polyvinylpyrrolidone ($(C_6H_9NO)_n$, K-30, SRL), Ethanol (Sigma Aldrich), Cesium bromide (CsBr, ≥ 99.5%, SRL), Bismuth bromide ($BiBr_3$, ≥ 98%, Sigma Aldrich), Silver bromide (AgBr, ≥ 99%, Sigma Aldrich), Hydrobromic acid (HBr, 48-49% in water), terpinol (≥ 99.5%, SRL), Dichloromethane (≥ 99.5%, SRL), and Methanol Extrapure AR (≥ 99.8%, SRL). All chemical compounds were used as received without any further purification.

6.2.2 Synthesis of CABB and DPSC Fabrication

The CABB synthesis process was followed as discussed in **Chapter 2**.[38] In a typical synthesis process, a first mixture of CsBr (0.4 M) and $BiBr_3$ (0.2 M) was dissolved in 10 mL of HBr and stirred for 1 hour at 110 °C. After complete dissolution of the precursors, 0.2 M AgBr was added to the solution, and the mixture was stirred vigorously for 2 hours at 130 °C. Therefore, cool it down overnight for proper CABB crystallization at RT. After 24 hours, the prepared solution was filtered using Whatman™ filter paper, washed using methanol, and dried overnight under low pressure. To prepare the CABB

absorber ink, 426 mg (0.4 M) of the synthesized CABB powder was dissolved in 1 mL of DMSO, and the mixture was stirred until complete dissolution. To fabricate HTL-free DPSCs using FT, FMT, and FTM ETLs, the CABB ink and ETL films were preheated at 75°C for 5 minutes. After filtration, CABB layer coating was performed in two steps, followed by an IPA antisolvent treatment to achieve a uniform, pinhole-free absorber layer. The preheated CABB ink was spin-coated onto the different ETLs at 1000 rpm for 10 s, then at 3000 rpm for 70 s, followed by an antisolvent treatment with 150 µL of IPA during the last 25 s. After CABB coating, all the films were heated at 250°C for 5 min to induce crystallization. To make rear contacts, carbon ink was prepared via mixing 0.5, 0.17, and 0.07 g of conductive carbon, graphite powder, and ethyl cellulose, respectively, in terpinol. Furthermore, the CABB layer was masked, and the carbon electrodes were coated using the doctor blade method, then dried at 80°C for 1 h. The DPSCs fabricated using **FT**, **FMT**, and **FTM** ETLs are referred to as **DPSC1**, **DPSC2**, and **DPSC3**, respectively (**Figure 6.1**).

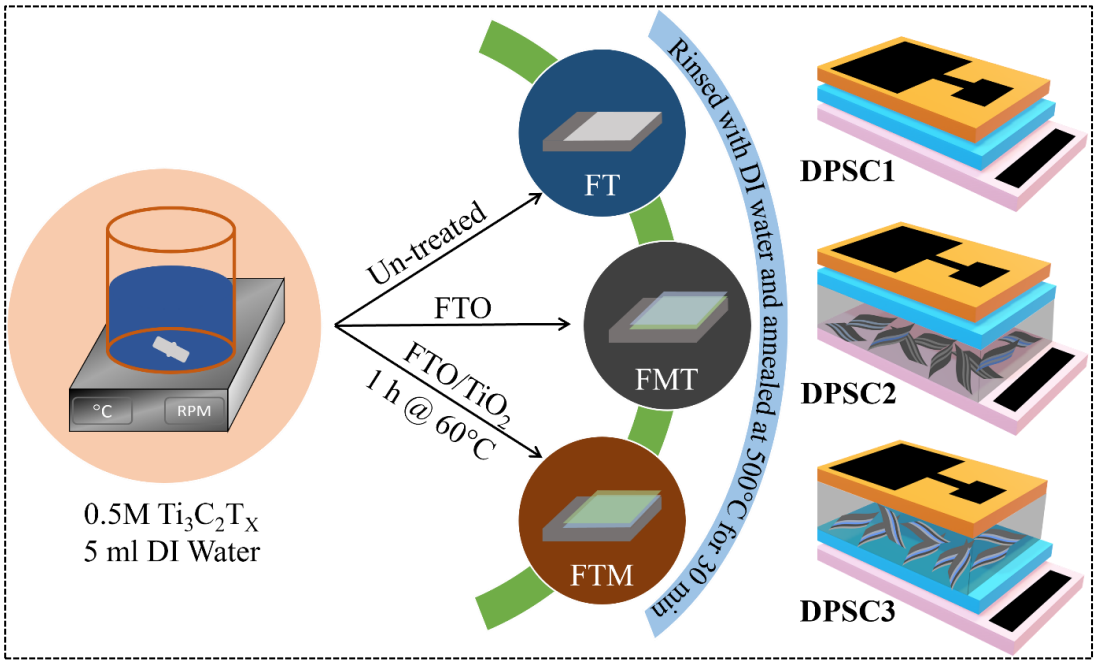

Figure 6.1 A typical $Ti_3C_2T_X$-MXene passivation process is followed to prepare FT-, FMT-, and FTM-type ETLs, resulting in the formation of **DPSC1**, **DPSC2**, and **DPSC3**, respectively.

6.3 Results and Discussion

6.3.1 Morphological Analysis

The octahedral crystals of CABB powder are shown in **Figure 6.2(a-b)**, exhibiting good uniformity and reproducibility. The CsBr and $BiBr_3$ compounds dissolved in concentrated HBr at 110 °C, enabling the formation of Cs^+ and Bi^{3+} solvated ions and bromide complexes in solution (**equations 6.1** and **6.2**). Subsequently, the addition of AgBr releases Ag^+ ions due to limited solubility, completing ionic incorporation and establishing the Ag-Bi ordered double perovskite framework (**equation 6.3**). Following overnight low-pressure drying to induce nucleation and crystallization, the alternating $AgBr_6$ and $BiBr_6$ octahedra assemble into a rock-salt ordered $A_2B'B'''X_6$ lattice, and the anisotropic surface energy distribution favours the stabilization of low-energy {111} facets, resulting in the characteristic octahedral morphology (**equation 6.4**). This morphology arises from the intrinsic face-centred cubic (FCC) ordering of B-site cations and the strong Ag-Br/Bi-Br coordination, which kinetically restricts growth along higher-energy facets and promotes the formation of well-defined octahedral crystals.

$$CsBr \rightarrow Cs^+ + Br^- \quad 6.1$$

$$BiBr_3 + Br^- \rightarrow [BiBr_4]^- \text{ (stable Bi-Br halide complex)} \quad 6.2$$

$$AgBr\ (s) \rightleftharpoons Ag^+ + Br^- \quad 6.3$$

$$2Cs^+ + Ag^+ + Bi^{3+} + 6Br^- \rightarrow Cs_2AgBiBr_6\ (s) \quad 6.4$$

Additionally, the Quantitative EDX spectra shown in **Figure 6.2(c)** confirm the stoichiometric presence of Cs, Ag, Bi, and Br atoms. Normalizing to Ag = 1 gives an empirical formula of ≈ $Cs_{2.19}AgBiBr_6$, which closely matches the ideal CABB stoichiometry. The minor deviations are within the common uncertainties of EDX/SEM sampling and quantification and may arise from surface inhomogeneity or residual precursor/adsorbed species. Elemental mapping (**Figure 6.2(d)**) further confirms a uniform spatial distribution of all four elements across the analyzed particles, indicating a homogeneous phase with no detectable Ag/Bi segregation or Br-deficient domains at the EDX resolution.

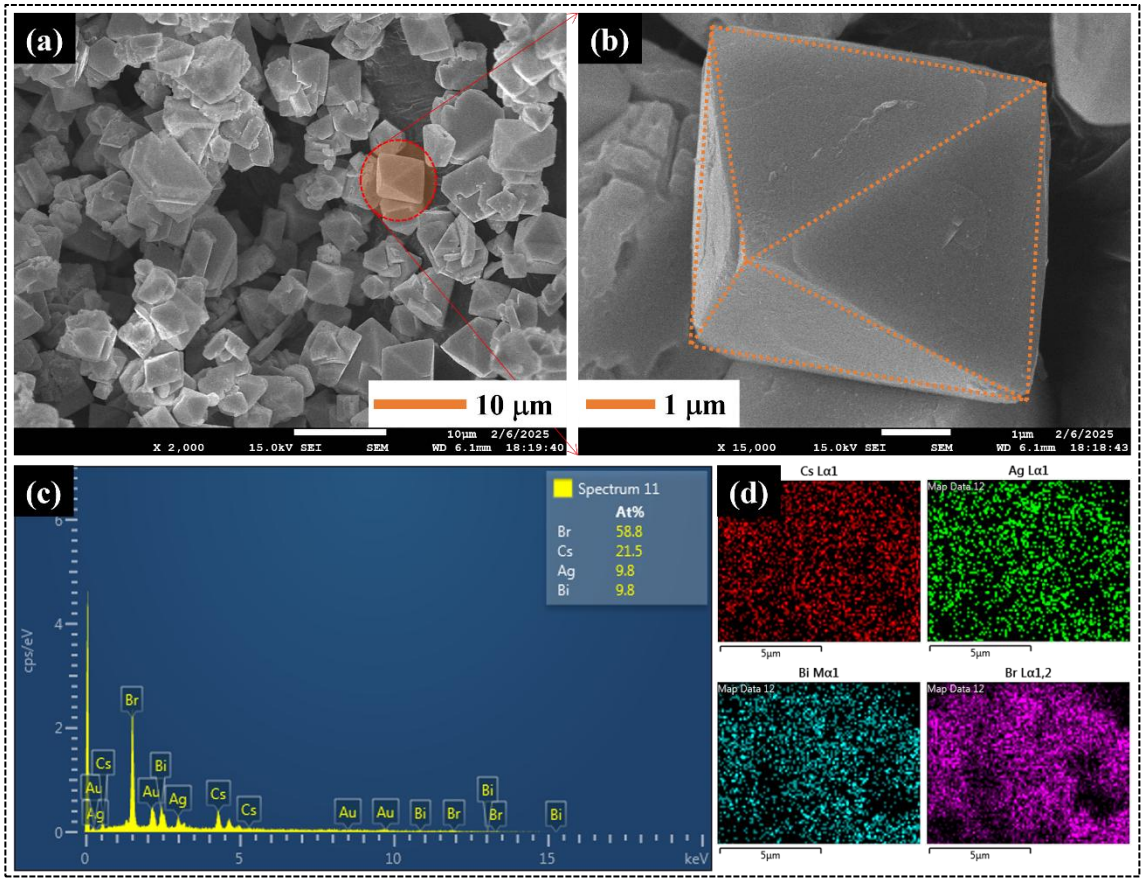

Figure 6.2 (a-b) FESEM images of octahedral CABB crystals, (c) corresponding EDX spectra, and (d) elemental mapping (Cs: red, Ag: green, Bi: cyan, and Br: pink).

The high-resolution TEM micrographs of octahedral CABB are shown in **Figure 6.3(a)**, which displays well-defined agglomerated particles, indicating homogeneous crystallite formation consistent with the sharp diffraction peaks observed in the XRD spectrum. The ImageJ analysis of the HRTEM image shown in **Figure 6.3(b)** reveals clear lattice fringes with interplanar spacings of $d_{(444)} = 0.15$ nm, $d_{(044)} = 0.21$ nm, and $d_{(222)} = 0.33$ nm planes. These measured d-spacings closely match the d-values obtained from XRD, confirming phase purity and validating the crystallographic indexing. The accompanying Fourier transform further reproduces the periodic lattice ordering, reinforcing the presence of long-range crystallinity.

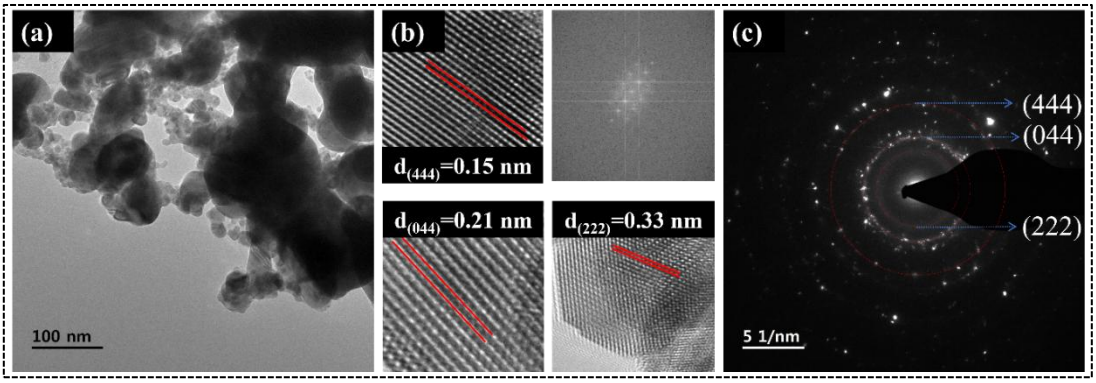

Figure 6.3 (a) High-resolution TEM image, (b) lattice spacing between (444), (044), (222) planes, and Fourier transform image, (c) SAED-pattern of octahedral CABB crystals.

The selected area electron diffraction (SAED) pattern in **Figure 6.3(c)** features randomly distributed bright diffraction spots that collectively form ring-like contours. Such semi-ringed and spotty patterns are characteristic of a polycrystalline material with multiple crystallite orientations, as confirmed by the XRD profile, which shows multiple intense reflections indicating the coexistence of several low-index planes. The consistency between TEM lattice imaging, SAED ring patterns, and XRD peak indexing demonstrates that the CABB powder is structurally well-ordered with polycrystalline domains, ensuring coherence between microscopic and bulk diffraction analyses.

TGA of the CABB crystals shown in **Figure 6.4(a)** indicates excellent thermal stability up to ~300 °C, with <1% weight loss between 200-300 °C, confirming that annealing at 250 °C preserves the cubic phase without detectable structural degradation. A significant mass loss of ~46% occurs between 500 and 700 °C, followed by continued decomposition at higher temperatures, attributed to the breakdown of the inorganic halide framework and the volatilization of organic components. This thermal behaviour indicates that CABB remains structurally intact at the processing temperature used for ETL coating, whereas crystalline decomposition dominates only at elevated regimes well above the device fabrication window. Additionally, the BET isotherm (**Figure 6.4(b)**) shows a low specific surface area of 535×10^{-3} m^2 g^{-1}, consistent with the dense crystalline nature of the CABB crystals. The adsorption-desorption profile indicates limited porosity, which aligns

with bulk-like crystal formation rather than nanostructured or highly porous morphologies. This microstructural compactness is beneficial for uniform film formation on ETLs and supports efficient charge transport in device integration.

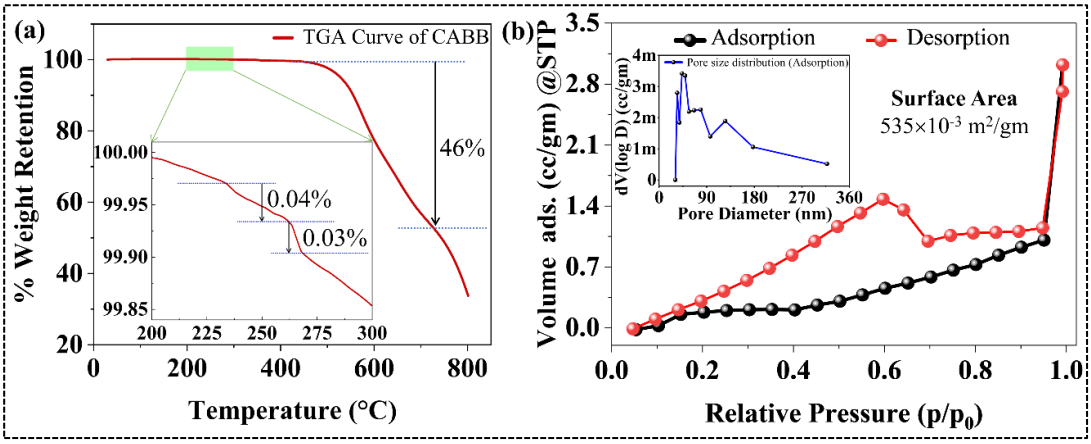

Figure 6.4 (a) Thermogravimetric Analysis (TGA) of CABB crystals, and (b) Brunauer-Emmett-Teller (BET) adsorption/desorption isotherms and pore-size distribution in CABB powder.

Furthermore, the top-view FESEM images of the prepared photoanodes reveal clear morphological differences arising from TiO_2 deposition and $Ti_3C_2T_X$ Passivation (**Figure 6.5**). The pristine FTO surface shown in **Figure 6.5(a)** exhibits the characteristic densely packed pyramidal/spheroidal grains of F-doped SnO_2, with grain sizes typically in the 50-80 nm regime. The surface is uniformly textured, with well-defined, closely interconnected SnO_2 grains, which are desirable for maintaining high optical transparency and electrical conductivity. This microstructure acts as the baseline morphology onto which the TiO_2 and $Ti_3C_2T_X$-MXene passivation layers are deposited.

Upon deposition of the c-TiO_2 and mesoporous ETL (**Figure 6.5(b)**), a significant morphological transformation is observed. The surface becomes highly porous, featuring a sponge-like, interconnected pore network resulting from the polymer-templated hydrolysis and condensation of titanium isopropoxide. This porous matrix, expected given the PVP-assisted sol-gel route, provides a large interfacial area, essential for efficient charge extraction from the perovskite absorber. However, the presence of large voids and

non-uniform porosity also implies potential recombination hotspots and ineffective coverage of the underlying FTO.

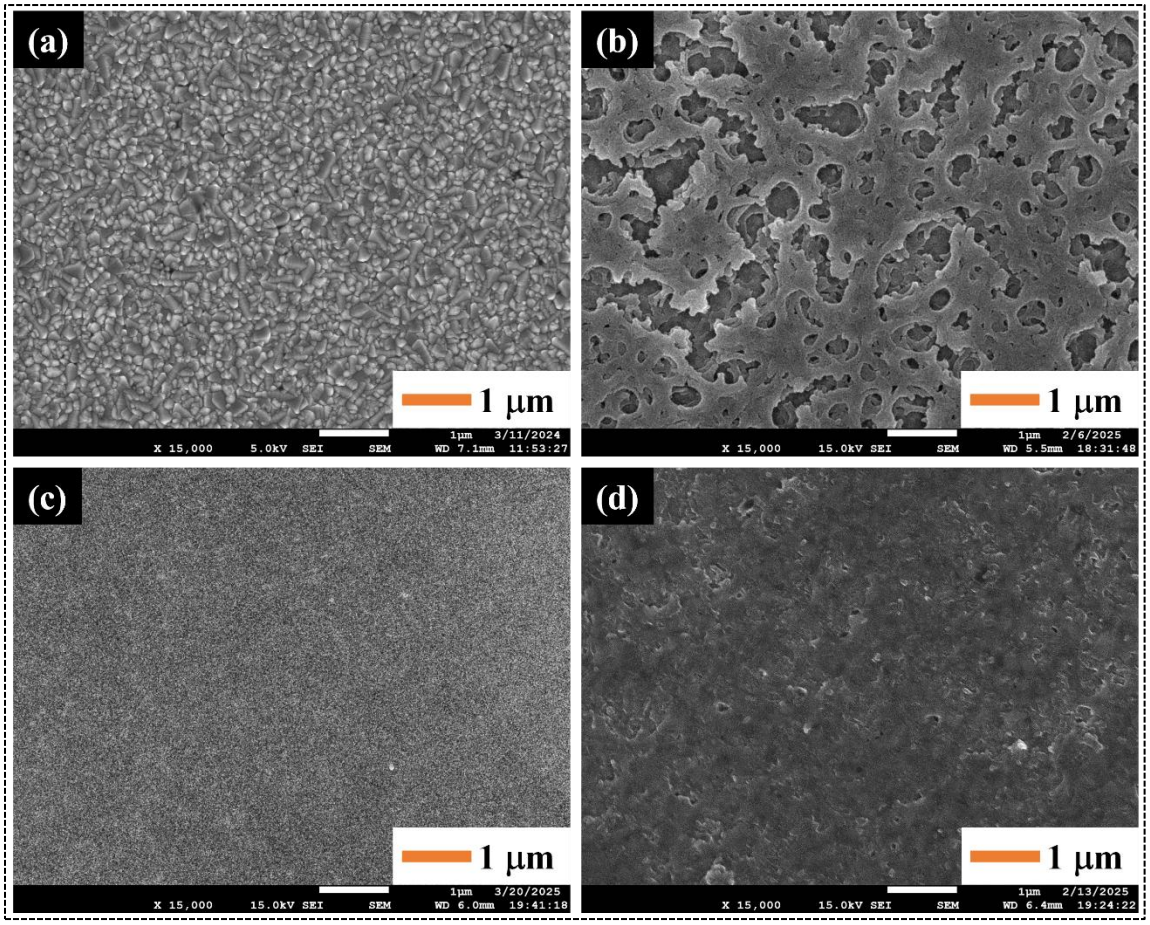

Figure 6.5 Top-view FESEM micrographs of (a) bare FTO, (b) **FT**, (c) **FMT** (FTO/Mx/TiO_2), and (d) **FTM** (FTO/TiO_2/Mx).

Therefore, dip-coating of $Ti_3C_2T_X$-MXene prior to TiO_2 deposition leads to a markedly smoother and more compact morphology, as shown in **Figure 6.5(c)**. The MXene nanosheets effectively infiltrate the nanoscale valleys of the FTO surface and serve as nucleation platforms for subsequent TiO_2 growth, resulting in a uniform, densely packed ETL. Compared to **Figure 6.5(b)**, the TiO_2 appears continuous with suppressed macro-porosity. This improved film connectivity is expected to reduce pinholes, enhance electronic coupling between FTO and TiO_2, and improve electron mobility due to $Ti_3C_2T_X$-MXene's metallic conductivity.

The microstructure confirms that MXene serves as an efficient interfacial buffer, promoting the formation of a compact TiO_2 ETL. However, when $Ti_3C_2T_X$-MXene is applied on top of the TiO_2 layer (**Figure 6.5(d)**), the surface retains the underlying TiO_2 texture but becomes more homogenized, with MXene flakes conformally coating the porous scaffold. The nanosheets appear embedded within the matrix, partially filling voids and smoothing sharp morphological features. This configuration forms an interface at the TiO_2/CABB junction by passivating surface defects and limiting trap-assisted recombination. Compared to **Figure 6.5(b)**, the reduction in visible macro-voids indicates successful infiltration and defect healing via MXene passivation, consistent with previous reports.[39]

6.3.2 Structural and Optical Studies

The structural properties of the as-synthesized CABB double perovskite powder were examined using X-ray diffraction (XRD), and the refined diffraction profile using the FullProf_Suite software is shown in **Figure 6.6(a)**. The experimental pattern exhibits a series of intense, well-defined Bragg reflections that can be indexed to the cubic double perovskite structure (space group Fm-3m, 225), confirming the formation of phase-pure CABB without detectable secondary phases. Prominent diffraction peaks located at $2\theta \approx$ 13.60°, 15.72°, 22.30°, 26.21°, 27.40°, 31.74°, 34.67°, 35.60°, 39.13°, 41.61°, 4549°, 47.71°, 48.42° correspond to the (111), (200), (220), (311), (222), (400), (331), (420), (422), (511), (440), (531) and (442) planes, which are characteristic of rock-salt ordered Ag^+/Bi^{3+} sublattices in CABB.

Rietveld refinement yielded excellent convergence with $\chi^2 = 2.66$, confirming that the refined lattice parameter ($a \approx 11.268 \pm 0.003$ Å) matches well with the reported literature value for cubic CABB, thereby demonstrating the chemical integrity of the synthesized powder.[40,41] The absence of peak splitting or additional reflections indicates that no lower-symmetry phases (e.g., tetragonal distortions) or impurity phases such as $CsPbBr_3$, AgBr, or BiOBr are present within the detection limit. This structural purity directly supports the uniform elemental distribution observed in EDX mapping (**Figure 6.2(c-d)**) and underpins the optoelectronic stability of the absorber used in device fabrication. All the refined parameters are summarized in **Table 6.1**, confirming their

reproducibility and good agreement with our previous study.[38] Additionally, XRD patterns of the as-synthesized and 250°C-annealed CABB powders show a systematic shift of all diffraction peaks toward higher 2θ values after heating.

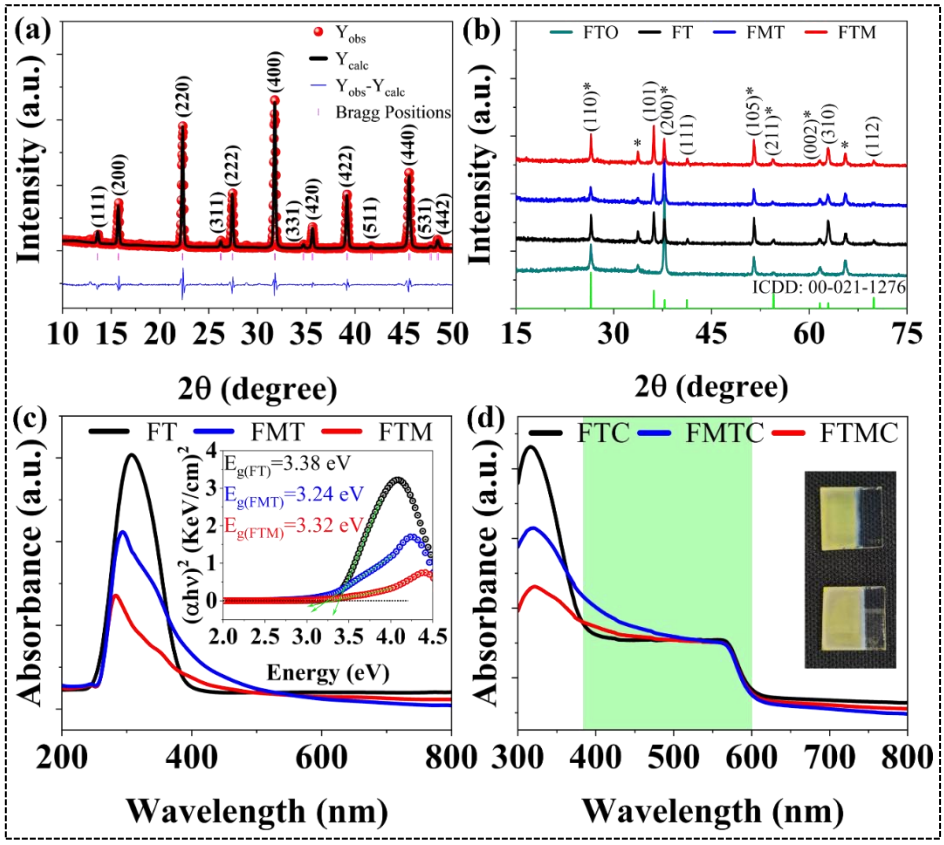

Figure 6.6 (a) Reitvil refined the XRD diffraction pattern of CABB powder, (b) Comparative XRD patterns of bare FTO, FT, FMT, and FTM, (c) UV-vis absorption spectra and Tauc's plot of FT, FMT, and FTM ETLs, and (d) UV-vis absorption spectra of CABB-loaded ETLs.

Table 6.5 Crystal type, space group, and lattice parameters obtained from refined p-XRD of CABB.

Crystal Structure	Space Group	Lattice Parameters		Position Parameters					
		a = b = c (Å)	Cell Volume (Å^3)	Atom	Occupancy	x	y	z	Multi-plicity
Cubic	Fm-3m	11.268	1430.74	Cs	0.043	0.75	0.25	0.75	8

	(225)	$\alpha = \beta = \gamma$		Ag	0.020	0.50	0.50	0.50	4
		90°		Bi	0.020	0.50	0.00	0.50	4
				Br	0.125	0.50	0.25	0.50	24

This indicates a reduction in lattice spacing (Bragg's law: $2dsin\theta = n\lambda$), consistent with lattice contraction (~0.43%), which translates identically to the lattice parameter "a" due to improved crystallinity, removal of residual solvent/moisture, loss of weakly bound species, and possible relaxation of internal strain. Such thermal-induced structural ordering aligns with the annealing step used for CABB films on **FT**, **FMT**, and **FTM**-ETLs, confirming that 250 °C promotes the formation of a more compact and well-crystallized CABB phase.

In **Figure 6.6(b)**, X-ray diffraction patterns of the FTO and ETL series **FT**, **FMT**, and **FTM** are plotted together and compared with the standard ICDD card No. 00-021-2176. All four diffractograms are dominated by the characteristic reflections of brookite TiO_2, showing excellent agreement with the ICDD reference.[42,43] The most intense TiO_2 reflections (indexed to the (110), (101), (200), (111), (105), (211), (002), (310), and (112) planes) are present in ETL, indicating that the TiO_2 crystalline framework remains intact after MXene treatments and the thermal annealing protocol.

The low-intensity reflections, such as (101), arise from the thin-film nature of the ETL and their overlap with stronger FTO peaks, consistent with the formation of nanocrystalline TiO_2. No distinct $Ti_3C_2T_X$-MXene peaks appear in the **FMT** and **FTM** samples, which is expected given the ultrathin loading, possible suppression of low-angle (002) stacking reflections, and partial structural disorder or oxidation of MXene during high-temperature annealing. Importantly, no additional impurity peaks are detected, confirming that neither TiO_2 nor MXene passivation introduces crystalline by-products. The synthesis procedure and associated morphological and structural characteristics of multilayered $Ti_3C_2T_X$-MXene have been thoroughly discussed in our previous work, and the same protocol is followed here without further alteration.[39]

Figure 6.6(c) shows the UV-vis absorption spectra of the **FT**, **FMT**, and **FTM**-ETLs, confirming a noticeable change in the absorption onset for the **FMT** and **FTM**-

ETL; while the pristine FT film exhibited a sharp onset, the MXene-passivated ETLs displayed a slightly diffused edge with a minor redshift. This redshift contributed to a reduction in the optical bandgap (E_g), as confirmed by the corresponding Tauc plots (inset of **Figure 6.6(c)**), yielding values of 3.38, 3.24, and 3.32 eV for the **FT**, **FMT**, and **FTM**-ETLs, respectively. The decrease in Eg for the **FMT** and **FTM**-ETL indicates improved UV-light blocking and possible alteration in defect states or electronic structure upon treatment. Furthermore, the UV-vis spectra of CABB-loaded **FTC**, **FMTC**, and **FTMC-ETLs** shown in **Figure 6.6(d)** revealed pronounced absorption extending from ~600 nm, confirming effective CABB loading and enhanced light-harvesting capability across the visible region (~400-600 nm).

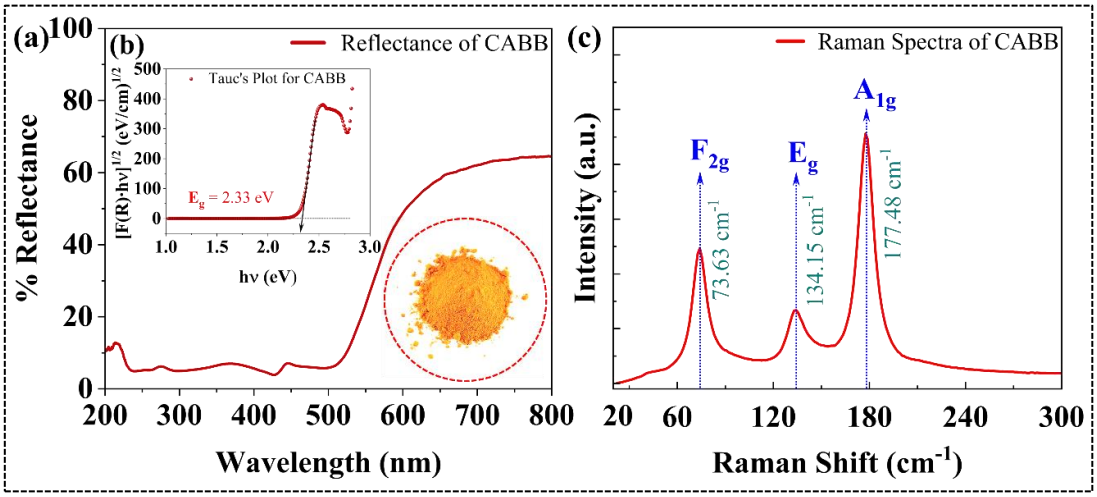

Figure 6.7 (a) Diffused reflectance spectra, (b) corresponding Tauc's plot, and (c) RAMAN spectra of CABB powder.

To validate this behaviour, diffuse reflectance spectroscopy (DRS) of CABB powder was performed, which shows a corresponding reflectance edge beginning around 600 nm (**Figure 6.7(a)**), consistent with the absorption onset observed in the absorption-mode UV-vis data (**Figure 6.6(d)**). Using the Kubelka-Munk transform of the DRS data, the E_g of CABB powder was determined to be ~2.33 eV (**Figure 6.7(b)**), which matches well with the observed visible-light absorption characteristics and confirms the intrinsic optical transition of the CABB phase. The Raman spectrum of CABB shown in **Figure 6.7(c)** exhibits characteristic low-frequency lattice vibrational modes, with the

F_{2g}, E_g, and A_{1g} phonon modes appearing at approximately 73.63, 134.15, and 177.48 cm^{-1}, respectively. These modes correspond to symmetric and asymmetric vibrations arising from the $[BiBr_6]^{3-}$ and $[AgBr_6]^{5-}$ corner-sharing inorganic octahedra, confirming the structural integrity and long-range order of the CABB phase. Their clear presence indicates good crystallinity and a well-preserved perovskite lattice.

In our previous study, the structural and chemical characteristics of the $Ti_3C_2T_X$ MXene employed for DSSC passivation were comprehensively validated using FESEM, XRD, and XPS analyses, confirming its layered morphology, phase purity, and surface termination chemistry.[39] Building on these earlier findings, the present work provides additional vibrational spectroscopic insights through FTIR and Raman analyses to further elucidate the bonding environment, surface functional groups, and residual species of $Ti_3C_2T_X$ MXene, which are relevant to its interfacial passivation behavior. The FTIR spectrum of $Ti_3C_2T_X$ MXene given in **Figure 6.8(a)** displays characteristic absorption bands confirming the retention of the Ti-C carbide framework and the formation of mixed surface terminations induced by chemical etching. The peak below ~600 cm^{-1} corresponds to Ti-C stretching vibrations, while features in the ~550-750 cm^{-1} region are attributed to Ti-O and Ti-O-Ti modes, indicating partial surface oxidation and the presence of oxygen-based terminations. The observation of C-F stretching further confirms fluorine termination arising from HF-assisted etching. Absorption bands in the ~1050-1150 cm^{-1} and ~16501700 cm^{-1} regions are assigned to C-O and C=O stretching vibrations, respectively, suggesting the presence of oxygenated surface species and/or residual solvent molecules. A broad band in the ~3200-3600 cm^{-1} region is attributed to O-H stretching, confirming the presence of abundant -OH terminations and surface-adsorbed water, with its breadth reflecting strong hydrogen bonding within the MXene interlayers, which are crucial in modulating its hydrophilicity, interlayer chemistry, and interfacial charge transfer behaviour relevant to energy conversion and optoelectronic applications.

Additionally, the Raman spectrum of $Ti_3C_2T_X$ MXene (**Figure 6.8(b)**) recorded using a 532 nm excitation laser in the range of 200-1800 cm^{-1} exhibits six characteristic peaks, confirming the successful formation of surface-functionalized MXene and the presence of residual synthesis-related species. The peak at ~267 cm^{-1} is attributed to the

vibrational contribution of H atoms associated with -OH surface terminations on $Ti_3C_2T_X$, reflecting hydrogen bonding and interlayer interactions introduced during the etching and post-treatment processes.

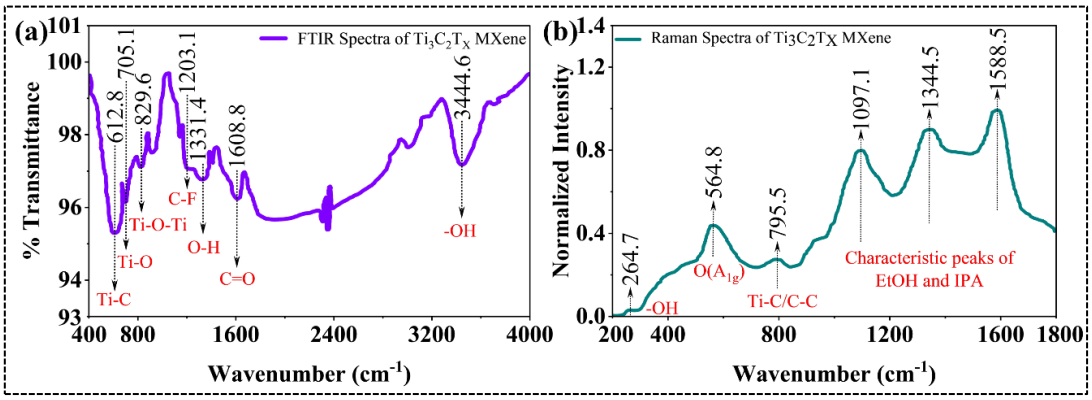

Figure 6.8 (a) FTIR, and (b) Raman spectra of bare $Ti_3C_2T_X$ MXene powder.

The Raman mode observed at ~565 cm^{-1} corresponds to the A_{1g} symmetric vibration of O atoms, indicative of Ti-O bonding arising from -O/-OH surface terminations and partial surface oxidation, which are intrinsic features of chemically etched MXenes. The peak located at ~797 cm^{-1} is assigned to Ti-C and C-C vibrational modes, confirming the preservation of the Ti_3C_2 carbide backbone after selective Al removal from the parent MAX phase. In addition to MXene-related vibrations, the peaks at ~1093, ~1346, and ~1589 cm^{-1} are attributed to the characteristic Raman modes of residual ethanol and isopropanol used during synthesis and washing, corresponding to C-O stretching, CH_3/CH_2 deformation, and C-C/C=C stretching modes, respectively. The presence of these peaks suggests weak physisorption or trace intercalation of alcohol molecules within the MXene layers or on the surface.

6.3.3 J-V Analysis

The J-V results, illustrated in **Figure 6.9(a-d)**, show the variation in PV parameters, including current density (J_{SC}), open-circuit voltage (V_{OC}), fill factor (FF), and power conversion efficiency (PCE), for FTO/ETLs/CABB/Carbon-structured HTL-free DPSCs.

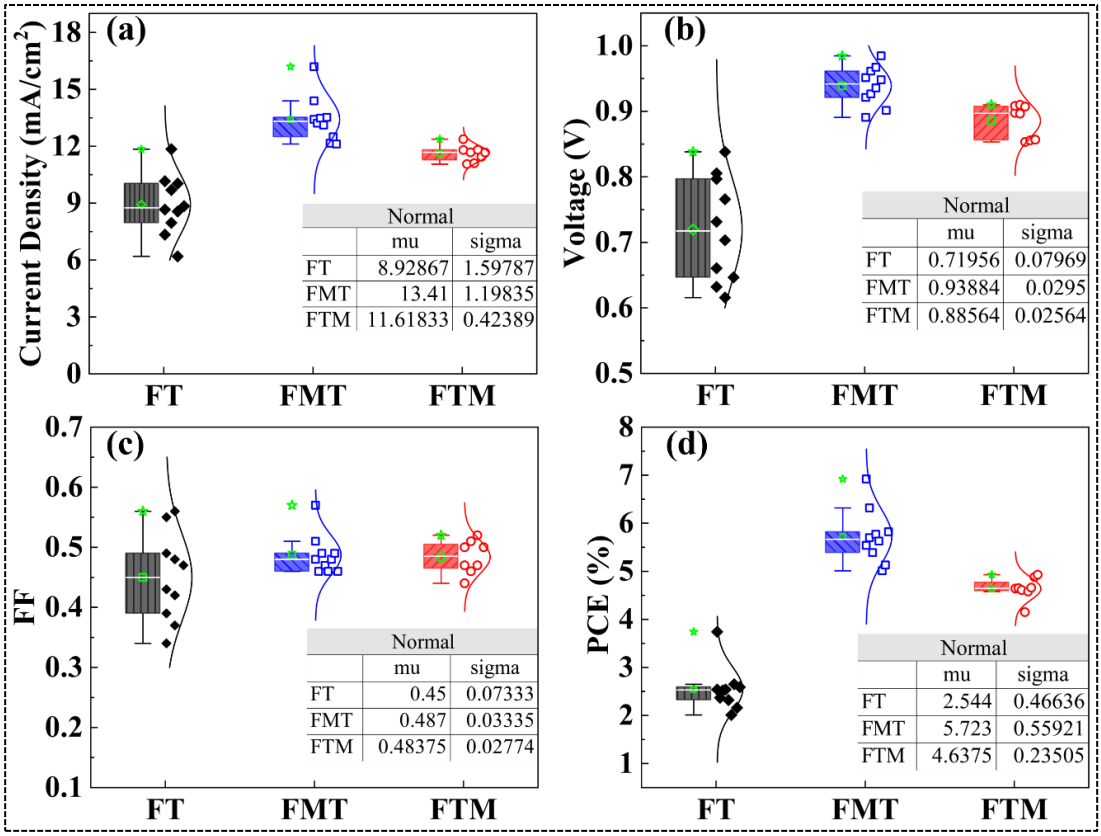

Figure 6.9 Statistical analysis of various PV-parameters, such as (a) J_{SC}, (b) V_{OC}, (c) FF, and (d) PCE for DPSCs fabricated using **FT**, **FMT**, and **FTM**-ETLs.

The J-V analysis clearly demonstrates that $Ti_3C_2T_X$ MXene-modified ETLs substantially enhance the performance of DPSCs compared to bare FT-ETLs. The **FMT**-based DPSCs yield the highest J_{SC} (16.19 mA cm^{-2}), V_{OC} (0.98 V), FF (0.57), and PCE (6.92%), indicating that the MXene interlayer at the FTO/TiO_2 interface effectively mitigates interfacial recombination, facilitates faster electron extraction, and improves band alignment at the FTO/Mx/TiO_2/CABB interface. In comparison, the **FTM** architecture delivers intermediate performance (PCE = 4.93%) with a higher V_{OC} (0.91 V) than **FT**, but a reduced FF, suggesting that MXene placed atop TiO_2 partially passivates surface traps, yet does not optimize the electron transport pathway to the same extent as the bottom-interfaced MXene. The lowest performance is observed in **FT**-based devices (PCE = 3.74%), which is consistent with greater charge recombination and weaker carrier collection in the absence of interfacial passivation.

All the J-V parameters and corresponding graphs for champion DPSCs utilizing distinct ETLs are summarized in **Table 6.2** and **Figure 6.10(a)**.

Table 6.6 Summary of all the J-V parameters of distinct DPSCs fabricated using FT, FMT, and FTM-ETLs.

DPSC	ETL used	J-V Parameters			
		J_{SC} (mA cm^{-2})	V_{OC} (V)	FF	PCE_{max} (%)
DPSC1	**FT**	11.85	0.84	0.56	3.74
DPSC2	**FMT**	16.19	0.98	0.57	6.92
DPSC3	**FTM**	12.37	0.91	0.52	4.93

The trend of **FMT** > **FTM** > **FT** is reproduced in the averaged device statistics, confirming reproducibility and minimizing statistical artefacts. The J-V characteristics of the **FT**, **FMT**, and **FTM-**based DPSCs correlate directly with their interfacial energetic landscape, as shown in **Figure 6.10(b-d)** and previously measured material properties.[44–46] In the **FT**-DPSCs, the direct FTO/TiO_2 interface forms a steep energy step (WF_{FTO} ≈ -4.7 eV vs. TiO_2 CBM ≈ -4.1 eV), which forces electrons to cross a high-energy (0.6 eV) mismatched barrier. This poor band matching enhances trap-assisted recombination at grain boundaries and heterogeneous FTO-TiO_2 contact regions, consistent with the lower J_{SC} (11.85 mA cm^{-2}), moderate V_{OC} (0.84 V), and the lowest PCE (3.74%). The structural and morphological evidence supports this, as the **FT**-ETL exhibits an irregular pore distribution, lower surface uniformity, and weaker optical absorption near the CB edge, resulting in fewer accessible conduction pathways and suboptimal electron extraction.

When a $Ti_3C_2T_X$-MXene interlayer is introduced beneath TiO_2 (**FMT** configuration), the band alignment becomes sequential and energetically downhill. The work function of $Ti_3C_2T_X$ MXene (~ -4.61 eV)[44] resides between FTO and TiO_2, forming a graded electron-transport ladder of CB_{CABB} (-3.72 eV), TiO_2 CBM (-4.1 eV), MXene (-4.61 eV), and FTO (-4.7 eV). This interfacial gradient minimizes potential barriers for electron injection and, together with MXene's metallic conductivity and abundant surface terminations (-O, -F, -OH), greatly suppresses interfacial recombination.

This improved charge extraction explains the highest J_{SC} (16.19 mA cm^{-2}) and V_{OC} (0.98 V), along with the highest FF (0.57) and maximum PCE (6.92%). These trends are consistent with earlier structural and morphological observations, which confirm that the MXene underlayers facilitate compact TiO_2 growth, reduce voids and boundary defects, and promote stronger anchoring of the absorber. Optical studies also indicate improved light harvesting and reduced back-surface reflection in **FMT**, providing a larger photogenerated carrier pool that the upgraded transport network can efficiently extract.

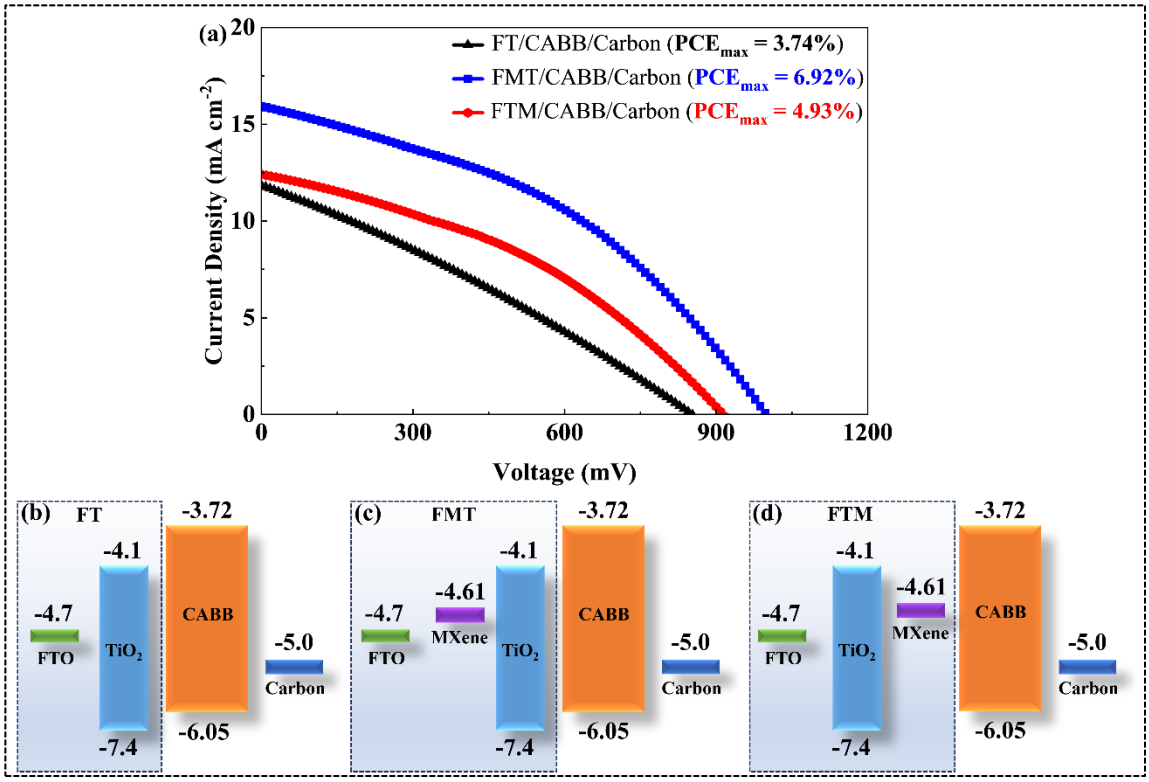

Figure 6.10 (a) J-V curves of all three best-performing DPSCs employing **FT**, **FMT**, and **FTM** electrodes. Typical electronically favourable band alignment for (b) FTO/TiO_2/CABB/Carbon, (c) FTO/Mx/TiO_2/CABB/Carbon, and (d) FTO/TiO_2/Mx/CABB/Carbon structured DPSCs.

However, in the **FTM** configuration, where $Ti_3C_2T_X$-MXene is placed above the TiO_2 but below the perovskite absorber, the passivation effect predominates over the extraction enhancement. Here, MXene suppresses surface traps at the TiO_2/CABB interface, reducing interfacial recombination and moderately improving electron injection

into TiO_2. This yields a higher V_{OC} (0.91 V) than **FT**, confirming better electronic passivation, but the absence of band-ladder conduction to FTO limits extraction efficiency, reflected in lower J_{SC} (12.37 mA cm^{-2}) and FF (0.52). The resulting PCE (4.93%) falls between that of **FT** and **FMT-**based DPSCs. This behavior aligns with prior structural and optical results, in which the MXene top layer enhances perovskite crystallization and interface quality, thereby reducing non-radiative recombination.

Collectively, the J-V outcomes map directly onto the engineered band configurations: **FMT** > **FTM** > **FT** is not incidental but a manifestation of how energetically graded electron-conduction pathways, defect mitigation, and light utilization synergistically influence carrier flux, recombination probability, and device efficiency. Further, this hierarchy aligns with AFM results, showing smoother surfaces and reduced nanoscale roughness for MXene-treated ETLs, which favour uniform CABB crystallization and reduced trap density. Moreover, EIS analysis further supports these findings by revealing a reduced charge-transfer resistance (R_{Ct}) and increased recombination resistance in MXene-modified devices, which directly correlates with the superior photovoltaic parameters of the FMT architecture. Collectively, the electrical, morphological, and electrochemical data converge to establish MXene underlayers as the most effective configuration for suppressing interfacial losses and maximizing device efficiency.

6.3.4 Surface Roughness and Topological Analysis

To understand the mechanics underlying the improved performance, AFM analysis of the **FT**, **FMT**, **FTM**, and **FMT/CABB** layers was performed, as shown in **Figure 6.11(a-d)** below. The AFM results clearly demonstrate that the MXene-underlayer configuration (**FMT**) provides the most favourable interfacial landscape for device operation compared to **FT** and **FTM**. The **FMT** surface exhibits significantly lower roughness values (root mean square roughness, R_q = 11.46 nm; average roughness, R_a = 8.98 nm) relative to **FT** (R_q = 16.38 nm; R_a = 12.89 nm) and **FTM** (R_q = 17.26 nm; R_a = 13.99 nm), indicating a smoother, more uniform electron-transport surface that suppresses local electric-field hotspots, minimizes microscopic voids and reduces the likelihood of shunt pathways. This smoother topography facilitates conformal perovskite coating, leading to enhanced charge collection and reduced non-radiative recombination.

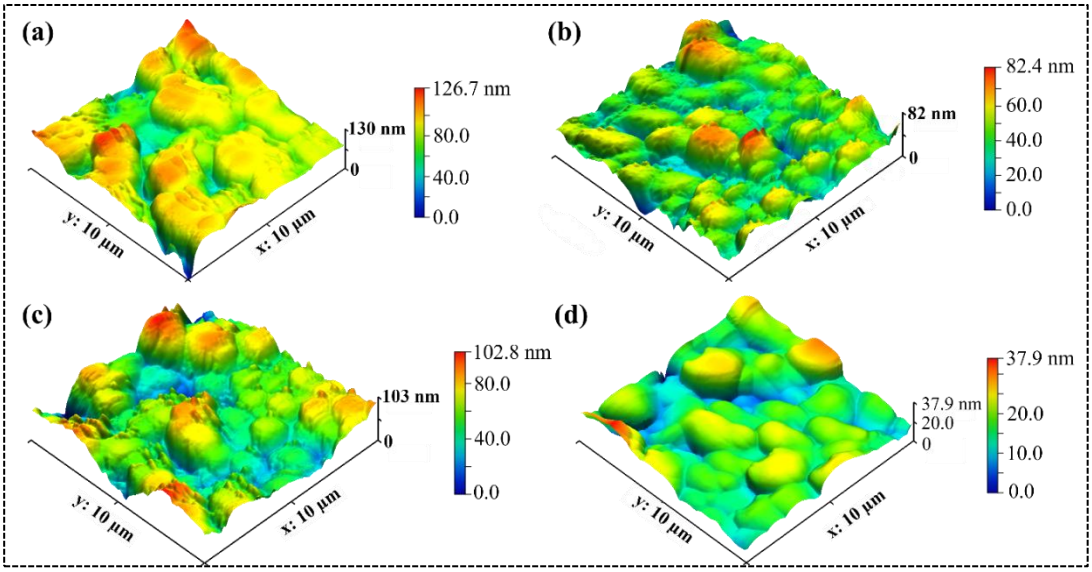

Figure 6.11 Surface roughness and topological features of (a) FT, (b) FMT, (c) FTM, and (d) FMT/CABB layers.

The superiority of the **FMT** interface is further reflected in the peak-to-valley roughness (R_z), which is drastically lower for **FMT** (79.97 nm) than **FT** (122.05 nm) and **FTM** (102.16 nm), implying fewer extreme surface asperities or deep valleys that could introduce trap states or hinder uniform crystal nucleation. The skewness (R_{sk}) trends reinforce this conclusion: **FT** (0.74) and **FTM** (0.06) show surfaces dominated by peaks or symmetric height profiles, whereas **FMT** shows a slight negative R_{sk} (-0.09), suggesting valley-filling and smoother terraces.

Table 6.7 Collective summary of all roughness and topological parameters of **FT**, **FMT**, **FTM**, and **FMT**/CABB layers.

ETLs	R_q (nm)	R_a (nm)	R_z (nm)	R_{sk}	R_{ku}
FT	16.38	12.89	122.05	0.74	3.55
FMT	11.46	8.98	79.97	-0.09	2.64
FTM	17.26	13.99	102.16	0.06	3.32
FMT/CABB	8.35	6.16	37.39	-0.83	2.19

After perovskite loading, the **FMT/CABB** layer becomes even more uniform (R_q = 8.35 nm; R_a = 6.16 nm), with a strongly negative R_{sk} = -0.83), indicating compact filling

of surface depressions and improved interfacial contact. Finally, kurtosis values (R_{ku}) below 3 for **FMT** = 2.64 and **FMT/CABB** = 2.19 confirm that these surfaces lack extreme height tails, in contrast to **FT** and **FTM** (> 3), which contain sharper peaks and troughs detrimental to device uniformity. Collectively, this set of AFM parameters provides a quantitative microstructural rationale for the performance hierarchy (**FMT** > **FTM** > **FT**), as smoother, less extreme, and more homogeneous interfaces enable superior perovskite crystallization, reduced defect density, and enhanced photovoltaic response. All these surface roughness and topological parameters are summarized in **Table 6.3**.

6.3.5 Charge Transport Properties

To elucidate the charge-transport characteristics of the **FTC**, **FMTC**, and **FTMC** electrodes, comprehensive electrochemical impedance spectroscopy (EIS) measurements were performed across a frequency window of 10^4 to 1 Hz, and the corresponding Nyquist responses are presented in **Figure 6.12(a)**. The impedance spectra of all electrodes were accurately modelled using the equivalent circuit $R_S + R_{Ct}/C_1 + R_{Rec}/C_2$ (inset of **Figure 6.12(a)**), ensuring reliable extraction of interfacial and bulk transport parameters. The complete set of fitted EIS parameters, including solution resistance (R_S), double-layer capacitance (C_1), charge-transfer resistance (R_{Ct}), constant-phase element (Q), recombination resistance (R_{Rec}), and chemical capacitance (C_2), is summarized in **Table 6.4**, forming the basis for the subsequent analysis of charge dynamics in **FT**, **FMT**, and **FTM** ETLs. Bode phase plots for the **FTC**, **FMTC**, and **FTMC** electrodes, shown in **Figure 6.12(b-d)**, were used to determine the characteristic maximum response (f_{max}), which serves as a key parameter for calculating the electron lifetime in the ETLs.

The EIS and the derived transport parameters provide a quantitative picture of how the different ETL architectures control charge extraction, recombination, and transport. The fitted EIS values (**Table 6.4**) and the calculated electrical quantities (**Table 6.5**) consistently indicate that the MXene-underlayer (**FMTC**)-based DPSCs are the superior PSC architecture. From the fitted EIS parameters extracted from the Nyquist plots in **Figure 6.12(a)**, a clear quantitative distinction among the **FTC**, **FMTC**, and **FTMC** electrodes is observed (**Table 6.4**). The series resistance (R_S) is lowest for **FMTC** (28.92 Ω) compared to **FTMC** (31.86 Ω) and **FTC** (38.05 Ω), corresponding to a ~24%

reduction relative to **FTC**. This decrease in R_S indicates reduced resistive losses across the FTO/ETL/CABB/electrolyte stack, attributed to the high electrical conductivity of the $Ti_3C_2T_X$ MXene interlayer, which enhances charge transport and interfacial electrical coupling at the FTO/TiO_2 interface.

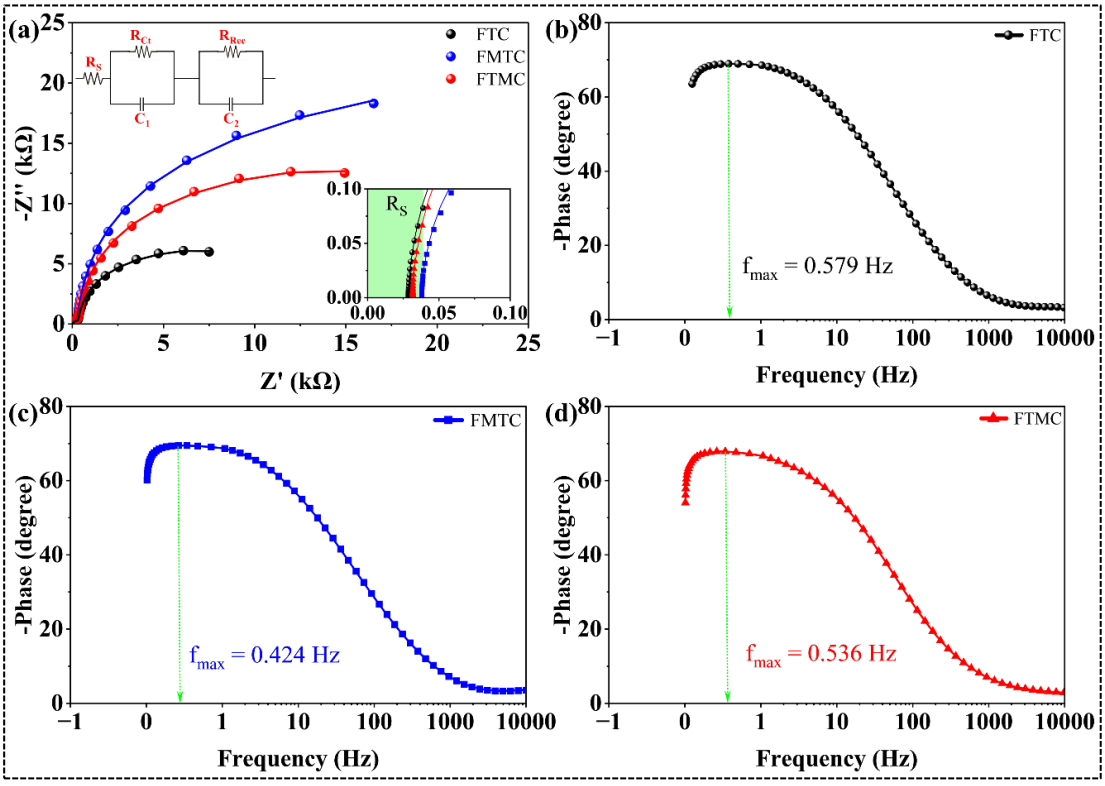

Figure 6.12 (a) Nyquist plot, (b-d) corresponding Bode plot of **FTC**, **FMTC**, and **FTMC** electrodes in 0.1M $TBAPF_6$ electrolyte in DCM.

Similarly, the charge-transfer resistance (R_{Ct}) at the ETL/CABB interface is lowest for **FMTC** (288.8 Ω), compared to **FTC** (300.7 Ω) and **FTMC** (312.3 Ω). Although the absolute variation is moderate, the consistent reduction in R_{Ct} for **FMTC** confirms faster interfacial charge-transfer kinetics, reflecting improved band alignment and reduced energy barriers for electron extraction when MXene is introduced beneath the TiO_2 layer. Most critically, the recombination resistance (R_{Rec}) shows a pronounced enhancement for **FMTC**, reaching 36.85 kΩ, approximately 3 times that of **FTC** (12.14 kΩ) and 1.45 times that of **FTMC** (25.34 kΩ). This substantial increase directly evidences effective suppression of interfacial and trap-assisted recombination, highlighting the key

role of MXene passivation at the FTO/TiO_2 interface in mitigating defect-mediated carrier losses.

Table 6.8 EIS fitted parameters (R_S, R_{Ct}, R_{Rec}, C_1, C_2, and f_{max}) obtained for CABB loaded **FT**, **FMT**, and **FTM**-ETLs in 0.1M $TBAPF_6$ electrolyte in DCM solution.

Passivated Electrodes	**R_S (Ω)**	**R_{Ct} (Ω)**	**C_1 (mF)**	**R_{Rec} (kΩ)**	**C_2 (mF)**	**f_{max} (Hz)**
FTC	38.05	300.7	0.278	12.14	1.091	0.579
FMTC	28.92	288.8	0.203	36.85	0.385	0.424
FTMC	31.86	312.3	0.191	25.34	0.426	0.536

The interfacial capacitances further support this conclusion. The C_1 and C_2 values for **FMTC** (0.203 and 0.385 mF, respectively) are significantly lower than those of **FTC** (0.278 and 1.091 mF), corresponding to reductions of ~27% and ~65%, respectively. Lower capacitance values are commonly associated with reduced interfacial trap density and diminished charge accumulation at defect sites, confirming more efficient carrier extraction and reduced charge storage in **FMTC**-based DPSCs. The reduced f_{max} (0.424 Hz) for **FMTC** further suggests slower recombination dynamics and longer carrier lifetimes (τ_e) than for **FTC** and **FTMC**. Collectively, this quantitative EIS analysis conclusively demonstrates that the **FMTC** electrode exhibits the most favourable charge-transport and recombination characteristics, directly correlating with its superior photovoltaic performance. The results validate MXene-underlayer passivation as an effective strategy for minimizing resistive losses, accelerating charge transfer, and suppressing interfacial recombination in HTL-free CABB-based double perovskite solar cells.

The derived transport parameters make the physical consequences explicit. The diffusion coefficient (D_e) and diffusion length (L_n) are particularly diagnostic of collection efficiency. **FMTC** shows a substantially larger $D_e = 10.84\times10^3$ $\mu m^2\ s^{-1}$ and the longest L_n = 63.80 μm compared with **FTC** ($D_e = 1.48\times10^3$ $\mu m^2\ s^{-1}$, L_n = 20.19 μm) and **FTMC** ($D_e = 5.54\times10^3$ $\mu m^2\ s^{-1}$, L_n = 40.57 μm). Because $L_n = \sqrt{(D_e\cdot\tau_e)}$, the large D_e and long τ_e in

FMTC combine to yield a L_n much greater than typical film thicknesses (~ 1 μm), ensuring nearly complete extraction of photogenerated electrons before recombination. This quantitatively explains the high charge-collection efficiency (η_{cc}) of 99.5% for **FMTC**, compared to 97.0% for **FTC** and 98.0% for **FTMC**. The effective diffusion lifetime (τ_D) is shortest for **FMTC** = 2.94 ms compared to **FTC** = 6.81 ms and **FTMC** = 3.66 ms, indicating faster steady-state diffusion/transit dynamics consistent with a higher D_e and more efficient extraction channel. Conductivity σ is similar across the samples but slightly higher for **FMTC** = 2.31×10^{-7} Ω cm^{-1} than for **FTC** = 2.22×10^{-7} Ω cm^{-1} and **FTMC** = 2.13×10^{-7} Ω cm^{-1}, reflecting the contribution of the conductive MXene interlayer to in-plane/out-of-plane transport and lower contact resistance.

Table 6.9 Summary of various calculated electrical parameters, such as electron lifetime (τ_e), diffusion length (L_n), diffusion Coefficient (D_e), charge collection efficiency (η_{cc}), effective diffusion lifetime of electron (τ_D), and conductivity (σ) for all three CABB-loaded FT, FMT, and FTM-ETLs.

Passivated Electrodes	τ_e (s)	L_n (μm)	D_e ($\mu m^2\ s^{-1}$)	η_{cc} (%)	τ_D (ms)	σ (Ω cm^{-1})
FTC	0.275	20.19	1.48×10^3	97.0	6.81	2.22×10^{-7}
FMTC	0.376	63.80	10.84×10^3	99.5	2.94	2.31×10^{-7}
FTMC	0.297	40.57	5.54×10^3	98.0	3.66	2.13×10^{-7}

Together, these electrical metrics justified the observed J-V behaviour shown in **Figure 6.9(a-d)**, where the **FMT**-based DPSC attains the highest J_{SC} = 16.19 mA cm^{-2}, V_{OC} = 0.98 V, FF = 0.57, and PCE = 6.92%. This improvement is because of (i) R_S and R_{Ct} are reduced (improved contact and faster interfacial kinetics), (ii) R_{Rec} is substantially increased (suppressed recombination), (iii) τ_e and L_n are maximized (long-lived carriers and efficient diffusion), and (iv) η_{cc} approaches unity (near-complete collection of photogenerated electrons). The **FTM**-based DPSC exhibits intermediate values of these parameters, corresponding to intermediate PV performance (J_{SC} = 12.37 mA cm^{-2}, V_{OC} = 0.91 V, PCE = 4.93%), consistent with an architecture that passivates the ETL/CABB interface but does not optimize the FTO/ETL contact as effectively as MXene under

layering. Meanwhile, the **FT**-based DPSC shows the poorest electrical metrics (highest R_S and R_{Ct} relative to performance, lowest R_{Rec}, shortest τ_e, and smallest L_n), which rationalizes its lowest J_{SC} and PCE.

Therefore, the charge-transport properties align seamlessly with the structural, morphological, and optical analyses. FESEM and AFM show that the MXene underlayer (**FMT**) produces a smoother, less asperous ETL that minimizes shunt pathways and promotes uniform, highly crystalline CABB deposition, as supported by XRD and TEM/SAED. UV-vis absorption confirms that all ETLs exhibit comparable light absorption, indicating that performance differences arise mainly from interfacial charge transport and recombination. The EIS-derived parameters, therefore, provide a quantitative and coherent explanation for the superior charge extraction and overall device efficiency enabled by MXene underlayer engineering.

6.4 Conclusions

This work demonstrates that engineering the electron-transport layer with $Ti_3C_2T_X$-MXene significantly enhances the interfacial charge dynamics, structural quality, and photovoltaic performance of CABB-based DPSCs. Introducing a $Ti_3C_2T_X$ MXene underlayer (**FMT**) reduces ETL roughness, as evidenced by a decrease in R_a from 12.89 nm in **FT** to 8.98 nm, enabling more uniform CABB crystallization and improved film-substrate contact. This structural refinement suppresses trap-assisted recombination, consistent with the sharp increase in recombination resistance (R_{Rec} rises from 12.14 kΩ in **FTC** to 36.85 kΩ in **FMTC**). Enhanced interfacial energetics and smoother pathways facilitate faster electron extraction, reflected in longer τ_e = 0.376 s and significantly extended L_n = 63.8 μm compared to **FT**. As a result of these coupled improvements, the **FMT**-based DPSC achieves the highest PV output (J_{SC} = 16.19 mA cm^{-2}, V_{OC} = 0.98 V, PCE = 6.92%), outperforming **FTM** and **FT** configurations. Overall, the results demonstrate that $Ti_3C_2T_X$ MXene-induced interface engineering directly governs defect suppression, charge transport, and recombination behaviour, thereby enabling a substantial increase in DPSC efficiency.

References

[1] A.S. Teja, A. Srivastava, J.A.K. Satrughna, M.K. Tiwari, A. Kanwade, S. Chand Yadav, P.M. Shirage, Optimal processing methodology for futuristic natural dye-sensitized solar cells and novel applications, Dye. Pigment. 210 (2023) 110997. https://doi.org/10.1016/j.dyepig.2022.110997.

[2] A. Kojima, K. Teshima, Y. Shirai, T. Miyasaka, Organometal Halide Perovskites as Visible-Light Sensitizers for Photovoltaic Cells, J. Am. Chem. Soc. 131 (2009) 6050–6051. https://doi.org/https://doi.org/10.1021/ja809598r.

[3] National Renewable Energy Laboratory, Best Research-Cell Efficiency Chart, 2026. https://www.nrel.gov/pv/cell-efficiency.

[4] A. Srivastava, J.A.K. Satrughna, M.K. Tiwari, A. Kanwade, S.C. Yadav, K. Bala, P.M. Shirage, Lead metal halide perovskite solar cells: Fabrication, advancement strategies, alternatives, and future perspectives, Mater. Today Commun. 35 (2023) 105686. https://doi.org/10.1016/j.mtcomm.2023.105686.

[5] A. Srivastava, P.M. Shirage, Operational Stability Management Approaches for Perovskite Solar Cells, in: Perovskite Sol. Cells Fundam. Approaches Mater. Process. Sustain. Futur., 1st ed., Springer Singapore, 2024: pp. 91–139. https://doi.org/https://doi.org/10.1007/978-981-97-7624-5_3.

[6] S. Chand Yadav, A. Srivastava, V. Manjunath, A. Kanwade, R.S. Devan, P.M. Shirage, Properties, performance and multidimensional applications of stable lead-free $Cs_2AgBiBr_6$ double perovskite, Mater. Today Phys. 26 (2022) 100731. https://doi.org/10.1016/j.mtphys.2022.100731.

[7] H. Ren, S. Yu, L. Chao, Y. Xia, Y. Sun, S. Zuo, F. Li, T. Niu, Y. Yang, H. Ju, B. Li, H. Du, X. Gao, J. Zhang, J. Wang, L. Zhang, Y. Chen, W. Huang, Efficient and stable Ruddlesden–Popper perovskite solar cell with tailored interlayer molecular interaction, Nat. Photonics. 14 (2020) 154–163. https://doi.org/10.1038/s41566-019-0572-6.

[8] L. Chao, Y. Xia, B. Li, G. Xing, L. Chao, Y. Xia, B. Li, G. Xing, Y. Chen, W. Huang, Room-Temperature Molten Salt for Facile Fabrication of Efficient and Stable Perovskite Solar Cells in Ambient Air, Chem. 5 (2019) 995–1006. https://doi.org/10.1016/j.chempr.2019.02.025.

[9] J. Qiu, Y. Xia, Y. Chen, W. Huang, Management of Crystallization Kinetics for Efficient and Stable Low-Dimensional Ruddlesden–Popper (LDRP) Lead-Free Perovskite Solar Cells, Adv. Sci. 6 (2019) 1800793. https://doi.org/10.1002/advs.201800793.

[10] J. Qiu, Y. Xia, Y. Zheng, W. Hui, H. Gu, W. Yuan, H. Yu, L. Chao, T. Niu, Y. Yang, X. Gao, Y. Chen, W. Huang, 2D Intermediate Suppression for Efficient Ruddlesden−Popper (RP) Phase Lead-Free Perovskite Solar Cells, ACS Energy Lett. 4 (2019) 1513–1520. https://doi.org/10.1021/acsenergylett.9b00954.

[11] K. Wang, Z. Jin, L. Liang, H. Bian, D. Bai, H. Wang, J. Zhang, Q. Wang, S. Liu, All-inorganic cesium lead iodide perovskite solar cells with stabilized efficiency beyond 15%, Nat. Commun. 9 (2018) 4544. https://doi.org/10.1038/s41467-018-06915-6.

[12] J. Liang, C. Wang, Y. Wang, Z. Xu, Z. Lu, Y. Ma, H. Zhu, Y. Hu, C. Xiao, X. Yi, G. Zhu, H. Lv, L. Ma, T. Chen, Z. Tie, Z. Jin, J. Liu, All-Inorganic Perovskite Solar Cells, J. Am. Chem. Soc. 138 (2016) 15829–15832. https://doi.org/https://doi.org/10.1021/jacs.6b10227.

[13] H. Yao, F. Zhou, Z. Li, Z. Ci, L. Ding, Z. Jin, Strategies for Improving the Stability of Tin-Based Perovskite ($ASnX_3$) Solar Cells, Adv. Sci. 7 (2020) 1903540. https://doi.org/10.1002/advs.201903540.

[14] X. Jiang, F. Wang, Q. Wei, H. Li, Y. Shang, W. Zhou, C. Wang, P. Cheng, Q. Chen, L. Chen, Z. Ning, Ultra-high open-circuit voltage of tin perovskite solar cells via an electron transporting layer design, Nat. Commun. 11 (2020) 1–7. https://doi.org/10.1038/s41467-020-15078-2.

[15] A.S. Shaikh, S.C. Yadav, A. Srivastava, A.R. Kanwade, M.K. Tiwari, S.M. Rajore,

J.A.K. Satrughna, M. Dhonde, P.M. Shirage, Dynamic synergy of tin in the electron-transfer layer and absorber layer for advancing perovskite solar cells: a comprehensive review, Energy Adv. 3 (2024) 1505–1552. https://doi.org/10.1039/D4YA00204K.

[16] G. Giorgi, Two-dimensional optical excitations in the mixed-valence $Cs_2Au_2I_6$ fully inorganic double perovskite, J. Mater. Chem. C. 6 (2018) 10197–10201. https://doi.org/10.1039/c8tc03496f.

[17] X. Zhao, J. Yang, Y. Fu, D. Yang, Q. Xu, L. Yu, S. Wei, L. Zhang, Design of Lead-Free Inorganic Halide Perovskites for Solar Cells via, J. Am. Chem. Soc. 139 (2017) 2630–2638. https://doi.org/10.1021/jacs.6b09645.

[18] M.R. Filip, S. Hillman, A.A. Haghighirad, H.J. Snaith, F. Giustino, Band Gaps of the Lead-Free Halide Double Perovskites Cs2BiAgCl6 and $Cs_2BiAgBr_6$ from Theory and Experiment, J. Phys. Chem. Lett. 7 (2016) 2579–2585. https://doi.org/10.1021/acs.jpclett.6b01041.

[19] C.N. Savory, A. Walsh, D.O. Scanlon, Can Pb-Free Halide Double Perovskites Support High-Efficiency Solar Cells?, ACS Energy Lett. 1 (2016) 949–955. https://doi.org/10.1021/acsenergylett.6b00471.

[20] C.J. Bartel, J.M. Clary, C. Sutton, D. Vigil-fowler, B.R. Goldsmith, A.M. Holder, C.B. Musgrave, Inorganic Halide Double Perovskites with Optoelectronic Properties Modulated by Sublattice Mixing, J. Am. Chem. Soc. 142 (2020) 5135–5145. https://doi.org/10.1021/jacs.9b12440.

[21] G. Kaur, A. Shukla, K.J. Babu, H. Bhatt, H.N. Gosh, Probing the charge transfer mechanisms in type-II $Cs_2AgBiBr_6$-CdSe composite system: ultrafast insights, Nanotechnology. 33 (2022) 485406. https://doi.org/10.1088/1361-6528/ac7dee.

[22] E. Greul, M.L. Petrus, A. Binek, P. Docampo, T. Bein, Highly stable, phase pure $Cs_2AgBiBr_6$ double perovskite thin films for optoelectronic applications, J. Mater. Chem. A. 5 (2017) 19972–19981. https://doi.org/10.1039/c7ta06816f.

[23] Z. Zhang, Q. Sun, Y. Lu, F. Lu, X. Mu, S.-H. Wei, M. Sui, Hydrogenated $Cs_2AgBiBr_6$ for significantly improved efficiency of lead-free inorganic double perovskite solar cell, Nat. Commun. 13 (2022) 3397. https://doi.org/10.1038/s41467-022-31016-w.

[24] M. Pantaler, K.T. Cho, V.I.E. Queloz, C. Fettkenhauer, I. Anusca, M.K. Nazeeruddin, D.C. Lupascu, G. Grancini, Hysteresis-Free Lead-Free Double-Perovskite Solar Cells by Interface Engineering, ACS Energy Lett. 3 (2018) 1781–1786. https://doi.org/10.1021/acsenergylett.8b00871.

[25] W. Ning, F. Wang, B. Wu, J. Lu, Z. Yan, X. Liu, Y. Tao, J.-M. Liu, W. Huang, M. Fahlman, L. Hultman, T.C. Sum, F. Gao, Long Electron – Hole Diffusion Length in High-Quality Lead-Free Double Perovskite Films, Adv. Mater. 30 (2018) 1706246. https://doi.org/10.1002/adma.201706246.

[26] M. Wang, P. Zeng, S. Bai, J. Gu, F. Li, Z. Yang, M. Liu, High-Quality Sequential-Vapor-Deposited $Cs_2AgBiBr_6$ Thin Films for Lead-Free Perovskite Solar Cells, Sol. RRL. 2 (2018) 1800217. https://doi.org/10.1002/solr.201800217.

[27] R. Fan, Y. Huang, L. Wang, L. Li, G. Zheng, H. Zhou, The Progress of Interface Design in Perovskite-Based Solar Cells, Adv. Energy Mater. 6 (2016) 1600460. https://doi.org/10.1002/aenm.201600460.

[28] Y. Bekenstein, J.C. Dahl, J. Huang, W.T. Osowiecki, J.K. Swabeck, E.M. Chan, P. Yang, A.P. Alivisatos, The Making and Breaking of Lead-Free Double Perovskite Nanocrystals of Cesium Silver–Bismuth Halide Compositions, Nano Lett. 18 (2018) 3502–3508. https://doi.org/10.1021/acs.nanolett.8b00560.

[29] W. Tress, M. Yavari, K. Domanski, P. Yadav, B. Niesen, P. Correa, A. Hagfeldt, M. Graetzel, Interpretation and evolution of open-circuit voltage, recombination, ideality factor and subgap irreversible degradation of perovskite solar cells, Energy Environ. Sci. 11 (2018) 151–165. https://doi.org/10.1039/c7ee02415k.

[30] Y. Liu, Y. Hu, X. Zhang, P. Zeng, F. Li, B. Wang, Q. Yang, M. Liu, Inhibited aggregation of lithium salt in spiro-OMeTAD toward highly efficient perovskite

solar cells, Nano Energy. 70 (2020) 104483. https://doi.org/10.1016/j.nanoen.2020.104483.

[31] A. Raj, M. Kumar, D.V. Singh, B. Singh, D.K. Dwivedi, A. Anshul, Physical parameter optimization and band alignment approach for efficiency improvement in $Cs_2AgBiBr_6$ based lead-free perovskite solar cells, Sci. Rep. 15 (2025) 32868. https://doi.org/https://doi.org/10.1038/s41598-025-02203-8.

[32] T. Luo, Y. Zhang, X. Chang, J. Fang, T. Niu, J. Lu, Y. Fan, Z. Ding, K. Zhao, S. Frank, Dual interfacial engineering for efficient $Cs_2AgBiBr_6$ based solar cells, J. Energy Chem. 53 (2021) 372–378. https://doi.org/10.1016/j.jechem.2020.05.016.

[33] L. Yang, Y. Dall'Agnese, K. Hantanasirisakul, C.E. Shuck, K. Maleski, M. Alhabeb, G. Chen, Y. Gao, Y. Sanehira, A.K. Jena, L. Shen, C. Dall'Agnese, X.F. Wang, Y. Gogotsi, T. Miyasaka, SnO_2-Ti_3C_2 MXene electron transport layers for perovskite solar cells, J. Mater. Chem. A. 7 (2019) 5635–5642. https://doi.org/10.1039/c8ta12140k.

[34] H.G. Lemos, R.M. Ronchi, G.R. Portugal, J.H.H. Rossato, G.S. Selopal, D. Barba, E.C. Venancio, F. Rosei, J.T. Arantes, S. F. Santos, Efficient $Ti_3C_2T_x$ MXene/TiO_2 Hybrid Photoanodes for Dye-Sensitized Solar Cells, ACS Appl. Energy Mater. 5 (2022) 15928–15938. https://doi.org/10.1021/acsaem.2c03474.

[35] J. Wang, C. Du, Y. Xue, X. Tan, J. Kang, Y. Gao, H. Yu, Q. Yan, MXenes as a versatile platform for reactive surface modification and superior sodium-ion storages, Exploration. 1 (2021) 20210024. https://doi.org/10.1002/EXP.20210024.

[36] A. Srivastava, P.M. Shirage, Overcoming Intrinsic and Extrinsic Challenges in Perovskite Solar Cells: A Pathway Toward Advancement, in: Perovskite Sol. Cells Fundam. Approaches Mater. Process. Sustain. Futur., 2024: pp. 55–89. https://doi.org/10.1007/978-981-97-7624-5_2.

[37] A. Srivastava, P.M. Shirage, Pioneering the Path: Unveiling Exciting Applications for Integrated Perovskite Solar Cells, in: Perovskite Sol. Cells Fundam. Approaches Mater. Process. Sustain. Futur., 1st ed., Springer Singapore, 2024: pp.

177–203. https://doi.org/https://doi.org/10.1007/978-981-97-7624-5_5.

[38] A. Srivastava, M. Kasliwal, P.M. Shirage, From HTL to HTL-free: Experimental and numerically modelled performance dynamics of $Cs_2AgBiBr_6$ double perovskite solar cells, Sol. Energy. 298 (2025) 113733. https://doi.org/10.1016/j.solener.2025.113733.

[39] A. Srivastava, Y. Ito, H. Lee, Y. Ohshita, A. Ogura, M. Dhonde, P.M. Shirage, Multilayered 2D $Ti_3C_2T_X$ - MXene : Best Interfacial Passivating Agent for Dye-Sensitized Solar Cells with V_{OC} Approaching 1 V, ACS Appl. Electron. Mater. 7 (2025) 1531–1549. https://doi.org/10.1021/acsaelm.4c02107.

[40] J. Barichello, G. Shankar, P. Mariani, A. Di, F. Matteocci, Unveiling the potential of $Cs_2AgBiBr_6$ perovskites for next-generation see-through photovoltaics, Mater. Today Energy. 46 (2024) 101725. https://doi.org/10.1016/j.mtener.2024.101725.

[41] S. Ullah, N. Alqarni, F. Khan, N. Awad, Investigation of lead-free $Cs_2AgBiBr_6$ double perovskites for application in solar cells, Phys. B Condens. Matter. 707 (2025) 417174. https://doi.org/10.1016/j.physb.2025.417174.

[42] A. Srivastava, J.A.K. Satrughna, M.K. Tiwari, A. Kanwade, S.C. Yadav, K. Bala, P.M. Shirage, Effect of $Ti_{1-x}Fe_xO_2$ photoanodes on the performance of dye-sensitized solar cells utilizing natural betalain pigments extracted from Beta vulgaris (BV), Energy Adv. 2 (2023) 148–160. https://doi.org/10.1039/d2ya00197g.

[43] A. Srivastava, B. Singh Chauhan, S. Chand Yadav, M. Kumar Tiwari, J. Akash Kumar Satrughna, A. Kanwade, K. Bala, P.M. Shirage, Performance of dye-sensitized solar cells by utilizing Codiaeum Variegatum Leaf and Delonix Regia Flower as natural sensitizers, Chem. Phys. Lett. 807 (2022) 140087. https://doi.org/10.1016/j.cplett.2022.140087.

[44] S.W. Koh, L. Rekhi, M.D. Birowosuto, Q.T. Trinh, J. Ge, W. Yu, A.T.S. Wee, T.S. Choksi, H. Li, Tuning the Work Function of MXene via Surface Functionalization, ACS Appl. Mater. Interfaces. 16 (2024) 66826–66836.

https://doi.org/10.1021/acsami.3c11857.

[45] S. Wang, Y. Liu, S. Wang, Y. Liu, Y. Liu, Z. Shi, J. Zhou, J. Zhu, Identifying the surface properties of $Ti_3C_2T_x$ MXene through transmission electron microscopy, Cell Reports Phys. Sci. 3 (2022) 101151. https://doi.org/10.1016/j.xcrp.2022.101151.

[46] M. Magnuson, P. Eklund, C. Polley, Fermiology and Band Structure of Oxygen-Terminated $Ti_3C_2T_x$ MXene, Phys. Rev. Lett. 134 (2025) 106201. https://doi.org/10.1103/PhysRevLett.134.106201.

Chapter 7

Conclusions and Scope for Future Work

The global energy crisis and growing environmental concerns demand the development of sustainable, low-cost, and environmentally benign photovoltaic technologies. This thesis addresses these challenges through systematic material innovation, bulk and interface engineering to enhance device efficiency and stability. Beginning with conventional DSSCs and progressing toward natural dyes and lead-free double perovskites, the work emphasizes economical sustainability without compromising performance. Particular focus has been placed on band gap tuning and interfacial passivation to improve charge transport and suppress recombination losses. Numerical simulations and experimental investigations were synergistically employed to identify performance bottlenecks and extract optimized DPSC parameters. The integration of dual-passivation strategies further enabled significant improvements in power conversion efficiency (PCE) through better band alignment. Overall, this chapter summarizes the thesis's key findings and outlines future research directions to bridge the gap among stability, scalability, and high efficiency in next-generation green photovoltaic systems.

7.1 Introduction

The core theme of this thesis is the development of economical, environmentally benign, and stable photovoltaic technologies through rational material selection and interface engineering. The research journey began with synthetic N719 dye-based DSSCs with passivated TiO_2 photoanodes, followed by a transition to naturally derived beetroot dye with Fe-doped TiO_2 photoanodes to promote sustainability and reduce cost. Although natural dyes offer ecological advantages due to their strong absorption in the visible region, their limited efficiency and stability have prompted the exploration of alternative photo absorbers. This led to the implementation of lead-free $Cs_2AgBiBr_6$ double perovskite (CABB) in an HTL-free architecture, achieving a PCE of 1.63% under open-air fabrication with >95% PCE retention after 200 h, highlighting its excellent environmental stability.

To understand the efficiency limitations, systematic numerical simulations using SCAPS-1D were conducted for HTL-based and HTL-free device architectures with TiO_2, SnO_2, WO_3, and ZnO as ETLs. The optimized HTL-based configuration yielded PCEs exceeding 27%, while HTL-free devices showed only ~4% lower efficiency, providing critical insights into defect tolerance, optimal thickness, doping density, interfacial recombination limits, and resistive parameters. Guided by these findings, dual interfacial passivation using 2D $Ti_3C_2T_X$ MXene at the FTO/TiO_2 and TiO_2/CABB interfaces was implemented to optimize the band alignment and suppress recombination. This strategy enhanced the experimental device's performance from 3.74% to a champion PCE of 6.92%, among the highest reported for CABB-based double perovskite solar cells.

Hence, special attention has been given to the role of doping, nano-structuring, interfacial passivation, and device engineering in optimizing charge transport, defect tolerance, and band alignment, making these materials highly promising for next-generation sustainable photovoltaic and optoelectronic applications.

7.2 Dissertation Summary

This thesis comprises seven chapters: Introduction (Chapter 1), Experimental and Characterization Techniques (Chapter 2), Experimental Works (Chapters 3-6), followed by Conclusions and Scope for Future Work (Chapter 7).

Specifically, ***Chapter 1*** focuses on the state-of-the-art dye-sensitized and perovskite solar cell technologies as promising alternatives to conventional silicon photovoltaics, highlighting their historical background, working mechanisms, benchmark results, types, and recent developments. The discussion includes key performance metrics, material selection criteria, and opto-electronic suitability for PV application. The selection of photoanodes, sensitizers, and absorber materials has been systematically discussed based on their electronic structure, band alignment, optical absorption behaviour, defect tolerance, and charge transport characteristics. Particular focus has been on environmentally benign, lead-free materials to address concerns about toxicity and long-term sustainability. The chapter concludes by defining the scope and objectives of the present research, which aims to develop efficient, stable, and economically viable photovoltaic devices through strategic material design and advanced interfacial engineering approaches.

Chapter 2 presents the experimental procedures and characterization techniques employed throughout this research. The synthesis approaches, including hydrothermal growth of Fe-doped 1D-TiO_2 nanorods, solution processing for electrolyte and CABB, preparation of 2D $Ti_3C_2T_X$ MXene passivator, and interfacial engineering strategies, were described to highlight their roles in tailoring the morphology, crystallinity, and defect density of photoanodes and absorber layers. Device fabrication techniques, such as spin coating, doctor-blade deposition, and thermal treatment, used to assemble DSSC and CABB-based double perovskite solar cell architectures are discussed in detail.

Additionally, comprehensive characterization methods were discussed, used to correlate material properties with photovoltaic performance. X-ray diffraction (XRD) was used for phase identification and structural analysis; FESEM with EDS provided morphological and compositional insights; TEM enabled high-resolution structural

investigation; AFM was performed to evaluate surface roughness parameters; XPS was conducted for surface chemical and oxidation state analysis; Raman spectroscopy was used to probe vibrational and phase characteristics; and UV-vis spectroscopy was employed to examine optical absorption and bandgap behaviour. Electrochemical impedance spectroscopy (EIS) was conducted to study charge-transfer resistance and recombination dynamics, while J-V measurements under AM 1.5G illumination were performed to evaluate photovoltaic performance, enabling a systematic assessment of device efficiency and charge-transport characteristics.

In ***Chapter 3***, the impact of interfacial passivation on the performance of DSSCs was systematically investigated using 2D $Ti_3C_2T_X$ MXene, compared with conventional treatments such as $TiCl_4$, toluene, and chlorobenzene. The incorporation of multi-layered MXene as an interfacial modifier significantly improved surface uniformity, suppressed recombination losses, and facilitated efficient charge transport owing to its high electrical conductivity and rich surface functional groups. The optimised FTO/c-TiO_2/MX-TNRs/N719/(I^-/I_3^-)/Carbon device achieved a PCE of 4.83%, markedly higher than 3.42% for the unpassivated counterpart, accompanied by a V_{OC} exceeding 1 V. Performance enhancement was supported by a ~57% reduction in surface roughness and ~82% decrease in charge transfer resistance, along with notable improvements in J_{SC} and overall charge collection efficiency. Compared to conventional passivation approaches, MXene demonstrated superior interfacial engineering capability, establishing its potential as an effective and scalable strategy for high-efficiency DSSC applications.

Chapter 4 builds upon the interfacial engineering strategy established in the previous chapter, transitioning towards a more sustainable photovoltaic approach by replacing the synthetic N719 dye with a ***naturally derived beetroot (Beta vulgaris) sensitizer***. While MXene-based passivation previously enhanced device performance, this chapter focuses on improving the intrinsic photoanode properties to compensate for the relatively lower efficiency of natural sensitizers. Fe-doped TiO_2 nanorod ($Ti_{1-x}Fe_xO_2$) photoanodes were synthesized via a hydrothermal method to enhance charge injection and suppress recombination. An optimal 5 at% Fe ($Ti_{0.95}Fe_{0.05}O_2$) incorporation increased the photocurrent density from 80 to 129.8 μA cm^{-2} and nearly doubled the PCE from 0.26%

to 0.52%. The integration of compact TiO_2 layers and low-cost Ni counter electrodes further improved charge collection while maintaining economic feasibility. Although challenges such as surface pinholes and dye degradation persist, this chapter demonstrates a cost-effective, environmentally benign DSSC configuration that extends the sustainability-driven framework established in the previous chapter.

In ***Chapter 5***, the sustainability-driven approach established before is extended to fully inorganic, lead-free double perovskite solar cells (DPSCs) based on $Cs_2AgBiBr_6$ (CABB). An HTL-free FTO/TiO_2/CABB/Carbon architecture fabricated under open-air conditions delivered a champion PCE of 1.63% with >95% retention after 200 h, demonstrating remarkable ambient stability. Charge-transport analysis revealed high recombination resistance (R_{Rec} = 1625 Ω), a long electron lifetime (τ_e = 0.226 s), efficient charge collection ($\eta_{cce} \approx$ 89.65%), and favourable diffusion parameters, confirming that interfacial stability governs long-term durability. However, the modest efficiency prompted the systematic execution of SCAPS-1D simulations to optimize both HTL and HTL-free configurations using TiO_2, SnO_2, WO_3, and ZnO as ETLs. ZnO emerged as the most effective ETL, yielding simulated PCEs of 27.30% (HTL-based) and 23.09% (HTL-free), with the efficiency reduction (~4%) in HTL-free devices attributed to enhanced interfacial recombination and limited charge extraction. This combined experimental-numerical investigation provides a strategic pathway to bridge the performance gap and positions CABB as a promising lead-free absorber for stable and sustainable next-generation photovoltaics.

Lastly, building on these foundations, ***Chapter 6*** advances device performance through targeted interfacial engineering. Here, a dual interfacial passivation strategy employing two-dimensional $Ti_3C_2T_X$ MXene was implemented in HTL-free FTO/TiO_2/CABB/Carbon DPSCs. Selective incorporation of MXene at the FTO/TiO_2 interface (**FMT**) significantly improved ETL uniformity, reduced surface roughness, and suppressed defect-induced recombination. Electrochemical analysis revealed superior charge-transport characteristics, including reduced series and charge-transfer resistances, enhanced recombination resistance, extended carrier lifetime, and improved diffusion length. Consequently, the **FMT**-based DPSCs achieved a champion PCE of 6.92% (V_{OC}

= 0.98 V, J_{SC} = 16.19 mA cm^{-2}, FF = 0.57), markedly outperforming bare and top-passivated configurations. These findings demonstrate that MXene-induced band-alignment optimization and defect passivation effectively govern interfacial charge dynamics, establishing a robust pathway to enhance the efficiency of stable, lead-free double perovskite solar cells.

7.3 Current Progress and Future Scope

Looking beyond single-device optimization, current progress is extending to integrated solar energy utilization through photovoltaic-thermal (PV/T) spectral splitter systems and PV-driven environmental remediation platforms. In the PV/T spectral splitter work, Ag-ZnO nanofluid-based optical filters were engineered to selectively transmit high-energy photons to the PV module while diverting sub-bandgap infrared radiation to a thermal collector. This approach addresses one of the key inefficiencies in conventional PV systems, thermalization losses, and temperature-induced performance degradation. By optimizing nanoparticle composition, concentration, and optical path length, the spectral management strategy enhances electrical output while simultaneously recovering thermal energy, thereby increasing overall solar utilization efficiency. Such hybrid systems offer a practical pathway to maximize exergy efficiency and reduce land-use intensity, particularly in densely populated, energy-constrained regions.

Concurrently, significant advancements have been achieved in PV-driven environmental remediation integrated with green hydrogen production. The development of Fe-doped TiO_2 photoanodes capable of simultaneously degrading pollutants and evolving hydrogen demonstrates a dual-functional energy-environment platform. By tuning band structure, carrier mobility, and interfacial charge transfer, the system achieves efficient visible-light absorption, enhanced reactive oxygen species (ROS) generation, and improved charge separation. This enables rapid degradation of organic contaminants, accompanied by measurable hydrogen evolution rates under solar illumination. Importantly, the reduction in charge-transfer resistance and the improved carrier lifetime confirm that optimized semiconductor interfaces can sustain both oxidation and reduction half-reactions without severe recombination losses. Such systems directly address two

global challenges, clean energy generation and water pollution, within a single operational framework.

From a sustainability perspective, PV-coupled water purification and hydrogen production systems are highly attractive for decentralized applications, particularly in rural or water-stressed areas. The ability to treat wastewater while generating value-added hydrogen fuel improves techno-economic feasibility and resource efficiency. Furthermore, integrating these systems with spectral-splitting PV/T modules could enable self-sustained, off-grid renewable energy hubs capable of electricity generation, thermal management, water treatment, and fuel production.

The future scope of this research is broad and interdisciplinary. In PV/T systems, further optimization of nanofluid stability, optical selectivity, and long-term thermal durability is essential for real-world deployment. Advanced modelling of photon-heat coupling and entropy generation analysis can refine system-level design. For PV-driven remediation, scaling the reactor architecture, enhancing catalyst robustness under continuous flow conditions, and improving solar-to-hydrogen (STH) efficiency will be critical. Integration with carbon-neutral fuel synthesis, desalination technologies, and smart microgrid infrastructure presents additional opportunities. Moreover, coupling high-voltage tandem PV modules with electrolyzers can elevate hydrogen production efficiency, facilitating industrial-scale green hydrogen generation.

Based on the systematic advancements achieved from ***Chapters 3*** to ***6***, spanning DSSCs, lead-free CABB DPSCs, MXene-based interfacial engineering, numerical optimization, and current progress made in PV/T spectral splitting and PV-driven environmental remediation, the following five strategic research targets provide directions for future goals to achieve superior performance, enhanced stability, and scalable sustainability:

1. **Ultra-Low Defect Interface Engineering for Near-Intrinsic Charge Transport**

   A key future objective is to minimize the interfacial trap density to below 10^{12} cm^{-2}, approaching near-intrinsic charge-transport behaviour in CABB-based

devices. Although MXene-assisted passivation has already reduced recombination losses, further suppression of interface defect density (N_{if}) is essential to limit trap-assisted recombination and maximize voltage output. This can be achieved through chemically bonded or self-assembled interlayers, molecular dipole engineering for precise band-edge alignment, atomic layer deposited (ALD) ultrathin passivation coatings (<5 nm) for conformal defect coverage, graded ETL/absorber junctions to avoid abrupt band discontinuities, and controlled surface termination to suppress halide vacancy formation in CABB. Collectively, these strategies are expected to enhance V_{OC}, improve charge-collection efficiency (η_{cce}), and ensure superior long-term operational stability.

2. Development of High-Mobility and Environmentally Stable ETLs

A critical future objective is the development of defect-controlled electron transport layers (ETLs) that exhibit electron mobility (μ_e) exceeding 50 $cm^2 V^{-1} s^{-1}$, while maintaining stable band alignment and resistance to photo-corrosion under ambient conditions. Although numerical optimization identified ZnO as a superior ETL, its practical realization requires controlled defect engineering and improved environmental robustness. Strategies include bandgap tuning through doped ZnO systems (e.g., Mg-ZnO), formation of composite ETLs such as ZnO-MXene or ZnO-graphene hybrids to enhance conductivity and interfacial compatibility, regulated oxygen-vacancy engineering to optimize carrier concentration without inducing recombination centres, and low-temperature solution processing for compatibility with flexible, scalable substrates. These advancements are expected to accelerate charge extraction kinetics, lower series resistance (R_S), and simultaneously improve fill factor (FF) and short-circuit current density (J_{SC}).

3. Long-Term Operational Stability Beyond 1000 Hours

A key future milestone is extending device durability to meet commercial benchmarks, with a target of retaining over 90% of the initial PCE beyond 1000 hours of operation under ISOS-standard thermal, humidity, and continuous illumination stress conditions. Although short-term stability (>95% PCE retention

over ~200 hours) demonstrates the effectiveness of MXene-based interface engineering, long-term degradation pathways must be further mitigated. This can be achieved through hydrophobic modification of carbon counter electrodes to suppress moisture ingress, advanced encapsulation using multilayer barrier polymers, grain-boundary passivation within CABB absorbers to limit defect-assisted degradation, and lattice-level engineering to suppress ion migration. Achieving this stability target will be decisive in translating HTL-free, MXene-modified DPSCs from laboratory-scale demonstrations to deployment-ready photovoltaic technologies.

4. **Hybrid PV-Driven Energy Harvesting and Environmental Remediation Systems**

A strategic future objective is the development of integrated hybrid systems that combine high-efficiency photovoltaic energy harvesting, green hydrogen production, thermal energy recovery, and wastewater remediation within a unified platform. The immediate performance target is to achieve solar-to-hydrogen (STH) efficiencies exceeding 5% alongside total solar utilization efficiencies greater than 75% through PV/T spectral management. Building on the demonstrated dual-functional PV-driven remediation systems and nanofluid-based spectral splitters, the next step is to optimize voltage matching between PV modules and electrochemical reactors while simultaneously enhancing optical–thermal management.

Engineering strategies include integrating high-V_{OC} tandem PV modules (>1.8 V output) to directly drive electrochemical reactions without external bias, catalyst-loaded photoelectrodes with reduced overpotentials for efficient hydrogen evolution and pollutant oxidation, and scalable flow-reactor architectures for continuous wastewater treatment. In parallel, the development of long-term stable plasmonic nanofluids with minimal agglomeration, selective optical filtering to suppress sub-bandgap thermalization losses, entropy-minimized thermal modelling, and hybrid PV-electrolyzer-thermal coupling platforms will enhance overall system exergy efficiency. Collectively, such hybrid engineering

approaches aim to create decentralized, land-efficient renewable hubs capable of simultaneous electricity generation, green hydrogen production, heat recovery, and water purification, thereby reducing system-level levelized cost of energy (LCOE) and advancing sustainable energy-environment integration.

Overall, the present progress demonstrates a shift from isolated device-level improvements toward multifunctional solar energy systems. By combining spectral management, advanced materials engineering, and integrated PV-photoelectrochemical platforms, this research contributes to a holistic renewable energy ecosystem that addresses energy security, environmental remediation, and sustainable development in a unified manner.

ANNEXURE A

COPYRIGHT PERMISSIONS FOR REPRODUCED FIGURES

A.1 Permission for Figure 1.1

Source: Srivastava, A., Shirage, P.M. (2024). Perovskite Solar Cells: Futuristic Reliable Renewable Energy Technology. In: Perovskite Solar Cells. Springer Tracts in Electrical and Electronics Engineering. Springer, Singapore. https://doi.org/10.1007/978-981-97-7624-5_1

Permission Details: Reuse permission obtained through Springer Nature License on 30 May 2026 for reuse in a doctoral thesis.

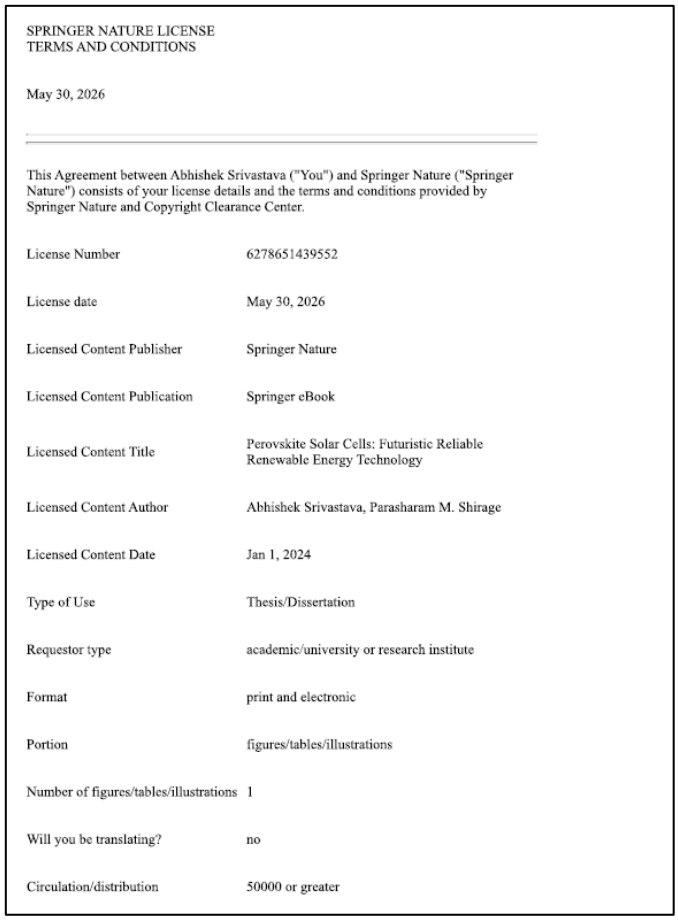

SPRINGER NATURE LICENSE
TERMS AND CONDITIONS

May 30, 2026

This Agreement between Abhishek Srivastava ("You") and Springer Nature ("Springer Nature") consists of your license details and the terms and conditions provided by Springer Nature and Copyright Clearance Center.

License Number	6278651439552
License date	May 30, 2026
Licensed Content Publisher	Springer Nature
Licensed Content Publication	Springer eBook
Licensed Content Title	Perovskite Solar Cells: Futuristic Reliable Renewable Energy Technology
Licensed Content Author	Abhishek Srivastava, Parasharam M. Shirage
Licensed Content Date	Jan 1, 2024
Type of Use	Thesis/Dissertation
Requestor type	academic/university or research institute
Format	print and electronic
Portion	figures/tables/illustrations
Number of figures/tables/illustrations	1
Will you be translating?	no
Circulation/distribution	50000 or greater

A.2 Permission for Figure 1.2 and 1.3

Source: Akula Surya Teja, Abhishek Srivastava, Jena Akash Kumar Satrughna, Manish Kumar Tiwari, Archana Kanwade, Subhash Chand Yadav, and Parasharam M. Shirage. "Optimal processing methodology for futuristic natural dye-sensitized solar cells and novel applications." *Dyes and Pigments* 210 (2023): 110997.

Permission Details: Reuse permission obtained through CCC RightsLink on 30 May 2026 for reuse in a doctoral thesis.

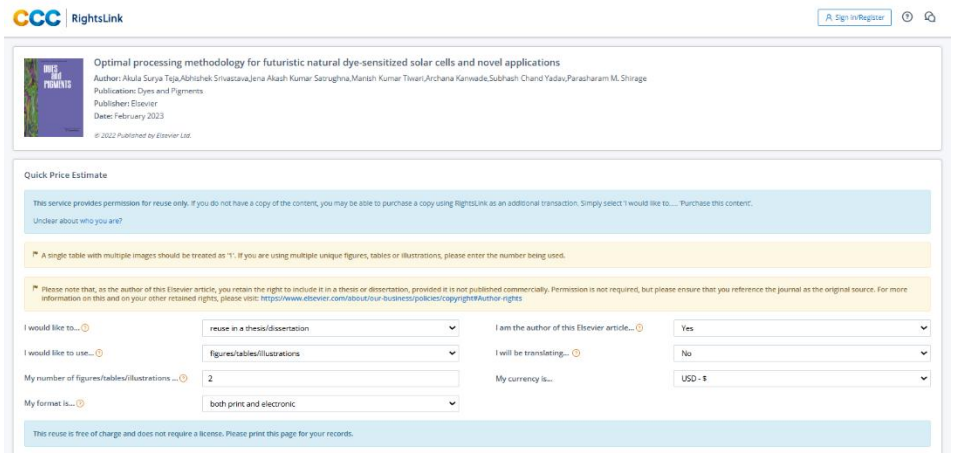

A.3 Permission for Figure 1.4

Source: Christopher Eames, Jarvist M. Frost, Piers RF Barnes, Brian C. O'regan, Aron Walsh, and M. Saiful Islam. "Ionic transport in hybrid lead iodide perovskite solar cells." *Nature communications* 6, no. 1 (2015): 7497.

Permission Details: Reuse permission obtained through CCC RightsLink on 30 May 2026 for reuse in a doctoral thesis.

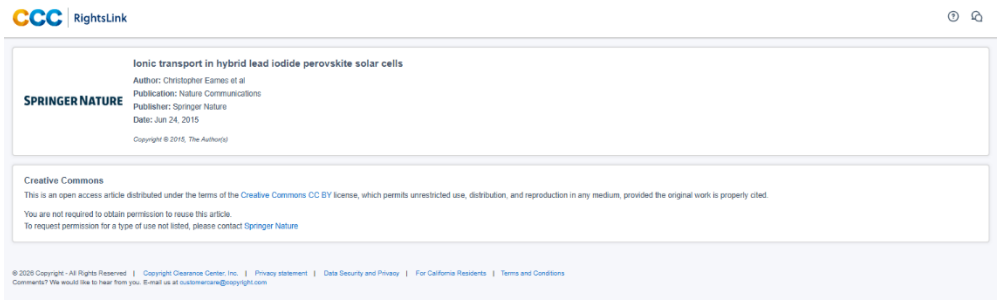

A.4 Permission for Figure 1.5(a-b)

Source: (a) Qi Chen, Nicholas De Marco, Yang Michael Yang, Tze-Bin Song, Chun-Chao Chen, Hongxiang Zhao, Ziruo Hong, Huanping Zhou, and Yang Yang. "Under the spotlight: The organic–inorganic hybrid halide perovskite for optoelectronic applications." *Nano today* 10, no. 3 (2015): 355-396.

(b) Qingde Sun, and Wan-Jian Yin. "Thermodynamic stability trend of cubic perovskites." *Journal of the American Chemical Society* 139, no. 42 (2017): 14905-14908.

Permission Details: Reuse permission obtained through CCC RightsLink and American Chemical Society License on 30 May 2026 for reuse in a doctoral thesis.

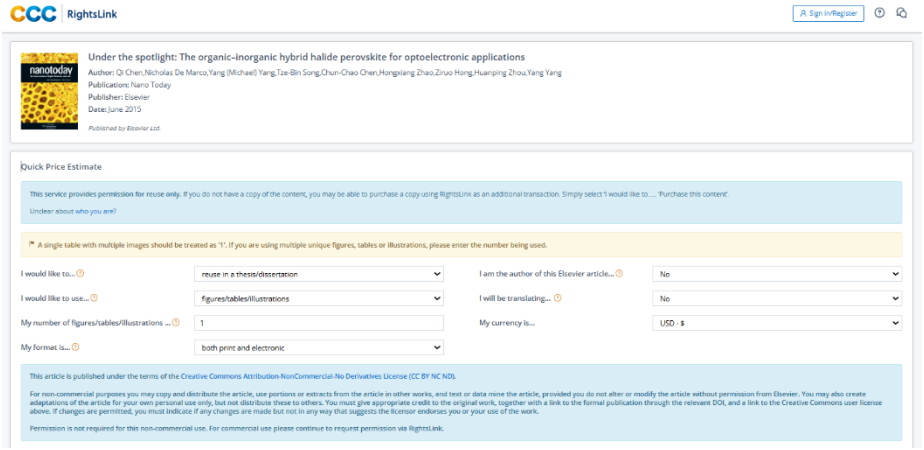

AMERICAN CHEMICAL SOCIETY LICENSE
TERMS AND CONDITIONS

May 30, 2026

This Agreement between Abhishek Srivastava ("You") and American Chemical Society ("American Chemical Society") consists of your license details and the terms and conditions provided by American Chemical Society and Copyright Clearance Center.

License Number	6278630546826
License date	May 30, 2026
Licensed Content Publisher	American Chemical Society
Licensed Content Publication	Journal of the American Chemical Society
Licensed Content Title	Thermodynamic Stability Trend of Cubic Perovskites
Licensed Content Author	Qingde Sun, Wan-Jian Yin
Licensed Content Date	Oct 1, 2017
Licensed Content Volume	139
Licensed Content Issue	42
Volume number	139
Issue number	42
Type of Use	Thesis/Dissertation
Requestor type	Non-profit
Format	Print and Electronic

A.5 Permission for Figure 1.6

Source: Abhishek Srivastava, Jena Akash Kumar Satrughna, Manish Kumar Tiwari, Archana Kanwade, Subhash Chand Yadav, Kiran Bala, and Parasharam M. Shirage. "Lead metal halide perovskite solar cells: Fabrication, advancement strategies,

alternatives, and future perspectives." *Materials Today Communications* 35 (2023): 105686.

Permission Details: Reuse permission obtained through CCC RightsLink on 30 May 2026 for reuse in a doctoral thesis.

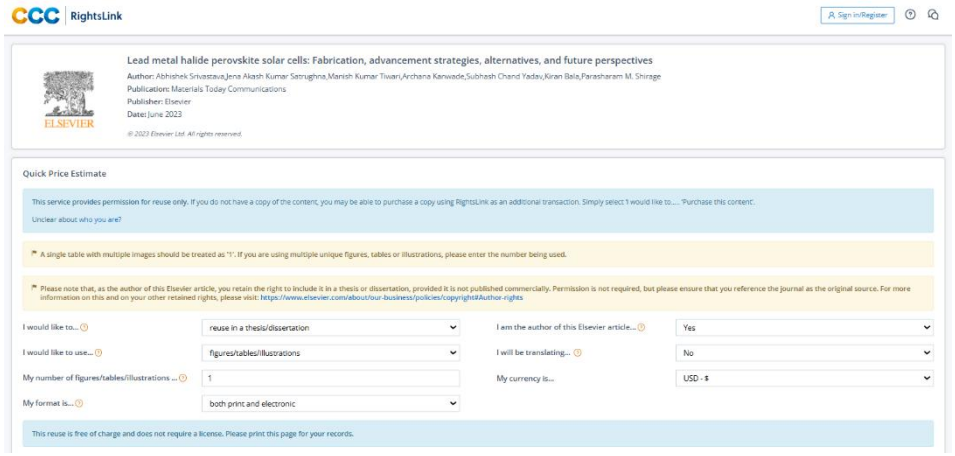

A.6 Permission for Figure 1.7

Source: William Shockley, and Hans Queisser. "Detailed balance limit of efficiency of p-n junction solar cells." In *Renewable energy*, pp. Vol2_35-Vol2_54. Routledge, 2018.

Permission Details: Reuse permission obtained through AIP Publishing License on 30 May 2026 for reuse in a doctoral thesis.

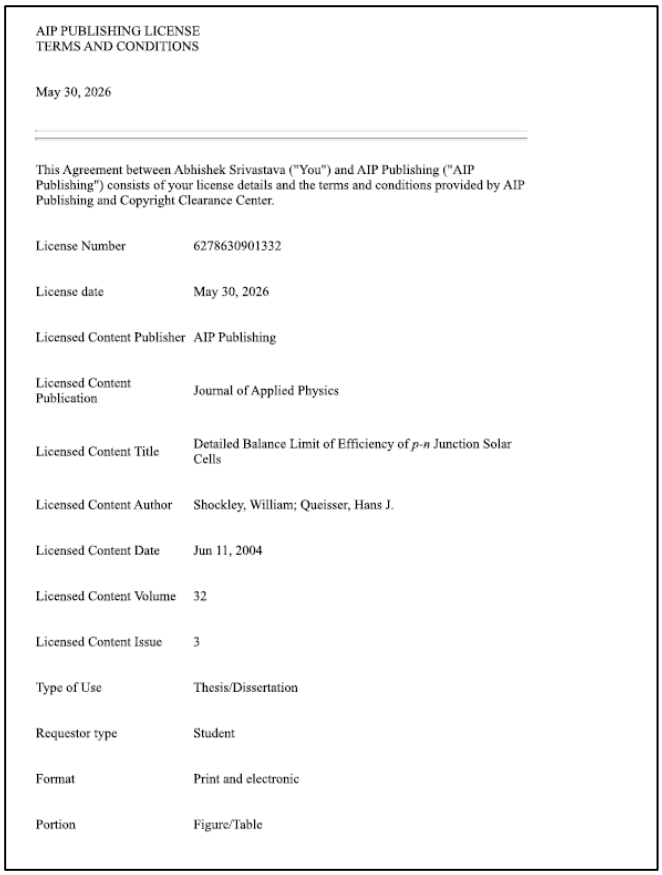

AIP PUBLISHING LICENSE
TERMS AND CONDITIONS

May 30, 2026

This Agreement between Abhishek Srivastava ("You") and AIP Publishing ("AIP Publishing") consists of your license details and the terms and conditions provided by AIP Publishing and Copyright Clearance Center.

License Number	6278630901332
License date	May 30, 2026
Licensed Content Publisher	AIP Publishing
Licensed Content Publication	Journal of Applied Physics
Licensed Content Title	Detailed Balance Limit of Efficiency of *p-n* Junction Solar Cells
Licensed Content Author	Shockley, William; Queisser, Hans J.
Licensed Content Date	Jun 11, 2004
Licensed Content Volume	32
Licensed Content Issue	3
Type of Use	Thesis/Dissertation
Requestor type	Student
Format	Print and electronic
Portion	Figure/Table

A.7 Permission for Figure 1.8

Source: Adam H. Slavney, Te Hu, Aaron M. Lindenberg, and Hemamala I. Karunadasa. "A bismuth-halide double perovskite with long carrier recombination lifetime for photovoltaic applications." *Journal of the American chemical society* 138, no. 7 (2016): 2138-2141.

Permission Details: Reuse permission obtained through American Chemical Society License on 30 May 2026 for reuse in a doctoral thesis.

AMERICAN CHEMICAL SOCIETY LICENSE
TERMS AND CONDITIONS

May 30, 2026

This Agreement between Abhishek Srivastava ("You") and American Chemical Society ("American Chemical Society") consists of your license details and the terms and conditions provided by American Chemical Society and Copyright Clearance Center.

License Number	6278631144273
License date	May 30, 2026
Licensed Content Publisher	American Chemical Society
Licensed Content Publication	Journal of the American Chemical Society
Licensed Content Title	A Bismuth-Halide Double Perovskite with Long Carrier Recombination Lifetime for Photovoltaic Applications
Licensed Content Author	Adam H. Slavney, Te Hu, Aaron M. Lindenberg, et al
Licensed Content Date	Feb 1, 2016
Licensed Content Volume	138
Licensed Content Issue	7
Volume number	138
Issue number	7
Type of Use	Thesis/Dissertation
Requestor type	Non-profit

A.8 Permission for Figure 1.9

Source: Abhishek Srivastava, Yuta Ito, Hyunju Lee, Yoshio Ohshita, Atsushi Ogura, Mahesh Dhonde, and Parasharam M. Shirage. "Multilayered 2D $Ti_3C_2T_X$-MXene: best interfacial passivating agent for dye-sensitized solar cells with V_{OC} approaching 1 V." *ACS Applied Electronic Materials* 7, no. 4 (2025): 1531-1549.

Permission Details: Reuse permission obtained through American Chemical Society License on 30 May 2026 for reuse in a doctoral thesis.

AMERICAN CHEMICAL SOCIETY LICENSE
TERMS AND CONDITIONS

May 30, 2026

This Agreement between Abhishek Srivastava ("You") and American Chemical Society ("American Chemical Society") consists of your license details and the terms and conditions provided by American Chemical Society and Copyright Clearance Center.

License Number	6278631288338
License date	May 30, 2026
Licensed Content Publisher	American Chemical Society
Licensed Content Publication	ACS Applied Electronic Materials
Licensed Content Title	Multilayered 2D Ti3C2TX-MXene: Best Interfacial Passivating Agent for Dye-Sensitized Solar Cells with VOC Approaching 1 V
Licensed Content Author	Abhishek Srivastava, Yuta Ito, Hyunju Lee, et al
Licensed Content Date	Feb 1, 2025
Licensed Content Volume	7
Licensed Content Issue	4
Volume number	7
Issue number	4
Type of Use	Thesis/Dissertation